UNIVERSITY OF SOUTHAMPTON
FACULTY OF ENGINEERING AND APPLIED SCIENCE
INSTITUTE OF SOUND AND VIBRATION RESEARCH

THE RADIATION FROM ACOUSTIC SOURCES WITHIN A FINITE LENGTH CIRCULAR DUCT IMMERSED IN WATER

Dean A. K. Hewlett

A thesis submitted for the award of
Doctor of Philosophy.

May 1995

UNIVERSITY OF SOUTHAMPTON
FACULTY OF ENGINEERING AND APPLIED SCIENCE
INSTITUTE OF SOUND AND VIBRATION RESEARCH

Abstract

The Radiation from Acoustic Sources within a Finite Length Circular Duct Immersed in Water

The radiation from waveguide and duct terminations is an important area in the field of acoustics. The radiation from acoustic sources in ducts has already been the subject of much attention, most of the work carried out in this area being associated with aero-engine noise. Consequently, with less obvious practical application, little attention has been paid to similar problems in water. In this thesis a mathematical model of the radiation from a source in a finite length duct is developed. This is an extension of an earlier study of the radiation from a semi-infinite duct. Whilst this model has been developed for a duct immersed in water, the expressions derived are equally applicable to air. However, since the duct examined in this thesis is in water, then it is realistic to examine the radiation from a duct that has a pressure release lining at the duct wall. This would be a futile study if conducted in air, since the pressure release boundary condition is impossible to achieve in that medium. Good approximations to an ideal pressure release boundary in water are possible in practice using a closed cell neoprene foam fixed to the duct wall. It is likely that such a lining could be used to reduce the sound radiated by a source within the duct. The mathematical model derived enables the pressure outside the duct to be calculated provided that the duct terminates in a rigid baffle. Experimental results are compared with those obtained from this model, and the agreement is found to be very good over a wide range of frequency. It found that the introduction of a pressure release lining at the duct wall will significantly reduce the sound power radiated by the source in the duct, when compared with a duct with a hard wall. Finally a spatial Fourier transform method is described for the prediction of the far-field pressure from measurements made near to the duct exit. Despite initial promise, this technique is found to have severe limitations, most notably associated with the numerical evaluation of the finite length two dimensional Fourier transform. Avoiding wraparound error is shown to be a major difficulty when using this technique to propagate a field an appreciable distance.

Acknowledgements

I would like to express my sincere gratitude to the following people who have helped me in the completion of this thesis. I owe a huge debt to my supervisors, Professor P. Nelson and Professor C. Morfey, who were a constant source of inspiration and without whom I would certainly never have completed this work. I would also like to thank the numerous staff in the ISVR with whom I have enjoyed many interesting discussions over the years. In particular I would like to thank Professor J. K. Hammond and Professor F. J. Fahy for their help during some difficult times.

No acknowledgement would be complete without my mentioning the following individuals who helped me in their own way: Naim Audio, Bob Berg, Michael Brecker, John Coltrane, Miles Davis, Dave Guardala, Henri Selmer, Wayne Shorter.

Finally, I would like to thank Dawn for her immeasurable love, support and understanding given to me over the years. I dedicate this thesis to her.

Hell, if you understand everything I say, you'd be me.

miles davis (1926 - 1991)

Contents

Chapter 1

Introduction

1.1 Overview

This thesis is concerned with the analysis of the sound field generated by an acoustic source within a finite length circular duct immersed in water. One of the primary reasons for this study is the investigation of the radiated acoustic energy from a source within a pressure release lined duct. A pressure release boundary is one in which the pressure vanishes over that boundary. Pressure release surfaces are impossible to achieve in air, and as such are rarely considered by acousticians working on problems associated with that medium. By contrast, approximate pressure release boundaries are commonly observed in underwater acoustics. Perhaps the most obvious example of an approximate pressure release boundary for sound waves in water is that provided by the water/air interface at a free water surface.

If it is required to reduce the radiation from a source within a duct, the logical first step would be examine the nature source mechanisms themselves to see if there were any way to reduce the output at the source. Unfortunately, it is not always possible to adequately model the source mechanisms, or to reduce the output of the source region. It is usually easier, and more practical to attempt to attenuate the acoustic energy as it travels within the duct. This attenuation is conventionally achieved by the application of either an absorptive acoustic treatment to the duct wall, or by the introduction of reactive elements within the duct. Both of these methods are aimed at attenuating the propagating acoustic energy within the duct. This approach has been widely used in the area of aero-acoustics for example, and has resulted in large quantities of published work solely concerned with the optimisation of the duct lining for different source types or duct geometries. The maximum attenuation possible is limited by the length of the duct; the energy distribution amongst the modes within the duct; and the type of acoustic treatment used. This limit may be satisfactory for long ducts or where only small reductions are required. Usually, however the duct is short, *and* large attenuation is required. In this situation, absorptive treatments would be ineffective as the duct is short. In the study of jet engine noise- the bulk of which of which was carried out during the 1960's and 1970's- trying to squeeze the "last ounce" of attenuation out of a

relatively short length of duct became the focus of much attention by researchers in aero-acoustics.

If the required attenuation of a noise source in a duct is not in air but in water, it is also possible to use acoustic treatment at the duct wall in a similar fashion to that used in air. Again if the duct is short, i.e. if the length to diameter ratio is less than one, these treatments will be severely limited in their ability to reduce the radiated sound from the open end of the duct. As mentioned above it is also possible to produce a pressure release boundary in water. It may be possible to capitalise upon this unique feature of water, and use it to reduce the radiation of the source *into* the duct. The acoustic power output of the source is a simple function of the real part of the acoustic radiation impedance of the source. The duct presents an impedance load into which the source is radiating. Changing the acoustic impedance of the duct wall will change this load that the source "sees". Thus there will be a different radiation impedance of the source for a hard wall duct and a pressure release lined duct. It is hoped that this difference between the two impedances will yield a lower output power for a pressure release lined duct. This is the principal noise reduction method described in this thesis, and it is fundamentally different from those commonly employed in air. It should be noted that no attempt is made to absorb the acoustic energy as it travels within the duct. No reduction of the acoustic energy is possible using a pressure release lining at the duct wall as there is no absorption at a pressure release boundary.

1.2 Organisation of the thesis

Originally, at the commencement of this project, an experimentally based approach for the analysis of the radiation of simple sources within a duct was developed. Previous work in the area of acoustic holography had indicated that it was possible to predict the far-field simply from measurements made near to a source. Therefore, a large percentage of the research effort was deployed in setting up an experimental rig to measure the field close to the end of a duct containing a source. It was believed that by measuring the acoustic pressure near to the open end of the duct, that this may be used to predict the far-field pressure by a wave propagation technique similar to those methods used in acoustic holography. In principle at least, it seemed possible to examine the far-field radiation from both types of duct, hard wall and pressure release, by measuring over a plane just outside the duct. Unfortunately, the propagation technique proved to be fraught

with numerical problems. Most of these were associated with the finite length Fourier transform. This experimental approach was therefore supplemented with a mathematical analysis of the duct radiation problem. Even though the measured pressure field sampled near to the end of the duct could not be used to predict the acoustic far-field, it is still valuable information, and may be used to check the accuracy of the analytical model.

The analytical study of the radiation from the duct is described in detail in Chapter 2. This model is based upon an earlier study by Zorumski (1973), who formulated a solution for the radiation from a semi-infinite duct terminating in a rigid baffle. Most importantly, Zorumski derived expressions for the modal radiation and reflection coefficients at the open end of the duct. Since the modes are coupled, one incident mode gives rise to an infinite series of reflected modes back into the duct. In Chapter 2, the Zorumski semi-infinite duct problem is extended to include the radiation from a duct of finite length. In principle, this model enables the calculation of the internal acoustic field within the duct containing any source distribution. In this thesis, the model is restricted to the examination of the radiation from a point monopole source within the duct. The analytical model solves the axial particle velocity over the two ends of the duct. Since the duct is terminated in a rigid baffle it is a straightforward task to calculate the externally radiated field using the Rayleigh integral. There are several important features of this model that should be made clear. The first is that it is analytically exact. Since the duct finishes in a rigid baffle at both ends of the duct, the calculation of the modal reflection coefficients at either end of the duct is not influenced by the field radiated by the other end. Secondly, the solution for the internal field is expressed in such a manner that it may be readily evaluated using a desktop computer. Also, whilst there is emphasis given to the study of hard walled and pressure release lined ducts in this thesis, it should be noted that the mathematical model derived in Chapter 2 is valid for any arbitrary wall impedance.

Chapter 3 describes the experimental work mentioned above, which measures the pressure over a large plane outside the duct. Whilst this data is not used to predict the far-field as was originally intended, it is still very useful as a comparison with results from the analytical model derived in Chapter 2. The field outside the duct is measured over a rectangular plane perpendicular to the duct axis. A total of 4096 separate pressure measurements are made of the external field. Due the very large number of measurements it was necessary to design the experiment so that it could be totally controlled by a computer. By adopting remote control of the

experiment it is possible to arrange for the computer to be made responsible for the location of the receiving hydrophone, the generation of the source signal, and the capture and analysis of the final pressure.
In Chapter 4 an acoustic propagation technique is described. As mentioned earlier, it was originally intended to use this technique to forward propagate the measured field from the end of the duct. However, it is shown in Chapter 4 that there are many numerical errors incurred when implementing this technique in practice. The most common causes of error are outlined in this chapter. It is found that most of the problems arise due to the 2D Fourier transform used to calculate the new field.

In the final chapter, conclusions and recommendations for future work are presented.

Chapter 2

Theoretical Analysis of Sound Radiated from a Source in a Duct of Finite Length

2.1 Introduction

In this chapter an analytical model will be derived of the sound field radiated from a circular duct containing an acoustic source. By comparison with the experimental approach that will be discussed Chapter 3, an analytical model potentially offers greater speed and flexibility. Given a rigorous analytical model of the duct radiation, it is much easier to examine the radiation from different source positions and different duct linings using a model than to attempt to measure the field experimentally. To illustrate this point, the experimental design that is described in Chapter 3, measures 4096 spatial points in the field just outside the duct. This process takes more than 40 hours to complete. Obviously, using experiments as an investigative tool is not an efficient approach, since any small change requires a repeat series of measurements, plus the time taken to set up the experiment and analyse the data. Furthermore, if a suitable analytical model was developed, it would be possible for a source to take any form, i.e. monopole, dipole, etc., and be located anywhere within the duct. By contrast, it has been shown by Hewlett (1992), that there are considerable practical difficulties in generating accurate, higher order acoustic sources in water for experimental purposes.

2.2 Literature review

To assist in the development of an analytical model, a literature review was conducted. Perhaps not surprisingly, the bulk of published work in the area of duct acoustics is concerned with applications in aero-acoustics. The requirement to reduce the noise of jet aircraft was responsible for a considerable number of analytical and experimental studies of duct acoustics in the 1960's and early 1970's. The following literature review, whilst certainly not exhaustive, has attempted to focus upon previous work that is believed to be the most applicable to the present problem. It is worth noting that despite the abundance of available literature, no reported work relating to the radiation of sound from a circular duct in water was found. It is believed that previous work investigating the radiation of sound from a duct in air, may be applied to a duct in water. However, there are

differences and assumptions that need to be made if using a theory derived for use in air is to be applied to a similar problem in water. Most notable amongst these differences are the following;

- The fluid loading upon the duct wall vibration is usually ignored in air, but this may be significant in water. In this thesis this effect will be ignored.

- There is great difficulty in obtaining acoustically rigid structures in water, whereas these are easy to achieve in air. Therefore if a duct is assumed to have a hard wall in water, then this may be difficult to achieve in practice. A more realistic approach would be to include wall vibration, and vibrational waves within the duct wall. These effects are considered to be beyond the scope of this thesis.

There is a significant, albeit subtle difference between the methods commonly adopted by researchers in the area of aeroacoustics and that proposed in this study. In the present context the attempted reduction in the far field pressure does not rely upon absorptive or reactive liners to provide attenuation within the duct. In this thesis it is intended to reduce the power radiated by modification of its radiation impedance. It is proposed that a pressure release liner at the duct wall will be used to introduce a region of vanishing pressure at the duct wall. It will be shown later in this Chapter that the modal amplitudes are calculated using the value of the mode shape function at the position of the source. If the source was a monopole placed near to a pressure release wall, then the value of the mode shape function at the source will be very small. Hence the source will be ineffective at driving the field within the duct. This method of source reduction is not possible in air, as an adequate pressure release lining is impossible to achieve in air. If the duct length to diameter ratio is small, absorptive liners would be limited in their ability to significantly reduce the acoustic radiation from the duct. This is not true when using a pressure release liner to modify the source, as it is only necessary to have a duct of sufficient length that the source may be modelled as one of higher multipole order. To what extent a duct should be lined with such a material is beyond the scope of this present study.

The following gives a summary of the objectives of the analytical model, and these objectives were used in selecting the literature chosen for discussion later.

- The analytical model should enable the calculation of both near and far-field pressures produced by a source in a circular duct, with a hard and pressure release lining at the wall.

- Preferably the model should be for a finite length duct since this is the most representative of the real duct radiation problems. Semi-infinite ducts are not usually realised in practice.

In conducting the review the following parameters were excluded from the analysis:

- Flow. The highest Mach number of interest in this thesis is extremely low ($M < 0.05$), and therefore the effects of flow upon the acoustic propagation within the duct may be ignored.

- In this thesis there is no attempt to model the rotational effect of the source, and attention is restricted to stationary distributions of simple multipole sources to investigate the effect of pressure release linings upon the radiated sound field. The acoustic field produced by rotating sources has been widely reported in the literature; e.g. Tanna and Morfey (1971), and Wright (1972 and 1976). The influence of rotation of the source upon the radiated acoustic field is dependent upon the rotational Mach number of the source, which in this case is very small.

Tyler and Sofrin (1962) have investigated the propagation and radiation from semi-infinite duct. Morse (1948), describes the propagation of modes as a time varying acoustic pressure distribution as seen at a stationary point within the duct. Morfey (1964), uses the phrase *spinning modes* to describe the acoustic field in the duct. Instead of a time varying field in fixed space, the propagating modes may be thought of as a time invariant pressure distribution across the duct cross-section that spins as it moves down the duct. The axial velocity of the propagating mode depends upon the frequency relative to the cut-off frequency, as does the angle the mode makes with the duct wall. Essentially as cut-off is approached the angle the mode makes with the duct wall becomes larger, so that the mode is further attenuated by any lining on the duct wall. Morfey shows pictorially the effect of cut-off upon the helical pattern that the duct mode makes as it is traced through the duct. As the frequency is reduced near to cut-off the helix becomes stretched,

until, at cut-off, the pattern is similar to a paddle wheel, and there is no net propagation down the duct. Equations describing the pressure distribution in a hard-walled duct are given for monopole and dipole sources placed within the duct. The corresponding acoustic intensity is also derived for these sources.

Both of the above studies by Tyler and Sofrin (1962) and Morfey (1964) have examined the acoustic radiation from a semi-infinite baffled duct. An expression for the radiation from such a duct is given in terms of modal amplitudes. Morfey (1964) has derived expressions for the real part of the acoustic impedance for the open end of the duct for (m,0) modes, where m denotes the azimuthal order of the duct mode. These can then be used to determine the sound power radiated from the duct.

The radiation efficiency of higher order acoustic duct modes from a hard-walled, circular and annular duct, terminating in a baffle have also been discussed by Morfey (1969). Graphs of the variation of radiation resistance with frequency are presented as a generalised relationship in terms of the mode cut-off frequency. Morfey concludes that the modal velocity distribution across the duct face radiates with an efficiency close to unity for a frequency appreciably above cut-off for a given mode. Below the cut-off frequency, radiation is shown to fall rapidly as the frequency is reduced. A method for calculating the acoustic radiation impedance of a hard walled circular duct is also given. However, the method requires that the duct is assumed to terminate at the end by an infinite baffle. For this reason the method ignores the effect of the acoustic radiation at angles greater than 90 degrees to the duct axis. The experimental work reported by Tyler and Sofrin (1962), has shown that in some cases near cut-off there is a significant contribution made to the far-field pressure from such *backward* radiation.

In the case of a duct terminated by an infinite baffle, Zorumski (1973) has published a method for calculating the modal impedance and reflection coefficients for a semi-infinite duct with arbitrary wall impedance. This paper contains a few important mistakes in the presentation of numerical results, but the analysis will be shown to be robust in a later section in this chapter. This is not a trivial problem to solve, however it is possible that the modal reflection coefficients may be used to calculate, mode by mode, the internal sound field within the duct. Since the duct ends in a rigid baffle, it is possible to use the Rayleigh Integral to calculate the pressure at any point outside the duct.

The acoustic propagation of sources within, and the subsequent radiation from, a rectangular duct is analysed in two companion papers by Doak (1973a, 1973b). Whilst the analysis presented is for a hard-walled rectangular duct, some very useful conclusions can be drawn from this study that will apply equally to a circular duct. In the first paper, Doak (1973a), describes the effects of source distributions within the duct. Unfortunately there does not appear to be any reference to the modes in the duct being coupled, as is illustrated by Zorumski (1973).

The second of these two papers is concerned with the effect of duct length on the sound field both inside and outside the duct. It is shown that internal reflections have an effect upon the radiation impedance, and what is more important for the production of sound power, the radiation resistance of the radiating source. An example is discussed in which a duct with one end was open and the other anechoic, thus producing a semi-infinite duct. It is not clear that the solution for the internal field includes the effect of the modes being coupled, which is discussed by Zorumski (1973).

The acoustic propagation within a cylindrical duct with soft walls has been discussed by Rice (1969) and (1975). Rice shows that as the sound propagates down a soft walled duct with a length to diameter ratio of greater than one, there is a redistribution of sound power toward the centre line axis of the duct. Rice also presents graphs showing the maximum attenuation possible for a given set of modes by optimising the wall impedance. These graphs are calculated by first optimising the impedance of the duct lining for each mode separately. In most practical cases however, there is more than one mode that is significant in carrying acoustic energy. The need to optimise the impedance of the lining for more than one mode will always compromise the maximum attenuation possible for each mode if treated separately.

Lansing and Zorumski (1973), have analysed the problem of a multi-sectioned duct by studying an infinite length rectangular duct containing flow. Zorumski (1974), has separately published work on acoustic propagation in a multi-sectioned circular duct. In this circular duct one end has a rigid wall in which a monopole source is located at the centre. The other end of the duct is terminated by an infinite baffle. At each interface between two different sections, and at the termination, the modes generated by the source are partially reflected and partially transmitted as a new set of modes into the adjacent section. This process therefore

results in a very complicated standing wave pattern within each duct section. A corresponding matrix solution is given for the equations describing the pressure distribution within the duct.

The radiation from a hard walled, semi-infinite circular duct that does not end in an infinite baffle, have been examined by several authors. The first analytical solution was obtained by Levine and Schwinger (1948), and this paper may be considered to be a pioneering study in this field. This paper gave the first rigorous solution based upon the Wiener-Hopf technique for the simple case of a plane wave propagating within the duct. Using this work, the inclusion of higher order modes within a hard walled duct was analysed by Weinstein (1969).

Due to the complexity of the Wiener-Hopf technique, the approach and results presented by Weinstein (1969) found little immediate engineering application. Not until the necessity to predict and reduce the noise level of commercial aircraft in the early 1970's did the technique become more widely used. Amongst the work that did apply the Wiener-Hopf technique, and incidentally the most readily applicable to the present problem, is that by Lordi *et al* (1971, 1973, 1974), and Homicz *et al* (1975). Mathematical expressions are given for the far-field radiation from an unbaffled circular duct given a certain internal incident mode upon the end of the duct. Whilst the expressions for the far-field radiation pattern are somewhat complex, the essential principle in calculating the far-field from modal reflection coefficients remains similar to that using the method of Zorumski (1973). However, the expressions for the field outside the duct are only applicable at a distance of many duct radii. This then rules out the possibility of using this analysis to compare with measured data near the duct exit. This highlights the difficulty of using a model of the duct that does not include a rigid baffle at the end of duct; namely that it prevents the use simple methods such as the Rayleigh Integral to calculate the external pressure field.

Lordi, Homicz and Rehm (1973) and (1974), have presented work for a similar radiation problem. The solution for the external radiation is written in terms of analytical expressions for the directivity pattern for a given mode. Following this analysis, Homicz and Lordi (1975), have shown that certain approximations may be made to this exact solution to enable useful information to be obtained about the radiation pattern without recourse to a digital computer. The location of the principal lobe in the radiation pattern can be calculated and the location of minima in the radiation pattern. A sample application of these simple formulae is also

given and compared with an exact solution. Useful qualitative information concerning the duct radiation pattern is also derived from the exact solution. Homicz and Lordi (1975) show that the number of lobes in the radiation pattern produced by a given duct mode is determined by the number of modes that may propagate freely in the duct above their cut-on frequency. It is not clear from this paper if this would also be true for a duct with soft walls. The previous work by Homicz and Lordi is based almost wholly upon the earlier work of Weinstein, but also includes the work by Lansing (1969), which used the Wiener-Hopf technique to examine the effect upon the radiated field of introducing a uniform axial flow within the duct.

An alternative computational method for the calculation of the radiation from a baffled and unbaffled, semi-infinite duct with hard walls is given by Beckemeyer and Sawdy (1975). An approximate solution based upon a spherical wave function technique is compared with other previously published methods for the unbaffled duct. Directivity patterns calculated using previous work are compared with those produced by the new method. Agreement is shown to be good for the example used of a plane wave incident on the end of the duct.

The case of a finite length duct, has been examined by Johnson and Ogimoto (1980). In this paper the Wiener-Hopf technique is used to calculate the internal and external acoustic fields. When examining a finite length duct, the possibility exists for there to be acoustic interaction between the two ends of the duct. Johnson and Ogimoto overcome this problem by only considering a duct in which the length is chosen to be sufficiently large that this interaction may be ignored.

This acoustic interaction between the ends of the duct is discussed extensively by Wang and Tszeng (1984). The effect of the interference between the two duct apertures is identified in the calculations of the radiation impedance, reflection coefficient, and subsequently the far-field radiation pattern. It is shown that the interference effects between the two ends reduces for high frequency waves and for long ducts. This effect can be understood by considering the radiation impedance of each end of the duct separately. The value of the radiation impedance is governed not only by the self impedance of the end, but also by a mutual impedance term between the two ends. It is intuitively obvious that the mutual impedance term will diminish as the relative length of the duct is increased compared to the wavelength. For higher order modes, Wang and Tszeng also make comparisons between the far field directivity patterns of different duct geometries

for a single duct opening (semi-infinite duct) and a double duct opening (finite length duct). The results presented indicate that for small values of *ka* the radiation at angles more than 90° to the duct axis is significant.

This fact has previously been observed by both Lordi *et al* (1974) and Lansing (1969). Because of this significant radiation at angles more than 90° to the duct axis, it is possible in a short length duct that the radiation from one end will directly interfere with the radiation from the other end of the duct. Therefore a difference in the directivity patterns for low values of *ka* with a short length duct, and a semi-infinite duct should be expected. Homicz and Lordi (1975), have demonstrated that modal order is shown to influence the radiation pattern of a short length duct, since the directivity pattern is related to the order of the incident mode. Graphs of the far field directivity are presented for the first 3 azimuthal mode orders. It is shown that as *ka* increases beyond a value of 6, the acoustic radiation at angles greater than 90° to the duct axis, reduces dramatically. For a longer length duct, these effects will be reduced because the two external fields have a greater separation than from a short duct.

Rice (1978), has applied approximations to Bessel functions in terms of a series of sine and cosine terms to describe analytically the radiation pattern produced by a large number of modes incident upon the end of a flanged, hard-walled duct. This is an extension of previous work by Saule (1977), which whilst not using the approximations made by Rice (1978), was limited to the special case of equal power in each mode. Rice compares the predicted far-field pressure given by both methods for an example that assumes equal power per mode. The agreement between the exact and approximate solutions is shown to be very good for a summation of 1000 modes. Rice makes the observation that the approximate solution does neglect the contribution from some of the side lobes. The exact solution however, shows that the number of side lobes is dependent upon the radial mode number *n*. This analysis follows from similar work conducted by Rice, (1976a) and (1976b), in which the attenuation characteristics of duct liners are optimised for different modes in the duct.

2.3 Summary and conclusions from the literature.

The analysis of acoustic propagation in cylindrical waveguides has been widely published in the literature. In particular, the case of a hard walled, infinitely long,

axisymmetric duct has often been studied. However, the infinitely long duct does not allow for the reflection of acoustic energy at a duct termination, or take into account sound radiation from an open end of the duct. It is thought that the case of either a semi-infinite or finite length duct would be more relevant for the purposes of the present study.

Before a derivation of an analytical model the following important observations from the literature are worth noting:

(i) The case of a duct terminated by an infinite baffle is simpler to model and has the added advantage that the acoustic near field may be calculated using the Rayleigh Integral. This would enable comparison between the measured experimental data and predictions, and would also enable the prediction of the important wavenumber spectrum near to the duct exit. It is necessary to arrange the measurement plane as close to the duct as possible for accurate far field predictions, and to avoid windowing problems at the edges of the measurement array. However it is essential to place the measurement plane sufficiently far away from the duct to avoid the measurement of high order evanescent modes close to the duct exit. These evanescent modes may cause aliasing due to finite bandwidth of the measurement system.

(ii) The disadvantage of using a baffled model is that it ignores all radiation at angles more than 90° to the duct axis. It has been reported in the literature that this error is large at low *ka* and low modal order. This may not be important given the high frequency nature of the source to be modelled.

(iii) Expressions for the far-field directivity associated with an unbaffled duct have been derived previously. However these are lengthy, and may take considerable time to compute over a wide frequency range. Also expressions are not available for the near-field of an unbaffled duct.

Having conducted a literature review, it is proposed that the calculation of the far-field radiation from the duct be divided into two separate problems. The first task is to calculate the internal acoustic field within the duct for a given acoustic source. Once this has been determined, then the pressure and particle velocity over the end of the duct can be specified. Assuming the duct is terminated by an infinite

baffle, the particle velocity over the end of the duct may then be used to calculate the acoustic pressure outside the duct using the Raleigh Integral. In this way it is possible to compare experimentally obtained pressure data over the 64x64 position array, with pressure values derived from the mathematical model.

The ultimate objective of the mathematical model is to describe and examine the propagation and radiation from a *finite length* duct containing a source. Given the level of complexity of the finite length duct problem, it is necessary to analyse several intermediate (and simpler) problems before attempting to solve for the finite length duct. This approach is extremely desirable as it avoids the underlying physical principles from becoming obscured by the detailed mathematics.

2.4 A simple model of the sound propagation within an infinitely long circular duct

In this section the important equations relating to the propagation of acoustic waves through a circular waveguide are presented. Before attempting to analyse the behaviour of a finite length duct, it is important to understand the physical principles of acoustic propagation within a simple circular duct. The most straight forward is perhaps the case of a uniform and infinitely long duct, with acoustic waves only travelling in the positive direction. This simple approach ignores reflections caused by discontinuities in the duct (such as an open end), but it does act as a useful vehicle for appreciating the more complex problem described later in section 2.6.

Morse (1948), has shown that the *positively travelling* pressure distribution in an infinitely long circular duct can be expressed as a series of duct modes. The complex pressure contribution from each mode may be written as (see figure 2.1)

$$p_{mn}(r,\theta,z) = A_{mn}J_m(k_r^{mn}r)e^{-j(m\theta+k_z^{mn}z)}. \qquad (2.4.1)$$

Where A_{mn} is an amplitude coefficient, and r, θ and z refer to the radial, azimuthal and axial components respectively. J_m is the Bessel function of the first kind of integer order m. Note also that each mode within the duct has its own axial wavenumber k_z^{mn}, and radial wavenumber k_r^{mn}. The indices, m and n refer to the azimuthal and radial order of the mode. The value of k_r^{mn} is determined by the boundary conditions at the duct wall, and the relationship between this radial

wavenumber and the axial wavenumber, k_z^{mn}, will be given later. A suppressed time dependence of $e^{j\omega t}$ is understood throughout.

Notice also that the pressure of each mode may be considered to be the product of a modal amplitude and phase terms, $A_{mn}e^{-jk_z^{mn}z}$, and a mode shape function, $J_m(k_r^{mn}r)e^{-jm\theta}$.

As there are no reflections, the total field within the duct is an infinite sum of these *forward propagating* duct modes, and is given by

$$p_{total}(r,\theta,z) = \sum_{m=-\infty}^{\infty}\sum_{n=0}^{\infty} A_{mn}J_m(k_r^{mn}r)e^{-j(m\theta+k_z^{mn}z)}. \tag{2.4.2}$$

Applying conservation of linear momentum in the radial direction to equation (2.4.1) gives

$$\frac{\partial u_r^{mn}}{\partial t} = -\frac{1}{\rho}\frac{\partial p_{mn}}{\partial r}, \tag{2.4.3}$$

where u_r^{mn} is the radial particle velocity of the $(m,n)^{th}$ order mode, and ρ is the density of the surrounding fluid medium.

This results in the following expression for the particle velocity in the radial direction, i.e. normal to the duct wall, for a single duct mode

$$u_r^{mn}(r,\theta,z) = -\frac{A_{mn}k_r^{mn}}{j\omega\rho}J'_m(k_r^{mn}r)e^{-j(m\theta+k_z^{mn}z)}, \tag{2.4.4}$$

where the prime on the Bessel function indicates a derivative with respect to the argument r.

The above equations for the pressure and particle velocity can be related to the acoustic impedance Z, at the duct wall by

$$Z = \left.\frac{p_{mn}}{u_r^{mn}}\right|_{r=a}, \tag{2.4.5}$$

where a is the duct radius. Using equation (2.4.5) it can be shown that the radial wavenumber satisfies the following relationship

$$J_m(k_r^{mn}a)+\frac{Zk_r^{mn}}{j\omega\rho}J'_m(k_r^{mn}a)=0, \tag{2.4.6}$$

which simplifies to

$$jk\,J_m(k_r^{mn}a)+\frac{Zk_r^{mn}}{\rho c}J'_m(k_r^{mn}a)=0. \tag{2.4.7}$$

Note also that the acoustic impedance at the duct wall, Z, may be defined non-dimensionally as

$$\frac{Z}{\rho c}=\zeta_r+j\zeta_x, \tag{2.4.8}$$

where ζ_r is the non-dimensional acoustic resistance, and ζ_x is the non-dimensional acoustic reactance of the duct wall.

Equation (2.4.6) above then becomes, in terms of the useful frequency parameter ka or Helmholtz number

$$jka\,J_m(k_r^{mn}a)+k_ra(\zeta_r+j\zeta_x)J'_m(k_r^{mn}a)=0. \tag{2.4.9}$$

From the above it can be seen that if the duct wall impedance is allowed to take both real and imaginary values then the radial wavenumber k_r^{mn} will also be complex. Thus for an arbitrary wall impedance, $\zeta_r+j\zeta_x$, then from equation (2.4.9) Bessel functions of complex argument must be computed to solve for k_r^{mn}.

However there are two limiting cases of particular interest in the present context, these are the hard wall and pressure release boundary conditions. The hard wall boundary condition requires that the particle velocity must be zero at the duct wall. (Or equivalently the momentum equation states that the pressure gradient must also be zero at the duct wall). From (2.4.3), and equating the particle velocity to zero results in the following condition for the radial wavenumber

$$J'_m(k_r^{mn}a) = 0. \tag{2.4.10}$$

Thus for any given value of m, there will be infinitely many values of $k_r^{mn}a$ that satisfy this equation, and these are given by the zeros of the Bessel function derivative, $J'_m(k_r^{mn}a)$. However, it will be shown that there exist only a *finite* number of $k_r^{mn}a$ values that represent modes that can propagate freely and carry acoustic energy. These correspond to modes that have real axial wavenumber.

The axial and radial wavenumbers are related by the following equation

$$k_z^{mn} = \sqrt{k^2 - k_r^{mn2}}. \tag{2.4.11}$$

By inspection of equation (2.4.11) it can be seen that there exists a maximum value of k_r^{mn} such that the axial wavenumber k_z^{mn} remains real. This is termed the *cut off frequency* for a given mode, and is given by the condition

$$k_z^{mn} = \sqrt{k^2 - k_r^{mn2}} = 0. \tag{2.4.12}$$

Alternatively, this may be viewed as there being a lower limit to k, (which may be the frequency of a source), such that the source may propagate waves within the duct of a certain modal order. Expressed in this way, the term *cut-on* is often used.

From the above it can be seen that if k_r^{mn} is larger than k then the axial wavenumber will be purely imaginary. From the expression for the acoustic pressure given by equation (2.4.1), then it can be seen that this represents an exponentially decaying, or evanescent wave. Referring to (2.4.2), the field may be described as an *infinite* series of modes, but there will be only be a *finite* number that can propagate within the duct.

The pressure release boundary condition at the duct wall requires a vanishing pressure when r is equal to the duct radius. Equation (2.4.1) gives the following solutions for $k_r^{mn}a$

$$J_m(k_r^{mn}a) = 0. \tag{2.4.13}$$

As before, the above equation represents an infinite series of solutions for $k_r^{mn}a$ which correspond to the cut on frequencies for all possible mode shapes across the duct.

In the discussion of both types of duct, the suffices m and n have an important physical interpretation. For any value of $k_r^{mn}a$, then this corresponds to a particular mode shape in the duct that has m diametrical pressure nodes and n circumferential pressure nodes.

2.5 The acoustic field produced by a point source within an infinite length circular duct.

The previous analysis provides a means of understanding the principles involved in the propagation of a series of acoustic modes within an infinitely long duct. However, the excitation of these modes has been overlooked. The source mechanisms were ignored and only the propagation of these modes was considered. This section introduces a point source within an infinitely long duct, and illustrates how the amplitude of each mode may be found from a knowledge of three source characteristics: the type, strength, and position of the source in the duct.

Consider an infinite length circular duct that contains some source distribution at an axial location given by $z=0$. Referring to figure 2.2, it can be seen that the duct is divided into two sections on either side of the source plane at $z=0$. In side one, each single *forward* propagating mode is given by equation (2.4.1) above, and is repeated here

$$p_{(1)}^{mn}(r,\theta,z) = A_{mn}J_m(k_r^{mn}r)e^{-j(m\theta+k_z^{mn}z)}. \qquad (2.5.1)$$

Explicitly, the present problem is to determine the value of the amplitude term, A_{mn}, for each mode. It will be shown that this is determined by characteristics of the source.

The sum of the pressures from all the forward propagating modes in side 1 gives the total pressure, which is given by

$$p_{(1)}(r,\theta,z) = \sum_{m=-\infty}^{\infty} e^{-jm\theta} \sum_{n=0}^{\infty} A_{mn}\, \psi_{mn}(kr) e^{-jk_z^{mn} z}. \tag{2.5.2}$$

The radial mode shape function, $\psi_{mn}(kr)$, is given by

$$\psi_{mn}(kr) = \frac{J_m(k_r^{mn} r)}{N_{mn}}, \tag{2.5.3}$$

where the term N_{mn} is a non-dimensional normalising coefficient. The exact form of this function will be derived later in the next section.

Following a similar approach to that in Section 2.4, it is possible to solve for the particle velocity in the axial direction. It will be shown that a knowledge of both the pressure and axial particle velocity is required to match the source with the acoustic mode amplitudes within the duct. For harmonic motion the momentum equation applied in the axial direction to a single mode, is given by

$$u_z^{mn}(r,\theta,z) = -\frac{1}{j\omega\rho} \frac{\partial p^{mn}(r,\theta,z)}{\partial z}. \tag{2.5.4}$$

Applying the momentum equation above to the acoustic pressure in equation (2.4.2), the total axial particle velocity in side 1 is given by

$$u_{z(1)}(r,\theta,z) = \frac{1}{\omega\rho} \sum_{m=-\infty}^{\infty} \sum_{n=0}^{\infty} k_z^{mn} A_{mn}\, \psi_{mn}(kr) e^{-j(m\theta + k_z^{mn} z)}, \tag{2.5.5}$$

which is equivalent to

$$u_{z(1)}(r,\theta,z) = \frac{1}{k\rho c} \sum_{m=-\infty}^{\infty} e^{-jm\theta} \sum_{n=0}^{\infty} k_z^{mn} A_{mn}\, \psi_{mn}(kr) e^{-jk_z^{mn} z}. \tag{2.5.6}$$

By a similar argument, the total pressure and total axial particle velocity in side two of the duct are given by

$$p^{(2)}(r,\theta,z) = \sum_{m=-\infty}^{\infty} e^{-jm\theta} \sum_{n=0}^{\infty} B_{mn}\, \psi_{mn}(kr) e^{jk_z^{mn} z}, \tag{2.5.7}$$

$$u_z^{(2)}(r,\theta,z) = -\frac{1}{k\rho c} \sum_{m=-\infty}^{\infty} e^{-jm\theta} \sum_{n=0}^{\infty} k_z^{mn} B_{mn}\, \psi_{mn}(kr) e^{jk_z^{mn} z}. \tag{2.5.8}$$

It is will be shown how the values of the coefficients A_{mn} and B_{mn} may be found by matching the pressure and particle velocity with that of the source.

Consider a point monopole source at an axial location $z = 0$, and azimuthal and radial locations of θ_s and r_s and respectively. For a monopole source within an infinitely long duct, by symmetry it is obvious that the modal amplitudes A_{mn} and B_{mn} will be equal for all corresponding values of m and n. Put simply it is reasonable that a monopole should radiate equally on either side of the source plane.

This principle is expressed by the continuity of acoustic pressure at the source plane $z = 0$, and for a monopole source[1]

$$p^{(1)} = p^{(2)}. \tag{2.5.9}$$

Therefore

$$A_{mn} = B_{mn}. \tag{2.5.10}$$

For a monopole source, there is a difference in the axial particle velocity at the source. This difference in the axial particle velocity immediately either side of the source plane at $z = 0$ is given by

$$\Delta u_z(r, \theta, z = 0) = \frac{2}{k\rho c} \sum_m e^{-jm\theta} \sum_n k_z^{mn} A_{mn} \Psi_{mn}(kr). \tag{2.5.11}$$

For a point monopole, then the source strength distribution over the duct cross section is given by

$$\frac{Q}{r_s} \delta(r - r_s) \delta(\theta - \theta_s), \tag{2.5.12}$$

---

[1] For an axial dipole source, the difference in acoustic pressure either side of the source plane is non-zero and may be equated to the dipole strength. However, for a dipole, the difference in particle velocity is zero either side of the source plane.

where θ_s and r_s are the azimuthal and radial locations of the source respectively, and Q is strength of the monopole source.

This may be verified by integrating equation (2.5.12) over the duct cross section, S, which shows that

$$\int_0^{2\pi}\int_0^a \frac{Q}{r_s}\delta(r-r_s)\,\delta(\theta-\theta_s)\,r\,dr\,d\theta = Q. \tag{2.5.13}$$

This difference in particle velocity either side of the source plane, may be equated to the source strength expression given by equation (2.5.12), giving

$$\frac{Q}{r_s}\delta(r-r_s)\,\delta(\theta-\theta_s) = \frac{2}{k\rho c}\sum_m e^{-jm\theta}\sum_n k_z^{mn}\,A_{mn}\,\psi_{mn}(kr). \tag{2.5.14}$$

The mode shape functions, $\psi_{mn}(kr)$, are orthogonal[2], such that

$$\int_S \psi_{mn}(kr)\,e^{-jm\theta}\psi_{pq}(kr)\,e^{jp\theta}\,dS = 1, \quad \text{for } m=p \quad \textit{and} \quad n=q, \tag{2.5.15}$$

$$\int_S \psi_{mn}(kr)\,e^{-jm\theta}\psi_{pq}(kr)\,e^{jp\theta}\,dS = 0, \quad \text{for } m\neq p \quad \textit{or} \quad n\neq q, \tag{2.5.16}$$

where S is the duct cross section. Therefore multiplying both sides of equation (2.5.14) by $\psi_{pq}(kr)\,e^{jm\theta}$ and integrating over the duct cross section S, and noting that $dS = r\,dr\,d\theta$, gives the following expression

$$\int_0^{2\pi}\int_0^a \frac{Q}{r_s}\delta(r-r_s)\,\delta(\theta-\theta_s)\,\psi_{mn}(kr)\,e^{-jm\theta}\,r\,dr\,d\theta = \int_0^{2\pi}\int_0^a \frac{2}{k\rho c}\sum_m e^{-jm\theta}e^{jp\theta}\sum_n k_z^{mn}\,A_{mn}\,\psi_{mn}(kr)\,r\,dr\,d\theta \tag{2.5.17}$$

Using the sifting property of the delta function (Bracewell, 1986), gives

$$Q\,\psi_{mn}(kr_s)\,e^{jm\theta_s} = \frac{2}{k\rho c}\int_0^{2\pi}\int_0^a k_z^{mn}A_{mn}\,\psi_{mn}{}^2(kr)\,r\,dr\,d\theta, \tag{2.5.18}$$

---

[2] see Appendix A

and performing the integral with respect to θ on the right hand side gives

$$Q\psi_{mn}(kr_s)e^{jm\theta_s} = \frac{4\pi A_{mn}k_z^{mn}}{k\rho c}\int_0^a \psi_{mn}{}^2(kr)\,r\,dr. \tag{2.5.19}$$

By definition of the normalised mode shape functions

$$\int_0^a \psi_{mn}{}^2(kr)\,r\,dr = 1. \tag{2.5.20}$$

Therefore equation (2.5.19) becomes

$$Q\psi_{mn}(kr_s)e^{jm\theta_s} = \frac{4\pi A_{mn}k_z^{mn}}{k\rho c}. \tag{2.5.21}$$

Thus the amplitude of each mode is given by

$$A_{mn} = \frac{k\rho c}{4\pi k_z^{mn}} Q\psi_{mn}(kr_s)e^{jm\theta_s}. \tag{2.5.22}$$

For a circular duct the mode shape function is a Bessel function, hence equation (2.5.22) may be expressed as

$$A_{mn} = \frac{Q\omega\rho}{4\pi k_z^{mn}} \frac{J_m(k_r^{mn}r_s)}{N_{mn}} e^{jm\theta_s}. \tag{2.5.23}$$

Therefore it can be seen from equation (2.5.18) that the value of amplitude of each mode is determined by the value of the mode shape function at the source position, θ_s and r_s, multiplied by the source strength at a single frequency ω.

2.6 The acoustic radiation from a semi infinite circular duct, terminating in rigid baffle.

In the previous sections, the important characteristics of the acoustic propagation within a circular duct have been demonstrated. However, this analysis dealt with a very special case, namely an infinitely long duct containing only modes travelling away from the source. Furthermore, since the duct was of infinite extent, there is no radiation from an open end.

Obviously, for many practical purposes the special case described above will not be sufficient to model the acoustic propagation. In particular for the present application it is necessary to include the effects of finite length, and radiation from the open ends. Also it is desirable to examine the radiation from the duct by different sources within it, and how a particular this radiation is effected as the source is moved near to the duct wall.

This section builds upon the understanding of the infinite duct given in sections 2.4 and 2.5, to examine the radiation from a semi infinite duct. This is a duct with only one open end, and the other may be considered to extend to infinity (or be terminated anechoically). As a reminder, the ultimate objective of the analysis is to describe and examine the propagation *and* radiation from a finite length duct containing a source. However, the additional analytical complexity incurred by assuming that the duct be terminated at *one* end is sufficient to warrant separate description.

The first step in the process is to divide the overall problem into two parts; by first examining the field within the duct, and then look at the radiation, given a particle velocity distribution over the open end of the duct. With a semi-infinite duct, there will be acoustic reflection at the open end caused by the impedance change as the sound propagates toward the open end. In this section the important parameters that are needed to calculate the internal acoustic field are derived.

It will be seen that the reflections at the open end of the duct are calculated by first finding the impedance of each mode. Whilst the general method of calculating these modal impedances follows that given by Zorumski (1973), considerable time has been taken to correct many of the errors found in this paper. Furthermore, a detailed derivation of all the principal equations and functions used are listed in separate appendices. Perhaps the most important of these errors is that the

expression for the modal impedances given by Zorumski was found to be incorrect regarding the sign of the real part. This error has been corrected in the analysis that follows. Therefore the approach taken in this section is taken from the paper by Zorumski, and corrections are made where appropriate. Equation (2.6.1) to equation (2.6.36) are those based upon this earlier work. The matrix solution for the finite length duct which follows is original work.

Consider a circular duct whose geometry is given by figure 2.3. The acoustic field within the duct is composed of forward and backward travelling acoustic modes. Using the expressions given by equations (2.4.2) and (2.4.4) the pressure and axial particle velocity within the duct are given by (a time dependence of $e^{j\omega t}$ is assumed throughout)

$$p(r,\theta,z) = \sum_{m=-\infty}^{\infty} e^{jm\theta} \sum_{n=0}^{\infty} \left[A_{mn}\, e^{-j\Omega_{mn} kz} + B_{mn}\, e^{j\Omega_{mn} kz} \right] \psi_{mn}(kr). \qquad (2.6.1)$$

Note the similarity between (2.4.2) and the above equation. Again each mode may be considered to be constructed from a mode shape function $\psi_{mn}(kr)\, e^{jm\theta}$, and an amplitude and phase term $A_{mn}\, e^{-j\Omega_{mn} kz}$. The axial particle velocity is given by

$$u_z(r,\theta,z) = \frac{1}{\rho c} \sum_{m=-\infty}^{\infty} e^{jm\theta} \sum_{n=0}^{\infty} \Omega_{mn} \left[A_{mn}\, e^{-j\Omega_{mn} kz} - B_{mn}\, e^{j\Omega_{mn} kz} \right] \psi_{mn}(kr), \qquad (2.6.2)$$

where Ω_{mn} may be considered to be a non-dimensional axial wavenumber which is related to the conventional axial wavenumber k_z^{mn} by

$$\Omega_{mn} = \frac{k_z^{mn}}{k}. \qquad (2.6.3)$$

The indices m and n refer to azimuthal and radial order respectively. A non-dimensional radial wavenumber λ_{mn} which is related to the conventional radial wavenumber k_r^{mn} is defined as

$$\lambda_{mn} = \frac{k_r^{mn}}{k}. \qquad (2.6.4)$$

The values of k_r^{mn} form an ordered sequence. As in section 2.4 the value of k_r^{mn} depends upon the boundary conditions at the duct wall. Equations (2.6.3) and (2.6.4) are related by the dispersion equation

$$\Omega_{mn} = \sqrt{1 - \lambda_{mn}^{\,2}}\,. \tag{2.6.5}$$

This is equivalent to equation (2.4.11). The mode shape function, $\psi_{mn}(kr)$, is normalised and given by

$$\psi_{mn}(kr) = \frac{J_m(\lambda_{mn} kr)}{N_{mn}}. \tag{2.6.6}$$

The eigenvalues λ_{mn} are determined by the boundary conditions at the duct wall. If the duct wall has an arbitrary wall admittance denoted by β_a where a is the duct radius, then the characteristic equation for the field within the duct is given by

$$j\beta_a J_m(\lambda_{mn} ka) + \lambda_{mn} J'_m(\lambda_{mn} ka) = 0\,, \tag{2.6.7}$$

where the prime on the second Bessel function in equation (2.6.7) refers to differentiation with respect to radius. This equation may be derived by applying the momentum equation to the duct wall in the radial direction to the pressure given as equation (2.6.1)

$$u_r = -\frac{1}{jk\rho c}\frac{\partial p}{\partial r}\bigg|_{r=a}. \tag{2.6.8}$$

Equation (2.6.7) gives the relationship between the radial wavenumber λ_{mn}, and the duct wall impedance β_a that may take any value. For an arbitrary, complex wall impedance, then λ_{mn} will be complex, and results from the computation of Bessel functions of complex argument. Much of analysis that follows makes specific reference to the simpler case of duct walls that are either rigid or pressure release. However, these are just two special cases for the duct wall impedance, and do not limit the potential application of this analysis to the study of ducts of complex wall impedance.

Using this notation, for the hard wall boundary condition β_a=0, solutions of equation (2.6.7) are given by the zeros of the derivative of the Bessel function, given by

$$\frac{\partial}{\partial r} J_m(\lambda_{mn} kr)\Big|_{r=a} = 0. \tag{2.6.9}$$

For the pressure release boundary condition at the duct wall, $\beta_a = \infty$, and

$$J_m(\lambda_{mn} ka)\Big|_{r=a} = 0. \tag{2.6.10}$$

The radial modes are orthogonal and therefore the normalising factor given in equation (2.6.6) is chosen such that

$$\int_0^a r\psi_{mn}{}^2(kr)dr = 1. \tag{2.6.11}$$

Substituting equation (2.6.6) into equation (2.6.11) and evaluating the integral gives the required form of the normalising function (Watson, 1962).

$$N_{mn} = \frac{a}{\sqrt{2}} \left\{ \left(1 - \frac{m^2}{\lambda_{mn}{}^2 k^2 a^2} \right) J_m{}^2(\lambda_{mn} ka) + J'_m{}^2(\lambda_{mn} ka) \right\}^{\frac{1}{2}}. \tag{2.6.12}$$

For the hard walled duct case, equation (2.6.12) may be further reduced using the relationship given in equation (2.6.9)

$$N_{mn} = \frac{a\, J_m(\lambda_{mn} ka)}{\sqrt{2}} \sqrt{1 - \frac{m^2}{\lambda_{mn}{}^2 k^2 a^2}}, \tag{2.6.13}$$

and for the pressure release boundary condition, from equation (2.6.10)

$$N_{mn} = \frac{a}{\sqrt{2}} J'_m(\lambda_{mn} ka). \tag{2.6.14}$$

The pressure and particle velocity at the end of the duct ($z = 0$), may be expressed in terms of duct modes as

$$p(\mathbf{r}_0) = \sum_{m=-\infty}^{\infty} e^{jm\theta_0} \sum_{n=0}^{\infty} P_{mn}\Psi_{mn}(kr_0), \tag{2.6.15}$$

$$u(\mathbf{r}_0) = \frac{1}{\rho c} \sum_{m=-\infty}^{\infty} e^{jm\theta_0} \sum_{n=0}^{\infty} V_{mn}\Psi_{mn}(kr_0). \tag{2.6.16}$$

Where, $\mathbf{r}_0$ is a position vector in circular co-ordinates, with components r_0 and θ_0 at the duct exit, (see figure 2.3), and where P_{mn} and V_{mn} are given by

$$P_{mn} = A_{mn} + B_{mn}, \tag{2.6.17}$$

$$V_{mn} = \Omega_{mn}(A_{mn} - B_{mn}). \tag{2.6.18}$$

If the duct is assumed to be terminated in a plane rigid baffle, the acoustic field outside the duct may be found using the Rayleigh Integral, and depends upon the axial velocity over the end of the duct. The Rayleigh Integral is given by

$$p(\mathbf{r}) = \frac{jk\rho c}{2\pi} \int_0^{2\pi} \int_0^a r_0 u(\mathbf{r}_0) \frac{e^{-jkh}}{h} dr_0 d\theta_0, \tag{2.6.19}$$

where the position vector $\mathbf{r}$ refers to points in the external field, $z \geq 0$, and where

$$h = \sqrt{r^2 + {r_0}^2 - 2r r_0 \cos(\theta - \theta_0) + z^2}. \tag{2.6.20}$$

Substituting equation (2.6.16) into equation (2.6.19) gives

$$p(\mathbf{r}) = \frac{jk\rho c}{2\pi} \int_0^{2\pi} \int_0^a r_0 \frac{1}{\rho c} \sum_{m=-\infty}^{\infty} e^{jm\theta} \sum_{n=0}^{\infty} V_{mn}\Psi_{mn}(kr) \frac{e^{-jkh}}{h} dr_0 d\theta_0, \tag{2.6.21}$$

which becomes

$$p(\mathbf{r}) = \frac{jk}{2\pi} \sum_{m=-\infty}^{\infty} e^{jm\theta} \sum_{n=0}^{\infty} V_{mn} \int_0^{2\pi} e^{jm\theta_0} \int_0^a r_0 \frac{e^{-jkh}}{h} \Psi_{mn}(kr_0) dr_0 d\theta_0. \tag{2.6.22}$$

Equation (2.6.21) gives the external field in terms of the modal velocities at the end of the duct. This equation is usually solved numerically. It is possible to express the function of h in a more convenient form to enable a tractable analytical solution for the *internal* field to be found. From Watson, (1962), the exponential term may be expressed as

$$\frac{e^{-jkh}}{h} = k\int_0^\infty \tau\left(\tau^2 - 1\right)^{-\frac{1}{2}} J_0(\tau kh)d\tau, \tag{2.6.23}$$

where τ is a dummy variable.

At the duct exit, the integrand of the Bessel function in (2.6.23) may be replaced using Neumanns addition theorem for Bessel functions (Watson, 1962).

$$J_0(\tau kh) = J_0\left(\tau k\left[r^2 + r_0{}^2 - 2r\,r_0\cos(\theta - \theta_0) + z^2\right]^{\frac{1}{2}}\right). \tag{2.6.24}$$

From Watson (1962)[3], then Neumanns addition theorem states that if a function is defined as $\gamma = \sqrt{Z^2 + z^2 - 2Zz\cos\phi}$, then

$$J_0(\gamma) = \sum_{m=-\infty}^{\infty} J_m(Z)J_m(z)e^{jm\phi}. \tag{2.6.25}$$

This gives, using equation (2.6.24)

$$J_0(\tau kh) = \sum_{m=-\infty}^{\infty} J_m(\tau kr)J_m(\tau kr_0)e^{jm(\theta-\theta_0)}. \tag{2.6.26}$$

Substituting equation (2.6.26) into equation (2.6.23) gives

$$\frac{e^{-jkh}}{h} = k\sum_{m=-\infty}^{\infty} e^{\left[jm(\theta-\theta_0)\right]}\int_0^\infty \tau\left(\tau^2 - 1\right)^{-\frac{1}{2}} J_m(\tau kr)J_m(\tau kr_0)d\tau. \tag{2.6.27}$$

Equation (2.6.22) for the pressure at the duct exit can now be expressed as

---

[3] p358, equation 1

$$p(\mathbf{r}_0) = jk^2 \sum_{m=-\infty}^{\infty} e^{jm\theta} \sum_{n=0}^{\infty} V_{mn} \int_0^{\infty} \tau\left(\tau^2 - 1\right)^{-\frac{1}{2}} J_m(\tau k r_0) \int_0^a r_0 \, J_m(\tau k r_0) \psi_{mn}(k r_0) \, dr \, d\tau \tag{2.6.28}$$

We know define the function, $D_{mn}(\tau)$ given by

$$D_{mn}(\tau) = k \int_0^a r_0 J_m(\tau k r_0) \psi_{mn}(k r_0) dr_0. \tag{2.6.29}$$

The integral above may be evaluated directly, Watson (1962)[4]

$$D_{mn}(\tau) = a \left[\frac{\tau \psi_{mn}(ka) J_m'(\tau ka) - \lambda_{mn} \psi_{mn}'(ka) J_m(\tau ka)}{\lambda_{mn}^{\,2} - \tau^2} \right]. \tag{2.6.30}$$

Then equation (2.6.28) may be expressed as

$$p(\mathbf{r}) = jk \sum_{m=-\infty}^{\infty} e^{jm\theta} \sum_{n=0}^{\infty} V_{mn} \int_0^{\infty} \tau\left(\tau^2 - 1\right)^{-\frac{1}{2}} J_m(\tau k r) D_{mn}(\tau) d\tau. \tag{2.6.31}$$

Equations (2.6.15) and (2.6.31) may now be used to solve for the modal pressure amplitudes in terms of the modal velocity amplitudes[5]

$$P_{mn} = \sum_{l=0}^{\infty} Z_{mnl} V_{ml}. \tag{2.6.32}$$

Where l is the radial order of the reflected mode, and n is the radial order of the incident mode. The above equation relates the modal pressure amplitudes within the duct to the modal velocity amplitudes. The term Z_{mnl} is the coupling impedance between the pressure and velocity.

Due to the symmetry of the duct, the azimuthal order is shared by the incident and reflected modes. In equation (2.6.32) Z_{mnl} is the modal generalised impedance, and is given by

---

[4] see Appendix B

[5] see Appendix C

$$Z_{mnl} = j\int_0^{\infty} \tau\left(\tau^2 - 1\right)^{-\frac{1}{2}} D_{mn}(\tau) D_{ml}(\tau) d\tau. \tag{2.6.33}$$

Equation (2.6.32) may be split into two integrals over the ranges (0,1) and (1,∞). Using a change of variable such that

$$\tau = \sin\phi, \tag{2.6.34}$$

$$\tau = \cosh\xi, \tag{2.6.35}$$

in those respective ranges given above. The expression for the generalised impedance then becomes[6]

$$Z_{mnl} = \int_0^{\frac{\pi}{2}} \sin\phi \; D_{mn}(\sin\phi) D_{ml}(\sin\phi) d\phi + j\int_0^{\infty} \cosh\xi \; D_{mn}(\cosh\xi) D_{ml}(\cosh\xi) d\xi. \tag{2.6.36}$$

Expressed in this way, it is possible to compute the real and imaginary parts of the radiation impedance separately. This statement is only true if the impedance at the duct wall is purely real, which is the case for a hard wall and pressure release wall. If the duct wall is made to take any complex impedance value, the expression for the radiation impedance given by equation (2.6.36) is still valid, but each integral in equation (2.6.36) will no longer produce purely real answers. The reason for this is that for a complex wall impedance, the value of the radial wavenumber will be complex, hence the terms λ_{mn} and λ_{ml} will be complex, and hence the computed functions $D_{mn}(\tau)$ and $D_{ml}(\tau)$ will be also have real and imaginary parts.

2.7 The calculation of the modal radiation impedance.

Upon inspection of equations (2.6.30) and (2.6.35) it would appear that they may contain poles at $\sin^2\phi = \lambda_{mn}^2$ and $\sin^2\phi = \lambda_{ml}^2$ for the real part, and for the imaginary part, poles at $\cosh^2\xi = \lambda_{mn}^2$ and $\cosh^2\xi = \lambda_{ml}^2$.

However, by application of L'Hôpital's rule, it is possible to show that the limiting value of the function $D_{mn}(\tau)$ in equation (2.6.30) is finite (full details are given in

---

[6] see Appendix C

Appendix D). This may be explained simply from examination of the function $D_{mn}(\tau)$ which is used to calculate the modal impedances

$$D_{mn}(\tau)=\left\{a\left[\frac{\tau\psi_{mn}(ka)J'_m(\tau ka)-\lambda_{mn}\psi'_{mn}(ka)J_m(\tau ka)}{{\lambda_{mn}}^2-\tau^2}\right]\right\}. \tag{2.7.1}$$

In the limit as $\tau\rightarrow\lambda_{mn}$ then the denominator tends to zero, and it would be reasonable on this evidence alone to expect the function $D_{mn}(\tau)$ would tend to infinity. However, as $\tau\rightarrow\lambda_{mn}$, the numerator also tends to zero. This can be seen by expanding the numerator of equation (2.6.30) as follows;

$$\tau\frac{J_m(\lambda_{mn}kr)}{N_{mn}}J'_m(\tau kr)-\lambda_{mn}\frac{J'_m(\lambda_{mn}kr)}{N_{mn}}J_m(\tau kr). \tag{2.7.2}$$

Figure 2.4a shows the value of the real and imaginary parts of the radiation impedance plotted against ka, for the plane wave mode, i.e. $m=0$, $n=0$, incident upon the end of a hard walled duct, and a plane wave reflected at the end of the duct. Figure 2.4b shows the mode shape of the incident and reflected modes. Examination of equation (2.6.32), shows that these radiation impedances may be considered to be the impedance of a radiated *m, l* order mode away from the open end of the duct, due to an incident *m, n* velocity mode at the end of the end. A plane wave radiating from the end of the duct is analogous acoustically to the textbook problem of radiation from a circular piston in an infinite rigid baffle. Consequently, the radiation impedances for each of these cases should yield identical results. A comparison of figure 2.4 with the radiation impedance of such a piston as given by Kinsler and Frey *et al* (1982) for example, shows that these two impedances are indeed identical.

In calculating these impedances, the integration in equation (2.6.36) was performed numerically using Simpson's Rule. Referring back to equation (2.6.36), then the for real part of the impedance the function is integrated over the range $0\leq\phi\leq\pi/2$. Accounting for the behaviour of the integrand in the region of $\sin^2\phi=\lambda^2_{mn}$ and $\sin^2\phi=\lambda^2_{ml}$ as noted above then this integration is straightforward. At first sight the integral required to compute the imaginary part of the impedance in equation (2.3.36) looks more difficult. This is because it is a semi-infinite integral, where the range of integration is given by $0\leq\xi\leq\infty$. Fortunately, due to the nature of the integrand this does not pose too many difficulties. Since the integrand is of the order of $\cosh^{-3}\xi$ then it follows that the

integrand is approximately zero for all values of ξ above about 10. At ξ=10, the value of $\cosh^{-3}\xi$ is 7.48×10^{-13}. For the calculation presented here the range of integration for the imaginary part was truncated at ξ=20. Using Simpson's rule for the integration both the real and imaginary parts were divided into 1000 strips, and all the computation of the integration was performed using MATLAB. As this software is optimised for speed in the calculation of vector and matrix problems it is extremely quick in performing the necessary summations required to evaluate an integral using Simpson's rule, which for completeness is given below as

$$A=\frac{1}{3}h(y_a+4y_1+2y_2+4y_3+\ldots+2y_{n-2}+4y_{n-1}+y_b), \tag{2.7.3}$$

where A is the value of the integral, $h=(b-a)/n$ is the width of each strip, $[a, b]$ is the range of integration, and n is the number of separate evaluation points strips over the integration range. The values $y_a \ldots y_b$ are the values of the integrand evaluated at each point n over the integration range. Thus the integration of a real function $y=f(x)$ from a to b is approximated by dividing the interval up into an even number of n points $x_1, x_2, x_3, \ldots\ldots x_{n-1}$. The corresponding ordinates at these points are $y_1, y_2, y_3, \ldots\ldots y_{n-1}$. The repeated numbers *4* and *2* in equation (2.7.3) form a vector known as the weighting function, **w**. Therefore to compute the value of A using MATLAB, it is first necessary to evaluate $y_1, y_2, y_3, \ldots\ldots y_{n-1}$ from the values of $x_1, x_2, x_3, \ldots\ldots x_{n-1}$. These can be determined very quickly by making the values $x_1, x_2, x_3, \ldots\ldots x_{n-1}$ a vector of length n. The vector of y values then follows from the integrand. The value of the integral A is simply the scalar or dot product of the weighting function vector **w** and the vector **y** which is given by $\mathbf{y}=y_1, y_2, y_3, \ldots\ldots y_{n-1}$.

Figure 2.5a shows the value of the real and imaginary parts of the impedance for the higher order mode, *m=0, n=0, l=2*, in a hard walled duct. This represents the coupling impedance of a plane wave mode incident upon the end of the duct (i.e. *m=0, n=0*), and a reflected 3rd radial order mode (*l=2*). Note that both the real and imaginary parts of the impedance are non-zero in the region of the cut-on frequency of the 3rd radial order mode at $ka=7.02$ (for *m=0*). The incident mode shape is shown in figure 2.4b, which is the familiar plane wave mode, and the reflected mode is shown in figure 2.5b. These, and all other mode shape plots are to illustrate the shape of the mode either incident or reflected at the end of the duct, and as such are do not have representative amplitude to the modes within the duct. Also the contour lines shown beneath the mode shape plot show the nodal lines of the mode shape. The number of these lines is directly related to the order

of the mode. For example, the $m=0$, $l=2$, reflected mode has 0 azimuthal nodal lines, and 2 radial nodal lines.

The observation of a significant degree of coupling between these modes is of vital importance as these coupling impedances cannot be ignored in the calculation of the reflection coefficients, and hence the internal and radiated acoustic fields for the values of ka of interest in this thesis.

It is important also to note the form of equation (2.6.33). It is clear from this equation that the radiation impedance of a m,n,l order mode will be the same as that for a m,l,n order mode in the same duct. To illustrate this, figure 2.6 shows the radiation impedance for a $m=0$, $n=0$, $l=1$ mode, and the impedance of a $m=0$, $n=1$, $l=0$ order mode. Clearly these are the same, as expected.

Figures 2.7 and 2.8 show the radiation impedance for a various modes in a hard wall duct. Figure 2.7 illustrates how the impedance changes for a fixed azimuthal order, while allowing n and l to vary. Alternatively, figure 2.8 shows the relationship between impedance and azimuthal order. Not surprisingly, the radiation impedance is greater when $n=l$, which corresponds to the radiation of an m,n order mode, due to a m,l mode at the end of the duct. It is expected that the coupling between these two modes will be greater than for two different radial orders.

By way of comparison with the above, figure 2.9a shows the impedance of the $m=n=0$ mode incident upon the end of the duct, and a $m=l=0$ order pressure mode radiated from the duct, for a pressure release boundary at the duct wall. Figure 2.9b, shows the mode shape for this mode in a pressure release lined duct. What is interesting to note about this mode shape is that it is clearly not a plane wave. As a result of the boundary condition within a pressure release lined duct, that there is zero pressure at the duct wall, then this explains why the pressure is zero at the extremities of the mode shape. The shape of the mode is explained by examining the generating function for the mode shape, which in this case is proportional to $J_0(k_r r)$. For the lowest order mode in a pressure release lined duct, then $k_r a$ is equal to 2.40. Therefore when the value of $r=a$, where a is the duct radius, then the mode shape is zero. Elsewhere it takes the form of the Bessel function. Since the value of $k_r a$ is non-zero for this lowest order mode, then this implies that there is a cut-on frequency for even this mode. If the source is

radiating at a frequency below $ka = 2.40$, then the total field inside the duct will be composed of evanescent modes.

Figure 2.10 shows the impedance in a pressure release lined duct for various modes with the same azimuthal order. Figure 2.11 shows the radiation impedance for various azimuthal orders in the same duct.

2.8 The modal reflection coefficients.

To solve for the internal field it is necessary to calculate the reflection coefficient for each mode incident upon the end of the duct. In this section it is shown how the expression for the modal impedances derived previously may be used to calculate the modal reflection coefficients at the duct exit.

The acoustic field within the duct is composed of a series of forward and backward propagating waves whose amplitudes are given by A_{mn} and B_{mn}. These two variables are related using the expressions in equations (2.6.17) and (2.6.18), which are repeated here

$$P_{mn} = A_{mn} + B_{mn}, \tag{2.8.1}$$

$$V_{mn} = \Omega_{mn}(A_{mn} - B_{mn}). \tag{2.8.2}$$

Substituting equations (2.8.1) and (2.8.2) into the expression for the impedance given by equation (2.6.32) gives

$$\sum_{l=0}^{\infty}(Z_{mnl}\Omega_{ml} + \delta_{nl})B_{ml} = \sum_{l=0}^{\infty}(Z_{mnl}\Omega_{ml} - \delta_{nl})A_{ml}, \tag{2.8.3}$$

where δ_{nl} is the Kronecker delta function defined as

$$\delta_{nl} = 0 \text{ for } n \neq l,$$

$$\delta_{nl} = 1 \text{ for } n = l.$$

Solving the above equation for B_{mn} results in an equation of the form

$$B_{mn} = \sum_{l=0}^{\infty} R_{mnl}\, A_{ml}. \tag{2.8.4}$$

The terms R_{mnl} are the reflection coefficients that can be related to the modal impedance $\mathbf{Z_{mnl}}$ by the following *infinite* matrix equation, (that is $l = \infty$ in principle). For a given value of azimuthal order, the reflection coefficients are given by

$$\mathbf{R_{nl}} = \left[\mathbf{Z_{nl}}\, \Omega_l + \mathbf{I} \right]^{-1} \times \left[\mathbf{Z_{nl}}\, \Omega_l - \mathbf{I} \right]. \tag{2.8.5}$$

Where $\mathbf{I}$ is the identity matrix defined as

$$\mathbf{I} = \begin{bmatrix} 1 & 0 & \dots & 0 \\ 0 & 1 & \dots & 0 \\ \vdots & \vdots & \ddots & \vdots \\ 0 & 0 & \dots & 1 \end{bmatrix}, \tag{2.8.6}$$

and where Ω_l is a diagonal matrix. For *fixed* azimuthal order m, Ω_l is given by

$$\Omega_l = \begin{bmatrix} \Omega_0 & 0 & \dots & 0 \\ 0 & \Omega_1 & \dots & 0 \\ \vdots & \vdots & \ddots & \vdots \\ 0 & 0 & \cdots & \Omega_L \end{bmatrix}. \tag{2.8.7}$$

Note that the m dependence has been suppressed in equations (2.8.5) and (2.8.7), and thus Ω_l given in equation (2.8.7) is only valid for *one value* of azimuthal order at a time, and generally will be different for each value of m. Here l is the radial order of the reflected modes, where $0 \le l \le \infty$.

The reflection coefficient matrix is defined as

$$\mathbf{R_{nl}} = \begin{bmatrix} R_{00} & R_{01} & \cdots & R_{0L} \\ R_{10} & R_{11} & \cdots & R_{1L} \\ \vdots & \vdots & \ddots & \vdots \\ R_{N0} & R_{N1} & \cdots & R_{NL} \end{bmatrix}, \tag{2.8.8}$$

and for fixed azimuthal order m, the impedance matrix is given by

$$\mathbf{Z_{nl}} = \begin{bmatrix} Z_{00} & Z_{01} & \cdots & Z_{0L} \\ Z_{10} & Z_{11} & \cdots & Z_{1L} \\ \vdots & \vdots & \ddots & \vdots \\ Z_{N0} & Z_{N1} & \cdots & Z_{NL} \end{bmatrix}. \tag{2.8.9}$$

Note the form of equation (2.8.4), since it illustrates the nature of the reflected field within the duct. For one incident mode upon the end of the duct, the reflected field takes the form of an infinite series of other modes with the same azimuthal order, but having *all* radial orders up to infinity. Obviously in practice it is not possible to compute the reflection coefficients for all the reflected modes as they are infinite in number. However, since only a finite number of modes may propagate freely in the duct at a given frequency, then it is possible to ignore modes that are highly evanescent, but not *all* evanescent modes.

Therefore to calculate both the impedance and reflection coefficients it is necessary to first truncate the number of reflected modes at some value of radial order at some value L. This truncation will have an impact on the accuracy of any calculated reflection coefficients given by equation (2.8.5).

The generalised reflection coefficients may be solved for by first finding the generalised impedances given by equation (2.6.33). Note these impedances are specific to each incident mode and duct wall impedance for a given value of ka.

The calculation of the reflection coefficients in practice, first requires that the azimuthal order be fixed. This reduces the order of the impedance from a 3 dimensional 'matrix' (m, n, and l all allowed to vary), to a conventional 2 dimensional matrix, which is readily manipulated on a computer. Secondly, it is necessary to calculate the reflection coefficient matrix, $\mathbf{R_{nl}}$ for a single frequency at a time. This is because the matrix of modal impedances is valid for a single frequency, and the diagonal matrix, Ω_l can only be calculated for a single frequency at a time. This can be shown by remembering that

$$\Omega_l = \frac{k_z}{k} = \sqrt{1 - \lambda_l{}^2}, \tag{2.8.10}$$

where the m dependence has been suppressed in the above equation.

Therefore in practice it is necessary to solve equation (2.8.5) for each value of m and k separately, which results in numerous $\mathbf{R_{nl}}$ matrices at each value of m and k. Consequently, the desired reflection coefficient for a given n, l order mode may be simply extracted from each of these $\mathbf{R_{nl}}$ matrices to give a reflection coefficient *vector*, which may be plotted as a function of ka.

As mentioned above, it is necessary to truncate the number of modes in the calculation of the reflection coefficients to a finite quantity for calculation. For this thesis, the values of ka under discussion are relatively small, i.e. $ka < 15$. Therefore the total number of modes that will be cut-on below this frequency is limited to approximately 30, for all possibilities of azimuthal and radial order, and for both the hard wall and pressure release lined duct. For modes that have cut-on frequencies above the driving frequency of the source, then the elements in the diagonal matrix Ω_l corresponding to these cut-off modes will be pure imaginary.

Furthermore, when calculating the reflection coefficient matrices given by equation (2.8.5), it is only necessary to include the radiation impedance of those modes that are either fully cut-on (i.e. $ka < 15$), and those modes that are only just cut-off. It has been found that no extra accuracy is gained by including modal orders for which the cut-on frequency is given by $ka > 20$.

Even taking into consideration the fact that the modal orders may be truncated, there remains a considerable computing overhead in first calculating the modal radiation impedances, (largely due to the numerical integration that is time consuming), and then the reflection coefficient matrices for a large number of modes. Indeed all the reflection coefficients used in this thesis were calculated using a 30 by 30 matrix for $\mathbf{Z_{nl}}$ $\mathbf{R_{nl}}$ and Ω_l. This is provides considerably greater accuracy in the resultant reflection coefficients than those reported by Zorumski (1973), and by Wang and Tszeng (1984).

Figure, 2.12 shows the reflection coefficient for a plane wave incident ($m = n = 0$), and a plane wave reflected at the end of a hard walled duct ($m = l = 0$).

It is interesting that unlike the impedance matrix, $\mathbf{Z_{nl}}$, the reflection coefficient matrix, $\mathbf{R_{nl}}$, is not symmetric. For example, consider the reflection coefficient R_{010} (the convention adopted here will be that the subscript for the modal orders will be written alphabetically, i.e. R_{mnl}), plotted against ka for a hard wall duct.

This is shown as figure 2.13. By comparison, R_{001} is shown as figure 2.14. It can be seen that these two reflection coefficients are not the same. This is due to nature of equation (2.8.5), which includes only the axial wavenumber matrix, Ω_l of the reflected modes, and not a corresponding matrix ,Ω_n, for the incident modes.

Figures 2.15 to 2.18 show different reflection coefficients for various modal orders in a hard walled duct. Figures 2.19 to 2.22 show the equivalent reflection coefficients for a pressure release lined duct.

To explain the importance of modal coupling it is necessary to examine the nature of the reflection coefficients at the end of the duct. These reflection coefficients determine the level of energy reflected back into the duct, together with the modal decomposition of this energy. At the end of the duct, energy is exchanged from a single incident *m,n* mode into an infinite series of *m,l* modes. If coupling could be ignored it would require that the modal reflection coefficients be zero for all $n \neq l$. This is the equivalent to requiring that the non-diagonal elements of the reflection coefficient matrix given in equation (2.8.8) be set to zero. The larger the value of these non-diagonal elements the larger the energy exchange between modes. Consider the case of a $m=1$, $n=1$ mode incident upon the end of a hard wall duct. The reflection coefficient for this mode incident and an $m=1$, $l=0$ mode reflected back into the duct is shown as figure 2.15. At ka=5.3, the value of the real part of the reflection coefficient is 0.4. If coupling were ignored, then at this value of ka, this would assume that this reflection coefficient has a value of 0. If the $m=1$, $n=1$ were dominant in terms of energy, and coupling were to be ignored then this would produce large errors in the calculated field, as a large proportion of the energy would be transferred to another mode within the duct. Because the reflection coefficient is non-zero for the case of the coupled $m=1$, $n=1$, $l=0$ mode reflected at ka=5.3, this will cause this reflected mode to interfere with the field within the duct either constructively or destructively at the source. This has a fundamental influence upon the radiation of the source as it will alter the radiation impedance of the source, which in turn dictates the modal amplitude of this mode at this frequency. This latter aspect involves the duct length, since the phase change of the reflected mode from the end of the duct to the source will depend upon the axial position of the source relative to the open end of the duct, and also the axial wavenumber of the mode.

In summary, it is not a trivial problem to state that coupling may be ignored or included. It will depend upon many factors; the source location, the frequency of the source and the length of the duct, and the source type. All of these in themselves will produce huge changes in the power distribution within the modes propagating within the duct. Depending upon which modes (if any) are significant in terms of energy, and the value of the reflection coefficient at a chosen frequency, will determine if coupling may be ignored or not. Most importantly, the effect of modal coupling cannot be accessed *a priori*, and requires the field be calculated with and without coupling to assess its importance.

2.9 A matrix solution for the acoustic field inside a finite length duct.

In this section the above analysis that calculates the modal impedances and reflection coefficients for semi-infinite duct is used to calculate the field within a finite length duct. To simplify the following analysis the problem is restricted to one of fixed azimuthal order, but allowing variable radial order modes. Using superposition it is possible to solve for the complete field within the duct, assuming a finite number of reflected modes.

In matrix notation, equation (2.6.1) may be written as

$$p_{(1)m}(r,\theta,z) = e^{jm\theta}\left\{\mathbf{a}^{\mathrm{T}}\,\mathbf{E}_{ma}(z)\,\psi_a(r) + \mathbf{b}^{\mathrm{T}}\,\mathbf{E}_{mb}(z)\,\psi_b(r)\right\} \tag{2.9.1}$$

where $p_{(1)m}(r,\theta,z)$ is the incident pressure in side one of the duct for a fixed azimuthal order m. The terms $\mathbf{a}^{\mathrm{T}}$ and $\mathbf{b}^{\mathrm{T}}$ are the transpose of a column vector of modal amplitudes, which have the following form

$$\mathbf{a}^{\mathrm{T}} = \begin{bmatrix} A_{m0} & A_{m1} & A_{m2} & \cdots & A_{mN} \end{bmatrix}, \tag{2.9.2}$$

$$\mathbf{b}^{\mathrm{T}} = \begin{bmatrix} B_{m0} & B_{m1} & B_{m2} & \cdots & B_{mL} \end{bmatrix}, \tag{2.9.3}$$

where A_N is the modal amplitude of the N^{th} radial order mode for a given azimuthal order as defined in equation (2.7.1). This vector is truncated at A_N where N is a suitably large value of the radial order such that the field may be described adequately. Usually the value of N will be determined by trial and error.

The term $\mathbf{E}_{ma}$ is a diagonal matrix of axial propagation factors, given by

$$\mathbf{E}_{ma} = \begin{bmatrix} e^{-j\Omega_{m0}kz} & 0 & \cdots & 0 \\ 0 & e^{-j\Omega_{m1}kz} & \cdots & 0 \\ \vdots & \vdots & \ddots & \vdots \\ 0 & 0 & \cdots & e^{-j\Omega_{mN}kz} \end{bmatrix}, \tag{2.9.3}$$

and $\mathbf{E}_{mb}$ is similarly defined. The term $\psi_a(r)$ is the column vector of mode shapes given by

$$\psi_a(r)^{\mathrm{T}} = \begin{bmatrix} \psi_{m0}(r) & \psi_{m1}(r) & \cdots & \psi_{mN}(r) \end{bmatrix}, \tag{2.9.4}$$

and $\psi_b(r)$ is similarly defined. The reflected field at the end of the duct may be expressed in a similar matrix form, except here the exponential sign in the terms within the matrix of equation (2.9.3) will be positive denoting a negative direction of propagation. The reflected and incident modes are related through a matrix of modal reflection coefficients. The relationship between the incident and reflected fields in side one of the duct may be defined as

$$\mathbf{E}_{mb}(z)\,\mathbf{b} = \mathbf{R}_1(z)\,\mathbf{E}_{ma}(z)\,\mathbf{a}, \tag{2.9.5}$$

where the matrix $\mathbf{R}_1(z)$ is defined as

$$\mathbf{R}_1(z) = \begin{bmatrix} R_{00}(z) & R_{01}(z) & \cdots & R_{0N}(z) \\ R_{10}(z) & R_{11}(z) & \cdots & R_{1N}(z) \\ \vdots & \vdots & \vdots & \vdots \\ R_{L0}(z) & R_{L1}(z) & \cdots & R_{LN}(z) \end{bmatrix} \tag{2.9.6}$$

The reflection coefficient matrices, $\mathbf{R}_1(0)$ and $\mathbf{R}_2(-l_1 - l_2)$, i.e. evaluated at either end of the duct, may be evaluated by the method derived by Zorumski (1973) and detailed in Section 2.8. This method may be used to calculate the value of $\mathbf{R}_1(z)$ and $\mathbf{R}_2(z)$ at any other location, z within the duct from a knowledge of the reflection coefficient at the ends of the duct. If the reflection coefficient were known at some axial location l, then equation (2.9.5) may be written

$$\mathbf{E}_{mb}(l)\,\mathbf{b} = \mathbf{R}_1(l)\,\mathbf{E}_{ma}(l)\,\mathbf{a} \tag{2.9.7}$$

Solving for **b** in equations (2.9.5) and (2.9.7) and then equating gives

$$\mathbf{R}_1(z) = \mathbf{E}_{mb}(z)\mathbf{E}_{mb}(l)^{-1}\mathbf{R}_1(l)\mathbf{E}_{ma}(l)\mathbf{E}_{ma}(z)^{-1} \tag{2.9.8}$$

and for side 2 of the duct

$$\mathbf{R}_2(z) = \mathbf{E}_{md}(z)\mathbf{E}_{md}(l)^{-1}\mathbf{R}_2(l)\mathbf{E}_{mc}(l)\mathbf{E}_{mc}(z)^{-1} \tag{2.9.9}$$

Rearranging equation (2.9.5) gives

$$\mathbf{b} = \mathbf{E}_{mb}(z)^{-1}\,\mathbf{R}_1(z)\,\mathbf{E}_{ma}(z)\,\mathbf{a} \tag{2.9.10}$$

Substituting equation (2.9.10) into equation (2.9.1) yields

$$p_{(1)m}(r,\theta,z) = e^{jm\theta}\mathbf{a}^{\mathrm{T}}\left\{\mathbf{E}_{ma}(z) + [\mathbf{E}_{mb}(z)^{-1}\,\mathbf{R}_1(z)\,\mathbf{E}_{ma}(z)]^{\mathrm{T}}\,\mathbf{E}_{mb}(z)\right\}\psi_a(r). \tag{2.9.11}$$

Since both $\mathbf{E}_{ma}(z)$ and $\mathbf{E}_{mb}(z)$ are diagonal matrices, then equation (2.9.11) for the pressure in side one of the duct reduces to

$$p_{(1)m}(r,\theta,z) = e^{jm\theta}\left\{\mathbf{a}^{\mathrm{T}}\,\mathbf{E}_{ma}(z)\,[\mathbf{I} + \mathbf{R}_1(z)^{\mathrm{T}}]\right\}\psi_a(r). \tag{2.9.12}$$

Applying a similar approach to the field within side 2 of the duct gives

$$p_{(2)m}(r,\theta,z) = e^{jm\theta}\left\{\mathbf{c}^{\mathrm{T}}\,\mathbf{E}_{mc}(z)\,[\mathbf{I} + \mathbf{R}_2(z)^{\mathrm{T}}]\right\}\psi_c(r). \tag{2.9.13}$$

For a monopole source at $z = -l_1$, in the plane of the source $\Delta p = 0$, and therefore equations (2.9.12) and (2.9.13) may be equated to give

$$\mathbf{a}^{\mathrm{T}}\,\mathbf{E}_{ma}(-l_1)\,[\mathbf{I} + \mathbf{R}_1(-l_1)^{\mathrm{T}}]\;\psi_a(r) = \mathbf{c}^{\mathrm{T}}\,\mathbf{E}_{mc}(-l_1)\,[\mathbf{I} + \mathbf{R}_2(-l_1)^{\mathrm{T}}]\;\psi_b(r). \tag{2.9.14}$$

Multiplying both sides of equation (2.9.14) by $\psi_a{}^{\mathrm{T}}$ (where it is assumed now that ψ_a and ψ_c have the same order), and integrating over the duct cross section S, gives

$$\int_S \mathbf{a}^{\mathrm{T}}\mathbf{E}_{ma}(-l_1)[\mathbf{I}+\mathbf{R}_1(-l_1)^{\mathrm{T}}]\psi_a(r)\psi_a(r)^{\mathrm{T}}\,dS = \int_S \mathbf{c}^{\mathrm{T}}\mathbf{E}_{mc}(-l_1)[\mathbf{I}+\mathbf{R}_2(-l_1)^{\mathrm{T}}]\psi_c(r)\psi_c(r)^{\mathrm{T}}\,dS \tag{2.9.15}$$

The orthogonality property of the mode shape vectors may now be used, such that

$$\int_S \psi(r)\,\psi(r)^{\mathrm{T}}\,dS = \mathbf{I}, \tag{2.9.16}$$

where S is the duct cross section, and $\mathbf{I}$ is the identity matrix. Therefore equation (2.9.15) reduces to

$$\mathbf{a}^{\mathrm{T}}\,\mathbf{E}_{ma}(-l_1)\,[\mathbf{I}+\mathbf{R}_1(-l_1)^{\mathrm{T}}] = \mathbf{c}^{\mathrm{T}}\,\mathbf{E}_{mc}(-l_1)\,[\mathbf{I}+\mathbf{R}_2(-l_1)^{\mathrm{T}}] \tag{2.9.17}$$

Simplifying (2.9.17) gives

$$\mathbf{a}^{\mathrm{T}}\mathbf{G}_1 = \mathbf{c}^{\mathrm{T}}\mathbf{G}_2, \tag{2.9.18}$$

$$\mathbf{c}^{\mathrm{T}} = \mathbf{a}^{\mathrm{T}}\mathbf{G}_1\mathbf{G}_2^{-1}, \tag{2.9.19}$$

where the matrices $\mathbf{G}_1$ and $\mathbf{G}_2$ are defined by

$$\mathbf{G}_1 = \mathbf{E}_{ma}(-l_1)\,[\mathbf{I}+\mathbf{R}_1(-l_1)^{\mathrm{T}}], \tag{2.9.20}$$

$$\mathbf{G}_2 = \mathbf{E}_{mc}(-l_1)\,[\mathbf{I}+\mathbf{R}_2(-l_1)^{\mathrm{T}}]. \tag{2.9.21}$$

For a fixed azimuthal order the axial particle velocity in side 1 of the duct is given by

$$u_{z(1)m}(r,\theta,z) = \frac{1}{\rho c}\,e^{jm\theta}\sum_{n=0}^{\infty}\Omega_{mn}\left[A_{mn}\,e^{-j\Omega_{mn}kz} - B_{mn}\,e^{j\Omega_{mn}kz}\right]\psi_{mn}(r). \tag{2.9.22}$$

The expression for the particle velocity given in equation (2.9.22) may be written in matrix form as

$$u_{z(1)m}(r,\theta,z) = e^{jm\theta}\left\{\mathbf{a}^{\mathrm{T}}\mathbf{K}_{ma}\,\mathbf{E}_{ma}(z)\,\psi_a(r) - \mathbf{b}^{\mathrm{T}}\mathbf{K}_{mb}\,\mathbf{E}_{mb}(z)\,\psi_b(r)\right\}, \tag{2.9.23}$$

where $\mathbf{K}_{ma}$ is a diagonal matrix containing the values of $\frac{\Omega_{mn}}{\rho c}$ for each axial wavenumber given by

$$\mathbf{K}_{ma} = \begin{bmatrix} \frac{\Omega_{m0}}{\rho c} & 0 & \cdots & 0 \\ 0 & \frac{\Omega_{m1}}{\rho c} & \cdots & 0 \\ \vdots & \vdots & \ddots & \vdots \\ 0 & 0 & \cdots & \frac{\Omega_{mN}}{\rho c} \end{bmatrix} \tag{2.9.24}$$

the matrix $\mathbf{K}_{mb}$ may be similarly defined. The particle velocity in side 2 of the duct is given by

$$u_{z(2)m}(r,\theta,z) = e^{jm\theta}\left\{-\mathbf{c}^{\mathrm{T}}\mathbf{K}_{mc}\,\mathbf{E}_{mc}(z)\,\psi_c(r) + \mathbf{d}^{\mathrm{T}}\mathbf{K}_{md}\,\mathbf{E}_{md}(z)\,\psi_d(r)\right\}. \tag{2.9.25}$$

Using the reflection coefficient relationships these equations become

$$u_{z(1)m}(r,\theta,z) = e^{jm\theta}\,\mathbf{a}^{\mathrm{T}}\left[\mathbf{K}_{ma}\,\mathbf{E}_{ma}(z) - [\mathbf{E}_{mb}(z)^{-1}\,\mathbf{R}_1(z)\,\mathbf{E}_{ma}(z)]^{\mathrm{T}}\,\mathbf{K}_{ma}\,\mathbf{E}_{mb}(z)\right]\psi_a(r)$$

. (2.9.26)

Which reduces to

$$u_{z(1)m}(r,\theta,z) = e^{jm\theta}\,\mathbf{a}^{\mathrm{T}}\mathbf{E}_{ma}(z)\left[\mathbf{K}_{ma} - \mathbf{R}_1(z)^{\mathrm{T}}\,\mathbf{K}_{ma}\right]\psi_a(r). \tag{2.9.27}$$

In side two of the duct the axial particle velocity is expressed by

$$u_{z(2)m}(r,\theta,z) = e^{jm\theta}\,\mathbf{c}^{\mathrm{T}}\left[-\mathbf{K}_{mc}\,\mathbf{E}_{mc}(z) + [\mathbf{E}_{md}(z)^{-1}\,\mathbf{R}_2\,(z)\mathbf{E}_{mc}(z)]^{\mathrm{T}}\,\mathbf{K}_{mc}\,\mathbf{E}_{md}(z)\right]\psi_c(r)$$

. (2.9.28)

Which reduces to

$$u_{z(2)m}(r,\theta,z) = e^{jm\theta}\,\mathbf{c}^{\mathrm{T}}\mathbf{E}_{mc}(z)\left[-\mathbf{K}_{mc} + \mathbf{R}_2(z)^{\mathrm{T}}\,\mathbf{K}_{mc}\right]\psi_c(r). \tag{2.9.29}$$

Equations (2.9.27) and (2.9.29) may be written as,

$$u_{z(1)m} = e^{jm\theta}\,\mathbf{a}^{\mathrm{T}}\,\mathbf{Y}_1(z)\,\psi_a(r) \tag{2.9.30}$$

$$u_{z(2)m} = e^{jm\theta}\ \mathbf{c}^{\mathrm{T}}\ \mathbf{Y}_2(z)\ \psi_c(r) \tag{2.9.31}$$

where the matrices $\mathbf{Y}_1$ and $\mathbf{Y}_2$ are defined by

$$\mathbf{Y}_1(z) = \mathbf{E}_{ma}(z)\left[\mathbf{K}_{ma} - \mathbf{R}_1(z)^{\mathrm{T}}\,\mathbf{K}_{ma}\right] \tag{2.9.32}$$

$$\mathbf{Y}_2(z) = \mathbf{E}_{mc}(z)\left[-\mathbf{K}_{mc} + \mathbf{R}_2(z)^{\mathrm{T}}\,\mathbf{K}_{mc}\right] \tag{2.9.33}$$

For a point monopole source, the source strength distribution over the duct cross section is given by

$$\frac{Q}{r_s}\delta(r - r_s)\,\delta(\theta - \theta_s) \tag{2.9.34}$$

where θ_s and r_s are the azimuthal and radial locations of the source respectively, and Q is strength of the monopole source. This may be verified by integrating equation (2.36) over the duct cross section, S which shows that

$$\int_0^{2\pi}\int_0^a \frac{Q}{r_s}\delta(r - r_s)\,\delta(\theta - \theta_s)\,r\,dr\,d\theta = Q \tag{2.9.35}$$

where $\delta(x)$ is the Dirac delta function. At the source, the differences in the axial particle velocities between sides *1* and *2* of the duct can be equated to the volume velocity of the source such that

$$\Delta u_{zm}(r,\theta,-l_1) = u_{z(1)m}(r,\theta,-l_1) - u_{z(2)m}(r,\theta,-l_1) = \frac{Q}{r_s}\delta(r - r_s)\,\delta(\theta - \theta_s) \tag{2.9.36}$$

which can be written as

$$\Delta u_{zm}(r,\theta,-l_1) = e^{jm\theta}\ \mathbf{a}^{\mathrm{T}}\ \mathbf{Y}_1\ \psi_a(r) - e^{jm\theta}\ \mathbf{c}^{\mathrm{T}}\ \mathbf{Y}_2\ \psi_a(r) = \frac{Q}{r_s}\delta(r - r_s)\,\delta(\theta - \theta_s) \tag{2.9.37}$$

To match the source to the field within the duct, the orthogonality property of the mode shape functions is again used. Multiplying both sides of equation (2.9.37) by $e^{-jm\theta}\ \psi_a{}^{\mathrm{T}}(r)$, and integrating over the duct cross section gives

$$\mathbf{a}^{\mathrm{T}}\,\mathbf{Y}_1(-l_1)-\mathbf{c}^{\mathrm{T}}\,\mathbf{Y}_2\,(-l_1)=Q\psi_a{}^{\mathrm{T}}(r_s)e^{-jm\theta_s} \tag{2.9.38}$$

where $\psi^{\mathrm{T}}(r_s)$ is a row vector of mode shape function evaluated at the radial source location r_s. Using the relationship between **a** and **c** in equation (2.9.19), equation (2.9.38) becomes

$$Q\psi^{\mathrm{T}}(r_s)e^{-jm\theta_s}=\mathbf{a}^{\mathrm{T}}\,\mathbf{Y}_1(-l_1)-\mathbf{a}^{\mathrm{T}}\,\mathbf{G}_1\mathbf{G}_2{}^{-1}\,\mathbf{Y}_2(-l_1)\,. \tag{2.9.39}$$

This can be simplified to give

$$\mathbf{q}^{\mathrm{T}}=\mathbf{a}^{\mathrm{T}}\,[\mathbf{Y}_1-\mathbf{G}_1\mathbf{G}_2{}^{-1}\,\mathbf{Y}_2], \tag{2.9.40}$$

where the source strength vector **q** is defined by

$$\mathbf{q}^{\mathrm{T}}=Q\psi_a{}^{\mathrm{T}}(r_s)e^{-jm\theta_s} \tag{2.9.41}$$

Equation (2.9.41) may be written in the compact form

$$\mathbf{q}^{\mathrm{T}}=\mathbf{a}^{\mathrm{T}}\,\mathbf{H} \tag{2.9.42}$$

where the matrix **H** is defined by

$$\mathbf{H}=[\mathbf{Y}_1-\mathbf{G}_1\mathbf{G}_2{}^{-1}\,\mathbf{Y}_2] \tag{2.9.43}$$

Rearranging equation (2.9.43), gives the modal amplitude vector **a**, as

$$\mathbf{a}=(\mathbf{H}^{\mathrm{T}})^{-1}\,\mathbf{q} \tag{2.9.44}$$

By solving equation (2.9.44), it is possible to solve for all the other modal amplitudes within the duct.

Solving for the modal amplitudes, the axial particle velocity given by equations (2.9.27) and (2.9.29) at either of the two ends of the duct may be evaluated. If the duct is chosen to be terminated in a rigid baffle, then it is possible to use the Rayleigh Integral to calculate the field radiated externally from the duct. Results

obtained using this model are presented in the next chapter where they are compared with experimental results.

2.10 Conclusions.

A derivation of an analytical model of the internal and external fields from a finite length duct terminating in a rigid baffle has been presented. This model offers greater potential flexibility than the experimental approach detailed in the next chapter. Using this model, it is possible to examine the effects of source location and duct wall impedance upon the externally radiated field. Furthermore, this analytical model will be used to examine the accuracy of the propagation technique described in Chapter 4, and to compare with the experimental results presented in Chapter 3.

It has been shown that the method for obtaining the far-field radiation from the duct may be subdivided into solving for the internal pressure and axial particle velocity, and then for the external pressure field. The previous work by Zorumski (1973) which concerned a semi-infinite, baffled, duct, has been extended to include a duct of finite length. The analytical model presented in this Chapter is exact. Due to the geometrical symmetry of the duct, then the reflection coefficients at one end of the duct will be the same as those at the other end. Therefore the reflection coefficients need only be calculated for one end of the duct. Also as the duct is baffled the two exterior fields from each end of the duct will not interfere with each other, and do not alter the reflection coefficients at either end of the duct. If the duct were unbaffled, then this would not be the case. It should also be made clear that this model is completely general, and it is possible to examine the radiation from sources within a duct with any impedance at the duct wall.

It has been established that the internal acoustic field produced by a source within the duct is constructed from an infinite series of forward and backward propagating modes, which are partially reflected at the ends of the finite length duct. Also these modes are coupled, and this coupling is important in the calculation of the modal reflection coefficients at the ends of the duct.

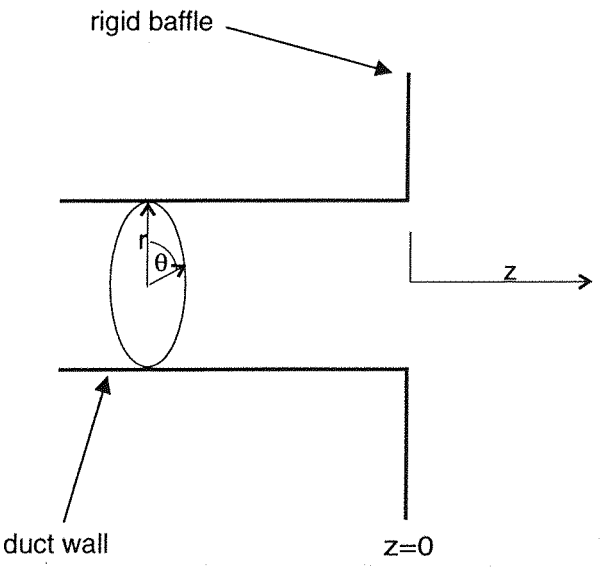

Figure 2.1 - The cylindrical geometry of a circular duct.

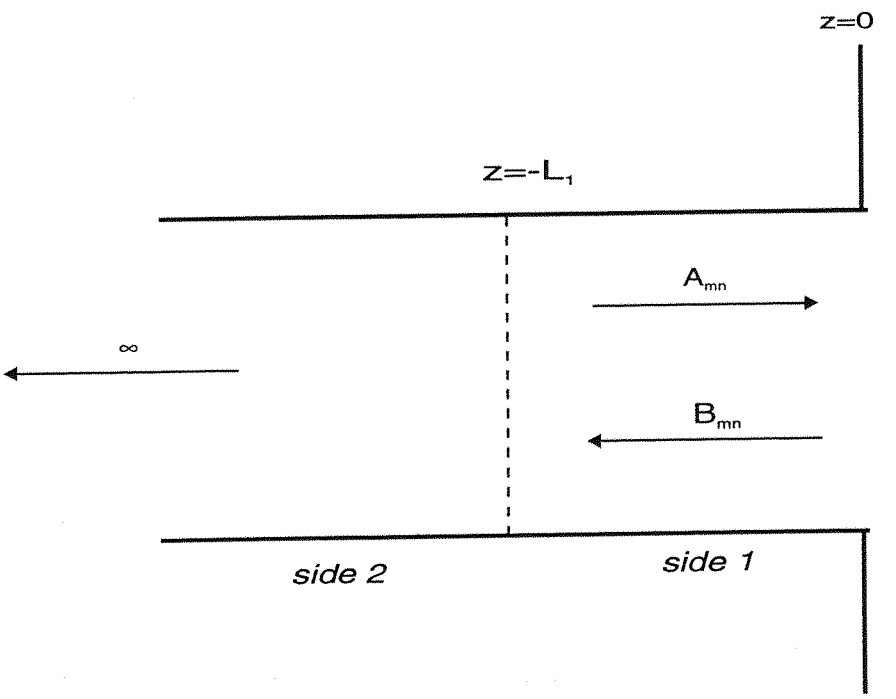

Figure 2.2 - The geometry for a semi-infinite duct.

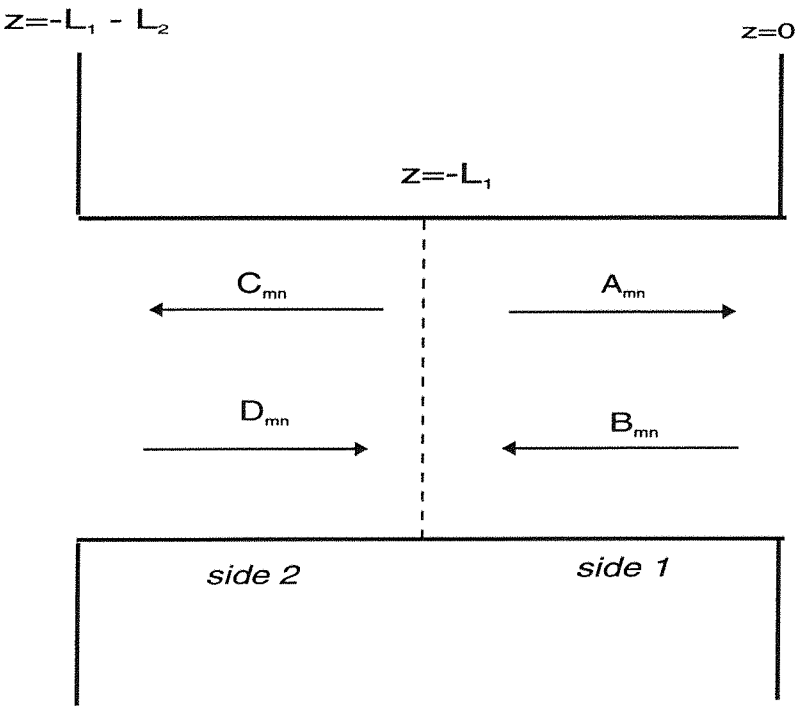

Figure 2.3 - The geometry for a finite length duct.

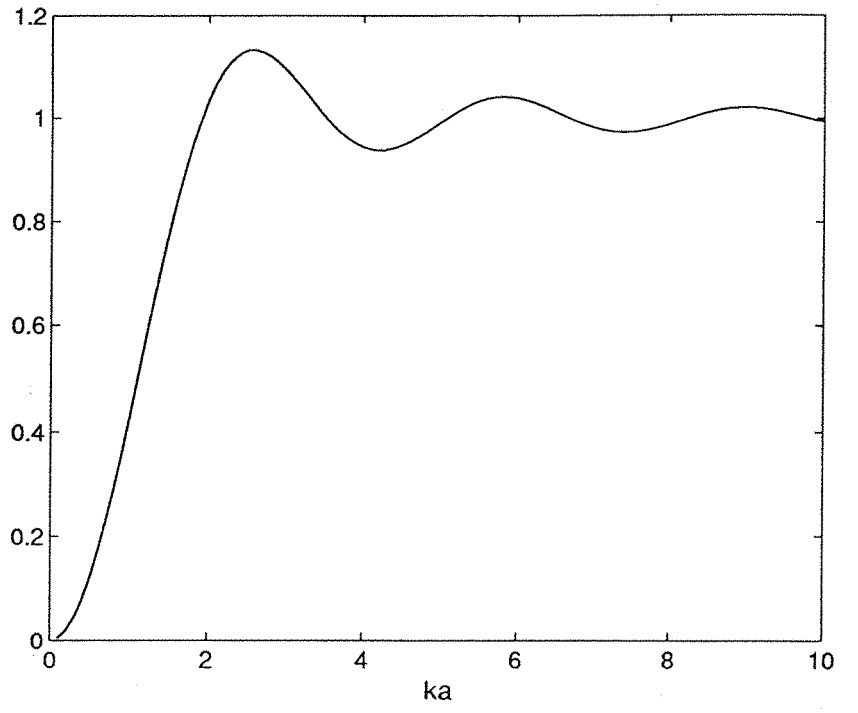

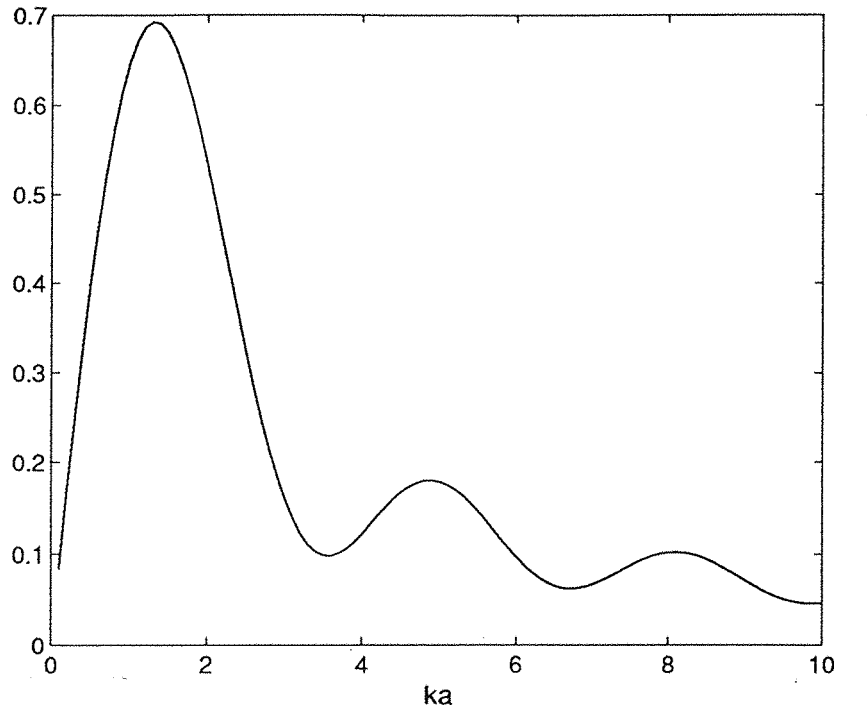

Figure 2.4a - The real and imaginary parts of the radiation impedance for an incident plane wave and a reflected plane wave (i.e. $m = n = l = 0$) within a baffled, hard walled duct. This is identical to a circular piston in a baffle.

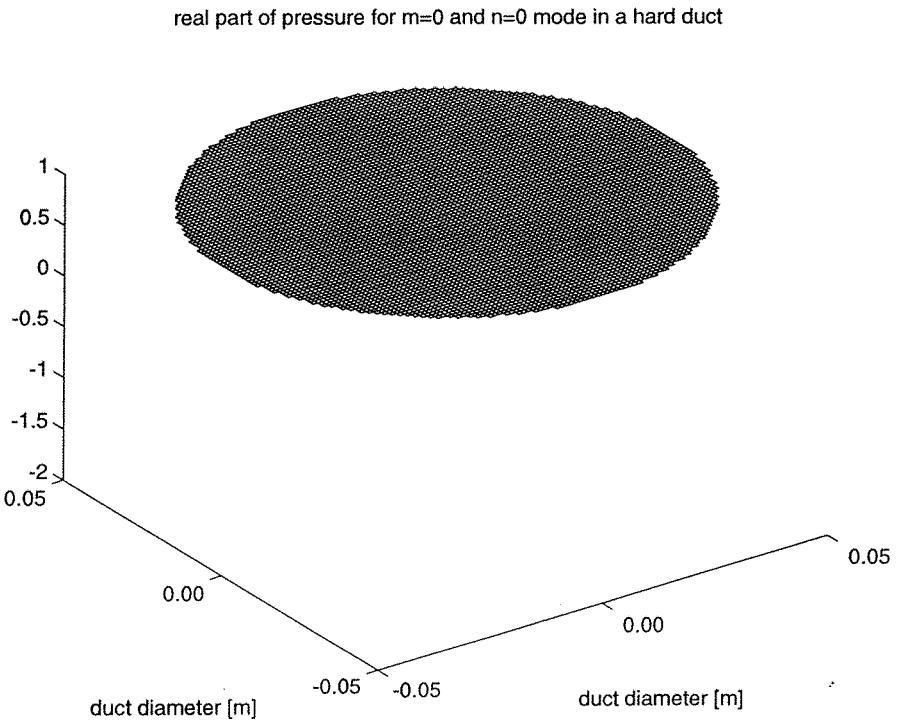

Figure 2.4b - The mode shape for the incident and reflected plane wave in figure 2.4.

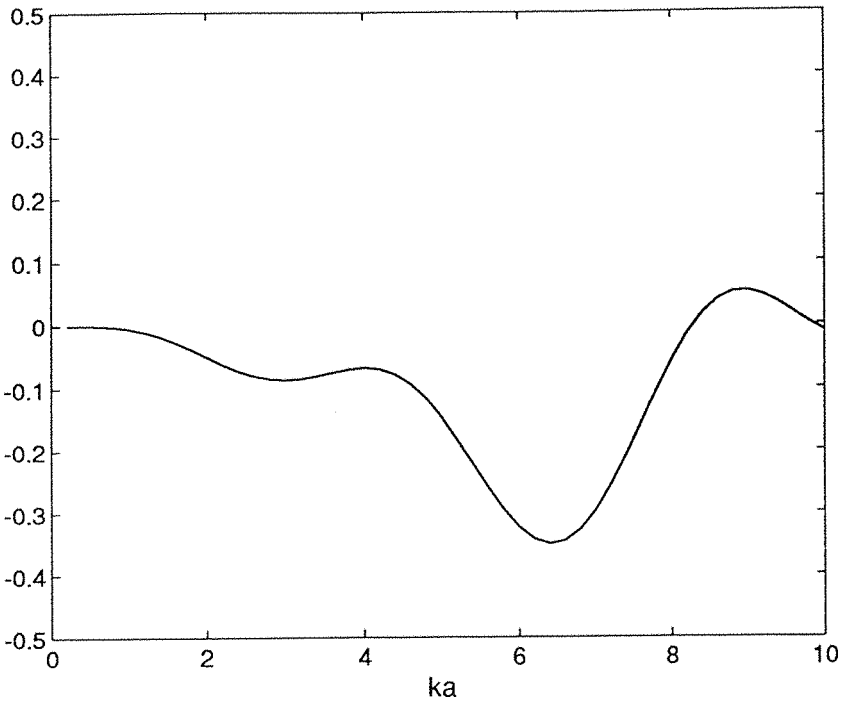

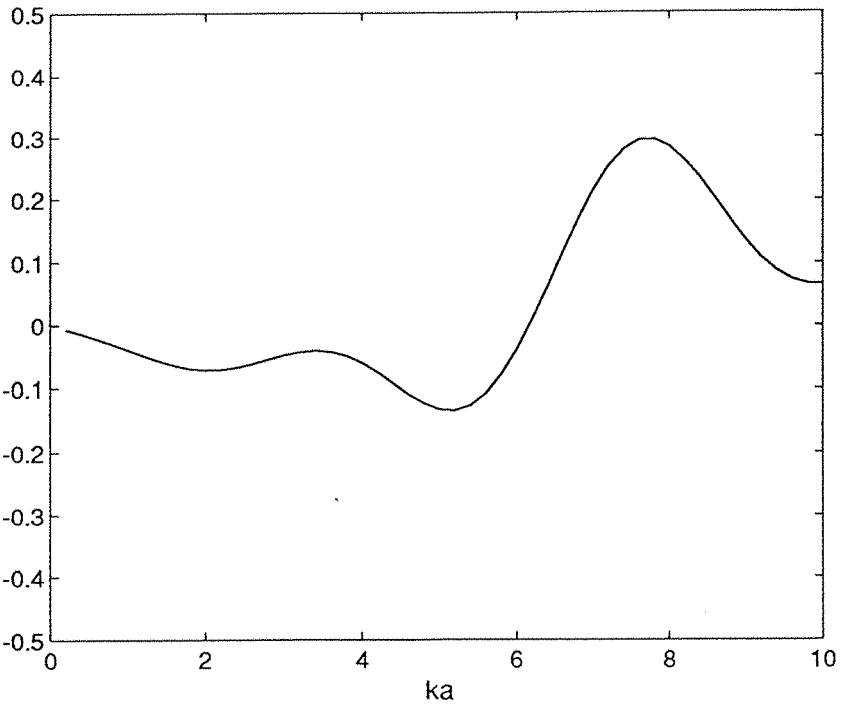

Figure 2.5a - The real and imaginary parts of the radiation impedance for an incident plane wave $m = n = 0$ and a reflected $m = 0, l = 2$ mode within a baffled, hard walled duct.

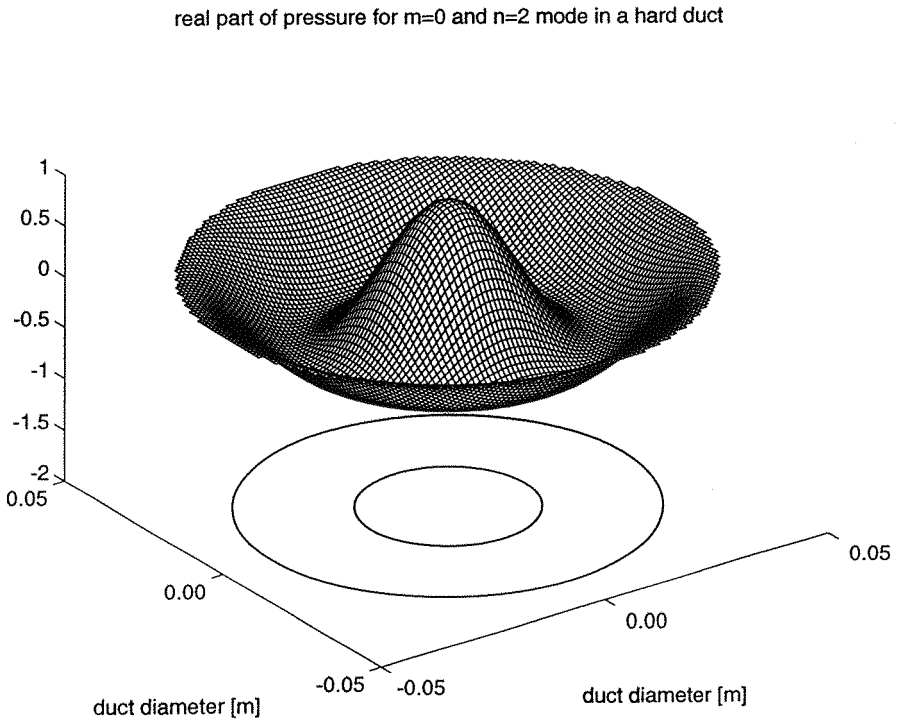

Figure 2.5b - The mode shape for the reflected mode $m = 0, l = 2$ mode figure 2.5.

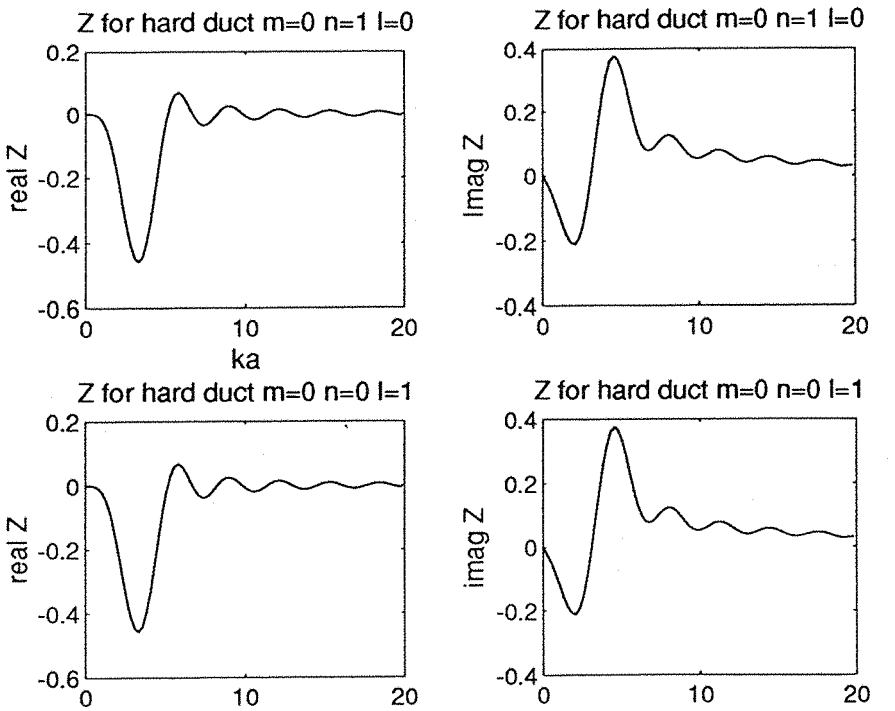

Figure 2.6a - A comparison between the real and imaginary parts of the radiation impedance for the $m = n = 0$, $l = 1$ mode,

and the $m = l = 0$, $n = 1$ mode in a hard walled duct.

These two impedances are the same due to the symmetry

of the impedance matrix Z_{mnl}, i.e. $Z_{mnl} = Z_{mln}$.

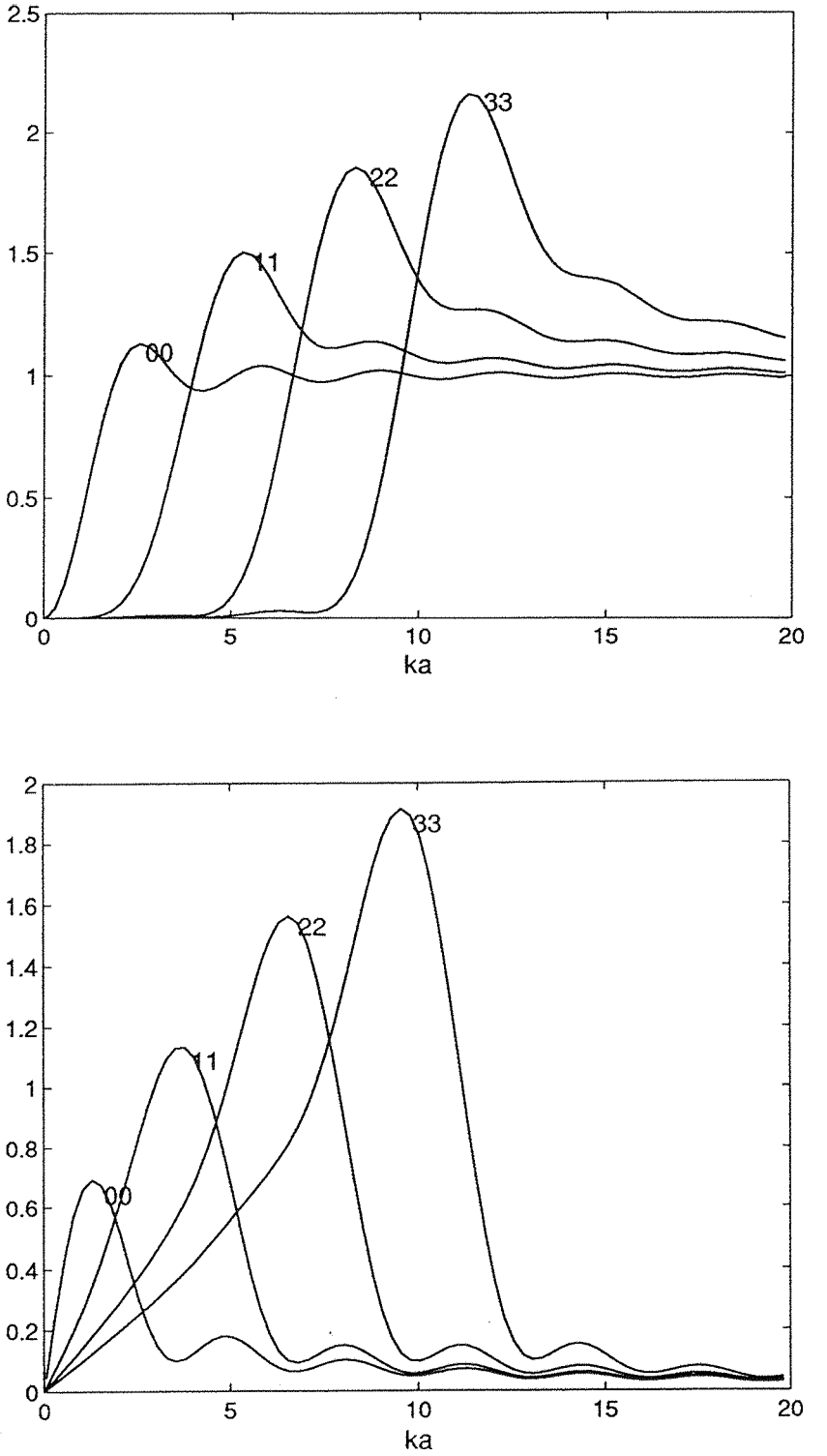

Figure 2.7a - A comparison of the real and imaginary parts of the radiation impedance Z_{mnl} for fixed azimuthal order ($m = 0$) for various radial orders within a hard walled duct. The numbers on the curves indicate the radial order of the incident mode and reflected mode respectively.

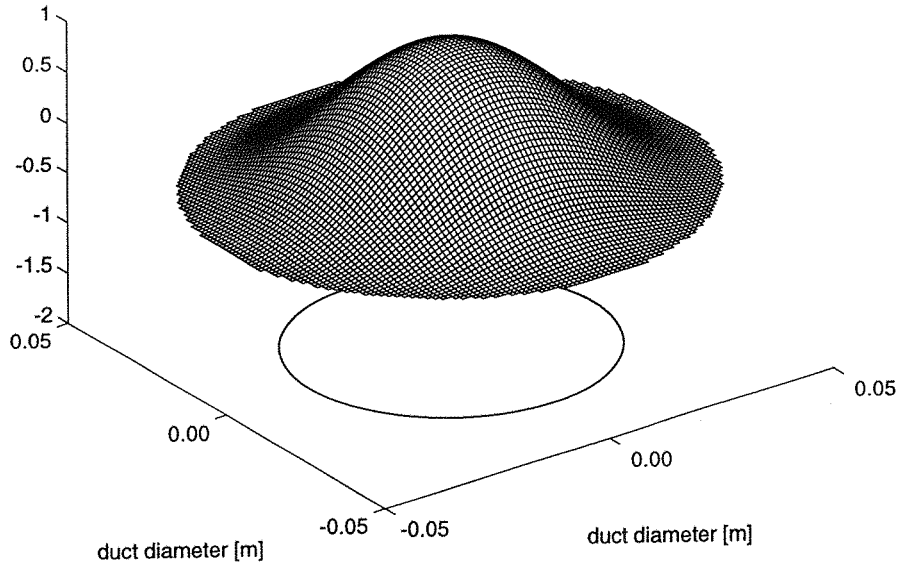

Figure 2.7b - The mode shape for the mode $m = 0, n = 1$ mode figure 2.7a.

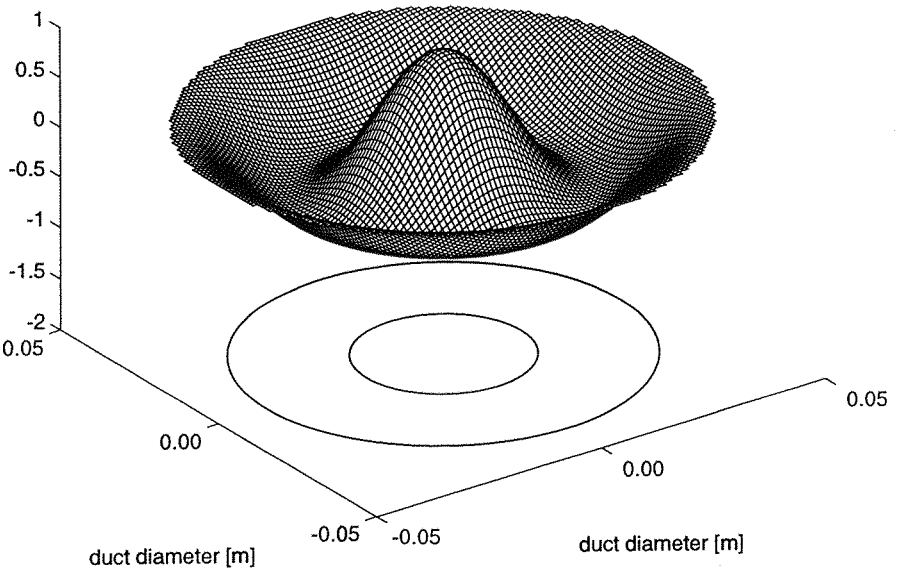

Figure 2.7c - The mode shape for the mode $m = 0, n = 2$ mode figure 2.7a.

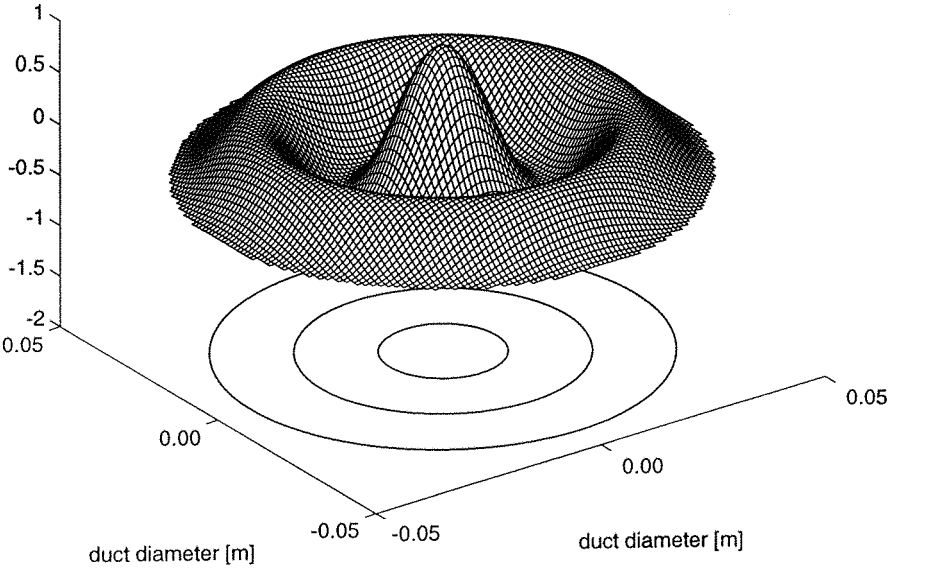

Figure 2.7d - The mode shape for the mode $m = 0, n = 3$ mode figure 2.7a.

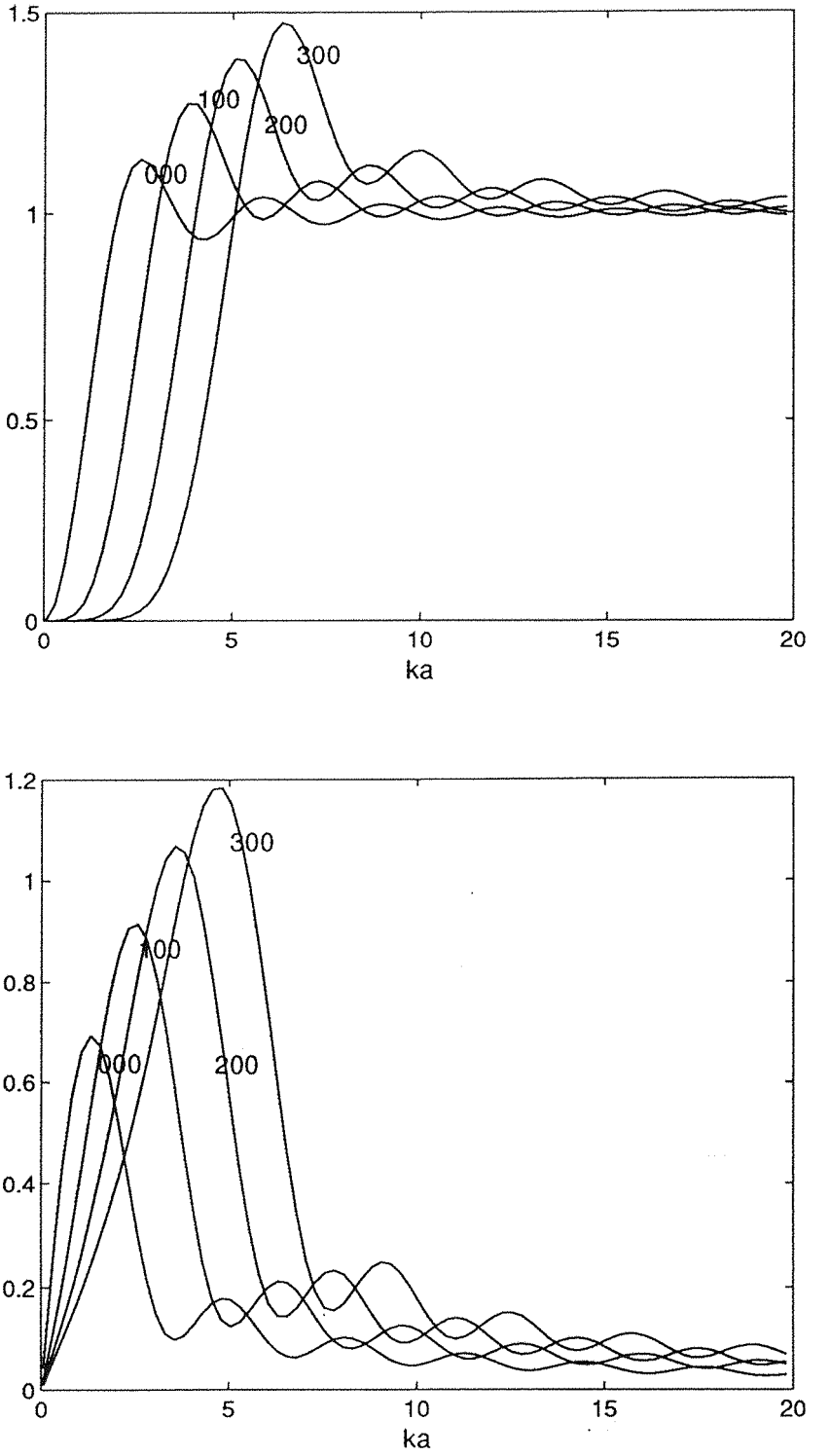

Figure 2.8a - A comparison of the real and imaginary parts of the radiation impedance Z_{mnl} for fixed radial order $(n = l = 0)$ for various azimuthal orders within a hard walled duct. The numbers on the curves indicate the modal order (mnl).

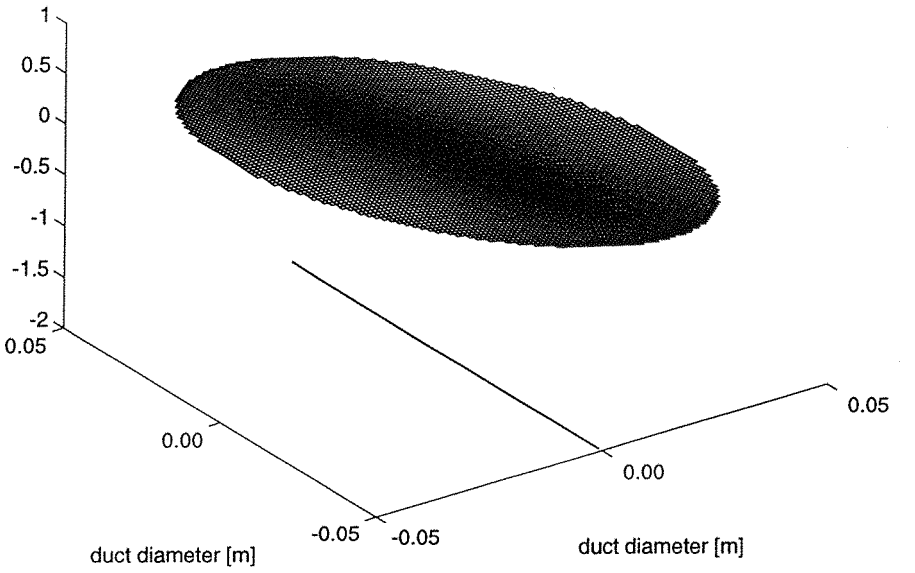

Figure 2.8b - The mode shape for the mode $m = 1, n = 0$ mode figure 2.8a.

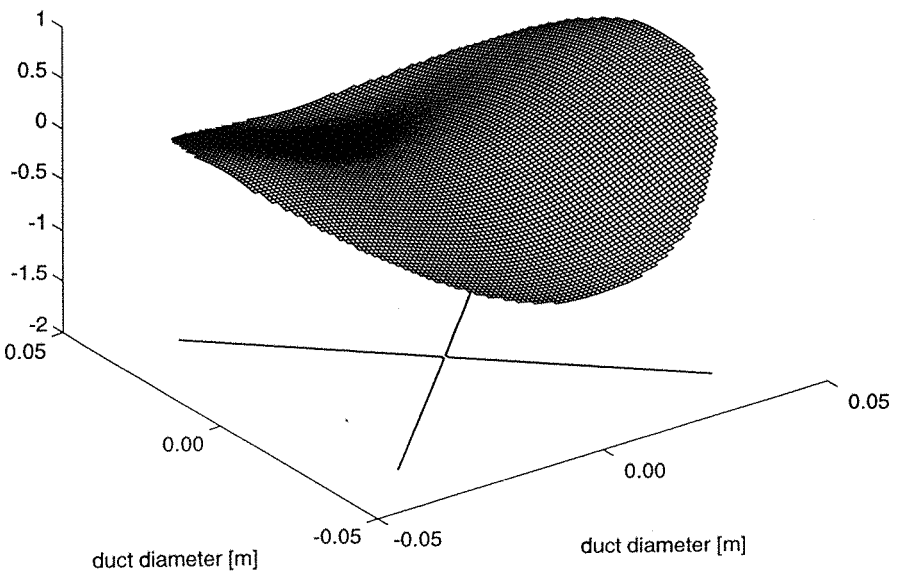

Figure 2.8c - The mode shape for the mode $m = 2, n = 0$ mode figure 2.8a.

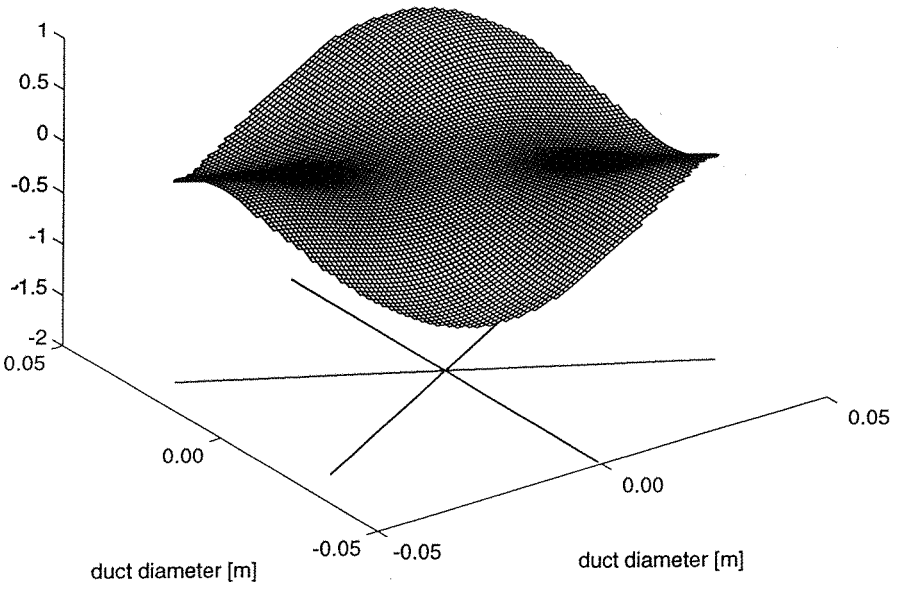

Figure 2.8d - The mode shape for the mode $m = 3, n = 0$ mode figure 2.8a.

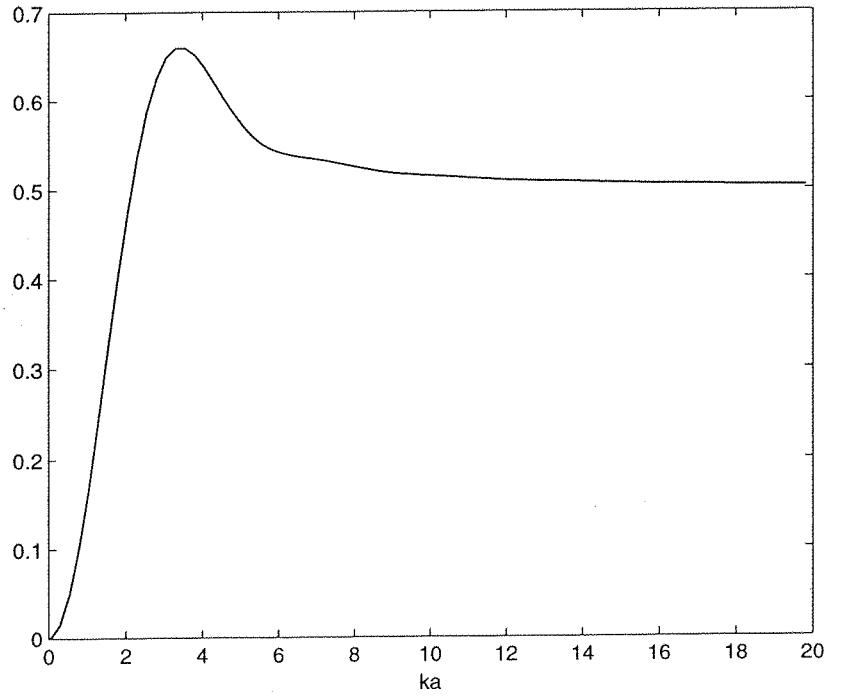

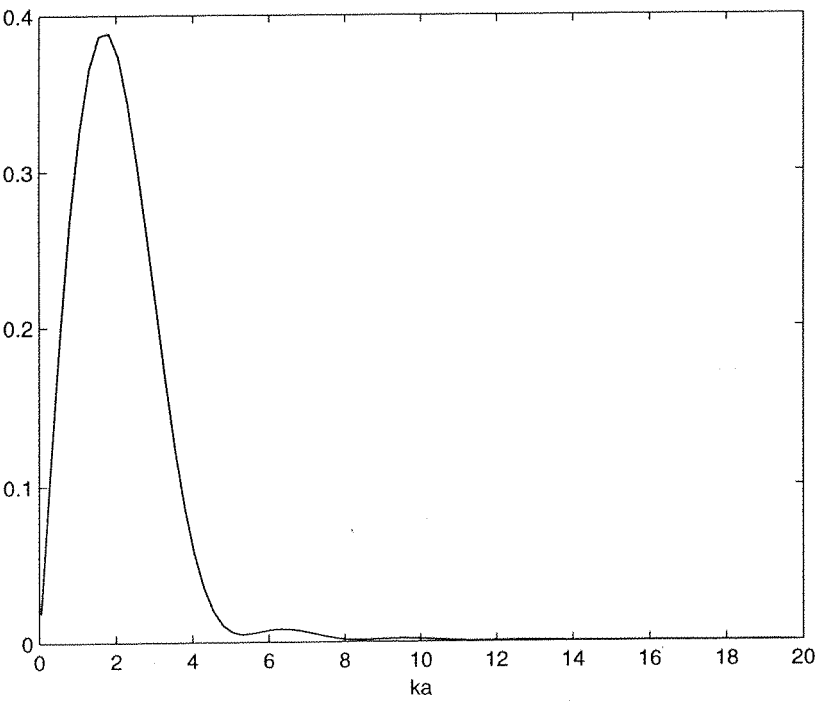

Figure 2.9a - The real and imaginary parts of the radiation impedance for an incident $m = n = l = 0$ mode and a reflected $m = n = l = 0$ mode within a baffled, pressure release lined duct.

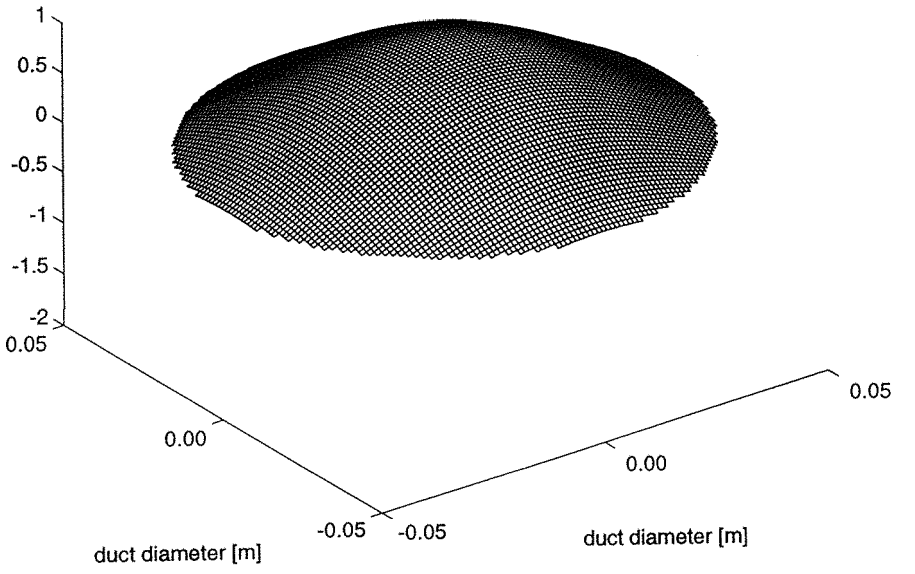

Figure 2.9b - The mode shape for the incident and reflected $m = n = l = 0$ mode in a pressure release lined duct as in figure 2.9a.

Note that this is not a plane wave as in the hard walled duct in figure 2.4a.

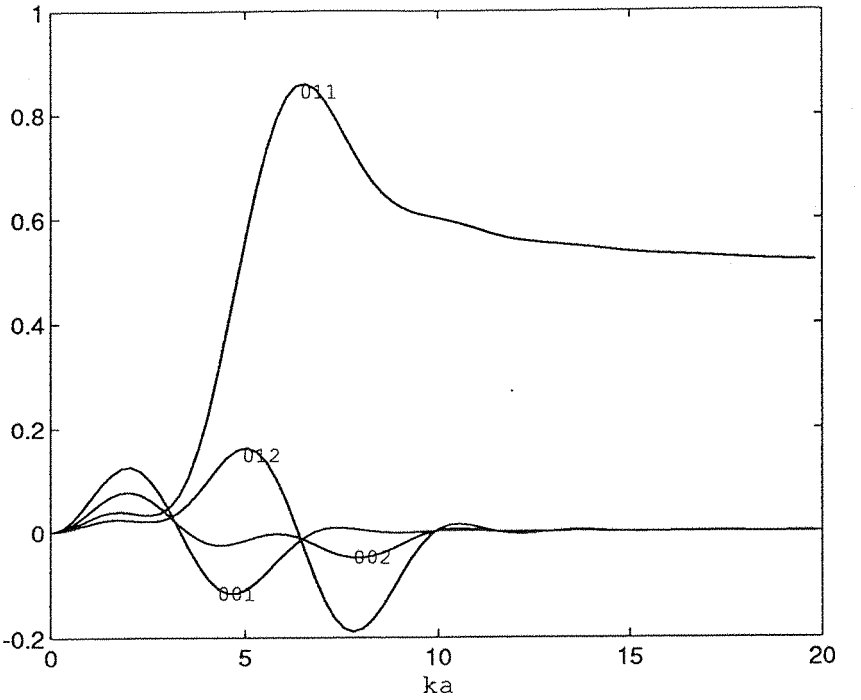

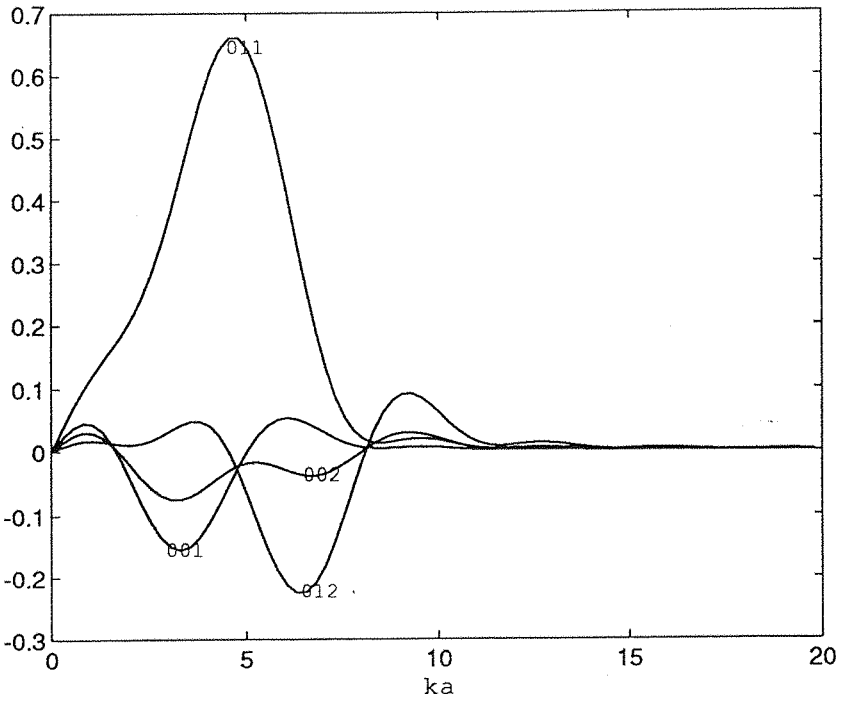

Figure 2.10a - A comparison of the real and imaginary parts of the radiation impedance Z_{mnl} for fixed azimuthal order ($m = 0$) within a baffled, pressure release lined duct.

The numbers on the curves indicate the modal order (mnl).

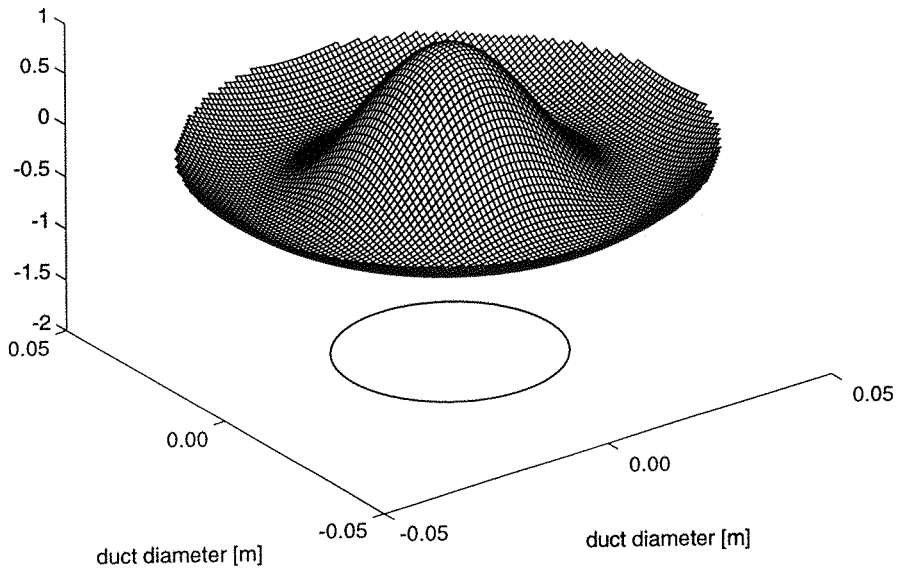

Figure 2.10b - The mode shape for the $m = 0, l = 1$ mode in figure 2.10a, for a pressure release lined duct

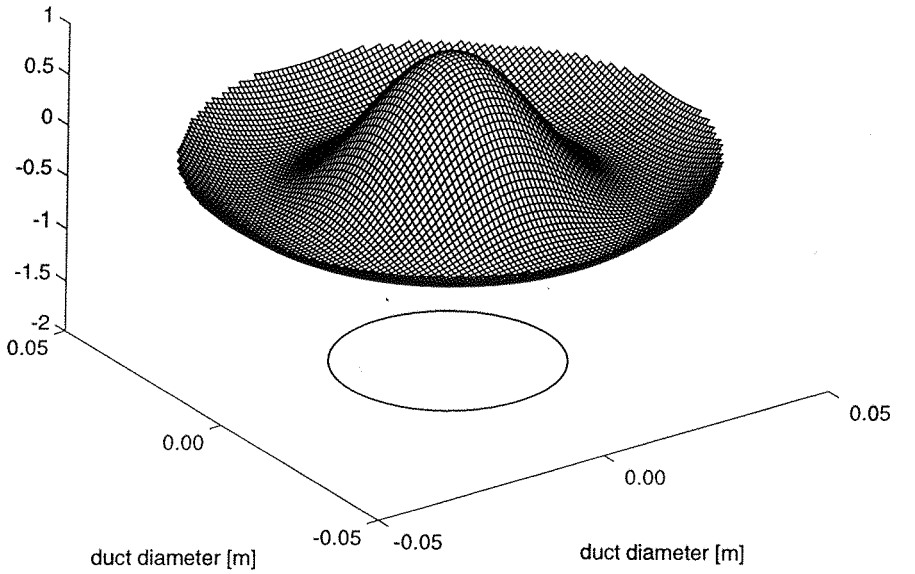

Figure 2.10c - The mode shape for the incident $m = 0, n = 1$ mode in figure 2.10a, for a pressure release lined duct

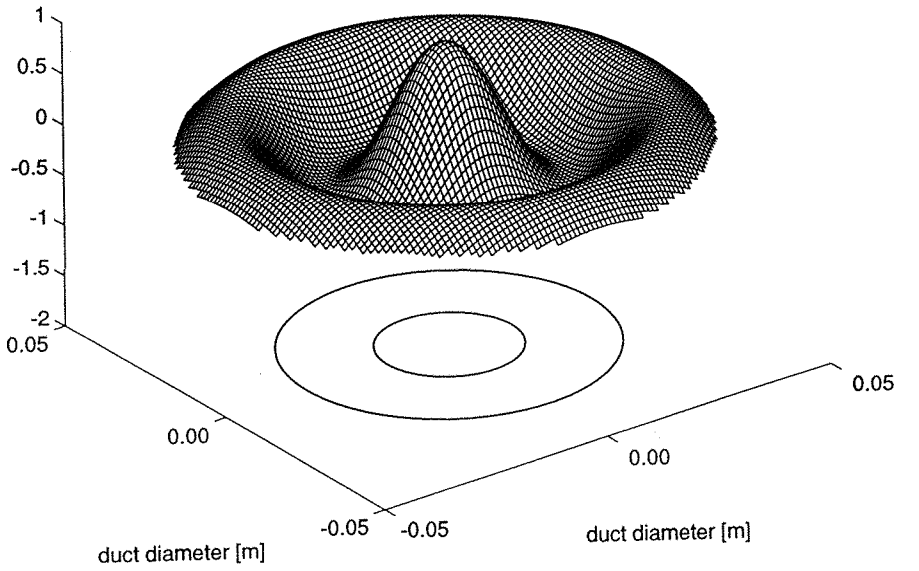

Figure 2.10d - The mode shape for the reflected $m = 0, l = 2$ mode in figure 2.10a, for a pressure release lined duct

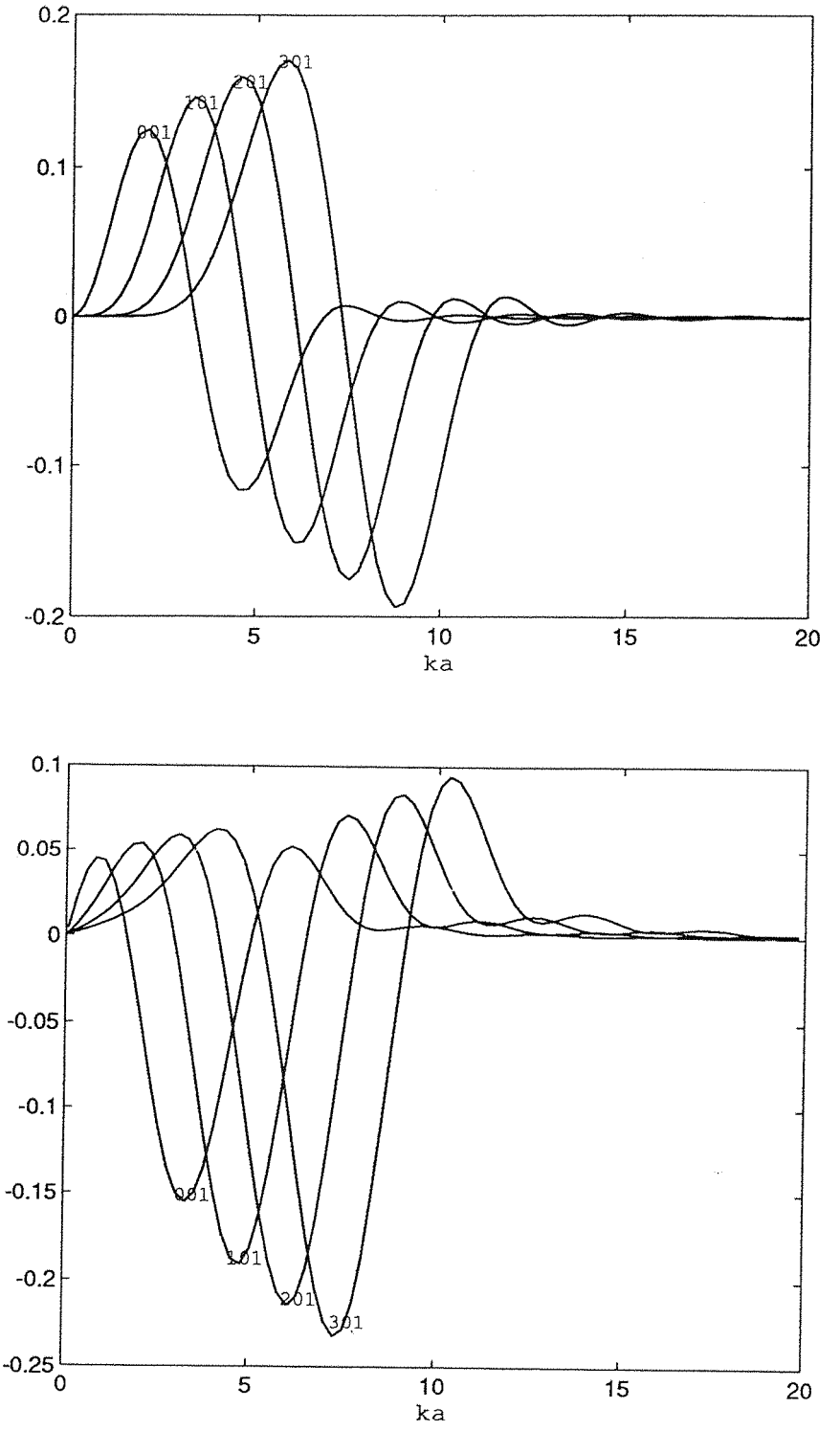

Figure 2.11a - A comparison of the real and imaginary parts of the radiation impedance Z_{mnl} for various modes within a baffled, pressure release lined duct. The numbers on the curves indicate the modal order (mnl).

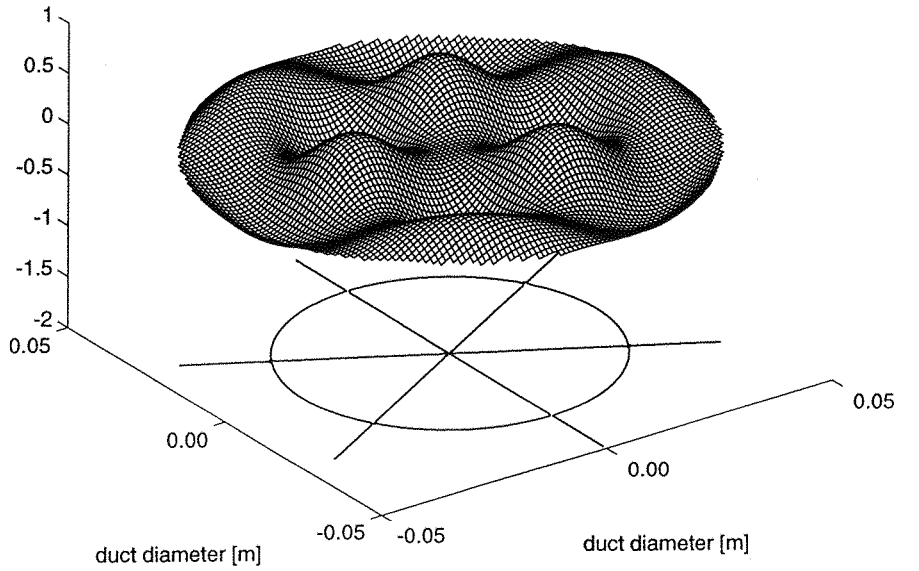

Figure 2.11b - The mode shape for the reflected $m = 3,\ l = 1$ mode in figure 2.11a, for a pressure release lined duct

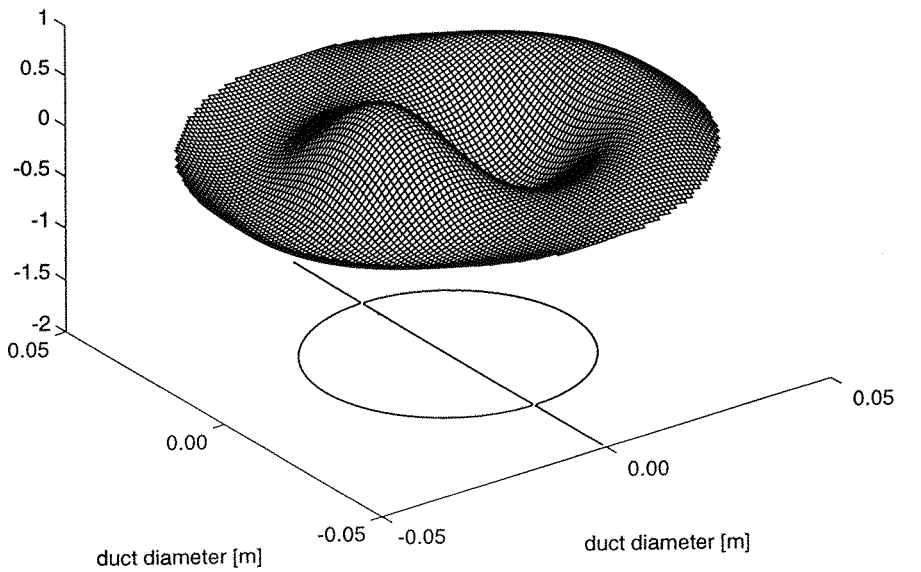

Figure 2.11c - The mode shape for the incident $m = 1, n = 1$ mode in figure 2.11a, for a pressure release lined duct

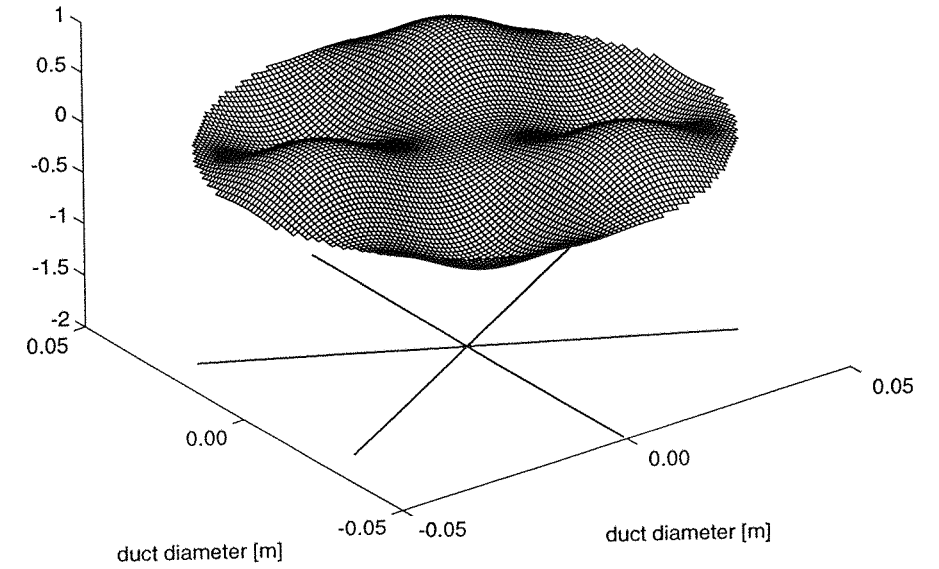

Figure 2.11e - The mode shape for the incident $m = 3, n = 0$ mode in figure 2.11a, for a pressure release lined duct

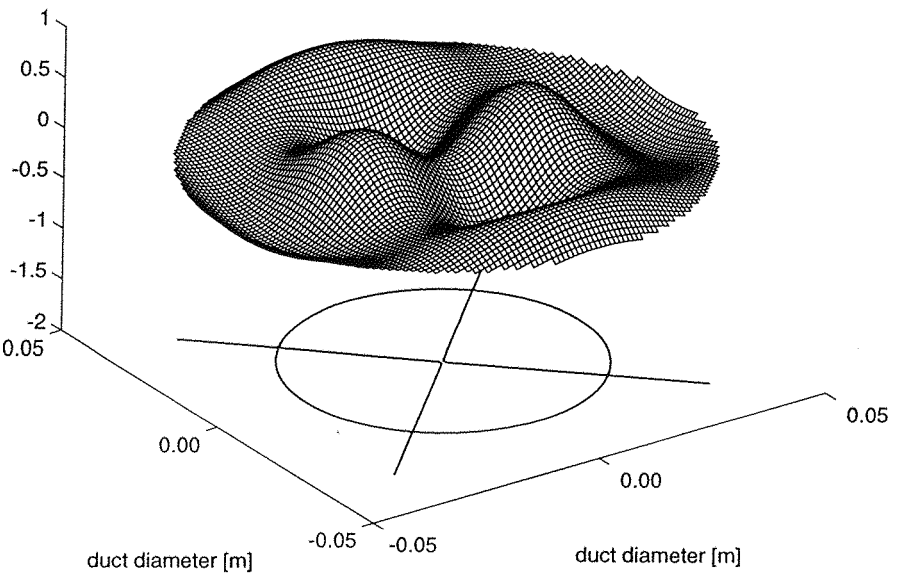

Figure 2.11d - The mode shape for the reflected $m = 2, l = 1$ mode in figure 2.11a, for a pressure release lined duct

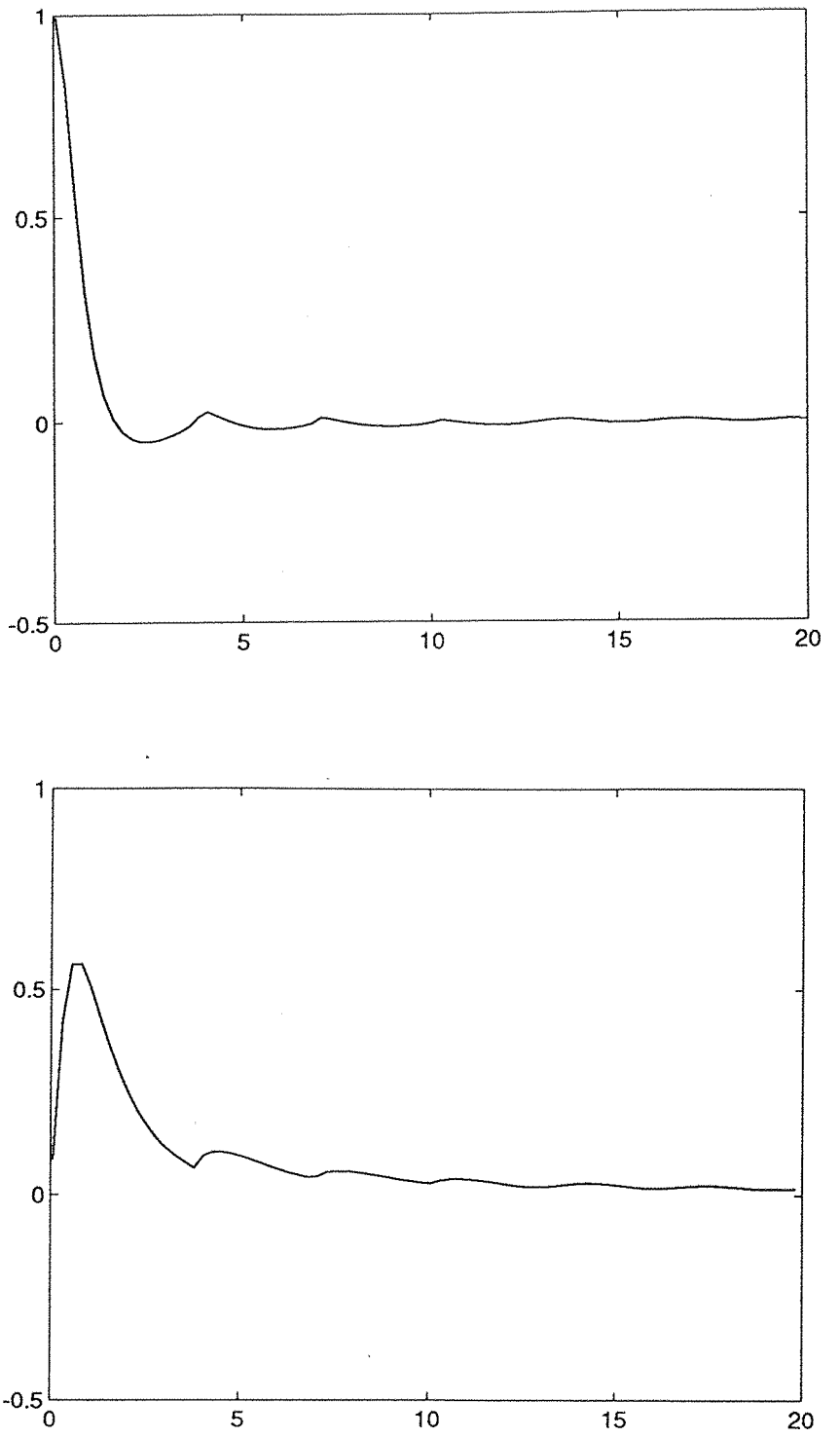

Figure 2.12 - The real and imaginary parts of the reflection coefficient for the plane wave mode within a hard walled duct. ($m = 0, n = 0, l = 0$)

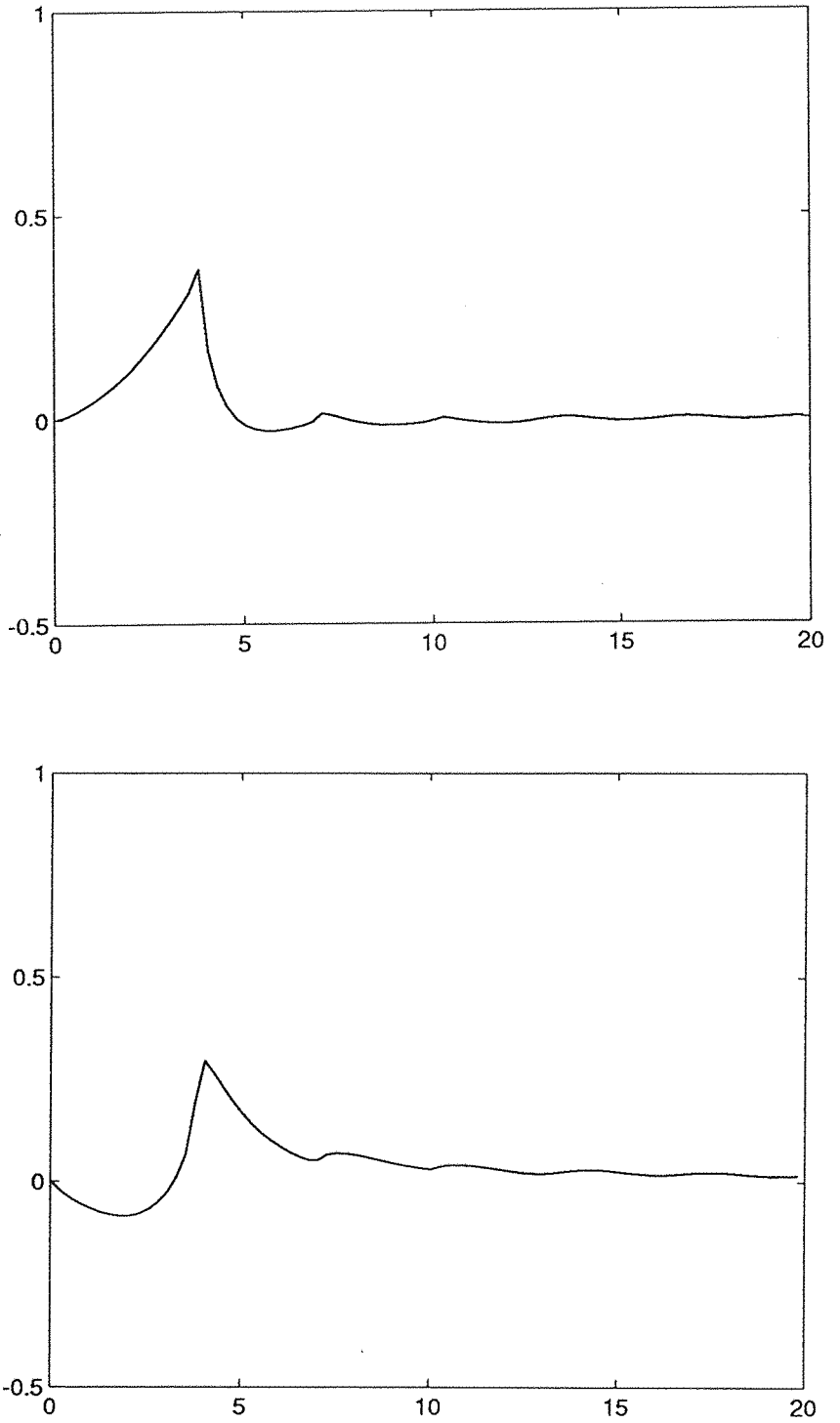

Figure 2.13 - The real and imaginary parts of the coupled reflection coefficient for an incident $m = 0, n = 1$ mode and a reflected $m = 0, l = 0$ mode within a hard walled duct.

Note that the value of this coupled reflection coefficient is significant around the cut-off frequency of the incident mode ($ka = 3.83$).

This indicates that coupling would be significant around this frequency

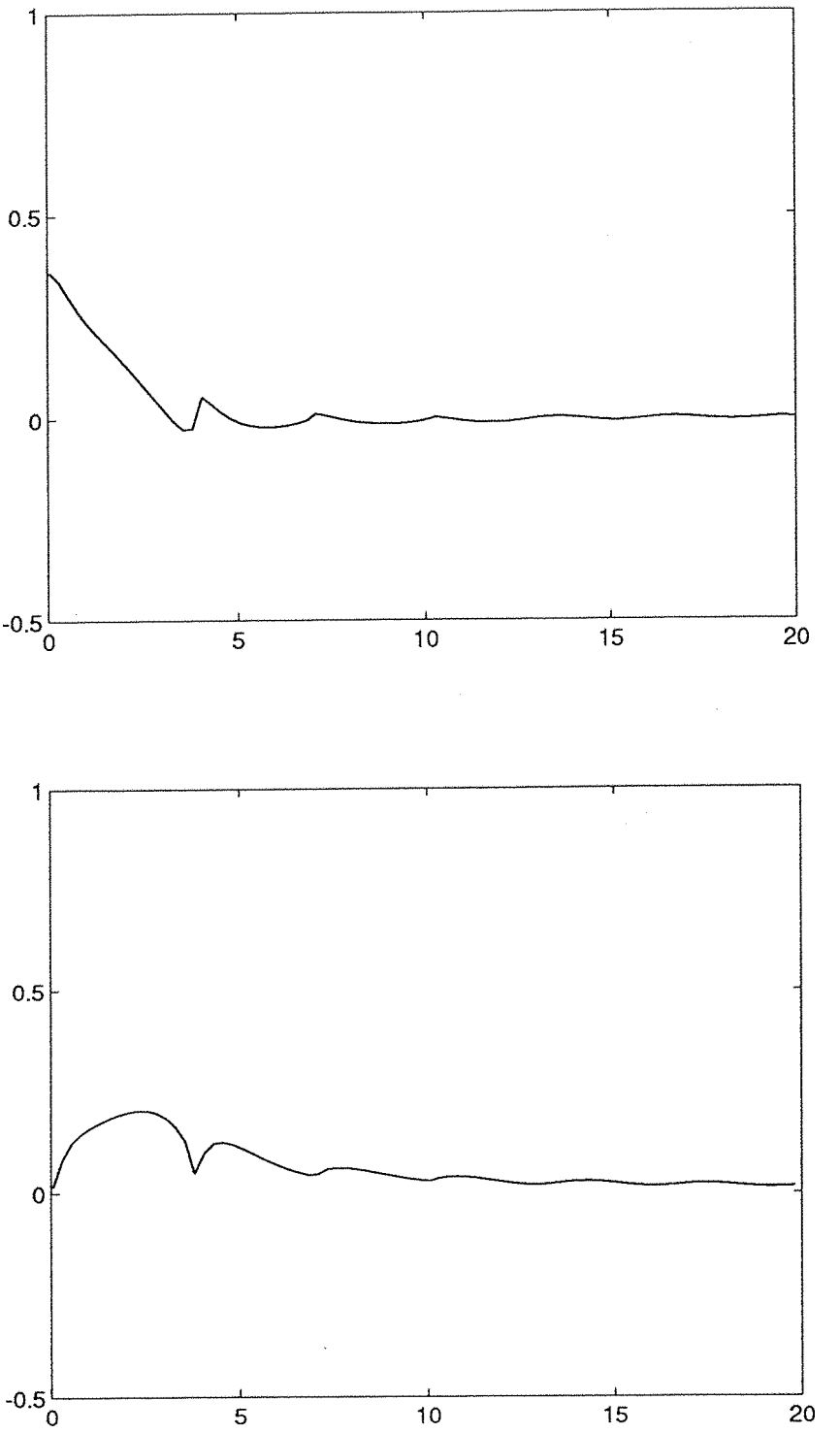

Figure 2.14 - The real and imaginary parts of the coupled reflection coefficient for an incident $m = 0, n = 0$ mode and a reflected $m = 0, l = 1$ mode within a hard walled duct. Note that the value of this coupled reflection coefficient is different from that given in figure 2.13. This indicates that the reflection coefficient matrix R_{mnl} is non-symmetric (i.e. $R_{mnl} \neq R_{mln}$)

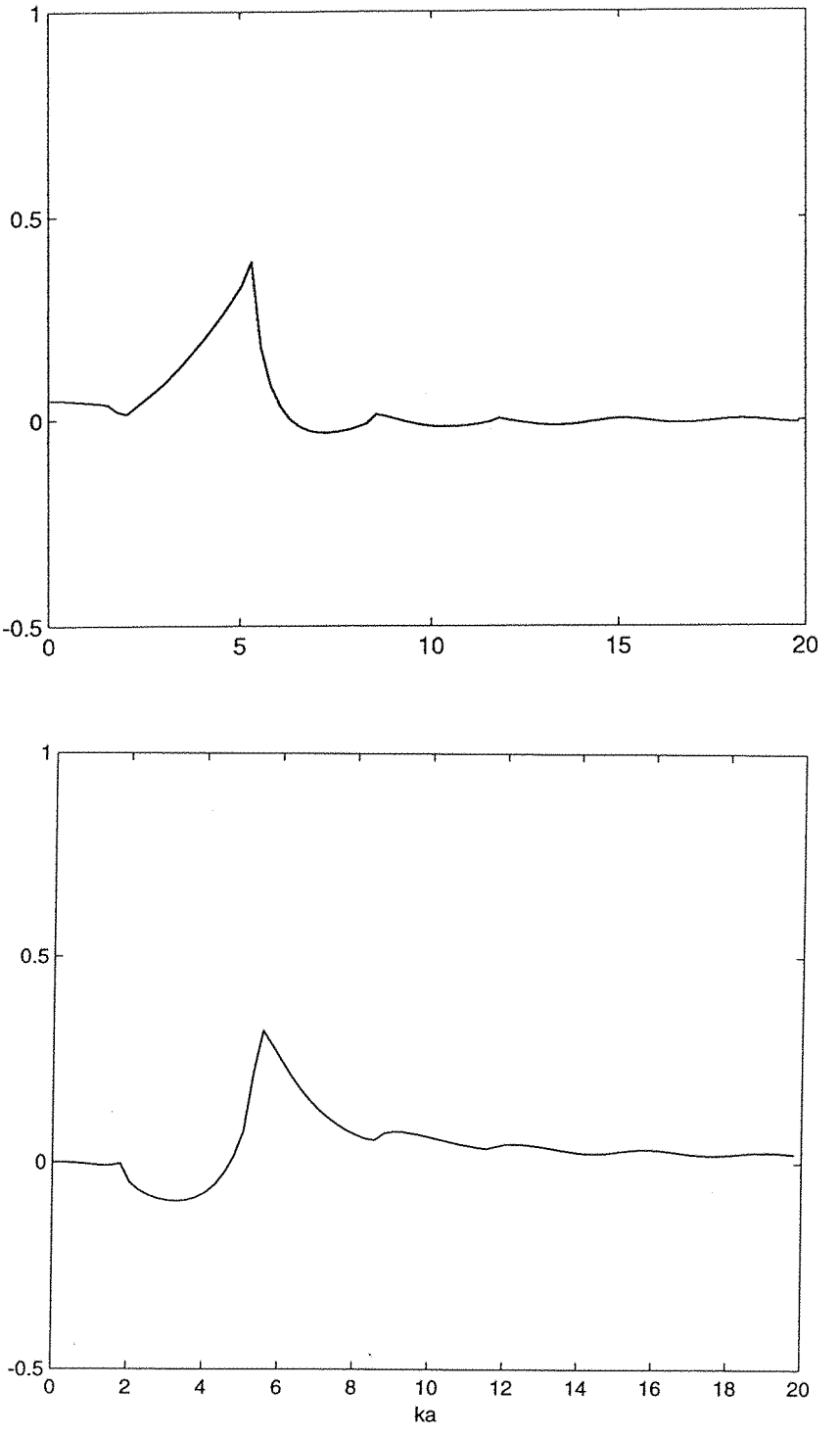

Figure 2.15 - The real and imaginary parts of the coupled reflection coefficient for an incident $m=1, n=1$ mode and a reflected $m=1, l=0$ mode within a hard walled duct. Note that the value of this coupled reflection coefficient is significant around the cut-off frequency of the incident mode ($ka=5.33$).

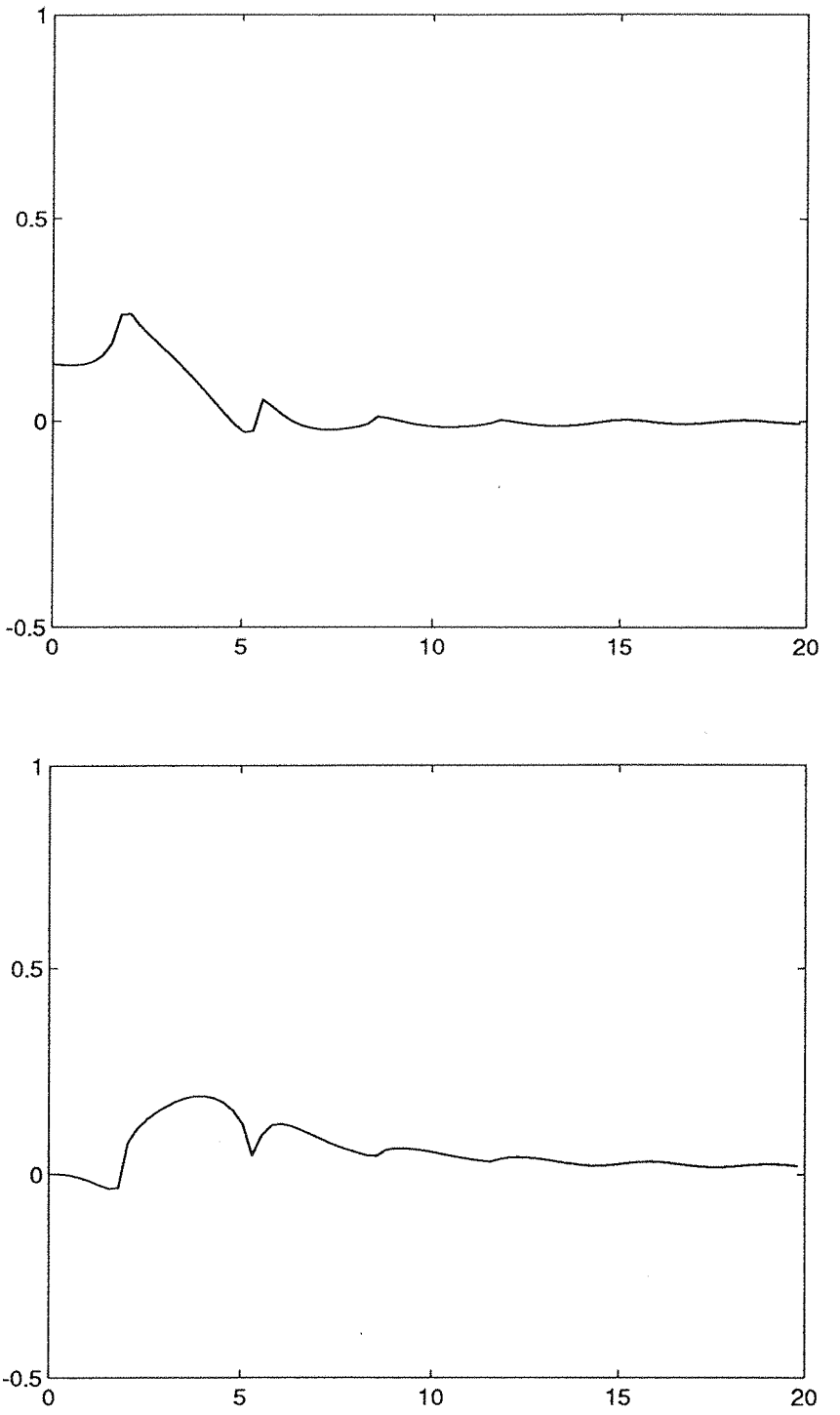

Figure 2.16 - The real and imaginary parts of the coupled reflection coefficient for an incident $m = 1, n = 0$ mode and a reflected $m = 1, l = 1$ mode within a hard walled duct. Note that the value of this coupled reflection coefficient is significant around the cut-off frequency of the incident mode ($ka = 3.83$).

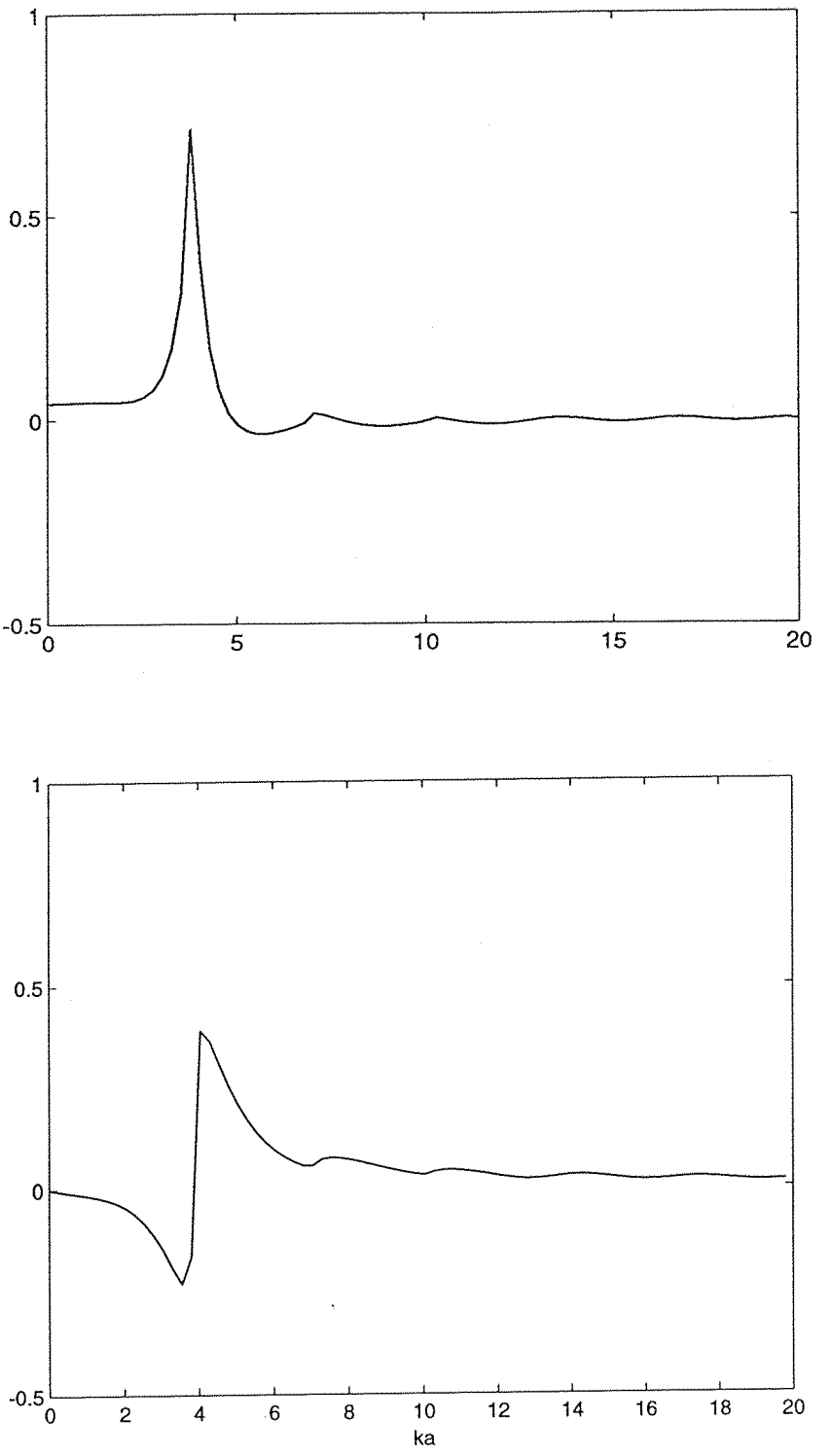

Figure 2.17 - The real and imaginary parts of the reflection coefficient for an incident $m = 0, n = 1$ mode and a reflected $m = 0, l = 1$ mode within a hard walled duct.

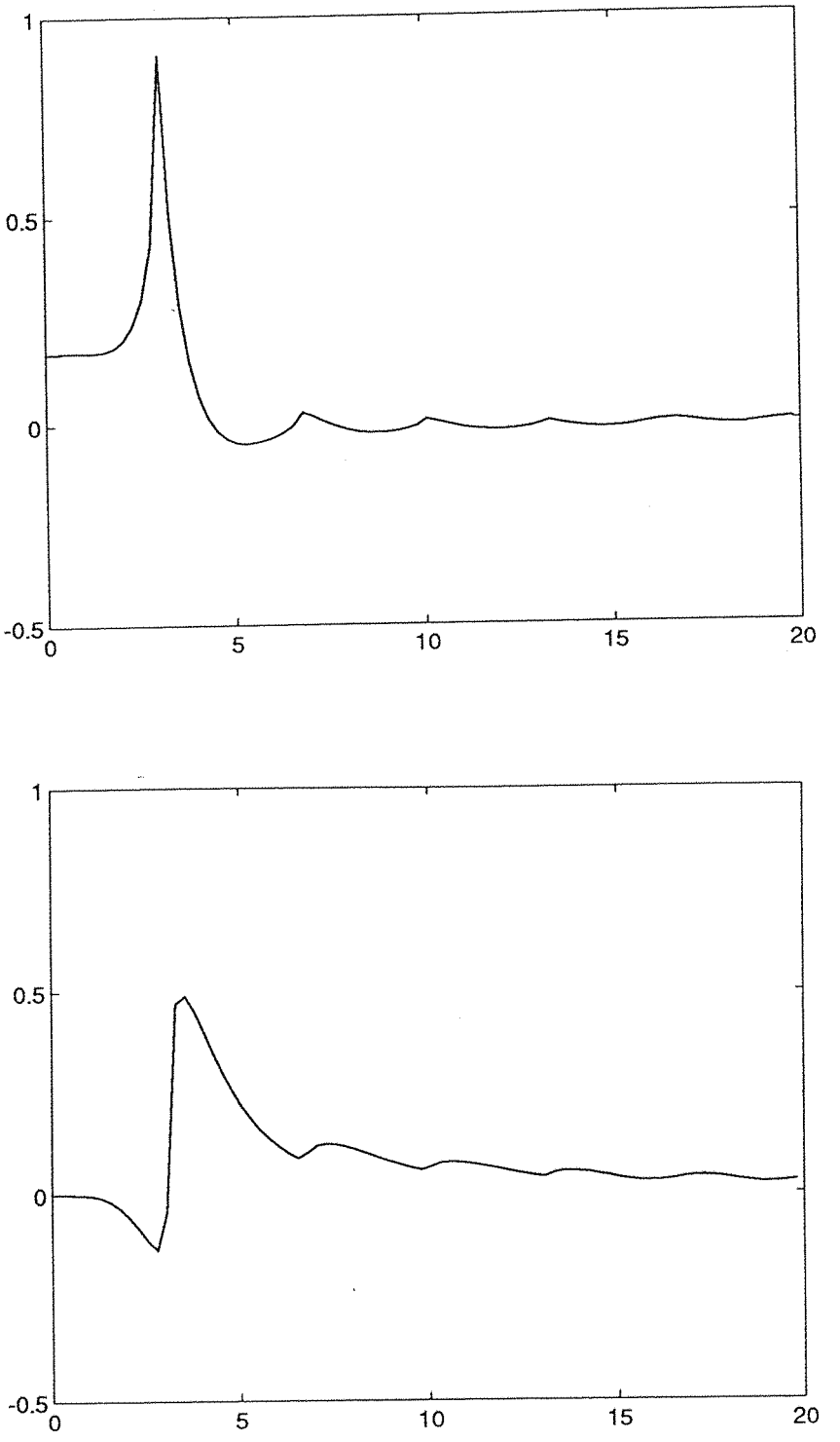

Figure 2.18 - The real and imaginary parts of the reflection coefficient for an incident $m = 2, n = 0$ mode and a reflected $m = 2, l = 0$ mode within a hard walled duct.

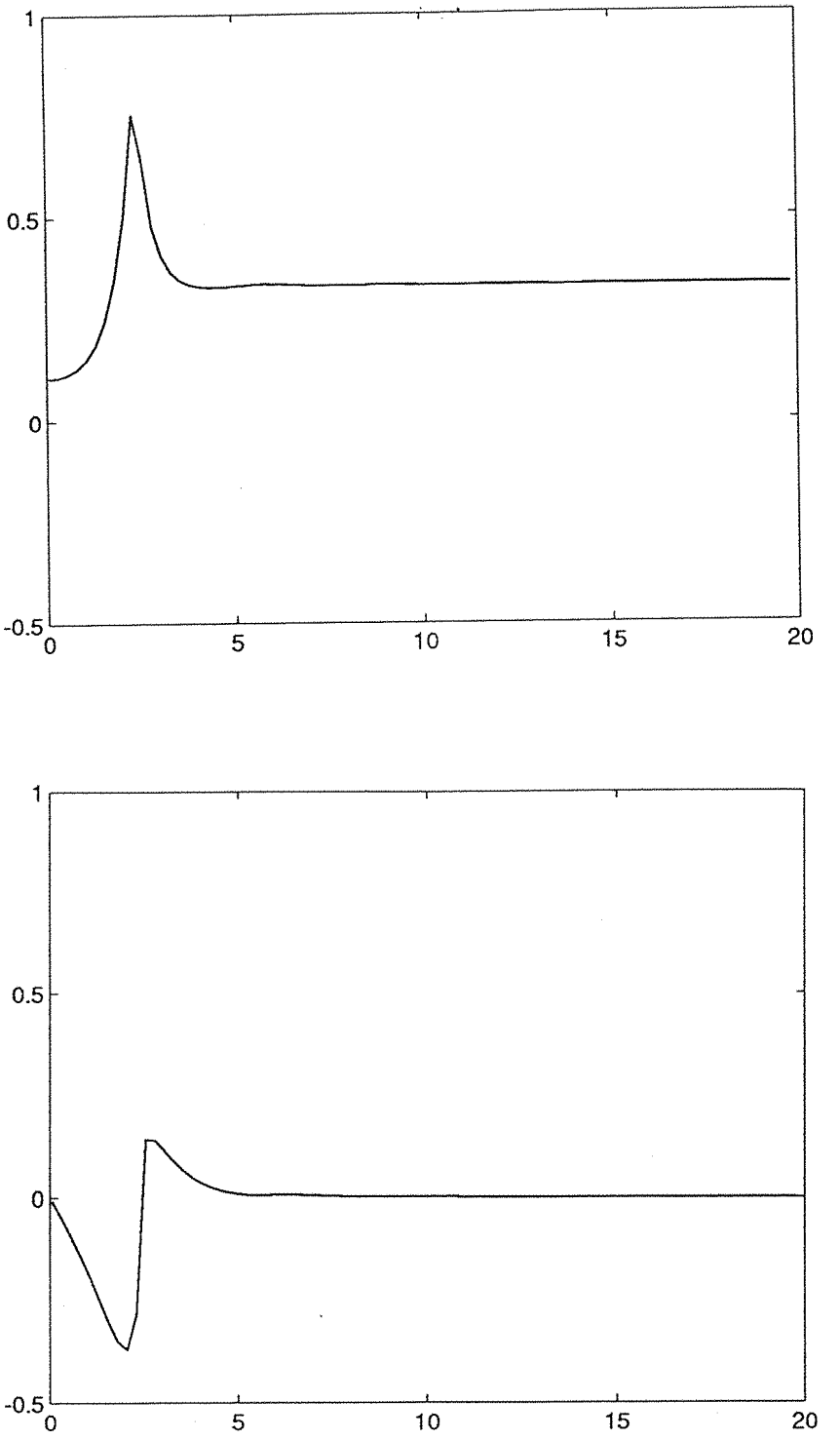

Figure 2.19 - The real and imaginary parts of the reflection coefficient for an incident $m = 0, n = 0$ mode and a reflected $m = 0, l = 0$ mode within a pressure release lined duct.

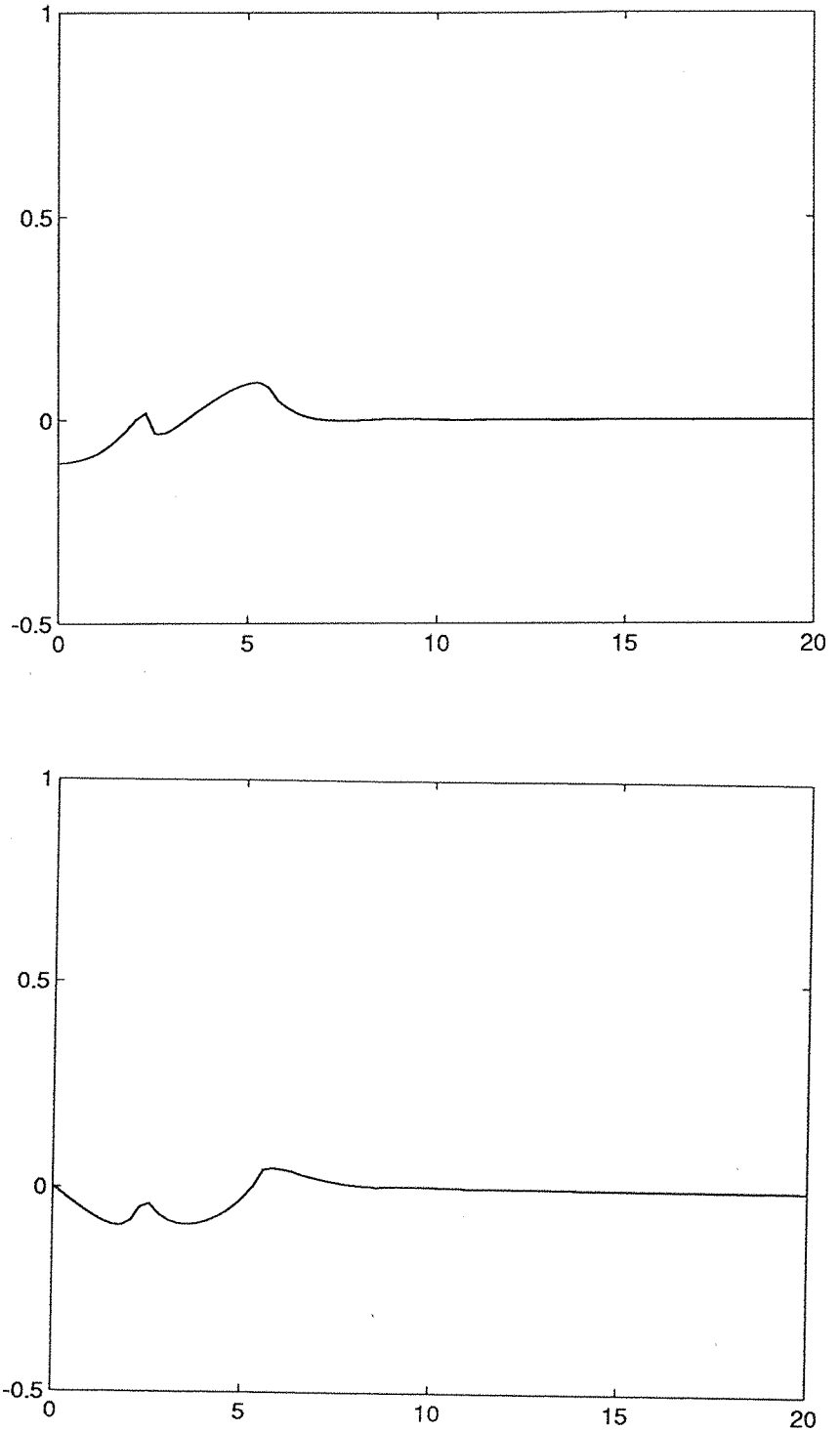

Figure 2.20 - The real and imaginary parts of the reflection coefficient for an incident $m = 0, n = 1$ mode and a reflected $m = 0, l = 0$ mode within a pressure release lined duct

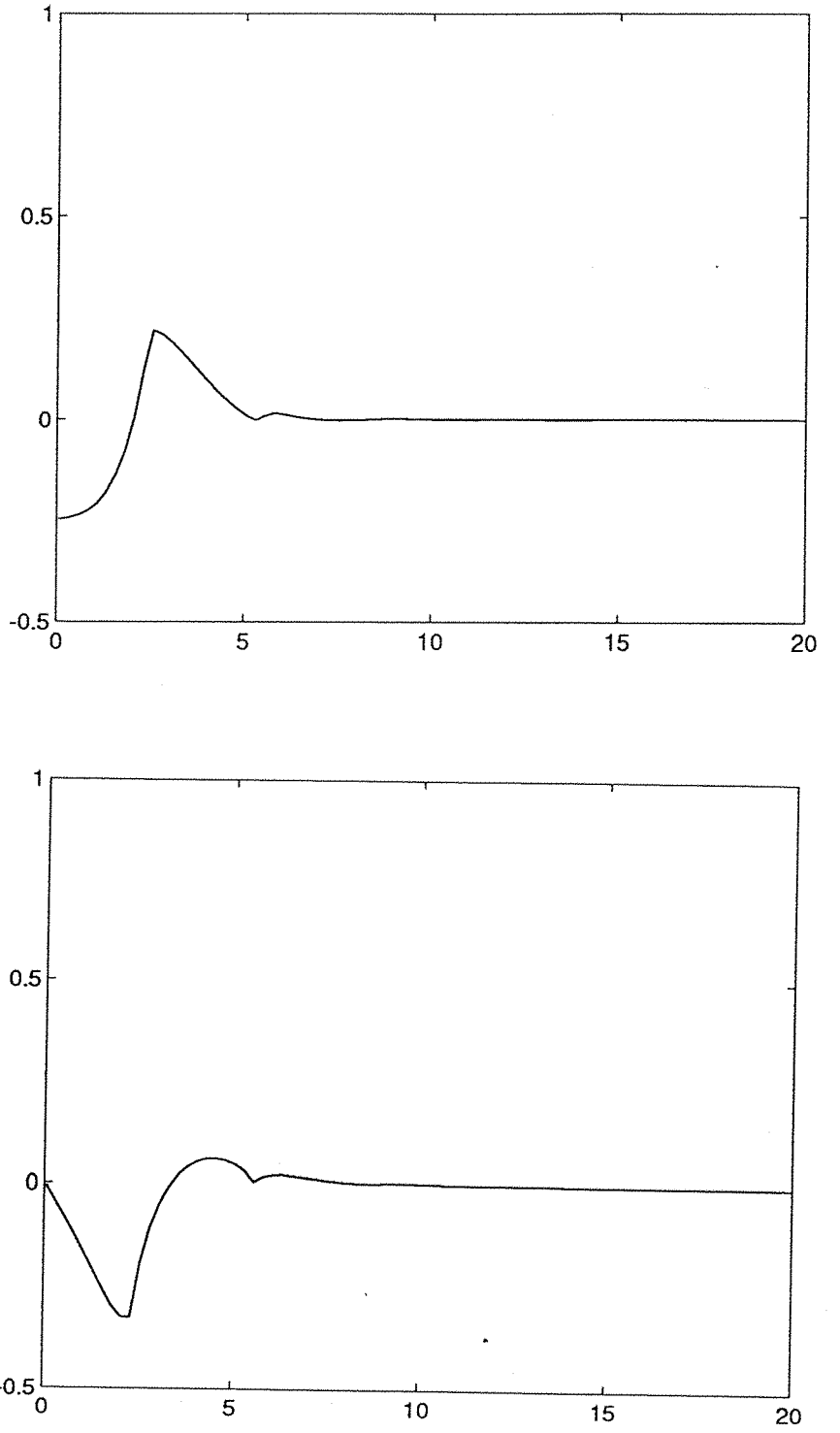

Figure 2.21 - The real and imaginary parts of the reflection coefficient for an incident $m = 0, n = 0$ mode and a reflected $m = 0, l = 1$ mode within a pressure release lined duct.

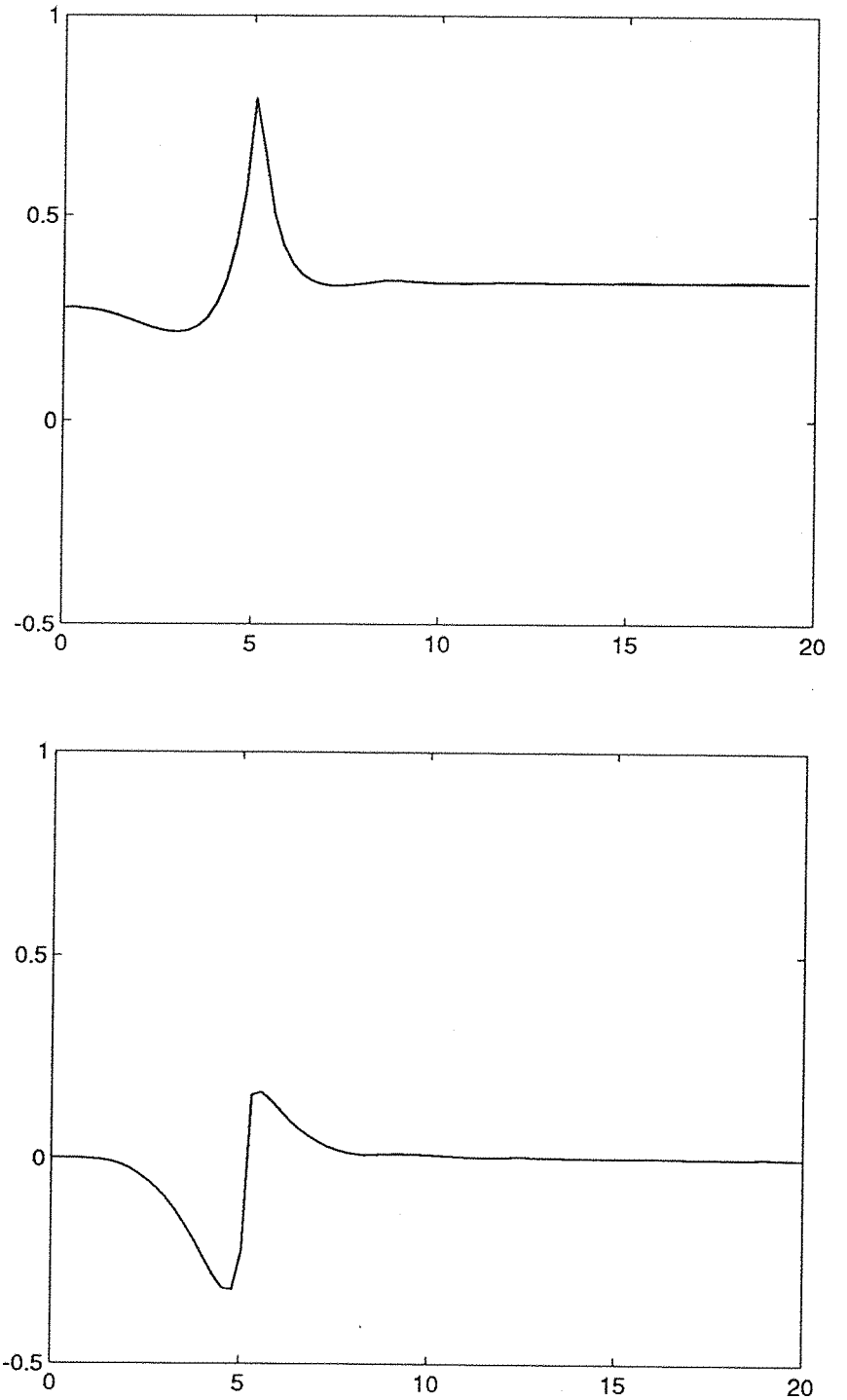

Figure 2.22 - The real and imaginary parts of the reflection coefficient for an incident $m = 2, n = 0$ mode and a reflected $m = 2, l = 0$ mode within a pressure release lined duct.

Chapter 3

Experimental Measurement of the Near-Field of a Circular Duct.

3.1 Introduction.

In the previous chapter an analytical model has been developed which enables the determination of the field radiated from a duct of finite length. In this chapter, the experimental measurement of the pressure radiated from a duct is presented. Results from these experiments are compared with theoretical predictions.

Originally, at the commencement of this project it was the intention to use measurements made near to the duct exit as a means of determining the far-field radiation. This technique relied upon the implementation of a 2 dimensional Fourier transform of the pressure field near to the end of the duct. Unfortunately, this method proved to be unsatisfactory, and the reasons for this are described in the next Chapter. However, the large volume of experimental data obtained by these experiments proved to be a useful means of comparison with the theoretical results obtained form the model developed in Chapter 2.

The measurement area consists of a square grid of equi-spaced points that are positioned close to the end of duct exit (see figure 3.1). To sample accurately the acoustic pressure at the end of the duct it is necessary to make measurements close to the duct exit. However, due to the discontinuity at the duct termination, high spatial wavenumbers are present close to the end of the duct. These high spatial wavenumbers take the form of evanescent wave components and consequently will decay with increasing distance from the duct. This decay is beneficial as it helps to reduce the contribution of these evanescent components to the measured data. A further beneficial factor is that the measurement hydrophone has a finite active area, and this behaves as a low pass spatial wavenumber filter. These two factors combined help to limit the measured amplitude of these very high spatial wavenumbers.

Even with the evanescent decay, and the filtering effect of the hydrophone, it is still possible that the field measured by the array will contain contributions from these high wavenumber components. However, without knowledge of the highest wavenumber component, it is impossible to prevent unwanted high wavenumber components from aliasing the sampled data if the sampling interval is not chosen correctly. The evaluation of the wavenumber spectrum of the acoustic field from an

analytical model is essential if the FFT propagation technique were to be used successfully. Put simply: aliased near-field data will result in aliased far-field data. Obviously this would result in incorrect predictions for the far-field.

In Chapter 2, an analytical model of the acoustic field within a finite length circular duct has been developed. This model allows the specification of the acoustic pressure and particle velocity over the end of the duct. The particle velocity will be used to calculate the radiation from the duct using the Rayleigh integral. In this chapter an experiment is described whose objective is the accurate measurement of the acoustic pressure near to the end of a circular duct immersed in water. Results from these measurements may then be used to compare with the analytical model derived in Chapter 2.

3.2 Experimental principle and description.

As stated above the objective of the experiment is to measure accurately the field radiated from the end of a duct. The simplest method of obtaining a large number of measurement points is to employ a single, scanning hydrophone that moves over an $x-y$ plane. As it is impractical and expensive to have a large number of pressure transducers to measure simultaneously the pressure in this plane, a single moving hydrophone receiver is substituted. This requires that the source signal is repeatable over time. In this way it is assumed that all the measurements were made simultaneously. The pressure field is sampled over a set of equi-spaced grid points giving the pressure as a function of x, y, and ω. By applying a Fourier transform to each of the pressure measurement time histories, it is possible to extract the ω dependence of the field, and to leave the pressure as function of two spatial co-ordinates at a single fixed frequency. Ideally, these pressure measurements must be both accurately located in the x-y plane, and be separated at such an interval as to avoid spatial aliasing of the field.

As there are many pressure measurements to be made, moving the hydrophone manually would be extremely time consuming. Therefore, it was decided to have the hydrophone incorporated in an automated $x-y$ traversing system, controlled by a computer. The computer can then control the positioning of the receiving hydrophone, the triggering of the source, and the capture and storage of the measured signal. A scaled diagram of the experimental design is given in figure 3.2.

There are practical considerations that need to be examined so that the measurements be made successfully. Ideally the measurements should be made in a free field using a continuous broadband source. In air, free field measurements may be simulated by conducting the measurements in an anechoic chamber. Unfortunately, anechoic materials offering good absorption over a large frequency range in water are prohibitively expensive. However it is possible to avoid reflections from the walls of a measurement tank by using a finite duration, impulse source signal. By adopting such an approach it is possible to capture totally the direct signal, and to finish measurement before the arrival of any reflected signals from the water surface, or sides of the tank. It should be noted that due the very high sound velocity in water, these reflections arrive very soon after the direct signal has been measured. Because of this the input signal must be of very short duration to avoid interference with the desired, direct signal from the duct.

Referring to the diagram shown as figure 3.2, the major components of the experimental rig are a fixed position source, an *x-y* traversing measurement hydrophone, a source generator, and an A-D capture system. The *x-y* traverse is controlled by computer as is the source generator. One of the requirements of the source is that it should have excellent repeatability. It is common to use a spark-source in underwater experiments, but it was found that this type of source does not possess the degree of repeatability required to be suitable in these circumstances. Specifically, the variation in the formation of the plasma spark, which is a random process, causes the time histories of the generated acoustic wave to be significantly different, not only in amplitude, but in the time duration of the impulse itself. Also the directivity characteristics of a spark source were also found to be a vary considerably. This results in differing spectra when compared in the frequency domain. It was therefore decided to use a hydrophone as a source, which offers much better repeatability.

The repeatability of the source when using a hydrophone can be seen from figure 3.3. The input signal to a Brüel and Kjær (B&K) type 8103 hydrophone used as the source, was a band-passed step function, filtered between 10 kHz and 70 kHz. The data was digitally converted using a Datalab DL2000 analogue to digital converter, which is programmable using an IEEE interface. It is clear from figure 3.3 that the repeatability of the source is extremely good. It also important that this repeatability may be sustainable over a long period. The source output was therefore measured 24 times, once every hour, for 24 hours. The results were found to be identical to those shown in figure 3.3. The source was generated using a Wavetek programmable signal generator, which is controlled by a computer through an IEEE 488 data bus. A

computer program was written which controls the generation of the source signal, and the triggering of that signal. Since the D-A converter is triggered by the start of the input signal, then this enables the phase of the radiated field to be established. To avoid reflections from the sides and water surface of the test tank, the source signal used was a band passed step function. This had a sufficiently short duration to avoid the reflections from the walls of the tank from interfering with the desired signal. From figure 3.3 it can be seen that the data length of the captured signal is 5.12×10^{-4} seconds. This was decided upon based upon the geometry and sampling requirements of the experiment. The highest frequency of the source was set as 75kHz, which set a lower limit upon the sample frequency of 150kHz. However, at this sampling frequency reflections from the sides of the tank were present at the end of the captured data. These were eventually removed by increasing the sample rate, with a fixed number of samples, so reducing the time 'window' of the captured signal.

As stated earlier, the motion and location of the receiving hydrophone are also controlled by the computer. Software was written to communicate with a CIL analogue to digital, digital to analogue converter that was used to measure the output from the positioning potentiometers responsible for the x and y directions.. A reference voltage of 9V is also available from the CIL, and this was used as the input to the potentiometers. As the receiving hydrophone is moved, the voltage output from each potentiometer will change linearly with distance moved. By measuring the voltage change over a fixed reference distance, (in this case 500mm), it is possible to calibrate the x-y traversing rig to obtain the voltage change per mm of motion. This was performed separately for both the x and y co-ordinates. Hence by calculating the voltage change per unit of motion, it also possible to obtain the required voltage that would be output from the potentiometers at a desired location in the x-y plane. A simple direct feedback loop is employed to move the receiving hydrophone to the desired location. First the computer calculates the voltages that would be output from the potentiometers at the desired location. The actual voltage is read by the CIL, and sent to the computer through an IEEE data link. The difference between the actual and desired voltages is considered to be an error voltage. This is multiplied by a constant, and is used as the D-A output from the CIL into a power amplifier and on to the motors that control the x-y motion. Whilst this approach is simple in theory, there were considerable practical problems in achieving a steady motion from one position to another due to friction, and bending of the supporting rods that form the core of x-y traverse. For this reason it was necessary to step incrementally from one position to another, instead of relying on the steady motion of the hydrophone alone. This combined with extra gain applied to error voltage at the extremities of the

measurement array overcame nearly all problems, apart from the odd freezing of the rig caused by insurmountable friction.

The sequence of events for the capture of data a desired location in the x-y plane is as follows:

(i) The computer calculates the voltage output from each position potentiometer at the desired location, based upon the traverse calibration.

(ii) These voltages are compared with the actual readings made using the CIL A-D converter.

(iii) The resulting difference, or error voltage, is used as a feedback to drive the motors that move the receiving hydrophone.

(iv) Once the voltage error has been reduced such that the position error is calculated to be less than ±0.25mm.

(v) When the receiving hydrophone is at the desired location the motors are stopped, another check is performed to verify the position, and then the source is triggered by the computer. The computer also triggers the Datalab A-D converter that is used to capture the signal from the source. The data is sent to the computer through the IEEE interface, and converted into a MATLAB binary file format, and then saved to disk. Each time history has a unique filename for easy identification, which includes the position in the array from which it was taken.

The process repeats for every position over the array. In practice, the array is divided into 64 columns containing 64 positions in each column. Each column of positions is measured sequentially, so that once the x co-ordinate position has been set, then the hydrophone is moved only in the vertical or y co-ordinate direction. A check of both the x and y positions is made before capture. This reduces the time required to scan the whole 64×64 points, which cover an area of 630×630 mm. Because the required accuracy, and the number of sample points in the array, the time taken to perform a complete capture of all 4096 points was approximately 40 hours.

3.3 Preliminary investigation using a point monopole source without a duct.

To ensure that the *x-y* traversing system was working correctly, it was necessary to begin measurements with a known source that could be compared easily with a well-known theoretical result. For this reason some preliminary measurements were made using a point monopole source generated from a B&K 8103 hydrophone driven as a source. If the traversing system was working correctly, these measurements would also act as a means of examining the accuracy of the hydrophone as an approximate point monopole source. It is intended to compare measured results obtained by placing a point monopole inside the duct, with predicted theoretical results, and for this reason is it very helpful if the hydrophone can be assumed to act as a point source.

The output from a monopole source is also useful in determining the size of required receiving array. Ideally, the array should be large enough so that the pressure at the extremes is negligible. However, there will be a finite limit on the size, dictated primarily by the size of the tank used to conduct the experiments. The nearer to the sides that the extreme measurement points are, the earlier the reflections will return from either the side walls, bottom of the tank, or from the free water surface at the top. A large enough distance is therefore required all around the array, so that these reflections may be easily gated out in the time domain. Another consideration, given that the data from the experiment was originally to be used to forward propagate the field from a source using a 2D Fourier transform, is that it would be beneficial to have the array constructed from a number of points corresponding to an integer power of two number of points, such as 32×32 or 64×64. If the number of data points in the array along either co-ordinate is not a power of two, then there are errors introduced by the 2D FFT routines. Given the above considerations, it was decided to arrange for the array to have 64×64 points, with a spacing of 10mm between data points. This would allow for the highest wavenumber component to be 75kHz (20mm wavelength) without aliasing in the spatial wavenumber domain. This gives the total number of points on the array as 4096, and a size of 640×640 mm. The number of data points captured at each location was fixed at 256, at a sample rate of 500kHz.

Figure 3.4 shows the pressure variation in the x-y plane for a monopole source produced using a hydrophone. The frequency is 46875Hz. The horizontal axes are the x and y array points (64×64), and the vertical axis is absolute pressure is measured in dB re. 1×10^{-6} Pa. What is most striking about this two dimensional plot is that it is clearly not what is to be expected from a point monopole source, since it contains obvious ripples on the right hand side corresponding to the maximum depth

measurement positions within the tank. At first these ripples were thought to be caused by early reflections from the bottom of the tank interfering with the direct signal. However, an analysis of a typical time history showed that the there were no signs of the expected early reflections. What was noticeable though, was that as the measurement hydrophone was lowered in to the tank to measure the data points near to the bottom of the tank, there was a noticeable change at the start of the captured data, and not at the end, which one would expect from a reflection. Since the monopole source was placed in the centre of the array, it is expected that the measured field would be circularly symmetric about this centre point. Consequently the time histories captured along the centre line of the array should be symmetrical about the mid point. However, it became clear that this was not the case, and there was some small signal arriving *before* the main direct signal when the data points are near to the bottom of the tank.

It is possible to understand the reason for this by referring to the components of the experimental rig. Referring specifically to the *x-y* traverse, the receiving hydrophone is supported by a brass rod, which is progressively lowered into the water to obtain measurements in the vertical direction. The brass rod, introduced a good structural path for the acoustic energy to be transmitted to the hydrophone; i.e. through wave transmission down the brass rod. This effect would obviously become more significant as the rod was lowered, and explained the ripples in figure 3.4 which occur at points of large depths of the receiving hydrophone. The reason for these being difficult to detect from a simple examination of the time histories, is that the speed of sound in brass is approximately 5200 m/s, and the geometry of the experimental rig conspired to result in the arrival of the energy from structural pathway to coincide with the direct acoustic signal through the water. Hence these interfered, and resulted in the ripples that are present in figure 3.4.

The above problems with the brass rod illustrate an important strength in analysing acoustic data in this way. If the output from the monopole were taken over a few points in a radius out from the source then the effect of the brass rod could have gone undetected. By separating the frequency components and examining them as a function on an *x-y* plane, it is possible to yield more information about the source and the measuring system itself, than would otherwise be available.

To overcome the influence of the brass rod, the receiving hydrophone was supported using a perspex rod that has an impedance very close to that of water. Further tests were undertaken using a monopole source. A typical result, again at 46875Hz is

shown in figure 3.5. It can be seen that the ripples in the pressure surface have now been removed. As a further safeguard, the supporting rod for the fixed hydrophone source was also replaced by one of perspex.

Figure 3.6 shows predicted pressure from a point monopole source using the same frequency and geometry as in figure 3.5 above. By comparison, figure 3.7 shows the error involved in the measured monopole field, as a difference compared to theoretical monopole using the same geometry. Clearly this error is very small. Possible explanations for the observed error between the measured and analytically derived monopole fields are mis-positioning of the array points in the x-y plane, and the directivity of the hydrophone as source.

3.4 The field from a hard walled, baffled duct containing a monopole source - a comparison between measured and theoretically derived results.

Having established that the hydrophone may be assumed to behave as a point source for the range of frequency considered in this project, it is now intended to use this as a means of comparing the pressure field measured near to the duct with results obtained from the mathematical model described in Chapter 2. To achieve this objective it is necessary to know the complex source strength of the hydrophone when used as a source, since this is one of the important input parameters to the mathematical model. The source strength was evaluated by measuring the complex pressure at known distances from the source at a given frequency. If this pressure field was produced by an ideal monopole, then the source strength can be calculated from the usual free field expression

$$p(r) = \frac{j\omega\rho q}{4\pi r} e^{-jkr}, \tag{3.4.1}$$

where $p(r)$ is the pressure at a radial distance r from the source, ω is the frequency, and q is the complex source strength.

The following experiments were conducted using a baffled duct, which unfortunately does not represent accurately a real ducted propeller system. If the duct is unbaffled it is not possible to use the Rayleigh integral as a means of calculation of the far-field. Lansing (1969) and Homicz and Lordi (1975) have observed that as ka increases beyond a value of 10 for an unbaffled duct, the acoustic radiation at angles greater than 90° to the duct axis, reduces dramatically. Expressions for the radiation from an unbaffled duct are available, (e.g. Lordi 1973 and 1974), but these are only valid when

the observer is in the far-field. Since it is desired to look at the radiation near to duct exit, then expressions for the pressure from an unbaffled duct are not applicable.

As mentioned earlier, acoustically rigid structures are very difficult to realise in water due to the very large density of the medium. Therefore to produce an ideal hard walled duct does present practical difficulties in water, unlike in air. Therefore, in an attempt to reduce the acoustic excitation of the duct wall by the source, the duct used for all the experiments is constructed from mild steel, and has dimensions of 135mm long and outer and inner diameters of 200mm and 100mm respectively. This gives a wall thickness of 50mm.

The geometry for the experiments using a duct is shown as figure 3.1. The grid size and spacing of points is kept constant for all the duct experiments and is the same as those for the monopole experiments discussed above. Figure 3.8, shows the absolute pressure at 31250Hz measured over the array. The source is a monopole placed initially along the duct axis, and at the mid-point along the duct length. The measurement location is 0.125m from the end of the duct. Due to the radial symmetry of the source within the duct, it is possible to consider only a 1 dimensional pressure field that is essentially a slice along the centre-line of the 2 dimensional pressure field as measured using the array. This saves considerable time when computing the radiated field using the Rayleigh integral. Figure 3.9 shows the theoretically predicted pressure for the same geometry and frequency. It can be seen that the agreement is very good between the experimental results and those derived analytically.

Figure 3.10 shows the radiation from the hard walled duct at 15625 Hz for the same geometry as above. Here ka has a value of 3.3. As expected, by reducing the value of ka, the acoustic energy is less focused toward the axis of the duct. Clearly the field is axisymmetric. This is to be expected, given the radial symmetry of the source within the duct. Figure 3.11 shows the pressure calculated from the mathematical model at this frequency. General agreement is found in figures 3.12 and 3.13, which show the measured and predicted pressure at 46875Hz.

The comparison between the experimental and theoretical results for the frequencies mentioned above illustrate that the analytical model has reasonable agreement with experimental measurement for the hard wall duct. However, whilst the general structure of the sound field is predicted, the level difference in some of the figures is often large. Given that the predictions for the pressure release lined duct discussed in the next section are much better, this would mitigate against there being a

fundamental problem with the theory or with the prediction software. It is believed that other sources of error based upon the physical nature of the problem would be a more realistic source of the observed discrepancies, these are:

- The error in the predictions Amy be due to the difficulty of reproducing a true hard wall in water for experimental purposes. The impedance mis-match between the water and the duct wall is such that excitation of the duct may be responsible for this error. Since the analytical model assumes that the normal particle velocity is zero at the duct wall, and this boundary condition is a fundamental assumption in the analysis, then if this is not the case in practice then there will be a error in the computed field. The same argument may be is true for the rigid baffle used for the experiments.

- The ideal point monpole source used in the analytical model is unrealisable in practice. Directionality of the source will change the way it drives the internal field within the duct relative to a true omni-directional monopole. This argument would also be true for the pressure release lined duct, but since the internal field is completely different (i.e. different boundary condition at the duct wall, different modal cut-on frequencies etc.), then it is impossible to rule out this being more significant in one duct from the other, without computing the field knowing the directivity characteristics of the source.

Having established this it is now possible to use the mathematical model to examine the influence upon the radiated pressure of introducing a pressure release lining at the duct wall. This can then be compared with the results when the same source is radiating within a hard wall duct. Using the mathematical model enables a wider range of variation in the location of the source to be obtained with greater ease than those obtained experimentally. Also it is much quicker to obtain theoretically produced results than to measure the field, as a typical measurement takes 40 hours, whereas a theoretical simulation takes a small fraction of this time. Another disadvantage of the experiment is that it is impossible to position the hydrophone source very close to the duct wall, due to the large rubber sheath covering the active element within the hydrophone. This rubber covering prevents the hydrophone active area from getting any closer than 2mm from the duct wall. This important limitation does not exist when considering results from the analytical model, as the source may be placed anywhere within the duct. Given the very good agreement between the experimental and theoretical results presented above, it is justifiable to examine the radiation from the hard and pressure release lined ducts using this model alone.

During the course of this project many experiments were conducted using different source and receiver locations, and using either a hard walled or a pressure release lined duct. The experimental data presented in this chapter is only a small selection of the total available. Space does not permit a presentation of all of the results. However, table 3.1 lists all of the experimental data which is available, and indicates the relevant parameters in the table. All experiments were conducted using a monopole source.

3.5 The field from a pressure release lined, baffled duct containing a monopole source - a comparison with experiment and the hard walled duct.

One of the primary reasons for this work is to explore the effect of applying a pressure release lining at the duct wall. There is a good reason to expect low radiation from a monopole source positioned near to the wall of a pressure released lined duct. This is related to the way in which the source drives the field within the duct. Not forgetting that the externally radiated pressure is a function of the axial particle velocity over the end of the duct, then an overall reduction in the amplitude of the modes within the duct will lead to reduction in the radiated energy. The amplitude coefficients for each mode are determined from the product of the source strength with the value of the mode shape function at the location of the source. To illustrate this, consider a monopole source located within an infinite length duct at a position given by r_s, θ_s. For this simple case, the modal amplitude coefficients are given by[1]

$$A_{mn} = \frac{Qk\rho c}{4\pi k_z^{mn}} \psi(r_s, \theta_s), \tag{3.5.1}$$

where A_{mn} is the modal amplitude coefficient, Q is the monopole source strength, and k_z^{mn} is the axial wavenumber. The final term $\psi(r_s, \theta_s)$, is the mode shape function evaluated at the position of the source. This function may be expanded into two separate functions of r and θ. Equation (3.5.1) then becomes

$$A_{mn} = \frac{Qk\rho c}{4\pi k_z^{mn}} \frac{J_m(k_r^{mn} r_s)}{N_{mn}} e^{jm\theta_s}, \tag{3.5.2}$$

where $J_m(k_r^{mn} r)$ is a Bessel function of the first kind and the normalising coefficient, N_{mn} is given by

---

[1] see Appendix A

$$N_{mn} = \frac{a}{\sqrt{2}} \left\{ \left(1 - \frac{m^2}{k_r^{mn2} a^2} \right) J_m{}^2 \left(k_r^{mn} a \right) + J'^2_m \left(k_r^{mn} a \right) \right\}^{\frac{1}{2}}. \tag{3.5.4}$$

For a pressure release lined duct, then equation (3.5.3) reduces to

$$N_{mn} = \frac{a}{\sqrt{2}} J'_m \left(k_r^{mn} a \right). \tag{3.5.5}$$

For the pressure release lined duct, the boundary condition requires that there be zero pressure at the duct wall. This means that the value of the radial part of mode shape function $\psi(r_s)$,will be zero at the duct wall. If the source is placed near to the duct wall then the value of $\psi(r_s)$ will be small. This function will become progressively smaller as the position of the source is moved nearer to the wall. From equation (3.5.1) above, this will give smaller values for the modal amplitude coefficients. Hence the source will not drive the field within the duct very effectively when the source is close to the wall for a pressure release boundary condition.

To achieve any practical radiation reduction, it is essential that a pressure release boundary condition can be achieved at the duct wall. Experiments conducted at the commencement of this project indicated that an extremely good pressure release boundary condition can be realised using closed cell, neoprene foam of 4 mm thickness, if backed by a rigid metal plate (Hewlett, 1989). In these experiments, one hydrophone was used as an acoustic source, and another was used as a receiver. A short pulse was used as the excitation from the source hydrophone. This was measured by the receiving hydrophone, which was placed between the source and a pressure release coated square steel plate measuring 1.2m by 1.2m, and having a thickness of 40mm. In this way both the incident and reflected waves were measured at the receiving hydrophone. Figure, 3.14 shows the time history measured at the receiving hydrophone. It can clearly seen from this figure that the incident and reflected pulses are separated in time. Also the reflected pulse is very close to a perfect inversion of the incident pulse. This indicates that the neoprene coating has reflected properties very similar to an ideal pressure release boundary condition. Figures 3.15 and 3.16, show the spectrum of the incident and reflected pulses. These were obtained by extracting the reflected and incident time histories shown in figure 3.14, and the applying a Fourier transform to each separately. It can be seen that the spectrum of the incident and reflected pulse is very similar, showing very little absorption or scattering from the coated plate.

A similar investigation by Caille (1988), found that for a closed cell neoprene foam to act as a good pressure release coating on the outside of a circular cylinder, then it was necessary to decouple the vibration of the coating from that of the cylinder. For a thin walled cylinder, it was found that vibrational wave motion in the cylinder wall reduced the effectiveness of the coating as pressure release surface. By carefully applying the coating to a thick walled metal cylinder, it was found that the neoprene material was a very good pressure release surface.

Calculated radiated pressures from a hard wall and pressure release lined duct were obtained from the theoretical model for various geometries. For ease of description in the figures that follow, the position of the source will be fixed and is always located mid-way along the z-axis, whereas the source will be varied over several radial locations. The radial distance from the centre of the duct will be denoted by r_s where the suffix s indicates the source. As the source is a monopole and is placed mid-way along the duct axis, the pressure radiated from either end will be identical. Therefore only the radiation from one end will be discussed. The distance at which the radiated field is calculated is denoted by z. This is measure of the distance from the centre point on the duct exit to the centre point on a square plane outside of the duct.

A comparison between prediction from the theoretical model and experimental measurements for a pressure release lined duct are shown as figures 3.17a to 3.17d. The four figures are for values of ka=3.3, 6.5, 9.8 and 13.1. It can be seen that the agreement between the theoretical results (the dashed line) and the experimental results (solid line) is very good. The structure of the sound field is predicted well, and the overall level difference is typically within 5dB. It is interesting to note that these results are even better than those obtained from the hard walled duct, and one possibility for this may be due to the boundary condition at the duct wall in the experiments being closer to the true pressure release liner used for the analytical predictions.

Figures 3.17e to 3.17h show the pressure predicted over a plane at a distance of z=0.125m from the open exit of a hard walled duct and a pressure release lined duct. The source in the centre of the duct (i.e. r_s=0), for four different frequencies. Note here that the pressure release duct pressure is dashed, whereas the solid line represents the hard walled duct. It can be seen that as the frequency is increased, the pressure release data becomes increasingly less than the corresponding pressure radiated from the hard walled duct.

The opposite extreme to the above is to place the source very close to the duct wall, and the to compute the radiated pressure. Figures 3.18 to 3.21 show the pressure from a hard walled duct with r_s=49mm, which represents the source being 1mm from the duct wall. As the source is no longer symmetric about the radial co-ordinate, these series of figures are shown as 2D pressure surfaces. The equivalent radiated fields for a pressure release lined duct are shown as figures 3.22 to 3.25. What is most noticeable is that even at the lowest frequency of 15625Hz (ka=3.272), that there is a large difference in the nature of the radiated field. However, despite the complexity of the plots, there does seem to be a reduction in the overall level with the pressure release lined duct. The pressures presented in these figures were calculated at a distance of 0.125m from the open end of the duct. This represents a distance of 2.5 duct radii. The onset of the geometric far field is normally defined by (Morfey, 1982)

$$R \geq \frac{L^2}{\lambda}, \tag{3.5.6}$$

where R is the distance from the source and L is the largest dimension of the source region. In this case, with L set to the duct diameter of 100mm, at 15625Hz R is equal to 0.1042m, and at 62500Hz R is equal to 0.4167m. Thus only the radiated pressure at 15625Hz is in the far-field.

3.6 The radiated sound power - a comparison between a pressure release and hard walled ducts

Using the analytical model it not only possible to obtain the radiated field but also the acoustic pressure and particle velocity over the end of the duct. This is very useful as the total power radiated from the duct may be calculated from these two parameters using the relationship

$$W = \tfrac{1}{2}\int_S \mathrm{Re}(p\,u^*)\,dS \tag{3.6.1}$$

where W is the sound power, Re denotes the real part, p is the pressure, and u^* is the complex conjugate of the particle velocity. This does of course ignore the directivity of the radiated energy, but is nevertheless extremely important in investigating the differences between the two types of duct.

Using the above equation, and having a knowledge of the pressure and particle velocity for different source locations enables the power reduction when using a pressure lining to be shown as a function of source location within the duct. Figures 3.26 to 3.29 show in dB this difference in sound power at four different frequencies of 15625, 31250, 46875 and 62500Hz (which represent values of *ka* of 3.27, 6.55, 9.81, and 13.09 respectively). At all frequencies the sound power reduction is substantial. Only at 15625Hz, and with the source in the centre of the duct is the radiated power greater than that for the hard walled duct. This may be partly explained by the different modal cut-on frequencies for the two ducts. At this relatively low value of *ka* at this frequency of 3.72, there are very few modes cut-on for either duct, and therefore comparisons between the radiated power may be influenced by the proximity of a modal cut-on frequency near to the frequency of the source. However, in all other respects the sound power reduction is very large at all positions of the source. As one would expect the sound power reduction increases as the source is moved towards the duct wall.

3.7 Conclusions

In this chapter an experiment to measure the pressure field close to the end of the duct has been described. This has been used to measure the field radiated from a hard walled duct. It has also been shown that the experimental results are in reasonable agreement with those obtained from the analytical model derived in Chapter 2. Where differences in the levels between the two different approaches, experimental and theoretical, are observed, these are most likely to be due to experimental error. As explained within this chapter, it is very difficult for example to generate an ideal hard wall boundary condition in water, and this alone may be responsible for the differences observed in the hard wall duct data. Also the source used is not omni-directional and therefore is not an ideal point monpole as used in the theoretical predictions.

Furthermore, it has been shown that the introduction of a pressure release lining at the duct wall has a significant effect upon the radiated sound power compared to a hard walled duct. Measurements of the sound pressure radiated from the duct have been compared with analytically derived data, and shown to be in good agreement. This has shown that the analytical model is accurate for this type of problem. Furthermore, it has been possible using this model to calculate the radiated field for various source locations within the duct.

Duct wall condition	z **(mm)**	r_s **(mm)**	**Data points**	r_s **(mm)**
hard	125	0	64×64	0
hard	125	10	64×64	10
hard	125	25	64×64	25
hard	125	45	64×64	45
hard	125	49	64×64	49
pressure release	125	0	64×64	0
pressure release	125	10	64×64	10
pressure release	125	25	64×64	25
pressure release	125	45	64×64	45
pressure release	125	49	64×64	49
hard	125	0	64×64	0
hard	125	10	64×64	10
hard	125	25	64×64	25
hard	125	45	64×64	45
hard	125	49	64×64	49
hard	50	0	64×64	0
hard	50	10	64×64	10
hard	50	25	64×64	25
hard	50	45	64×64	45
hard	50	49	64×64	49
pressure release	50	0	64×64	0
pressure release	50	10	64×64	10
pressure release	50	25	64×64	25
pressure release	50	45	64×64	45
pressure release	50	49	64×64	49
hard	50	0	64×64	0
hard	50	10	64×64	10
hard	50	25	64×64	25
hard	50	45	64×64	45
hard	50	49	64×64	49

Table 3.1 - A complete list of experimental data

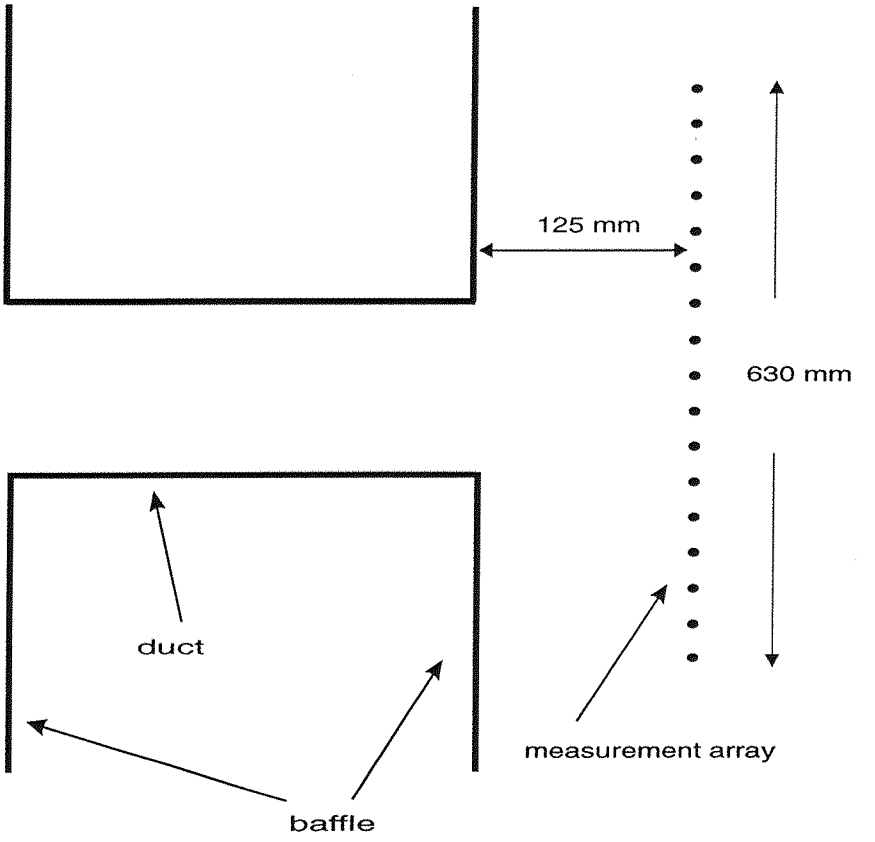

Figure 3.1 - A diagram of the measurement array and duct for the experiments.

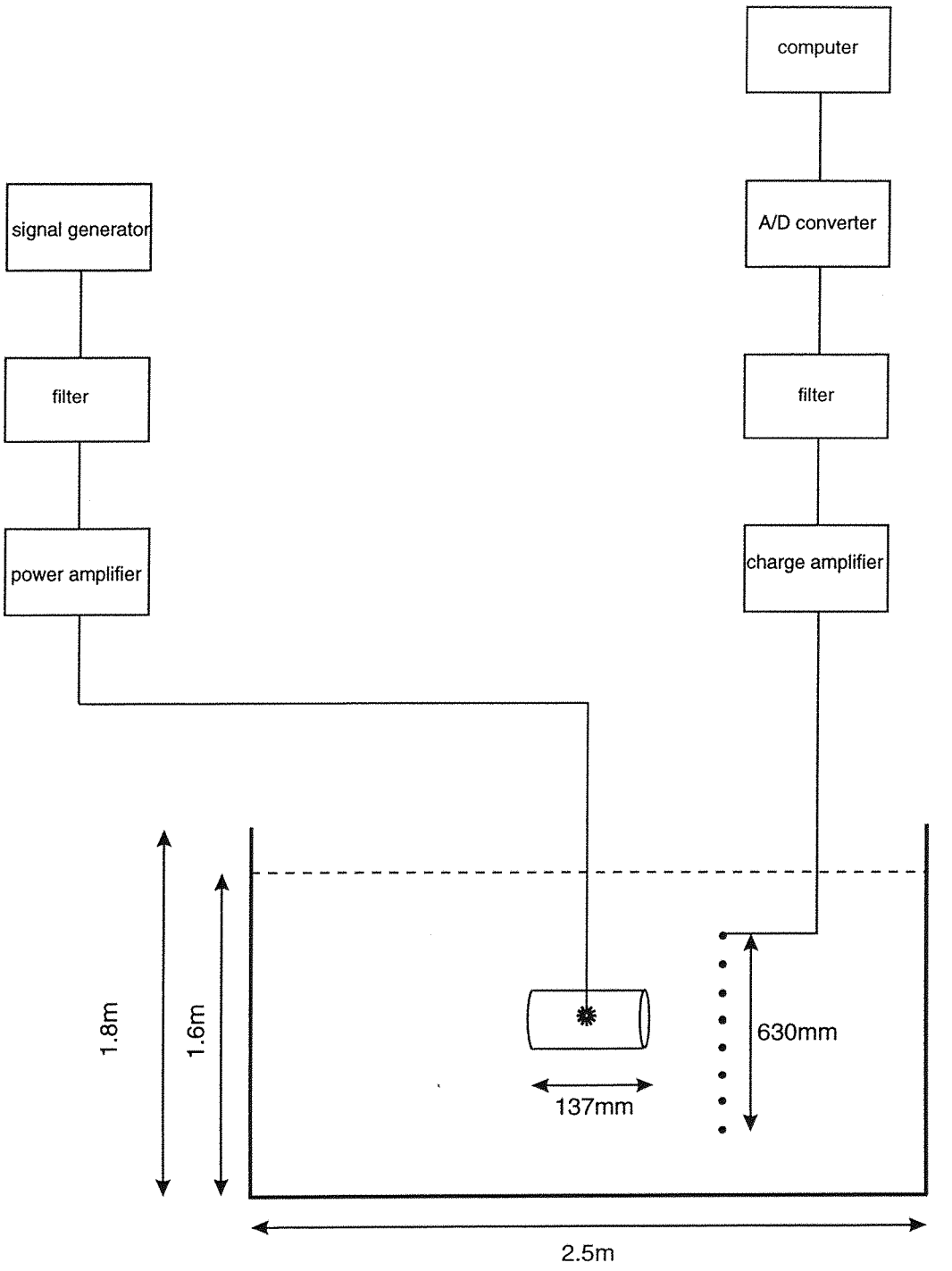

Figure 3.2 - A scaled diagram of the experiment rig, showing the location of the duct and array within the measurement tank.

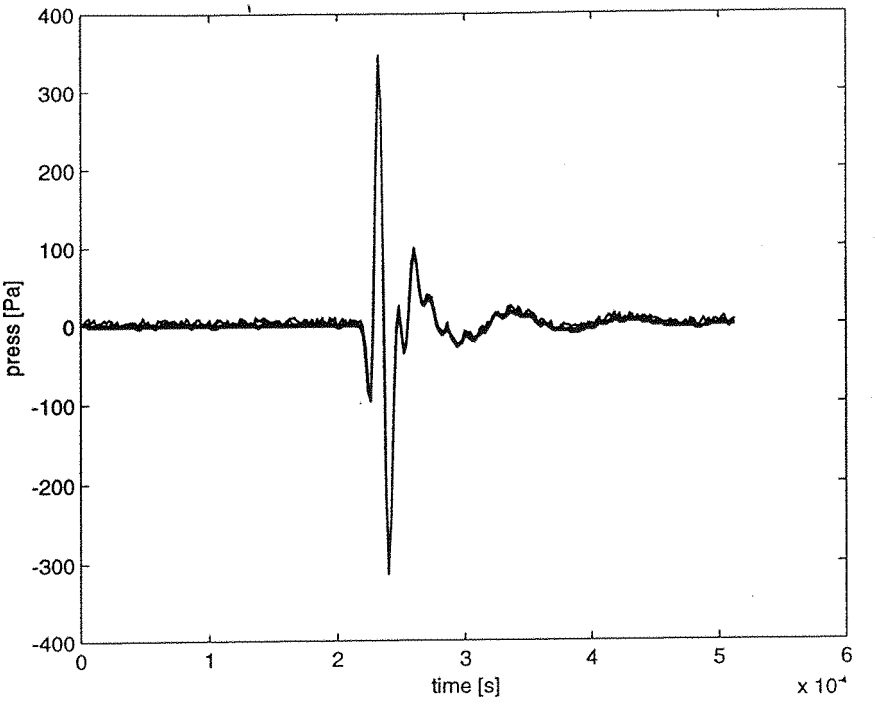

Figure 3.3 - A total of 24 time histories recorded over a 24 hour period, indicating the good repeatability of the source.

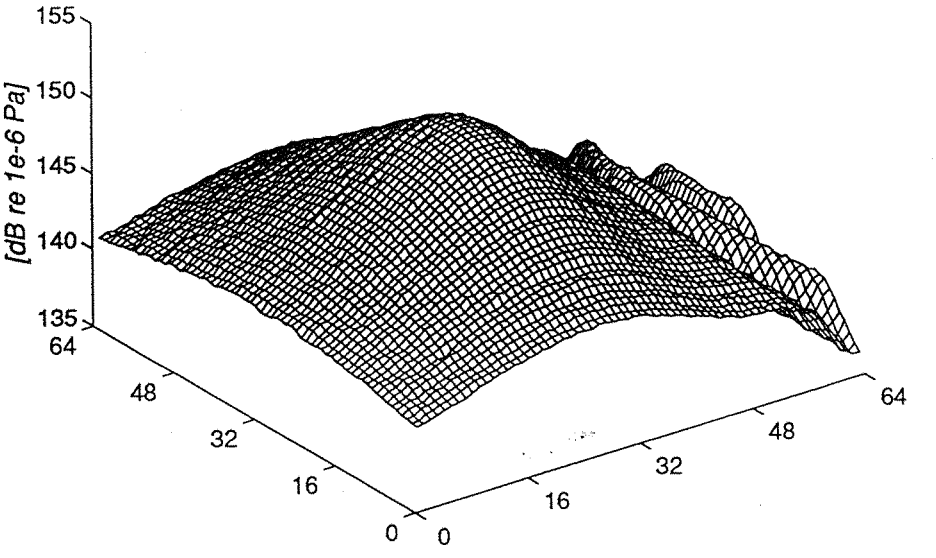

Figure 3.4 - The magnitude of the pressure in dB re. 1×10^{-6} Pa at 46875Hz from a point monopole source measured using a brass supporting rod for the receiving hydrophone.

Note the interference from the early arrival of the structural waves through the brass rod.

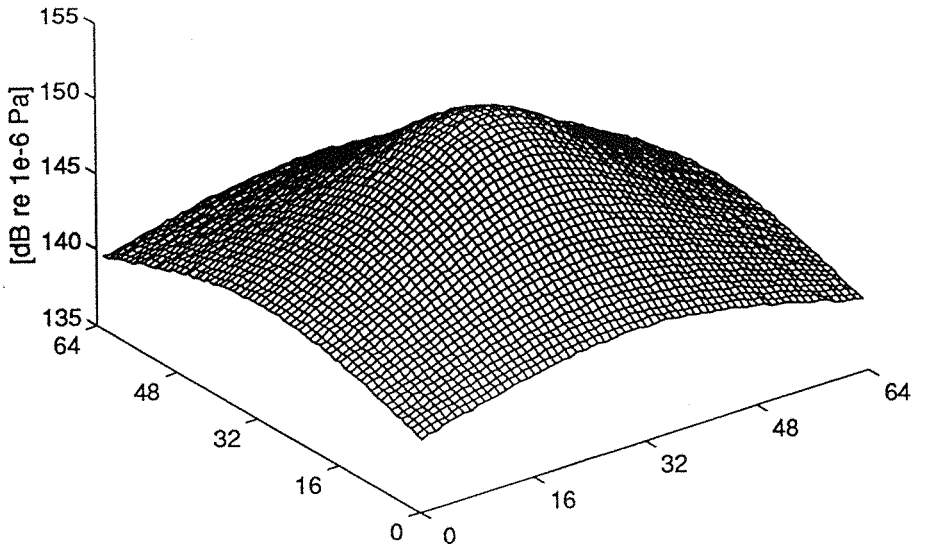

Figure 3.5 - The magnitude of the pressure in dB re.1×10^{-6} Pa at 46875Hz from a point monopole source measured using a perspex supporting rod for the receiving hydrophone.

Note the interference from the early arrival of the structural waves is now absent.

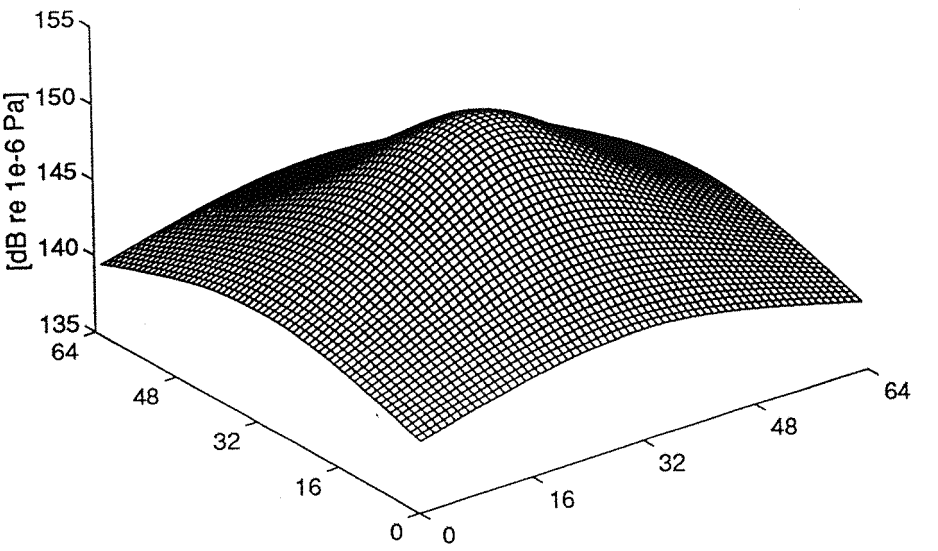

Figure 3.6 - The magnitude of the pressure in dB re.1×10^{-6} Pa at 46875Hz from a theoretically generated point monopole source.

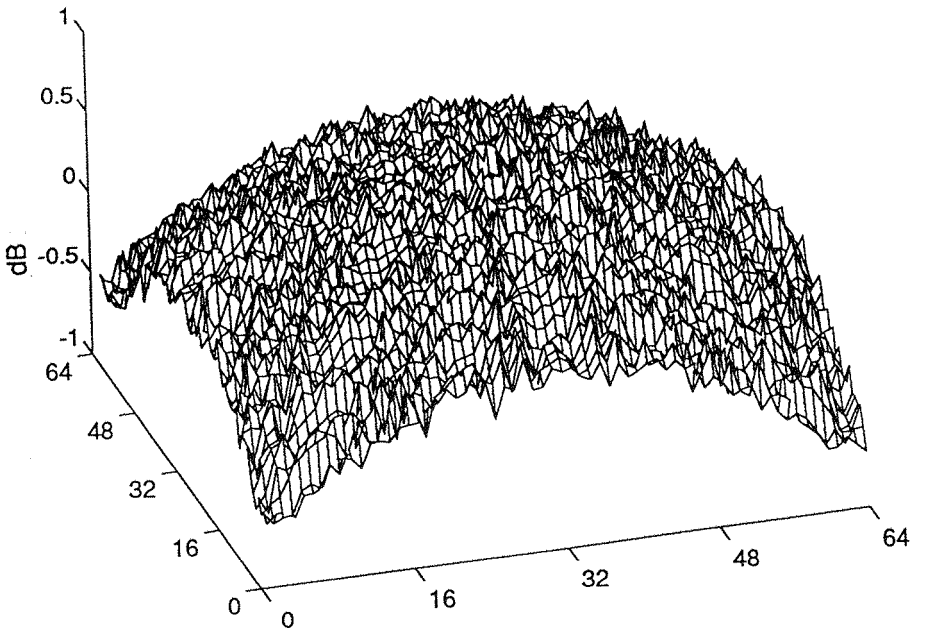

Figure 3.7 - The magnitude of the difference between the measured and theoretical pressure for a monopole source in dB re.1×10^{-6} Pa at 46875Hz.

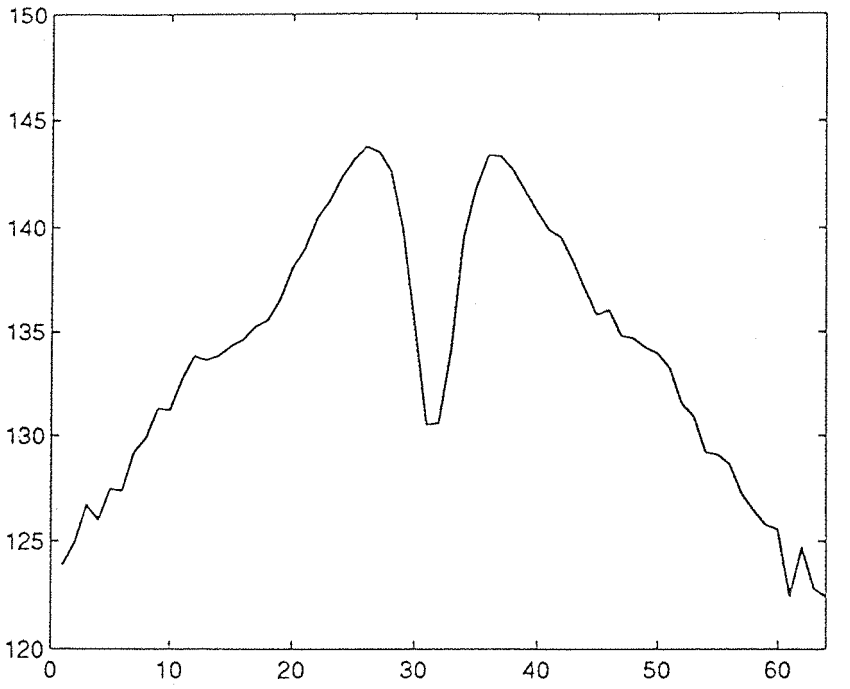

Figure 3.8 - The magnitude of the measured pressure in dB re.1×10^{-6} Pa at 31250Hz for a monopole source within a hard walled duct.
Source is placed in the centre of the duct $r_s = 0$, and $ka = 6.5$.
Array plane is 0.125m from the centre line of the duct exit.

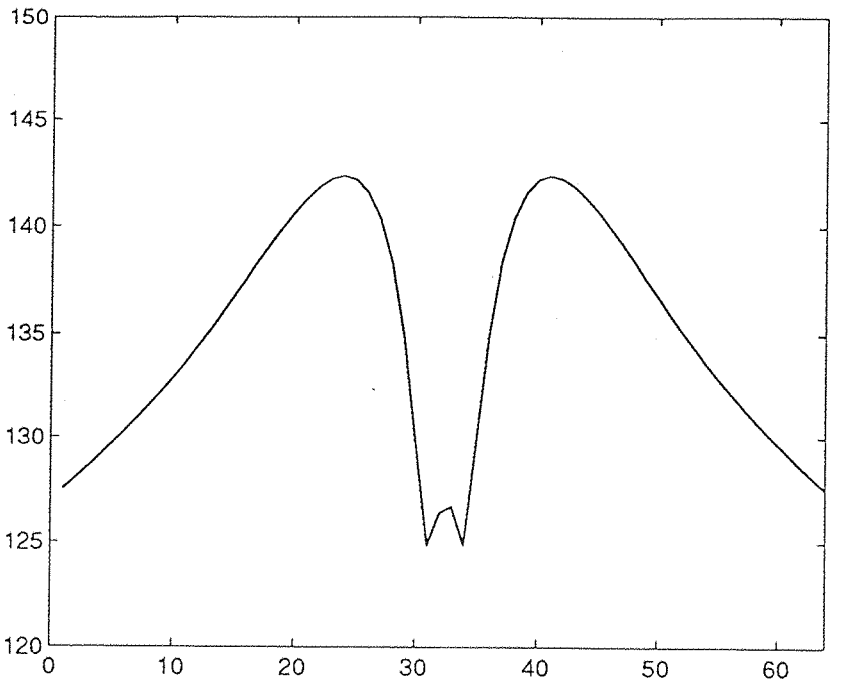

Figure 3.9 - The magnitude of the theoretical pressure in dB re.1×10^{-6} Pa at 31250Hz for a monopole source within a hard walled duct.
Source is placed in the centre of the duct $r_s = 0$, and $ka = 6.5$.
Theoretical array plane is 0.125m from the centre line of the duct exit.

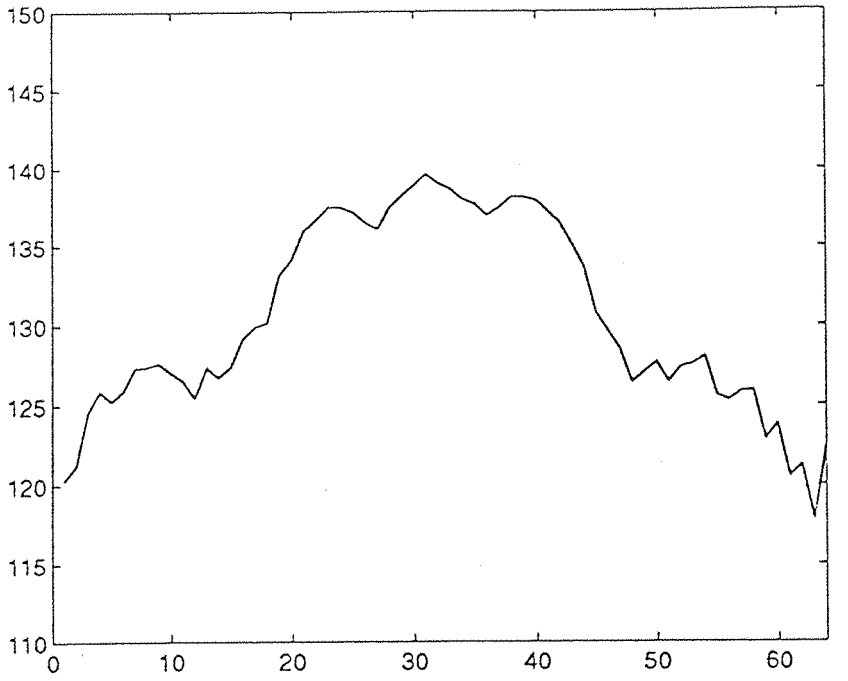

Figure 3.10 - The magnitude of the measured pressure in dB re.1×10^{-6} Pa at 15625Hz for a monopole source within a hard walled duct.
Source is placed in the centre of the duct $r_s = 0$, and $ka = 3.3$.
Array plane is 0.125m from the centre line of the duct exit.

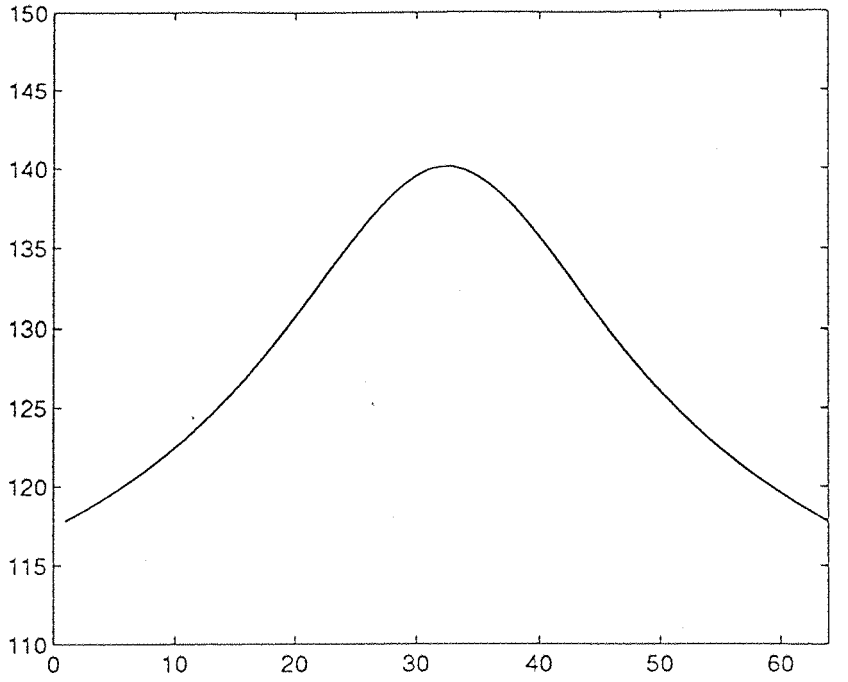

Figure 3.11 - The magnitude of the theoretical pressure in dB re.1×10^{-6} Pa at 15625Hz for a monopole source within a hard walled duct.
Source is placed in the centre of the duct $r_s = 0$, and $ka = 3.3$.
Theoretical array plane is 0.125m from the centre line of the duct exit.

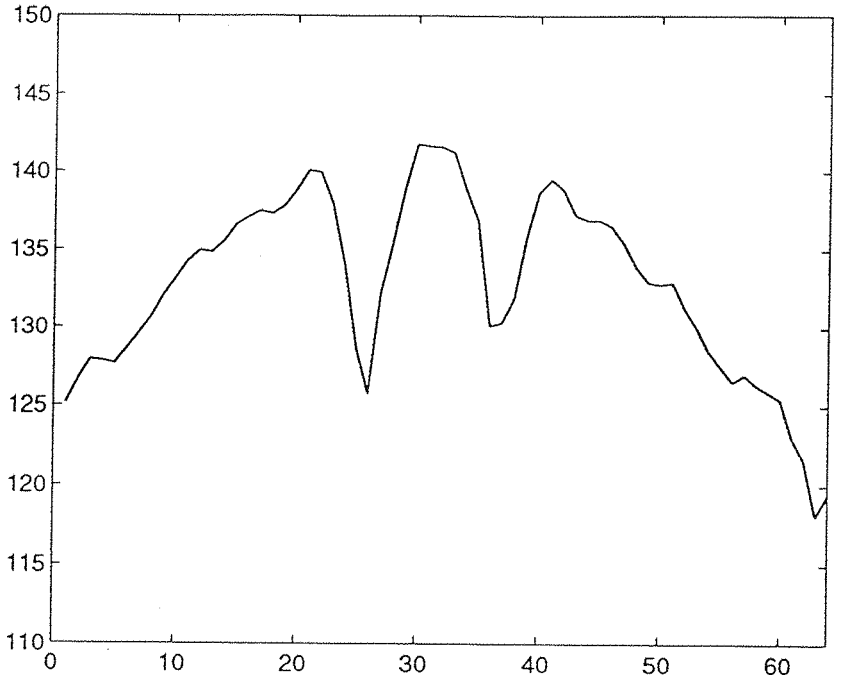

Figure 3.12 - The magnitude of the measured pressure in dB re.1×10^{-6} Pa at 46875Hz for a monopole source within a hard walled duct.
Source is placed in the centre of the duct $r_s = 0$, and $ka = 9.8$.
Array plane is 0.125m from the centre line of the duct exit.

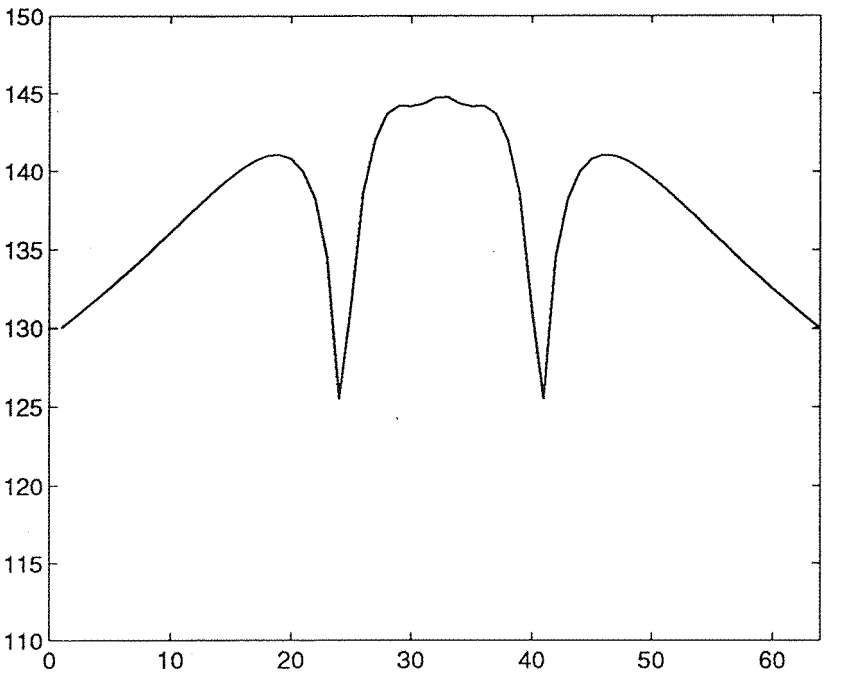

Figure 3.13 - The magnitude of the theoretical pressure in dB re.1×10^{-6} Pa at 46875Hz for a monopole source within a hard walled duct.
Source is placed in the centre of the duct $r_s = 0$, and $ka = 9.8$.
Theoretical array plane is 0.125m from the centre line of the duct exit.

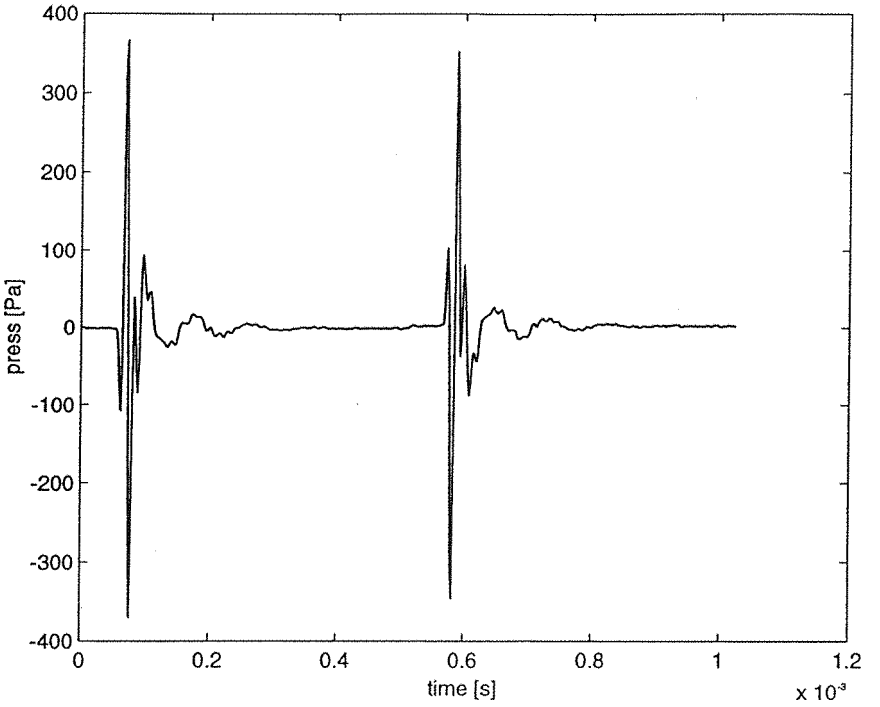

Figure 3.14 - The magnitude of the measured incident and reflected time histories from a neoprene coated steel plate.
Note the required phase inversion of reflected time history.

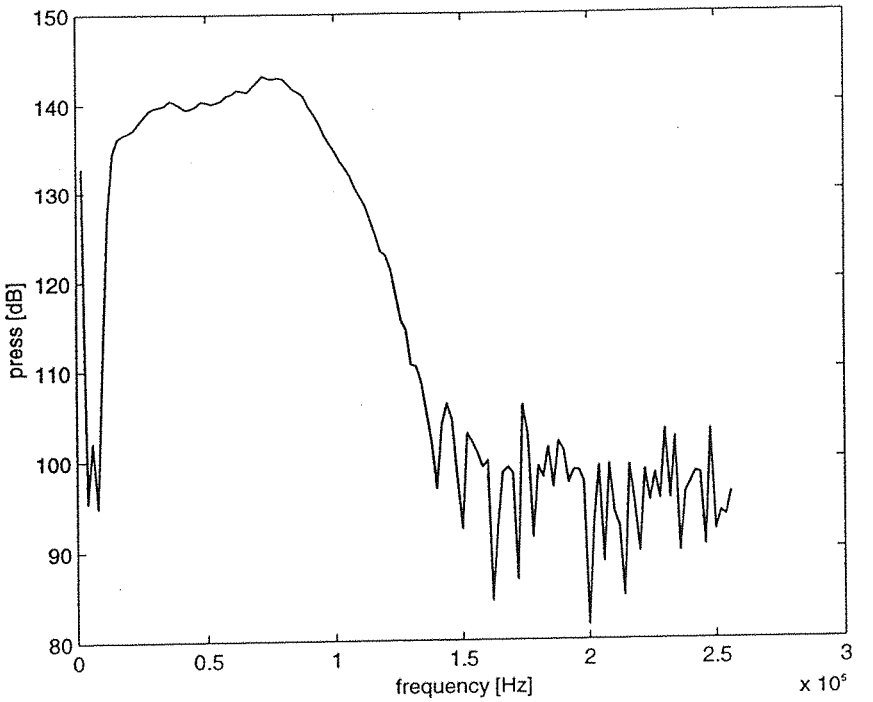

Figure 3.15 - The magnitude of the measured incident spectrum from figure 3.14 in dB re. 1×10^{-6} Pa.

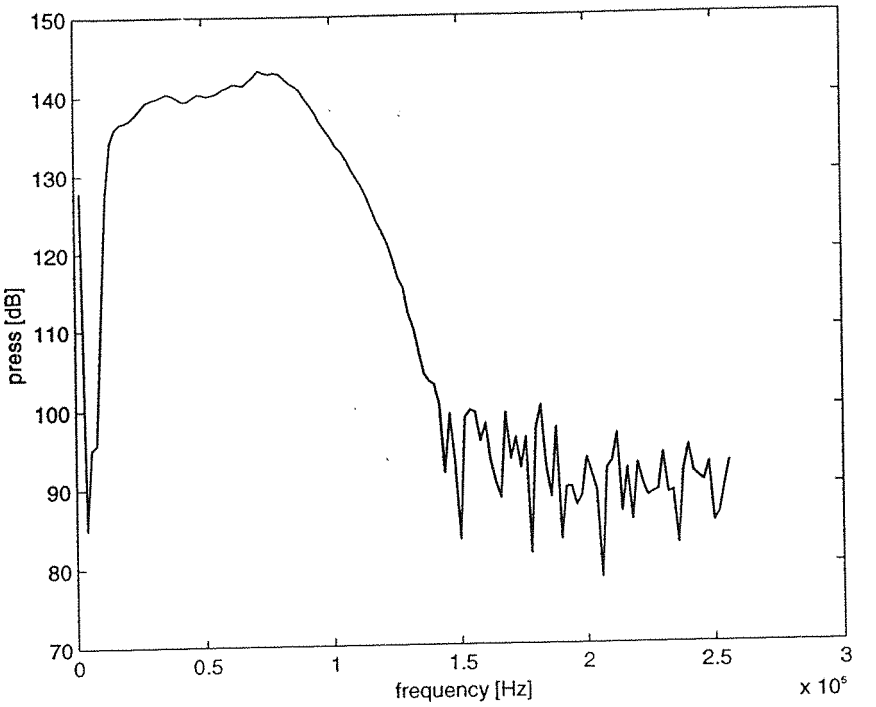

Figure 3.16 - The magnitude of the measured reflected spectrum from figure 3.14 in dB re. 1×10^{-6} Pa.

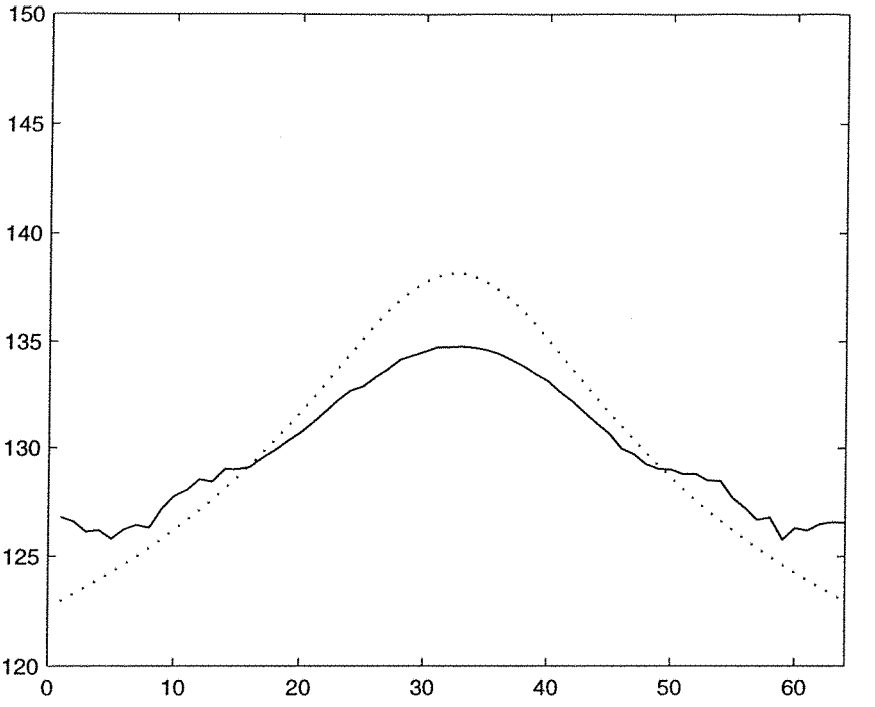

Figure 3.17a - The magnitude of the theoretical (dashed line) and experimental (solid) pressures in dB re.1×10^{-6} Pa at 15625Hz
for a monopole source within a pressure release lined duct.
The source is placed in the centre of the duct $r_s = 0$, and $ka = 3.3$.
The theoretical array plane is 0.125m from the centre line of the duct exit.

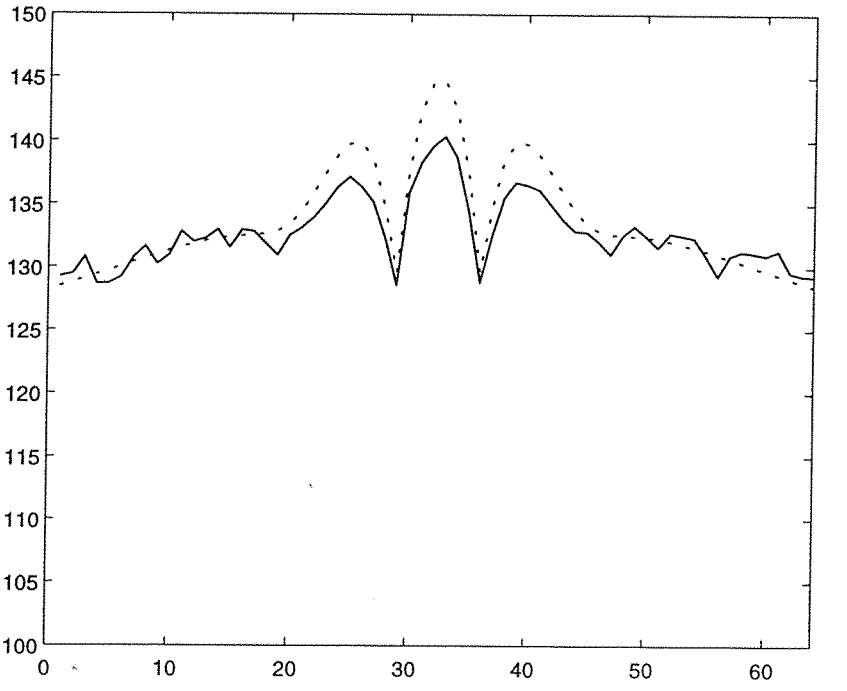

Figure 3.17b - The magnitude of the theoretical (dashed line) and experimental (solid) pressure in dB re.1×10^{-6} Pa at 31250Hz
for a monopole source within a pressure release lined duct.
The source is placed in the centre of the duct $r_s = 0$, and $ka = 6.5$.
The theoretical array plane is 0.125m from the centre line of the duct exit.

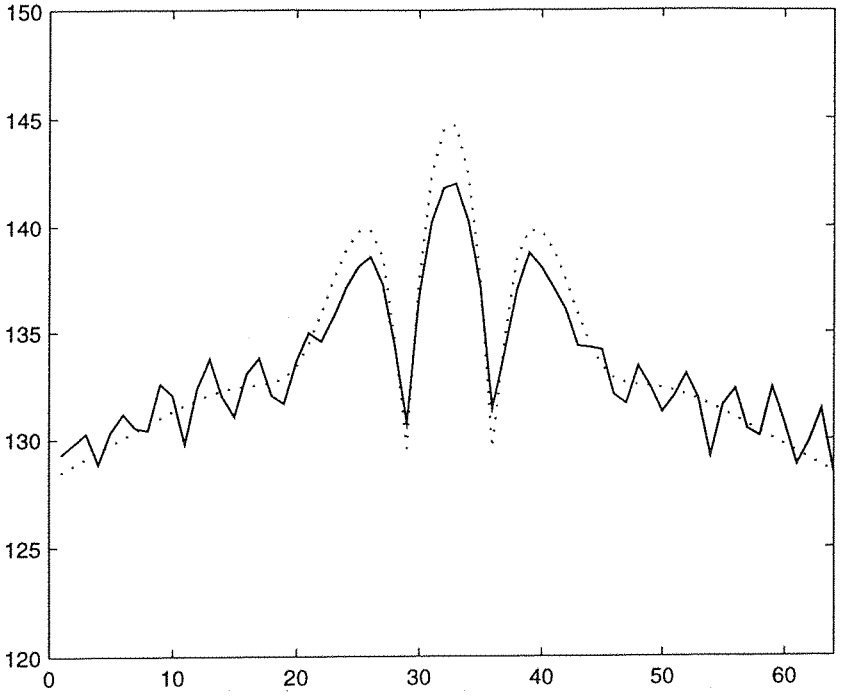

Figure 3.17c - The magnitude of the theoretical (dashed line) and experimental (solid) pressure in dB re.1×10^{-6} Pa at 46875Hz
for a monopole source within a pressure release lined duct.
The source is placed in the centre of the duct $r_s = 0$, and $ka = 9.8$.
The theoretical array plane is 0.125m from the centre line of the duct exit.

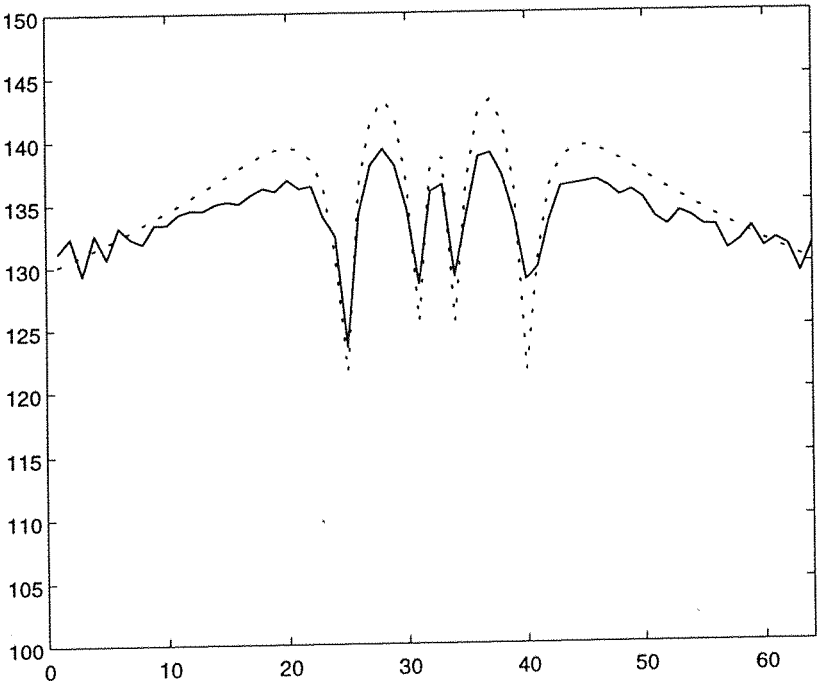

Figure 3.17d - The magnitude of the theoretical (dashed line) and experimental (solid) pressure in dB re.1×10^{-6} Pa at 62500Hz
for a monopole source within a hard walled and pressure release lined duct.
The source is placed in the centre of the duct $r_s = 0$, and $ka = 13.1$.
The theoretical array plane is 0.125m from the centre line of the duct exit.

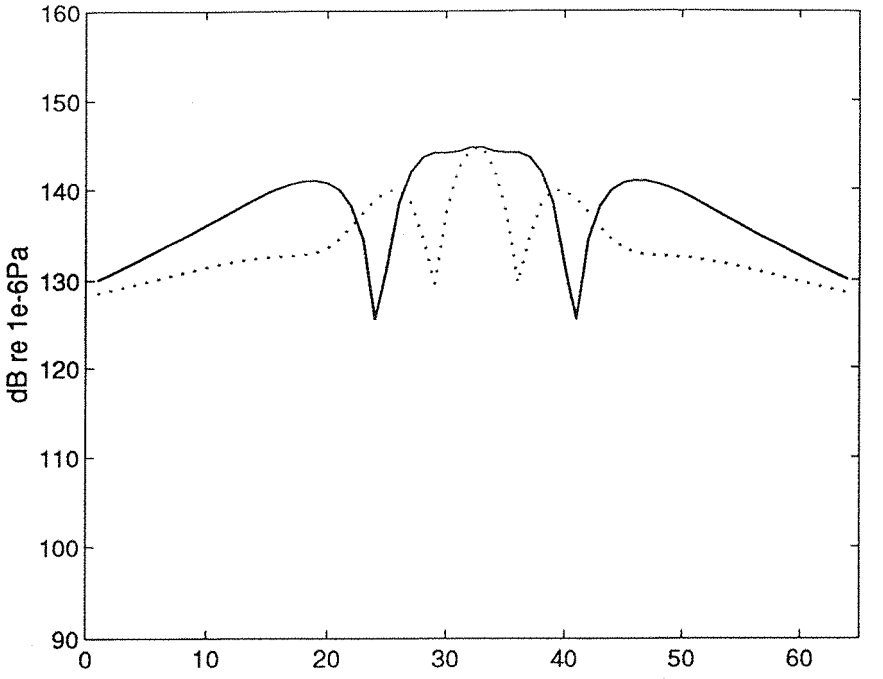

Figure 3.17g - The magnitude of the theoretical pressure in dB re.1×10^{-6} Pa at 46875Hz
for a monopole source within a hard walled and pressure release lined duct.
The dashed line is the field from the pressure release duct, and the solid line the hard walled duct.
The source is placed in the centre of the duct $r_s = 0$, and $ka = 9.8$.
The theoretical array plane is 0.125m from the centre line of the duct exit.

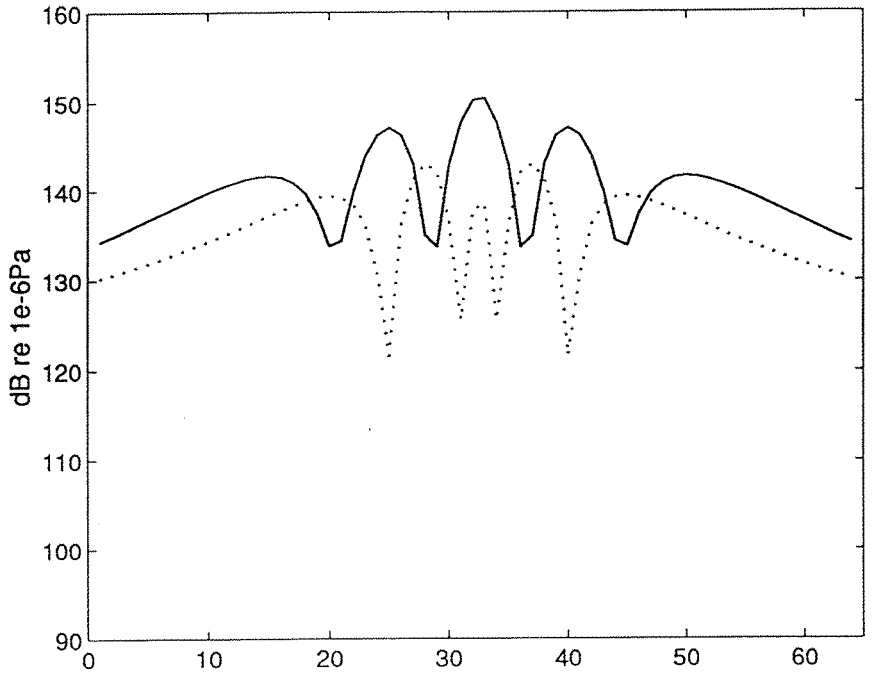

Figure 3.17h - The magnitude of the theoretical pressure in dB re.1×10^{-6} Pa at 62500Hz
for a monopole source within a hard walled and pressure release lined duct.
The dashed line is the field from the pressure release duct, and the solid line the hard walled duct.
The source is placed in the centre of the duct $r_s = 0$, and $ka = 13.1$.
The theoretical array plane is 0.125m from the centre line of the duct exit.

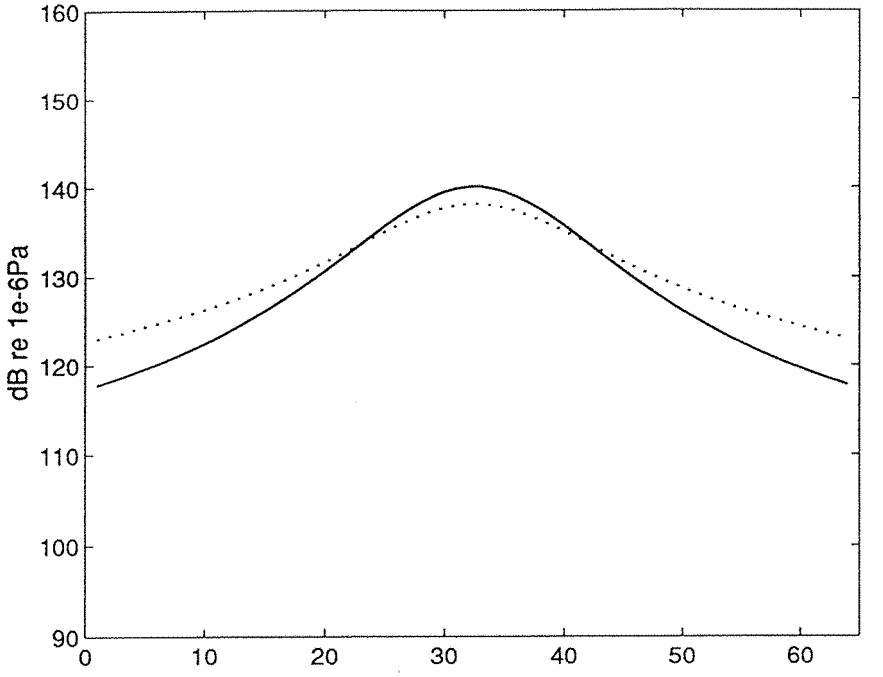

Figure 3.17e - The magnitude of the theoretical pressure in dB re.1×10^{-6} Pa at 15625Hz
for a monopole source within a hard walled and pressure release lined duct.
The dashed line is the field from the pressure release duct, and the solid line the hard walled duct.
The source is placed in the centre of the duct $r_s = 0$, and $ka = 3.3$.
The theoretical array plane is 0.125m from the centre line of the duct exit.

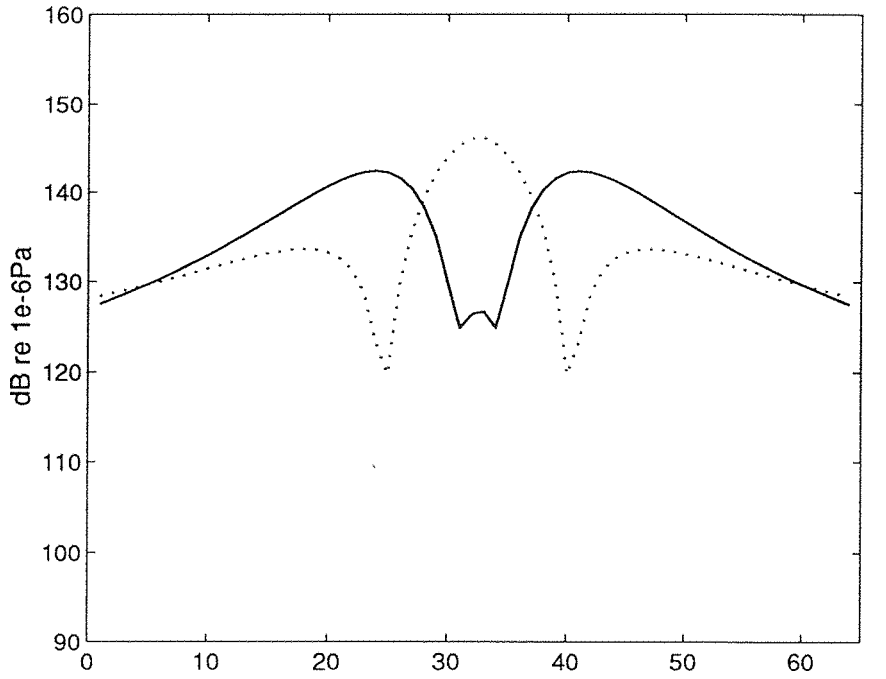

Figure 3.17f - The magnitude of the theoretical pressure in dB re.1×10^{-6} Pa at 31250Hz
for a monopole source within a hard walled and pressure release lined duct.
The dashed line is the field from the pressure release duct, and the solid line the hard walled duct.
The source is placed in the centre of the duct $r_s = 0$, and $ka = 6.5$.
The theoretical array plane is 0.125m from the centre line of the duct exit.

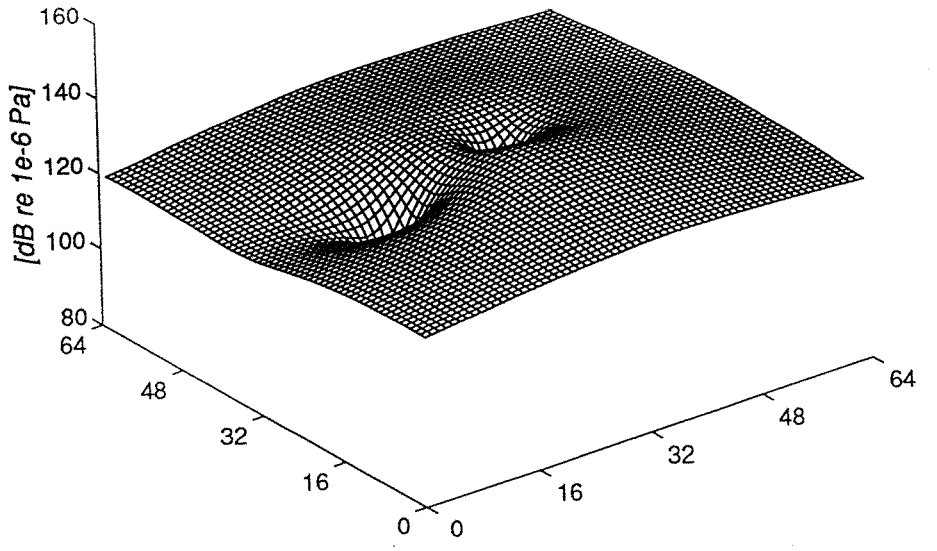

Figure 3.18 - The magnitude of the theoretical pressure in dB re.1×10^{-6} Pa at 15625Hz for a monopole source within a hard walled duct.
Source is placed at a radius of $r_s = 49$mm, the duct radius is 50mm, and $ka = 3.3$.
Theoretical array plane is 0.125m from the centre line of the duct exit.

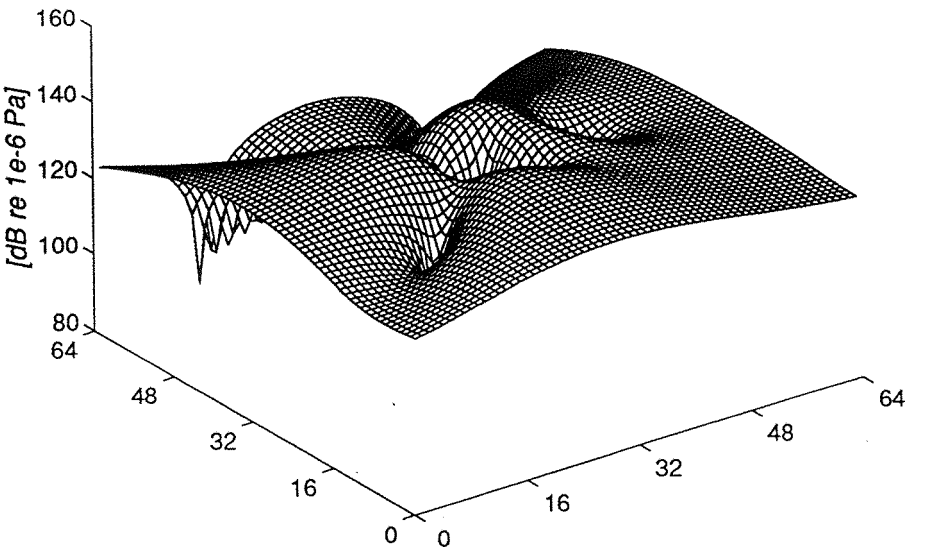

Figure 3.19 - The magnitude of the theoretical pressure in dB re.1×10^{-6} Pa at 31250Hz for a monopole source within a hard walled duct.
Source is placed at a radius of $r_s = 49$mm, the duct radius is 50mm, and $ka = 6.5$.
Theoretical array plane is 0.125m from the centre line of the duct exit.

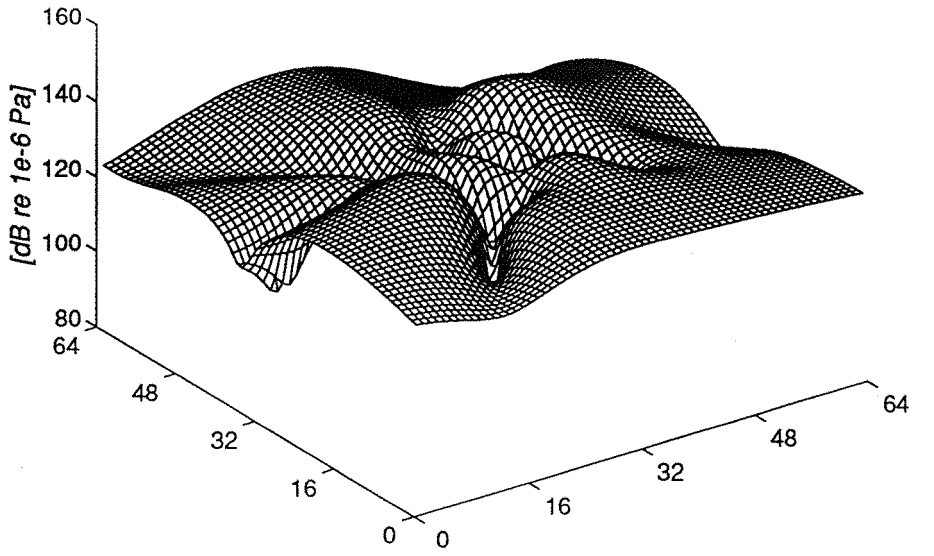

Figure 3.20 - The magnitude of the theoretical pressure in dB re.1×10^{-6} Pa at 46875Hz for a monopole source within a hard walled duct.
Source is placed at a radius of $r_s = 49$mm, the duct radius is 50mm, and $ka = 9.8$.
Theoretical array plane is 0.125m from the centre line of the duct exit.

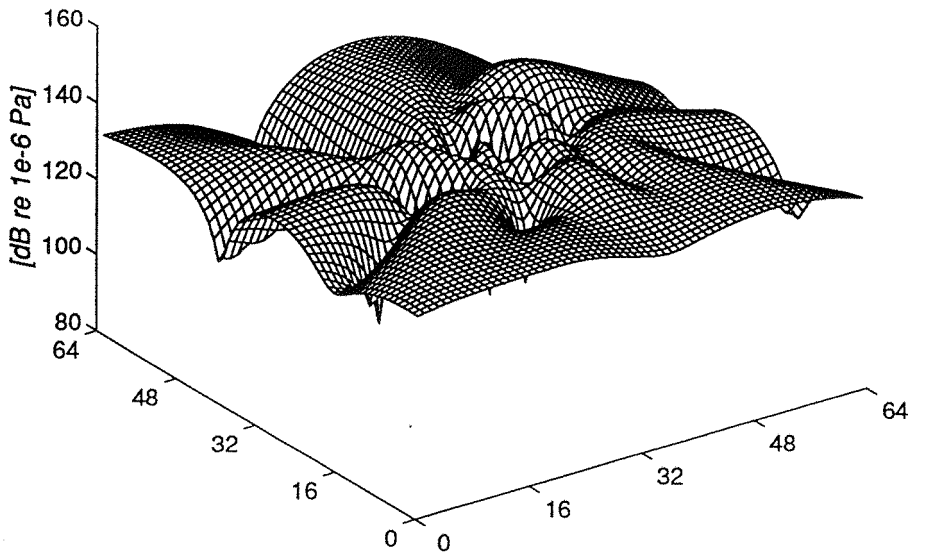

Figure 3.21 - The magnitude of the theoretical pressure in dB re.1×10^{-6} Pa at 62500Hz for a monopole source within a hard walled duct.
Source is placed at a radius of $r_s = 49$mm, the duct radius is 50mm, and $ka = 13.1$.
Theoretical array plane is 0.125m from the centre line of the duct exit.

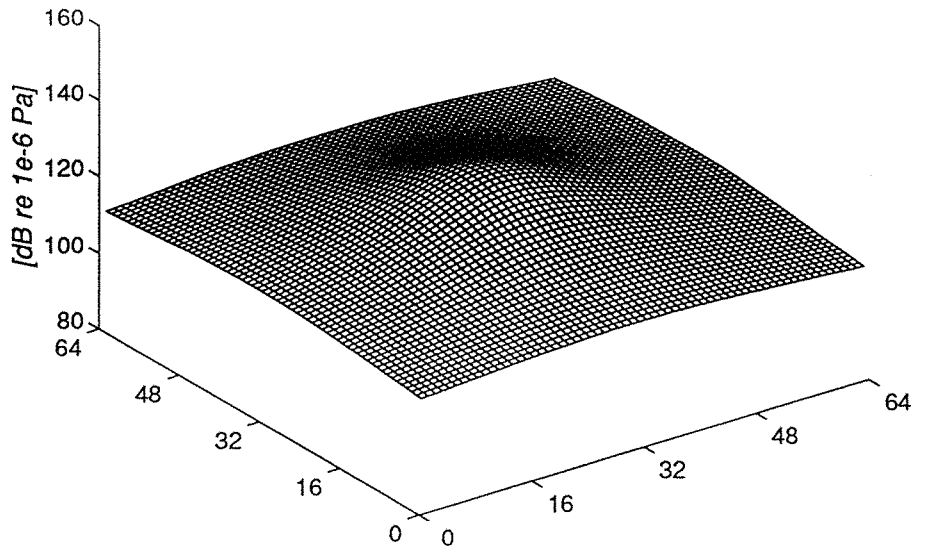

Figure 3.22 - The magnitude of the theoretical pressure in dB re.1×10^{-6} Pa at 15625Hz for a monopole source within a pressure release lined duct.
Source is placed at a radius of $r_s = 49$mm, the duct radius is 50mm, and $ka = 3.3$.
Theoretical array plane is 0.125m from the centre line of the duct exit.

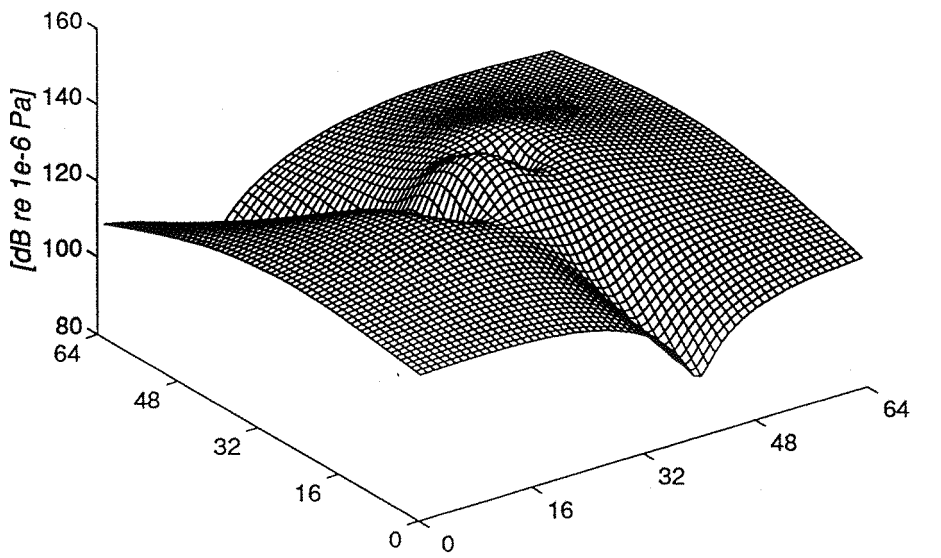

Figure 3.23 - The magnitude of the theoretical pressure in dB re.1×10^{-6} Pa at 31250Hz for a monopole source within a pressure release lined duct.
Source is placed at a radius of $r_s = 49$mm, the duct radius is 50mm, and $ka = 6.5$.
Theoretical array plane is 0.125m from the centre line of the duct exit.

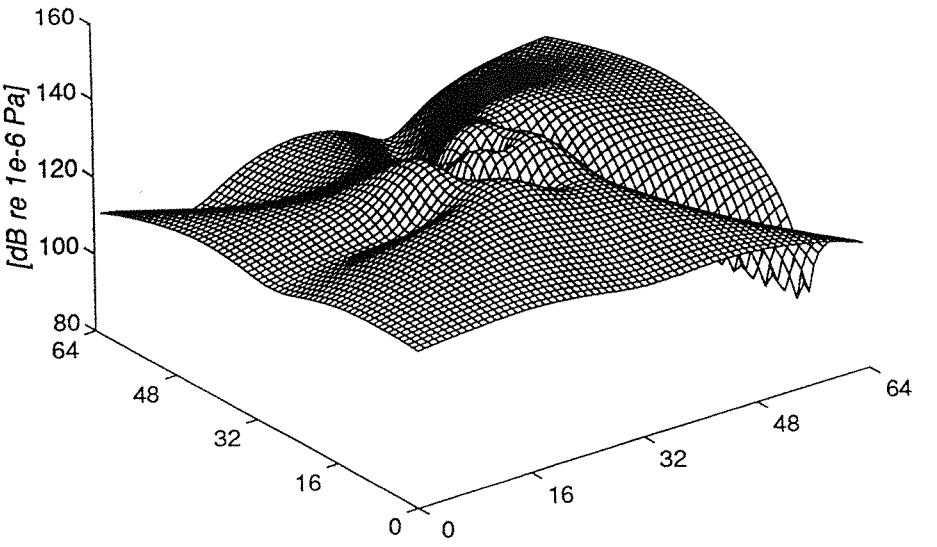

Figure 3.24 - The magnitude of the theoretical pressure in dB re.1×10^{-6} Pa at 46875Hz for a monopole source within a pressure release lined duct.
Source is placed at a radius of $r_s = 49$mm, the duct radius is 50mm, and $ka = 9.8$.
Theoretical array plane is 0.125m from the centre line of the duct exit.

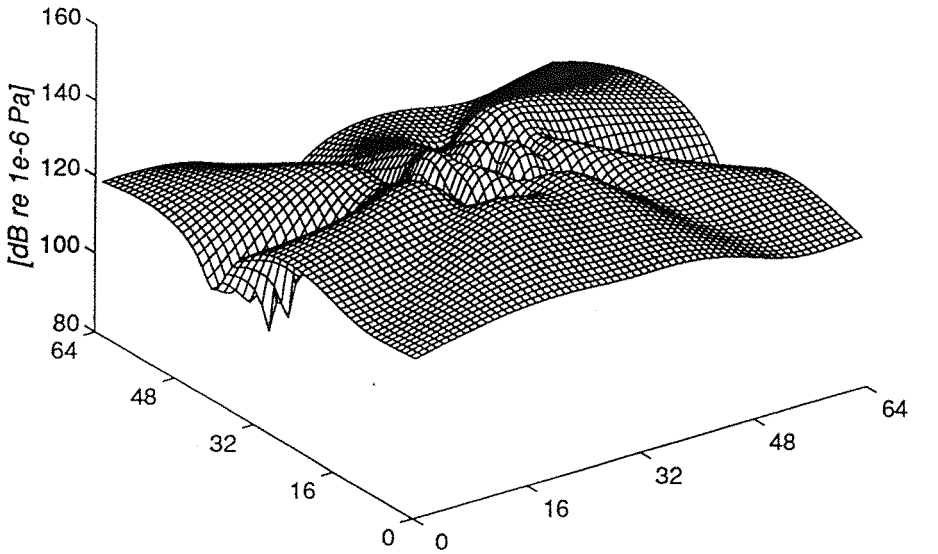

Figure 3.25 - The magnitude of the theoretical pressure in dB re.1×10^{-6} Pa at 62500Hz for a monopole source within a pressure release lined duct.
Source is placed at a radius of $r_s = 49$mm, the duct radius is 50mm, and $ka = 13.1$.
Theoretical array plane is 0.125m from the centre line of the duct exit.

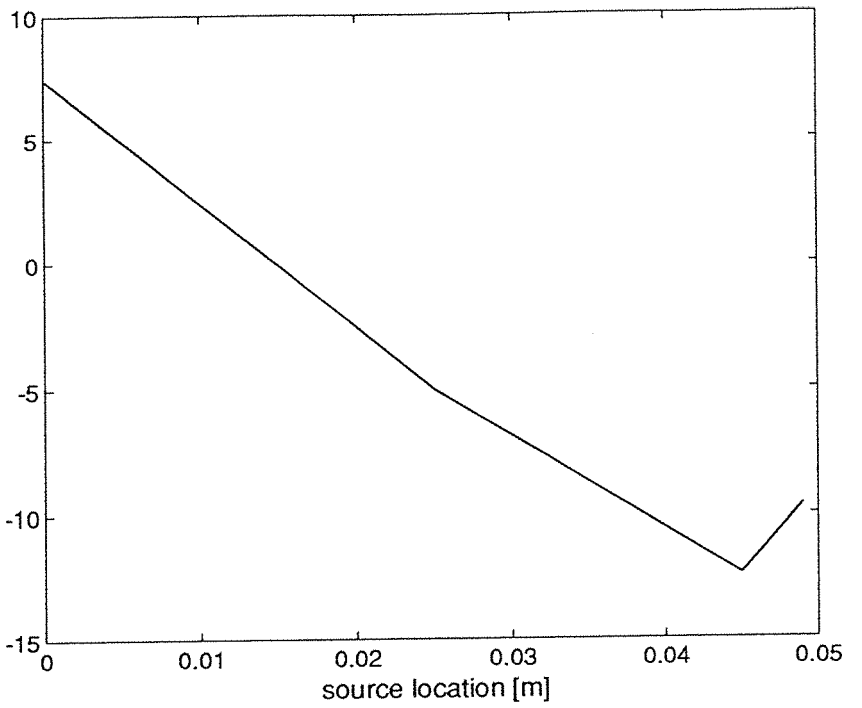

Figure 3.26 - The theoretical sound power reduction using a pressure release lined duct in place of a hard walled duct as a function of source location, for a monopole source at 15625Hz ($ka = 3.3$).

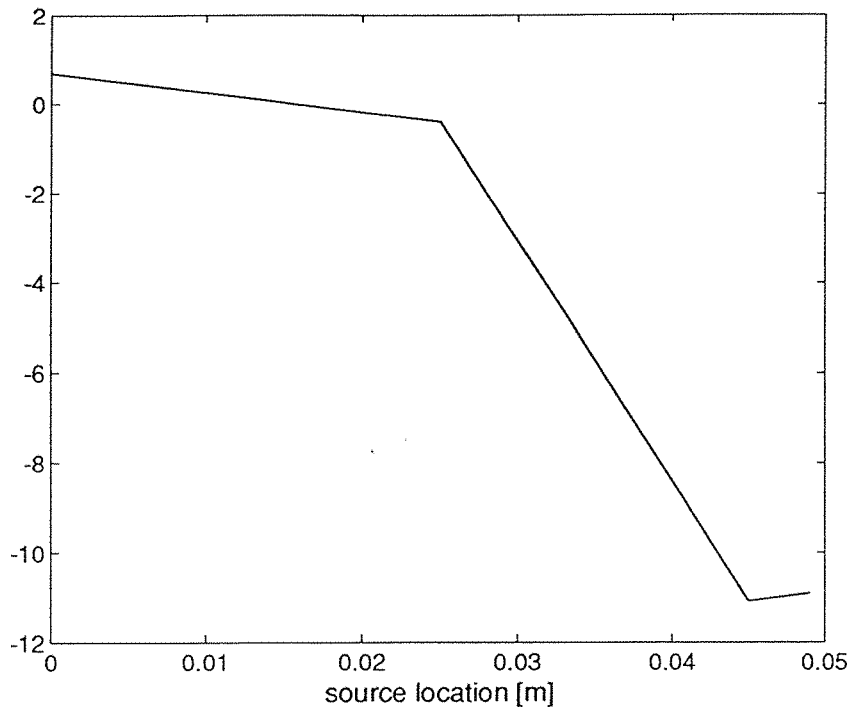

Figure 3.27 - The theoretical sound power reduction using a pressure release lined duct in place of a hard walled duct as a function of source location, for a monopole source at 31250Hz ($ka = 6.5$).

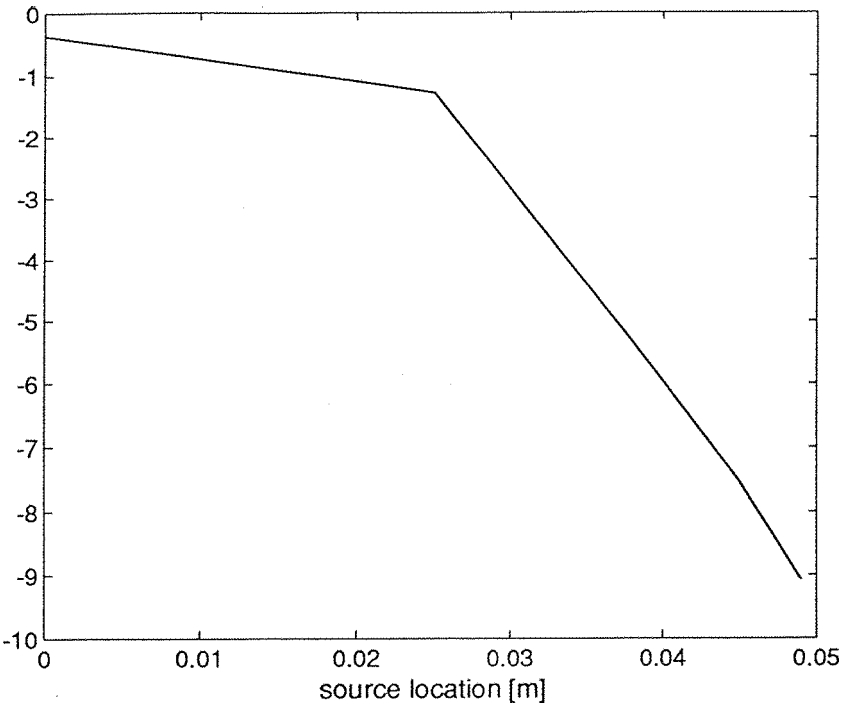

Figure 3.28 - The theoretical sound power reduction using a pressure release lined duct in place of a hard walled duct as a function of source location, for a monopole source at 46875Hz ($ka = 9.8$).

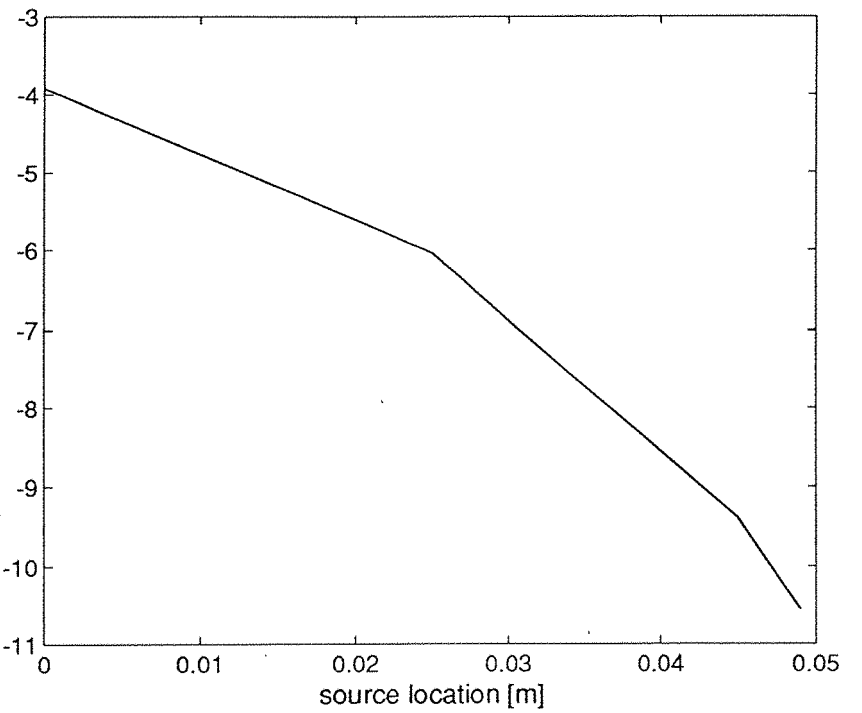

Figure 3.29 - The theoretical sound power reduction using a pressure release lined duct in place of a hard walled duct as a function of source location, for a monopole source at 612500Hz ($ka = 13.1$).

Chapter 4

Techniques for Estimating the Radiated Field from Near Field Measurements

4 1 Introduction

In this chapter, techniques are examined which offer the potential to determine the acoustic pressure at one region in an acoustic field, from the pressure at another region. At the outset of this project it was intended that results obtained from the experiment described in Chapter 3 would be used for this purpose. It was intended that a measured plane of pressure values obtained close to the duct exit could be used to predict the far field radiation from the duct.

These propagation techniques are perhaps most useful where the source cannot easily be described analytically. In these cases measured acoustic data is often the only way to determine the radiated field. If this data is measured near to the source, then it may be desirable to be able predict the far-field radiated by the source using this measured data. This is the basic objective of many of the propagation techniques that will be examined later in this chapter. Furthermore, to measure directly in the far field is sometimes impractical, and often impossible. Generally this requires a very large, low noise, free field. Of course, simulation of a free field underwater is possible using an anechoically lined tank for example, but in water anechoic materials that work well over a large frequency range can be prohibitively expensive. For this reason it is necessary to use near field data to predict the pressure in the far field.

This chapter reviews and describes many propagation techniques, but in particular concentrates upon a method that is based upon a 2 dimensional Fourier Transform of the original pressure field. By way of introduction to this, and the other propagation techniques, the most fundamental approach to calculating the radiation from an acoustic source, the Kirchoff-Helmholtz integral, will be described. It will be shown that this is the basis of the most significant propagation techniques.

4.2 The Kirchoff-Helmholtz integral and the radiation from complex source distributions.

Arguably one of the most important problems in the field of acoustics is the calculation of the acoustic radiation from complex sources distributions. The most fundamental approach of calculating the radiation from an acoustic source is found by solving the Kirchoff-Helmholtz integral equation. However, for all but very simple geometries, tractable analytical solutions to this equation can not be obtained. Solutions require a knowledge of both the surface pressure and velocity to specify the acoustic field at a receiver point. These two parameters are often difficult obtain, either by analysis or experiment. It is for this reason that approximations and simplifications[1] to the full Kirchoff-Helmholtz integral equation have been derived and are frequently used.

The most widely used of these simplifications applies to radiation from a planar source region, where the Kirchoff-Helmholtz integral reduces to the Rayleigh integral. It will be shown that by subdividing the source region into small elemental sources over a finite range in space, and because the acoustic radiation from these elemental sources is known analytically, the far-field amplitude and phase may be obtained from a sum of the contributions from each of these elemental sources. The Rayleigh integral has many advantages not least of which is that it is simple and exact. However, the successful implementation of the Rayleigh integral, may require a large number of these elemental sources and hence a large number of calculations to determine the radiated field. Typically, for any reasonably sized source region, together with high frequency radiation, the number of such calculations is counted in tens of thousands.

To derive the Rayleigh integral and to aid the description of the many propagation techniques reviewed in the next section, it is necessary to begin with the inhomogeneous Helmholtz equation, given by

$$(\nabla^2 + k^2)p(\mathbf{x}) = \nabla \bullet \mathbf{f}_{vol}(\mathbf{x}) - j\omega\rho_0 q_{vol}(x), \tag{4.2.1}$$

where $\mathbf{f}_{vol}(\mathbf{x})$ is the distribution of complex force per unit volume and $q_{vol}(x)$ the distribution of complex volume velocity per unit volume acting on the fluid. Solutions to this equation are found using a suitably chosen Green function, and applying Green's Theorem results in the following integral expression, (see for example Nelson and Elliott, 1992)

---

[1]Not withstanding approximate numerical techniques such as boundary element methods.

$$p(\mathbf{x}) = \int_V Q_{vol}(y) G(\mathbf{x}|\mathbf{y})\, dV + \int_S [G(\mathbf{x}|\mathbf{y}) \nabla_y p(\mathbf{y}) - p(\mathbf{y}) G(\mathbf{x}|\mathbf{y})] \bullet \mathbf{n}\, dS. \qquad (4.2.2)$$

Referring to figure 4.1, the pressure at some point $p(\mathbf{x})$ produced by some complex volume source strength in the volume V, can be found by solving the integrals on the right hand side of equation (4.2.2). The first is a volume integral, and the second is a contribution from a surface integral, which requires specification of not only the pressure on the surface S, but also the pressure gradient, $\nabla_y p(\mathbf{y})$ on S and the Green function $G(\mathbf{x}|\mathbf{y})$. If the Green function is chosen to be the free space Green function, $g(\mathbf{x}|\mathbf{y})$ given by

$$g(\mathbf{x}|\mathbf{y}) = \frac{e^{-jk|\mathbf{x}-\mathbf{y}|}}{4\pi|\mathbf{x}-\mathbf{y}|}, \qquad (4.2.3)$$

and there is zero source strength within V, then the integral expression given in equation (4.2.2) reduces to the Kirchoff-Helmholtz integral equation

$$\int_S [g(\mathbf{x}|\mathbf{y}) \nabla_y p(\mathbf{y}) - p(\mathbf{y}) g(\mathbf{x}|\mathbf{y})] \bullet \mathbf{n}\, dS = \begin{cases} p(\mathbf{x}), & \mathbf{x} \text{ within } V \\ 0, & \mathbf{x} \text{ outside } V \end{cases}. \qquad (4.2.4)$$

The terms on the left hand side of equation (4.2.4) can be shown to have a physical interpretation. The conservation of momentum equation for harmonic excitation gives

$$\nabla_y p(\mathbf{y}) = -j\omega\rho_0\, u(\mathbf{y}). \qquad (4.2.5)$$

The first term of the integral in (4.2.4) can be written as

$$-\int_S g(\mathbf{x}|\mathbf{y}) j\omega\rho_0\, \mathbf{u}(\mathbf{y}) \bullet \mathbf{n}\, dS = \int_S g(\mathbf{x}|\mathbf{y}) j\omega\rho_0\, q_{surf}\, dS\mathbf{x}|\mathbf{y}, \qquad (4.2.6)$$

where $q_{surf}(\mathbf{y}) = -\mathbf{u}(\mathbf{y}) \bullet \mathbf{n}$ is a volume velocity per unit surface area, and therefore represents a monopole distribution of source strength. Also the second term in equation (4.2.4) may be written as

$$-\int_S p(\mathbf{y}) \nabla_y g(\mathbf{x}|\mathbf{y}) \bullet \mathbf{n}\, dS = \int_S \mathbf{f}_{surf}(\mathbf{y}) \nabla_y g(\mathbf{x}|\mathbf{y})\, dS, \qquad (4.2.7)$$

where $\mathbf{f}_{surf}(\mathbf{y}) = p(\mathbf{y})\mathbf{n}$ is a force per unit area acting at the surface S. This is equivalent to a distribution of dipole sources on the surface S. It is possible to solve the Kirchoff-Helmholtz equation in some circumstances, and for the present

application it is useful to examine the case where the Green function is chosen such that $\nabla_y G(\mathbf{x}|\mathbf{y}).\mathbf{n} = 0$ on the surface S which is the case for a rigid surface. Equation (4.2.4) then becomes

$$p(\mathbf{x}) = \int_S G(\mathbf{x}|\mathbf{y}) \nabla_y p(\mathbf{y}) \bullet \mathbf{n}\, dS. \tag{4.2.8}$$

For the case of S being an infinite plane rigid boundary, the Green function becomes the hard walled Green function, $G(\mathbf{x}|\mathbf{y}) = 2g(\mathbf{x}|\mathbf{y})$. The Kirchoff-Helmholtz integral equation then reduces to the Rayleigh integral given by

$$p(\mathbf{x}) = 2j\omega\rho_0 \int_S g(\mathbf{x}|\mathbf{y}) \mathbf{u}(\mathbf{y}) \bullet \mathbf{n}\, dS. \tag{4.2.9}$$

Thus it can be seen that the Rayleigh integral is a special case of the more general Kirchoff-Helmholtz equation, and represents the acoustic field produced by some surface velocity, as equivalent to a sum of monopole sources on the plane S. Since we have assumed that S is an infinite plane then the integration in equation (4.2.9) must in principle be made over the region $-\infty \le x \le \infty$ and $-\infty \le y \le \infty$ for Cartesian co-ordinates. However the range of integration may be truncated if $\mathbf{u}(\mathbf{y}) \bullet \mathbf{n}$ is only finite over a given portion of S. In this case the integrand will be zero for all but the region of $\mathbf{u}(\mathbf{y}) \bullet \mathbf{n} \neq 0$.

4.3 A review of the literature on acoustic field propagation techniques.

In this section a literature review is discussed which examines previous work aimed at calculating the acoustic pressure field at a desired location, from a knowledge of the field at another location.

Pachner (1956a) has developed a method for determining the directivity of a source at an arbitrary distance, from measurements made of the instantaneous values of the field at another distance from the source. The field is decomposed into an infinite series of spherical wave components, and together with suitable measurements made of the acoustic field, are shown to be sufficient to determine the directivity pattern of the source. In a subsequent paper, (1956b), Pachner, shows how the theory developed in (1956a) may be applied to fields consisting of the superposition of travelling waves and standing waves.

Approximations to the technique derived by Pachner (1956a) have been reported, most notably by Horton and Innis (1961), and Baker (1962). Horton and Innis show that it is possible to evaluate the far-field radiation pattern from pressure measurements alone made over a closed surface S, which contains the source. As a starting point it is shown that if the Helmholtz equation is to be solved by using a Green Function of the form $\exp(jkr/r)$ requires a knowledge of the normal pressure gradient, $\partial p/\partial n$ over S and the pressure p. Normally the pressure gradient is not a measured quantity[2], and therefore approximations to the pressure gradient are discussed. These approximations to the pressure gradient are then used to solve the Helmholtz equation, and the accuracy of the resultant computed far-field is tested by comparison with measured data. If however, a Green Function is chosen which vanishes over the surface S, it is shown that the far-field may be evaluated in terms of only pressure measurements over S. The resulting formula for the far-field is more complicated than the Helmholtz formula, but it does not require a knowledge of $\partial p/\partial n$.

Baker (1962), adopts a similar method for the calculation of the far-field pressure, by using approximations to the normal component of the pressure gradient in the near field of the source. A large amount of data is presented comparing the pressure field as predicted using suitable approximations with measured experimental data.

In a slightly different problem, Trott (1964) uses measurements made in the near field of a source to determine the directivity of underwater acoustic transducers. This employs the principle of reciprocity combined with the above work by Horton and Innis and Pachner.

Schenck (1968) reviewed the integral methods that have been used until that time for the calculation of the acoustic radiation from sources. These are a simple source formulation derived from potential theory, a surface Helmholtz integral formulation given by Copley (1967) and (1968), and an interior Helmholtz integral formulation. It is shown that each of these formulations has potential computational problems for some wavenumbers, caused by discontinuities in the integral formulations. To overcome this problem, a combination of the interior and surface formulations of the Helmholtz integral equation is proposed, and is denoted by the acronym CHIEF, which refers to the Combined Helmholtz integral Equation Formulation. Examples of the

---

[2]Pressure gradients may be measured using a two hydrophone technique similar to that used in acoustic intensity measurements.

predicted radiation from a cylinder are given, and are shown to be in good agreement with the conventional Helmholtz integral equation.

Koopman and Benner (1982) have developed a technique based upon the Helmholtz integral to determine the sound power radiated from complex sources such as machinery. The method requires a knowledge of the geometry and the modal characteristics of the sources' vibrating surfaces, so that the pressure on the surface may be computed. The source is then divided into planar surfaces consisting of rectangles and triangles, and the required surface integration performed over each element. What makes this work different from that given above, is that here it is intended that the technique be compatible with finite element methods, i.e. they should share the same grid system. The approximation of the closed surface surrounding the source by planar elements results in the integration over a 3 dimensional surface being replaced by two dimensional ones. This reduces the computation time considerably. The accuracy of this approximation is demonstrated by calculating the pressure on the surface of a uniformly pulsating sphere and an oscillating sphere.

An alternative to using the Helmholtz integral equation directly, relies on the principle of decomposing an arbitrary wave field into a series of plane wave components. This principle has been widely used in optics and the study of electromagnetic waves. Authors such as Linfoot (1964), Clemmow (1966) and Goodman (1968) have established this technique for the analysis of different types of electromagnetic field. The work by these authors indicated that the Fourier integral representation of a spatial wave field could be used to examine the propagation of this field. In particular it was established that by adopting this Fourier description of the field, greatly assisted in the solution of complex wave problems such as diffraction and scattering. It should be noted that to decompose a 3 dimensional field, the resulting Fourier Transform has the dimensions of space and time, requiring a 4 dimensional transform. However, the number of dimensions of the Fourier Transform may be reduced by considering only one frequency component at a time, and working in a plane, $x-y$ geometry. The resulting Fourier Transform is 2 dimensional, and there are several readily available routines that may be used to compute a 2D FT.

The first reported work of the application of the Fourier Transform explicitly to the propagation of an acoustic field was by Stepanishen and Benjamin (1982). The two-dimensional Fourier Transform of an acoustic field is used to propagate forward this field as an $x-y$ plane. Examples are given for differing source descriptions, and the

effects of filtering in both time and space are briefly mentioned. It is also shown that it is possible to predict the far-field pressure from velocity measurements made on a planar surface using this technique.

Further use of the Fourier Transform to evaluate the Rayleigh integral for planar radiators has been reported by Williams and Maynard, (1982). It is shown that the Fourier Transform offers a much faster method for calculating the far-field pressure from a vibrating plane body than the Rayleigh integral. Using the Rayleigh integral requires the splitting up of the vibrating surface into an $N \times N$ array of points. The subsequent far-field pressure calculation requires approximately N^4 multiplication and additions. Using the Fourier Transform only requires $N \log_2(N)^2$, thus providing a more rapid way of obtaining numerical results for large array sizes. Computations with the Fourier Transform for rectangular plates are given, and these are compared with exact solutions.

Williams (1983), has also studied the acoustic radiation from unbaffled thin plates in air using a Fourier transform form of the Rayleigh integral. The near field pressure and velocity of the plates are evaluated using an iterative technique, and this is used to calculate the radiation. As an example of the technique, the radiation from an unbaffled vibrating circular disk is computed and is shown to agree well with an exact solution for a small distance (less than a wavelength) away from the disk. It is also shown that the use of the Fourier transform to perform the integration in the Rayleigh equation, offers a large saving in computation time, compared with standard integration techniques.

The use of the Fourier Transform to propagate acoustic fields in cylindrical co-ordinates has also been studied. Candel and Chassaignon (1984), have used the Fourier Transform to examine the radiation from cylindrical sources. Here the propagation takes the form of cylindrical waves, and certain properties of the source may be used to simplify the radiation problem. If the source demonstrates circular symmetry, then it is possible to replace the conventional 2D Fourier Transform with a 1D Hankel transform. Instead of measuring over a square grid as is necessary using the 2D Fourier Transform, the field need only be measured along one radius assuming a circularly symmetric field. In practical terms this can offer large savings in both data capture and subsequent analysis. Good agreement is found between the propagated field of data measured from a dipole source, and an exact solution.

When a source of light or an illuminated object (i.e. a scatterer of light waves) is observed it is possible to obtain a good impression of the size, shape and source strength. Since acoustics is also the study of a wave phenomenon, it is reasonable to attempt to reconstruct the size and shape of an acoustic source by measuring the scattered sound. Acoustic Holography (AH), is an attempt to apply such an analogy and the theories of optical holography to acoustic fields.

Before going further, it should be noted that there exist important differences between task of source reconstruction, and the problem of forward propagation into the far-field. The most significant of these differences concerns the inclusion evanescent components of the field. For the complete reconstruction of a source, the evanescent components measured at some distance from the source, must be increased in amplitude exponentially as the field is propagated *toward* the source. This amplification may be large for highly evanescent components in the field. Thus any error in the measurement of these components will be magnified by this amplification, and will result in completely the wrong results for the reconstruction. For forward propagation this is not a problem, as the evanescent components decay as the field is propagated, and may be ignored completely in the far-field. There is also a practical signal to noise problem in measuring all the evanescent field necessary for complete reconstruction when using NAH. Because any instrumentation will have a finite signal to noise ratio, it may not be possible to measure adequately all the evanescent field. If this is the case then it is only possible to reconstruct the overall behaviour of the source, but the fine details with dimensions less than the wavelength in the surrounding medium cannot be reconstructed. Therefore to maximise the level of detail in the reconstruction it is helpful to make measurements very near to the source, hence the addition of word *near field* when attempting to reconstruct the source. This problem in measuring the evanescent field, and the subsequent amplification of any error, is a major limitation in the practical application of NAH (Matzumtoto, 1991).

It should also be observed that to amplify the evanescent components it is first necessary to know which wavenumbers are indeed evanescent and which are freely propagating. This is can only be achieved by having an *a priori* knowledge of the wavenumber spectrum of the source. This is another limitation of the technique, and it will be shown later that this *a priori* knowledge is not only restricted to NAH but also to the method of forward propagation of an acoustic field, but for different reasons.

However, despite the differences mentioned above between the present application and those of AH, there are many similarities, and in particular many of the difficulties

encountered in the practical application of AH are the same as those when attempting to propagate into the far-field.

The first thorough statement of the principles and practical aspects of AH and NAH are given in two companion papers as a result of a considerable research effort carried out at Penn State University, USA. The first of these papers is by Maynard and Williams (1985), which describes the theoretical basis of AH and points to important differences between optical and AH. It is also noted by the authors that many of the limitations previously imposed upon AH are without foundation, and are a result of mimicking the practices of optical holography and applying them in acoustics. To distinguish between previous AH and that defined in the paper, Maynard uses the phrase '*Generalised Holography*' that is applicable to acoustic fields. NAH can then be shown to be a special case of this general principle. The practical implementation of NAH is demonstrated by use of a 16×16 array of microphones measuring 3m×3m. Provided certain important considerations are observed, then the technique is shown to be successful. However, it will be shown later in this chapter, that many of the sources of error in using NAH difficult to overcome, and in some cases may result in abandonment of the technique in preference to say, the Rayleigh integral.

The reconstruction of an underwater acoustic source using Near field Acoustic Holography (NAH), has been reported by Williams *et al* (1985a). Measurements are made of the acoustic pressure of a source over a 2D plane surface very close to the source. This pressure map is essentially a hologram containing amplitude and phase information, which a can be used to backward propagate the field to reconstruct the source surface normal velocity and pressure.

The above work is extended by the authors to examine the structure borne intensity of plates underwater (Williams *et al* 1985b). The 2 dimensional structural intensity inside the plate is computed from pressure measurements made very close to the surface of the plate. This work is an extension of NAH and relies upon some of the fundamental techniques employed in NAH.

The second of the two companion papers to the paper by Maynard and Williams discussed above is presented by Veronesi and Maynard (1986). This paper concerns the sources of error involved in the computer implementation of NAH. The authors explain some of the difficulties in employing finite length and discrete Fourier transforms. Problems caused by the sampling of a finite region in space, and the consequent infinite transforms becoming finite are discussed. The effects of sampling

in wavenumber space are also discussed and the effect of incorrect sampling upon the image reconstruction. It will be shown later that poor sampling in the wavenumber domain has a very large influence upon a propagated pressure field when attempting to predict the far field from near field data. Veronesi and Maynard indicate that these problems may be overcome by artificially increasing the size of the measurement area by filling out with zeros. This is of course analogous to increasing the sample length in a time history to reduce the frequency interval Δf. However, it will be shown in section 4.4 that there exists an unavoidable link between the propagation distance and the sampling requirements of the original pressure or velocity field.

4.3.1 Summary and conclusions from the literature.

The literature reviewed above discusses different methods to estimate the acoustic field at one spatial region from a knowledge of the field in another region. Despite the apparently wide disparity in the techniques reviewed, all are fundamentally based upon the Kirchoff-Helmholtz integral equation, the Rayleigh integral being a special case of this integral equation. Acoustic Holography offers a way to propagate a measured pressure distribution using a spatial and temporal Fourier Transform of the initial pressure field. It will be shown in the next section that the wavenumber decomposition of the field necessary to use the Fourier Transform technique originates from the Fourier transform of the Helmholtz equation. One of the advantages of using the Fourier Transform is that it offers reductions in computation time when compared to the standard Rayleigh integral.

Whilst there is no doubt that the use of the Fourier transform is quicker than the summations required by the Rayleigh integral, the absolute time difference when using these two techniques must be put into perspective. For small array sizes the time saved by using the FFT approach will be negligible when compared to the Rayleigh integral. Also any previously published work that aims to compare these two techniques must be viewed against a background of increased performance and availability of personal computers and desktop workstations. For example, Stepanishen and Benjamin published their paper in 1982, when high volume, complex mathematical processing would have been undertaken using a mainframe computer. The capital and running costs of using such computers (which were often shared by many users) was expensive. Consequently, there was a real need to develop techniques that limited the time taken to perform computational problems. The Fourier Transform technique described by Stepanishen and Benjamin, offered a

potential time saving. Given the speed of computers in 1982, it is not difficult to imagine the Rayleigh integral being viewed as being slow by comparison to this new technique. However, the processing speed of computers has increased dramatically since 1982, and this has been coupled with an increase in the availability of fast personal computers and desktop workstations, which are much faster than the mainframe computers of 10 years ago.

This being acknowledged, it is valid to question the need to use the spatial Fourier Transform technique as a route to faster computation. These potential advantages may be further questioned when it is remembered that the Rayleigh integral is *exact*. It will be shown that whilst the theoretical derivation of the spatial Fourier Transform technique is similarly exact, errors may arise due to the sampling necessary for digital computation using the FFT algorithm.

4.4 Theoretical principles of the wavenumber transform.

This section describes the principle of decomposing an arbitrary acoustic field into a series of plane wave components, using a wavenumber transform. This method is similar to that employed in NAH and to that suggested by Stepanishen and Benjamin (1982).

Starting with the 3 dimensional Helmholtz equation for a harmonic sound field

$$\left(\nabla^2 + k^2\right) p(x,y,z) = 0. \tag{4.4.1}$$

and applying the 2 dimensional transform

$$F(k_x,k_y) = \int_{-\infty}^{\infty}\int_{-\infty}^{\infty} f(x,y)\, e^{j(k_x x + k_y y)}\, dx\, dy, \tag{4.4.2}$$

to the Helmholtz equation results in

$$\int_{-\infty}^{\infty}\int_{-\infty}^{\infty}\left(\frac{\partial^2}{\partial x^2}+\frac{\partial^2}{\partial y^2}+\frac{\partial^2}{\partial z^2}+k^2\right) p(x,y,z)\, e^{j(k_x x + k_y y)}\, dx\, dy = 0, \tag{4.4.3}$$

where, $p(x,y,z)$ is a 3 dimensional the pressure field at a fixed single frequency k. If the 2D Fourier transform of the pressure field is denoted by, $P(k_x,k_y,z)$, then the

derivatives in the above equation, with respect to x and y are $-k_x^2 P(k_x,k_y,z)$, and $-k_y^2 P(k_x,k_y,z)$ respectively. The derivative with respect to z may be taken outside the two integrals, to give

$$\left(k^2 - k_x{}^2 - k_y{}^2 + \frac{\partial^2}{\partial z^2}\right) P(k_x,k_y,z) = 0. \tag{4.4.4}$$

This has a solution of the form

$$\hat{P}(k_x,k_y,z) = A\, e^{-jk_z z}, \tag{4.4.5}$$

where A is an arbitrary constant determined by the boundary conditions. The solution to the transformed Helmholtz equation, can be seen to have the form of a plane wave propagating in the positive z direction with the wave number k_z.

The wavenumber k_z is given by

$$k_z = \sqrt{k^2 - k_x^2 - k_y^2}\,. \tag{4.4.6}$$

From equation (4.4.6) clearly k_z will be either real or imaginary number, depending on the nature of the term with the square root. For real k_z the following condition must be satisfied

$$k^2 \geq k_x^2 + k_y^2. \tag{4.4.7}$$

If the condition in equation (4.4.7) is not upheld then k_z will be purely imaginary, and this represents an exponentially decaying wave in the positive z direction. Furthermore, to satisfy the Sommerfeld radiation condition, the imaginary part of k_z (if it exists), must always be taken to be negative.

The general solution to the transformed Helmholtz equation given by (4.4.3) can be used to show that if $P(k_x,k_y,z_h)$ is the measured wavenumber transform at $z = z_h$ then the wavenumber transform at any other plane z is simply given by

$$P(k_x,k_y,z) = P(k_x,k_y,z_h) e^{-jk_z(z-z_h)}. \tag{4.4.8}$$

Using the inverse Fourier transform

$$f(x,y)=\frac{1}{(2\pi)^2}\int_{-\infty}^{\infty}\int_{-\infty}^{\infty}F(k_x,k_y)\,e^{-j(k_x x+k_y y)}\,dk_x,dk_y. \tag{4.4.9}$$

The expression in equation (4.4.9) may be used to determine the pressure on another plane at z

$$p(x,y,z)=F^{-1}\left\{P(k_x,k_y,z_h)e^{-jk_z(z-z_h)}\right\}. \tag{4.4.10}$$

The above equation is similar to that presented by Maynard and Williams (1985) discussed previously. In principle, the prediction of the new pressure at z, is an extremely fast and straightforward procedure. However, in practice problems may arise in the implementation of equation (4.4.10). One of the major causes of error in this technique will be shown to arise from incorrect sampling of the exponential term in equation (4.4.10). This exponential term may be referred to as the *propagator function*, and will be denoted as

$$g(k_z,z)=e^{-jk_z(z-z_h)}. \tag{4.4.11}$$

4.5 Practical implementation of the wavenumber transform and some important sources of error in the computation of the far-field pressure.

The preceding mathematical analysis is exact, and by the implementation of equation (4.4.10) it is theoretically possible to calculate a 3 dimensional acoustic field from measurements made in one plane only. However, it will be shown in the sections to follow that serious problems may arise when implementing equation (4.4.10) in practice. The reason for these problems is that the infinite Fourier transform integral in equation (4.4.10) is a continuous function, whereas in practice it will be replaced by its discrete, and finite length, counterpart that is usually calculated numerically using the FFT algorithm. For any general source distribution it is not possible to find an analytical form for the Fourier transform in equation (4.4.10) hence the need for numerical analysis. Indeed, to find an analytical solution for the Fourier transform requires a complete knowledge of the source region. If this knowledge were available, then there would be no need to use this technique at all, as the field could be completely defined based upon this source description.

the wild oscillations in these function when multiplied by the original 2DFFT of the pressure field given as figure 4.39. At a propagation distance corresponding to ten wavelengths and the real and imaginary parts of $g_s(n,k_z,z)$ are clearly under sampled (figure 4.40).

From the above series of figures using a smaller sampling increment in real space, demonstrate that the errors introduced by the FFT technique are increased when the array is optimised for a higher frequency that currently under investigation. In any practical measurement system this places considerable restrictions upon the suitability of the FFT technique to propagate the field from a source at several frequencies using a fixed array.

It is argued that there is little advantage in using the FFT to solve a convolution integral if it is necessary to first calculate a function in real space, then massage that function to avoid errors introduced in the numerical processing in the FFT. Indeed the number of points required to both avoid aliasing of the propagator function and to avoid wraparound soon become prohibitive. The suggestion of Veronesi and Maynard (1986) is to calculate the Green function in space, and take a 2D FFT of this real space function to obtain $\hat{G}_N(k_x,k_y,z)$. As a illustration of the difficulty of even then obtaining correct results, *six* different Green functions are presented which may or may not be appropriate in a given situation. However there is little information to guide the reader as to which Green function would be most appropriate to their application. Veronesi and Maynard (1986) compare results using the six Green functions with the Rayleigh integral, for a plane velocity source. Even with an optimised Green function, errors are still apparent for a propagation distance of 3 wavelengths. In terms of the application of the FFT propagation technique to this thesis, then it is more accurate to stay completely in the spatial domain and use the Rayleigh integral, rather than spend time trying to avoid the signal processing limitations imposed by the discrete FFT algorithm.

4.7 Sound power measurement.

Whilst the propagation of an acoustic field by the 2D FFT is practically difficult to realise, there are some advantages in simply taking a 2D FFT of a sampled source region and not propagating it at all. With care it is possible to overcome some of the above numerical problems. Several useful properties of an acoustic field that can be obtained when the field has been decomposed into a series of plane wave components

using the 2D FFT. Most obviously, one of the main advantages of transforming an arbitrary pressure distribution into a series of plane waves is that the impedance of plane waves is known, i.e. ρc. Therefore it is possible to convert from pressure values to those of velocity and vice versa[3].

In the real space domain, a harmonic pressure and velocity field are related by the Euler equation

$$\nabla p(x,y,z) = -j\omega\rho_0\, u(x,y,z). \tag{4.7.1}$$

If the pressure and velocity fields are now replaced by their 2D Fourier transform, then equation (4.7.2) becomes

$$\nabla P(k_x,k_y,z_h) = -j\omega\rho_0\, U(k_x,k_y,z_h). \tag{4.7.2}$$

Since the pressure field is now constructed from plane wave components, each of which has an exponential space dependence of the form $\exp(-jk_x x)$, then the real space derivatives in equation (4.7.2) may be replaced by $-jk_x$, $-jk_y$ and $-jk_z$ to give

$$U_\eta(k_x,k_y,z_h) = P(k_x,k_y,z_h)\frac{k_\eta}{\rho_0 ck}. \tag{4.7.3}$$

where U_η, $\eta = x,\ y,\ z$, denotes the three components of the particle velocity. The multiplier $k_\eta/\rho_0 ck$ has the from of a wavenumber response function and dimensions of admittance. The reciprocal of this term has dimensions of impedance, and may be written

$$Z = \frac{\rho_0 ck}{k_\eta} \tag{4.7.4}$$

As an example, consider a plane of pressure values at $z = 0$, which represent the end of a duct. This field may be decomposed into a series of plane wave components using the 2D FFT. This results in the field being a function of wavenumber variables, which are related by the equation,

$$k_z = \sqrt{k^2 - k_x^2 - k_y^2} \quad for \quad k^2 > k_x^2 + k_y^2, \tag{4.7.5}$$

---

[3]Converting from velocity to pressure values can present problems in certain circumstances - see Lahti, 1989.

$$k_z = -j\sqrt{k_x^2 + k_y^2 - k^2} \quad for \quad k^2 < k_x^2 + k_y^2. \tag{4.7.6}$$

It has been seen that since the field is now a series of plane waves, it is possible to express the ratio of the pressure and acoustic particle velocity (the impedance) easily, since this is known for plane waves to be equal to ρc of the medium. If k_z is real then propagation to the far field occurs and the real radiation impedance may be defined as

$$Z = \frac{\rho c k}{k_z} = \frac{\rho c k}{\sqrt{k^2 - k_x^2 - k_y^2}}, \tag{4.7.7}$$

$$Z = \frac{\rho c k}{k_z} = \frac{\rho c k}{\sqrt{k^2 - k_x^2 - k_y^2}}, \tag{4.7.8}$$

or

$$Z = \rho c \left[1 - \left(\frac{k_x^2 + k_y^2}{k^2} \right) \right]^{-\frac{1}{2}}. \tag{4.7.9}$$

The jump from real to imaginary k_z at the point $k^2 = k_x^2 + k_y^2$ has a major effect upon the radiation, and therefore the circle $k^2 = k_x^2 + k_y^2$ in the k_x, k_y plane has been termed the radiation circle. For all values of k_x and k_y outside this circle, then this represents an evanescent decaying plane wave that does not propagate into the far field or carry any net acoustic power. Values of $k_x$and k_y within the radiation circle represent propagating plane waves. It is possible to translate from pressure to velocity using the wavenumber domain expression

$$\hat{P}(k_x, k_y) = \hat{U}_z(k_x, k_y) Z, \tag{4.7.10}$$

where $\hat{U}_z$ is the transform of the particle velocity in the z direction. Using equation (4.7.8) this becomes

$$\hat{P}(k_x, k_y) = \hat{U}_z(k_x, k_y) \frac{\rho c k}{k_z}. \tag{4.7.11}$$

The intensity follows and is simply given by

$$I = \hat{P}(k_x, k_y) \hat{U}_z^*(k_x, k_y). \tag{4.7.12}$$

The sound power may be calculated using the following expression (Lahti 1989)

$$\Pi = \iint_{k_x,k_y<k} \mathrm{Re}\left[\hat{P}(k_x,k_y)\hat{U}_z^*(k_x,k_y)\right] dk_x\, dk_y. \tag{4.7.13}$$

Real values for the integrand are obtained if $k^2 > k_x^2 + k_y^2$, and the Re[ ] operation may be dropped if integrated within the radiation circle. Using the relationship given in equation (4.7.11) it is possible to express the sound power in terms of pressure or particle velocity only. For the case of pressure measurements, the sound power is given by

$$\Pi = \iint_{k_x,k_y<k} \mathrm{Re}\left[\hat{P}(k_x,k_y)\hat{P}^*(k_x,k_y)\frac{k_z}{\rho ck}\right] dk_x\, dk_y \tag{4.7.14}$$

$$\Pi = \iint_{k_x,k_y<k} \left|\hat{P}(k_x,k_y)\right|^2 \frac{k_z}{\rho ck} dk_x\, dk_y \tag{4.7.15}$$

As a check on the technique, a field was simulated on computer within a hard walled and pressure release lined duct, and this was sampled using a very large (512 by 512) array of points at the duct exit. The difference between the power when using the hard wall and pressure release lining was within ± 1dB of the results obtained using the method in Chapter 3, where the sound power was calculated using the equation

$$W = \tfrac{1}{2}\int_S \mathrm{Re}(p\,u^*)\, dS \tag{4.7.16}$$

However, with less points than 512 by 512 noticeable errors were observed. Figure 4.41 shows difference between the sound power calculated with the 'exact' expression given by equation (4.7.16), and the sound power calculated using the 2D FFT method in equation (4.7.15). It can be seen that for a fixed number of points at the maximum frequency of k, then this results in less points being available for the calculation of the sound power at lower frequencies. As the frequency is lowered, then this has the effect of reducing the diameter of the radiation circle in the wavenumber domain. Since the sound power is only calculated from points in the wavenumber domain within the radiation circle, then there will be less points as the frequency of interest is reduced.

It can be seen from figure 4.41 that the 2D FFT introduces an error the calculation of the sound power, and this error increases with reduced frequency. A possible

explanation for this is in the nature of the finite sampling in the wavenumber domain. For discrete sampled data the continuous variables k_x and k_y are only calculated at discrete points. Thus the continuous domain is represented by a finite number of small 'patches'. For equal number of sample points in the k_x and k_y directions, then these patches will be small squares, with the centre of the patch being at a k_x, k_y co-ordinate in the wavenumber domain. Therefore the continuous wavenumber domain is averaged over the area of the patch. In the calculation of the sound power, only those patches inside the radiation circle are used in the calculation, but the is a difficulty in ignoring those patches which lie on the radiation circle. Patches whose centres lie just outside the radiation circle contain a contribution from the wavenumber domain inside the radiation circle, but this is ignored in the calculation of the sound power. Similarly patches whose centres lie just inside the radiation circle, contain a contribution from outside the radiation circle, and this is included in the calculation of the sound power. The problem reduces to a simple geometric one; that of representing a circle - in this case the radiation circle - by a number of small squares. The bigger the squares relative to the size of the circle, the less like a circle the resulting shape is.

It is worth noting that serious instability occurs when using the FFT to calculate the radiated pressure from a known velocity distribution. From equation (4.7.8) then

$$\tilde{P}(k_x,k_y) = \tilde{U}_z(k_x,k_y)\frac{\rho ck}{k_z}, \tag{4.7.17}$$

and if k_x and k_y lie on the radiation circle, then k_z is zero. This is a major problem and was completely overlooked in all the fundamental papers on NAH including what were considered to be the pioneering work by Stepanishen and Benjamin (1982), and Williams and Maynard, (1982). The latter paper was a means of replacing the Rayleigh integral with the FFT for a vibrating plate of known velocity distribution. If the original field is a pressure field, then this is not a problem, but since these two papers used the FFT to calculate the propagation from vibrating plates, it is surprising that they did not mention of the problem of the instability caused by the pole on the radiation circle. There is no way to ignore the pole on the radiation circle and it this severely limits the ability of the FFT to calculate the pressure field from a vibrating plate. It was only later that Veronesi and Maynard (1986), attempted to deal with the problem. Their suggestion was to apply a smoothing function that averages out the values of k_z either side of the radiation circle in the wavenumber domain. This prevents the value of k_z from become infinite, but has no physical basis. Fortunately, when propagating into the far field it is possible to ignore all values of $k_x$and k_y which lie outside the radiation circle. But for values of $k_x$and k_y near to k, then there

will always be a sampling problem due to the pole on the radiation circle causing k_z to become very large as k_x and k_y approach k.

For pressure to velocity conversion, rearrangement of equation (4.7.15) gives

$$\tilde{U}_z(k_x,k_y)=\tilde{P}(k_x,k_y)\frac{k_z}{\rho ck}, \tag{4.7.18}$$

and is well behaved as long as $k>0$. In the context of this thesis, measurements of pressure have been made, and not particle velocity. For this reason it possible to ignore the effect of the pole on the radiation circle in equation (4.7.16), and calculate sound power in terms of pressure only, as given by equation (4.7.12).

4.8 Conclusions

In this chapter techniques to calculate the field at one location from a knowledge of the acoustic field at another location have been discussed. Since it is not usually possible to solve the Kirchoff-Helmholtz equation to find the radiation from an acoustic source, then approximations to this have been developed. For a planar source, it has been shown that the Kirchoff-Helmholtz equation may be simplified to a well-known form - the Rayleigh integral. This may be used satisfactorily where either the normal velocity or pressure[4] is known over a finite sized plane, and is zero outside that region. it is often the case that these requirements are not met, or else the problem is not concerned with planar geometries.

A literature review has shown that there exist several methods to obtain the pressure at another region, given some knowledge of the field at another region. In particular, it has been shown that the propagation of a plane of pressure is theoretically possible using the 2D Fourier Transform. This technique arises from the 3 dimensional Fourier transform of the Helmholtz equation and is exact when the pressure is a continuous function of space. This offers a potential time saving over the Rayleigh integral, as the number of calculations is required to predict the propagated field is reduced. Unfortunately, a continuous analytical expression for the pressure variation over a plane in space is not normally available. Therefore it usual to sample the pressure at discrete intervals. However, in this chapter it has been shown that many practical problems arise when using the discrete form of the Fourier transform. The previous

[4] For a plane of pressure requires the use of the second form of the Rayleigh Integral.

exact expressions referred to previously are derived in continuous space, are now replaced by their discrete space equivalents. These latter expressions are not exact.

Errors arise due to incorrect sampling of the pressure field or propagator function, and the periodic nature of the DFT used to propagate the original pressure plane. It has been shown that whilst the original pressure field may have been sampled adequately, then it does not immediately follow that the propagated field will be free from error. It has been established for example, that the correct number of samples for a given frequency of excitation of the source, is determined by the spacing of k_z and the propagating distance z. This dependence upon the propagation distance z, is entirely different from the Rayleigh integral. In the latter, the distance from the original velocity field to the observer location does not influence the sampling requirements of that velocity distribution. Also it has been shown that a much more serious problem is wraparound error. This can occur even in a well-sampled pressure field, and to avoid this requires many more data points to be added to the original array. Unfortunately, the inclusion of these extra points means that it is often simpler and quicker to use the Rayleigh integral, which is exact, and does not suffer from these problems. Finally, it has been shown that if a 2 dimensional Fourier transform of the field is successfully made, then useful information about the field may be found without propagating to another plane. Using the 2 D FFT, the field may be decomposed into a sum of plane wave components. This gives simple expressions for the sound power and the source directivity. However, great care must be taken to ensure the are sufficient samples in the wavenumber domain to enable a calculation of the directivity or sound power to be made successfully.

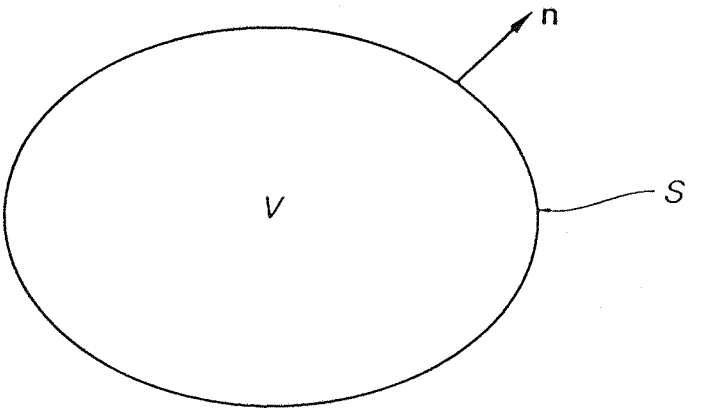

Figure 4.1 - The volume V in a medium and its bounding surface S.

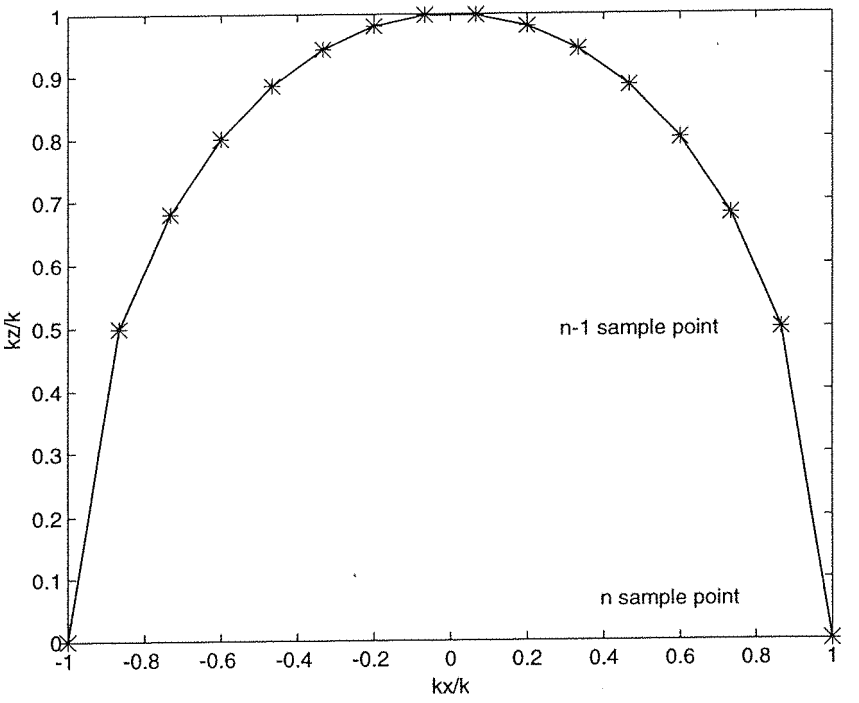

Figure 4.2a - Real k_z vs. k_x for 16 samples. ($\delta x = .5$m, $\lambda = 1$m).

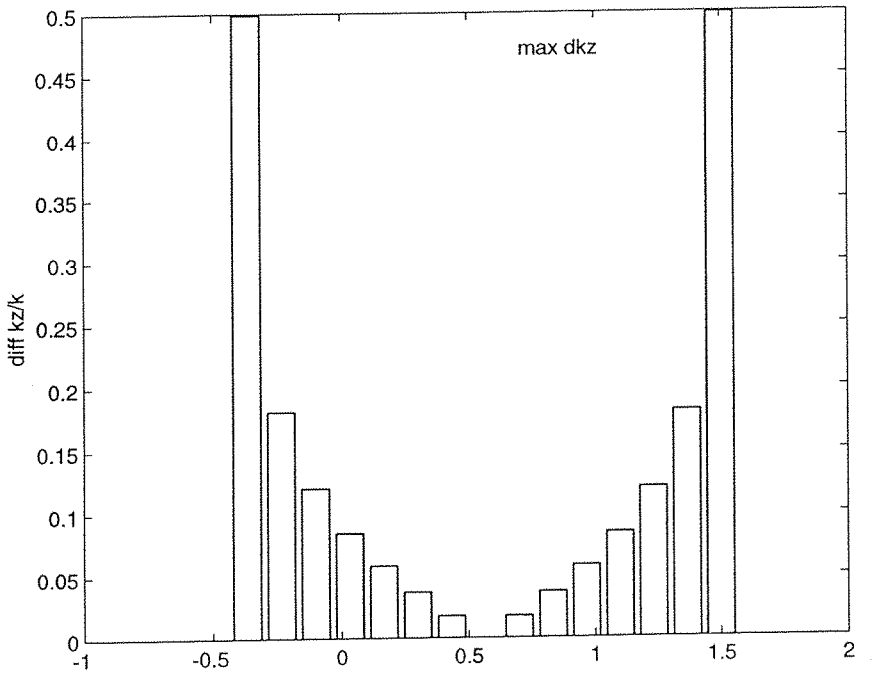

Figure 4.2b - Non-uniform spacing in real k_z vs. k_x for 16 samples. ($\delta x = .5\text{m}$, $\lambda = 1\text{m}$).

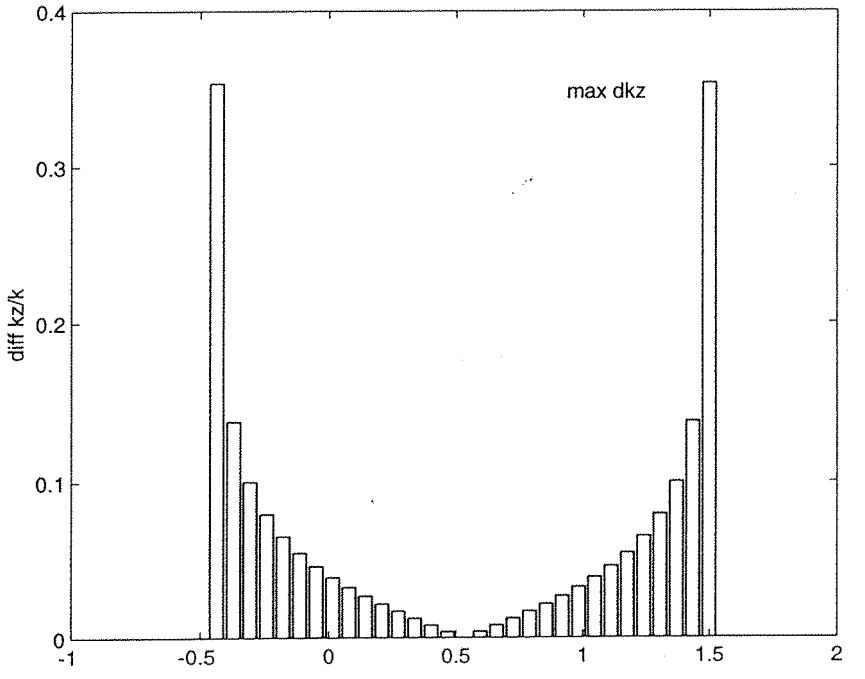

Figure 4.3 - Non-uniform spacing in real k_z vs. k_x for 32 samples. ($\delta x = .5\text{m}$, $\lambda = 1\text{m}$).

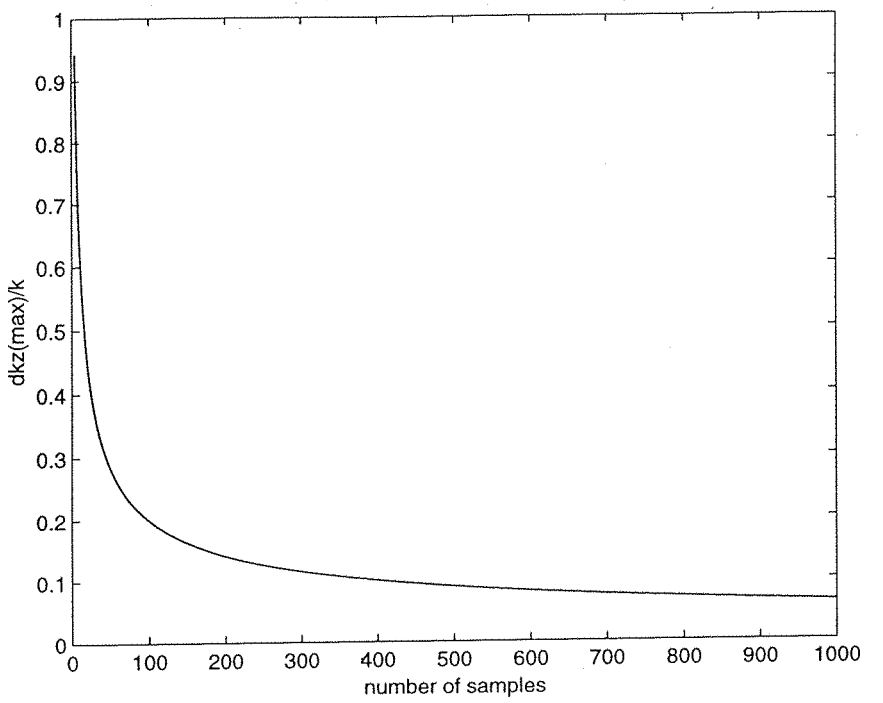

Figure 4.4 - Values of real $\delta k_{z(\max)}/k$ as a function of the number of samples, N.

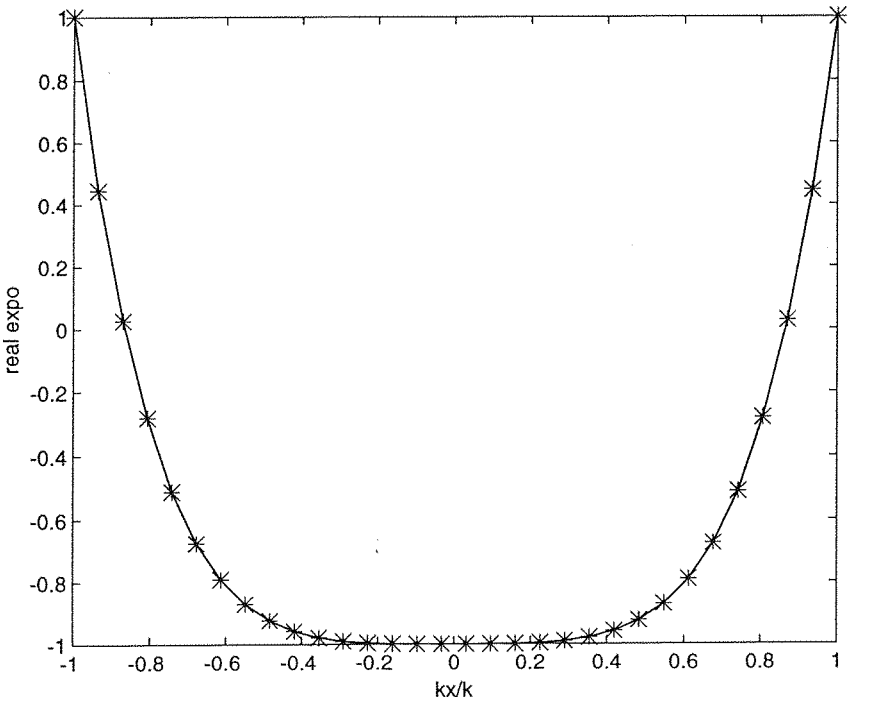

Figure 4.5 - Real part of the propagator function $g_s(n,k_z,z)=e^{-jn\delta k_z(z-z_h)}$ vs. k_x/k (N=32, δx =.5m, $\lambda=1$m, z=0.5m, $\delta k_x=0.4054$).

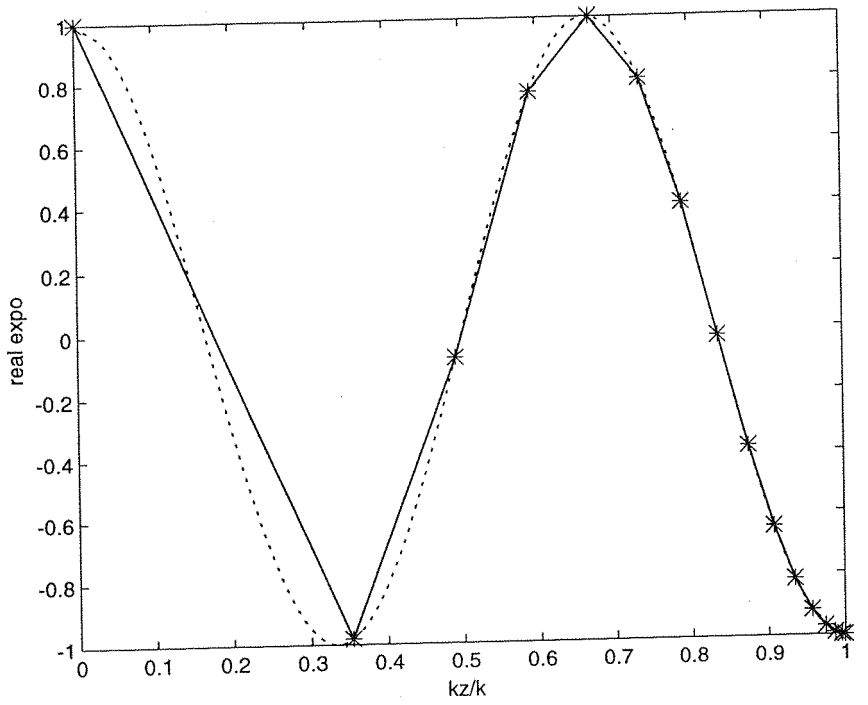

Figure 4.6a - Real propagator function, $\mathrm{Re}\{g_s(n,k_z,z)\}$ vs. k_z/k

(N=32, δx =.5m, $\lambda = 1$m, z=1.5m, $\delta k_x = 0.4054$).

Solid line indicates the calculated values of $\mathrm{Re}\{g_s(n,k_z,z)\}$, and the dashed line shows the theoretical exact values obtained from a continuous version of $\mathrm{Re}\{g_s(n,k_z,z)\}$.

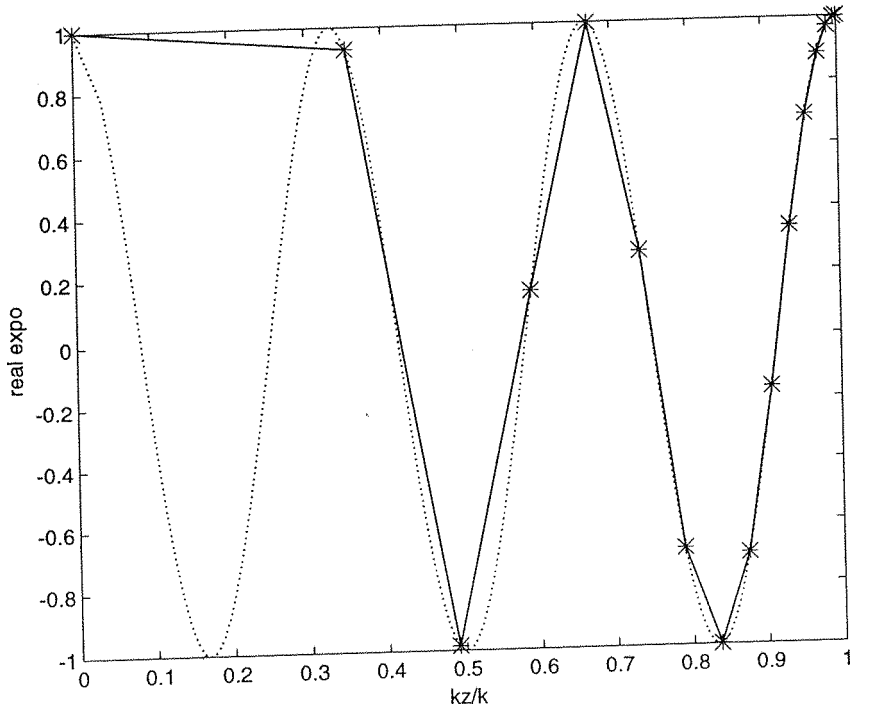

Figure 4.6b - Real propagator function, $\mathrm{Re}\{g_s(n,k_z,z)\}$ vs. k_z/k

(N=32, δx =.5m, $\lambda = 1$m, z=3.0m, $\delta k_x = 0.4054$).

Solid line indicates the calculated values of $\mathrm{Re}\{g_s(n,k_z,z)\}$, and the dashed line shows the theoretical exact values obtained from a continuous version of $\mathrm{Re}\{g_s(n,k_z,z)\}$.

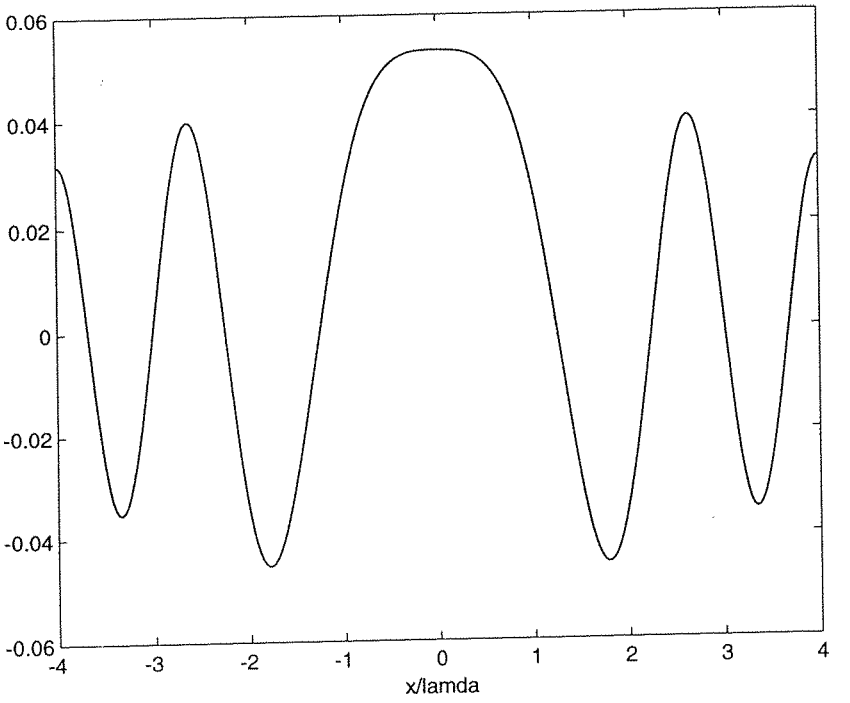

Figure 4.7 - Real spaced derived propagator function, $G_N(x,y,z)=\frac{je^{jkR}}{2\pi R}$ vs. k_x/k (N=32, δx =.5m, $\lambda=1$m, z=3.0m, $\delta k_x=0.4054$).

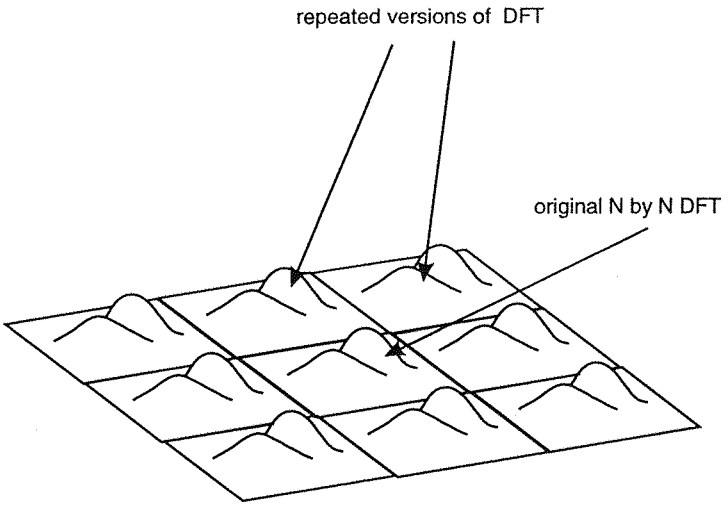

Figure 4.8a - Repeated versions of the pressure array due to the finite length DFT.

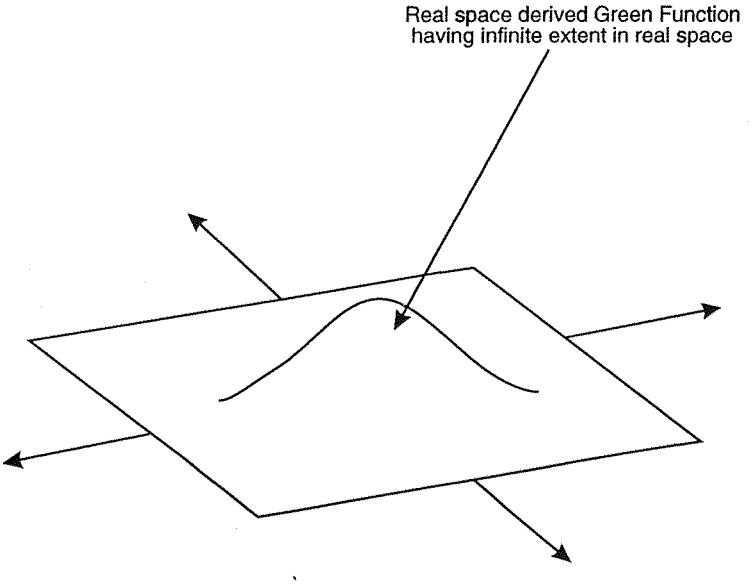

Figure 4.8b - The propagator function which is convolved in real space with figure 4.8a.

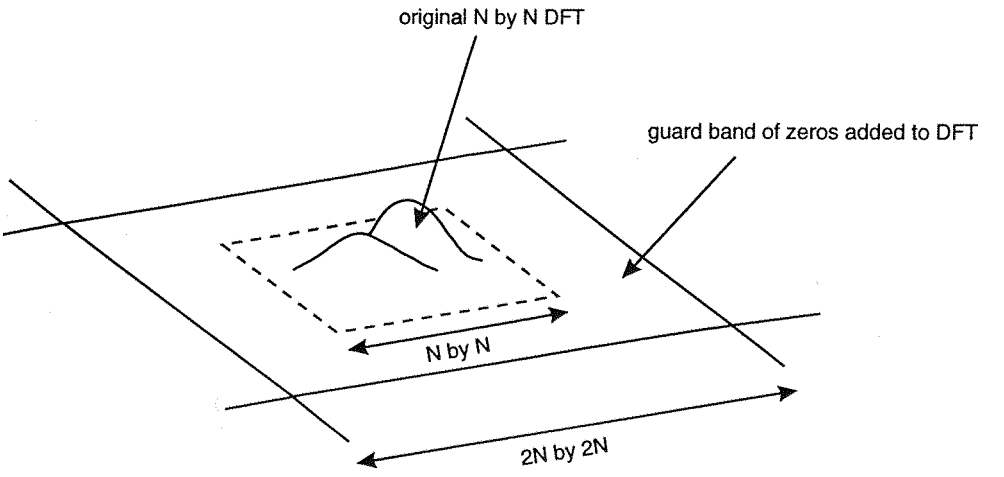

Figure 4.9a - The original pressure array with a guard band of zeros added to help avoid wraparound error.

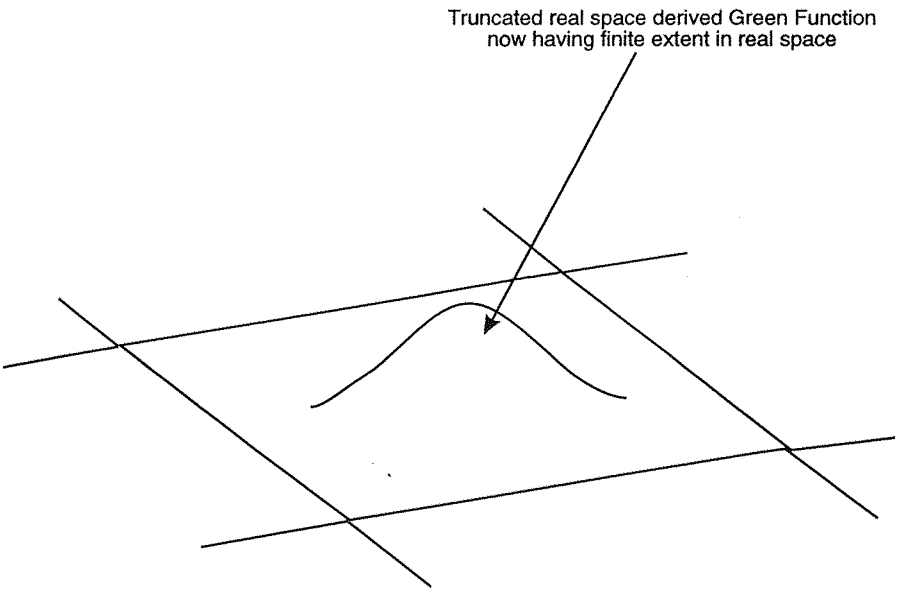

Figure 4.9b- The truncated real spaced derived Green function.

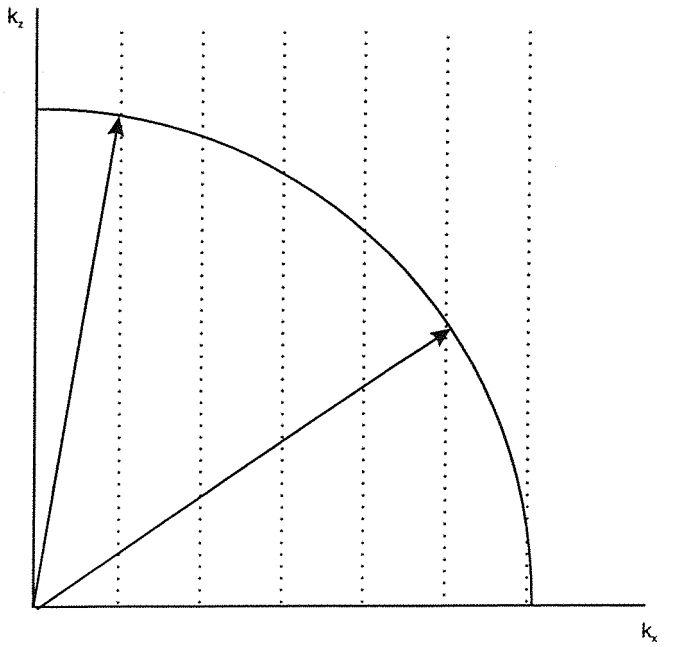

Figure 4.10a - The angle of resolution in the wavenumber domain (k-space) for 32 samples, $k_x = k$.

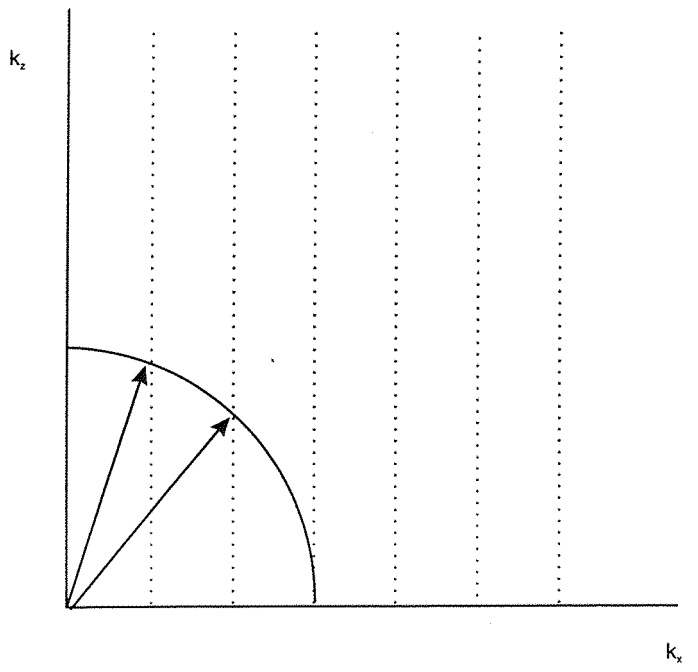

Figure 4.10b - The angle of resolution in the wavenumber domain (k-space) for 32 samples, $k_x = 0.5k$

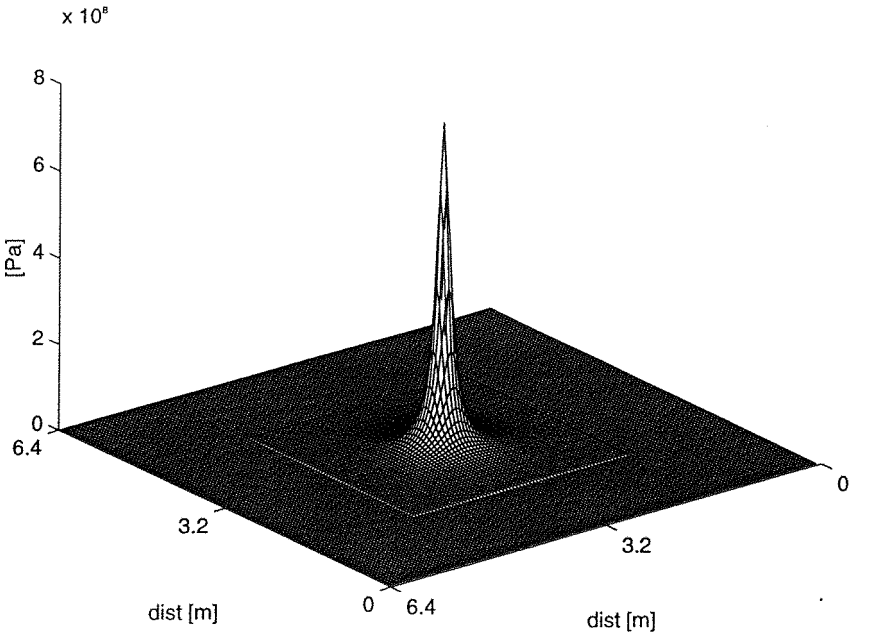

Figure 4.11 - A theoretical array of pressure values from monopole source.
Original array size is 64×64.
A guard band of zeros is added to increase the array size to 128×128.
(N=128×128, $\delta x = 0.05$m, $\lambda = 0.1$m, $h = 0.1$m, z=0.0m).

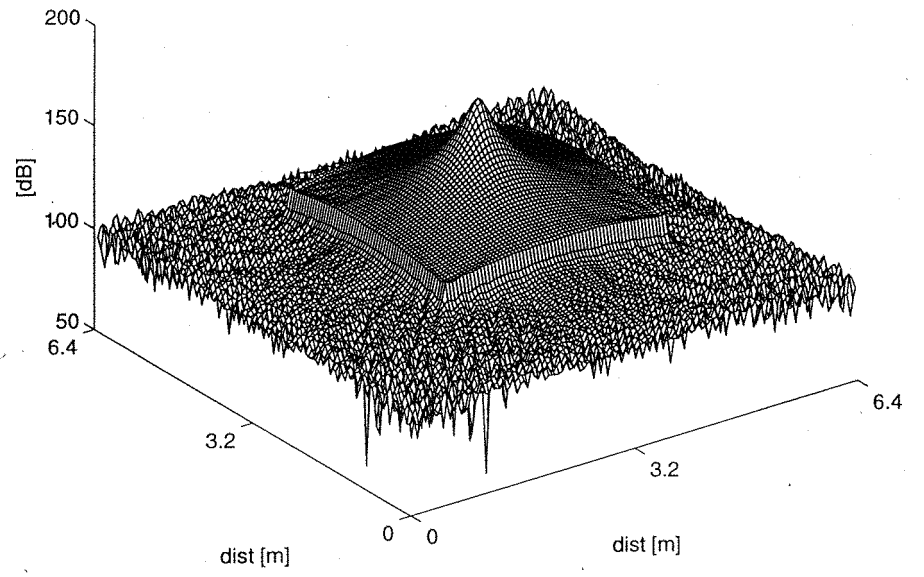

Figure 4.12 - The pressure data in figure 4.11 propagated a distance of 0.01m using the 2D FFT.
(N=128×128, $\delta x = 0.05$m, $\lambda = 0.1$m, $h = 0.11$m, z=0.01m).

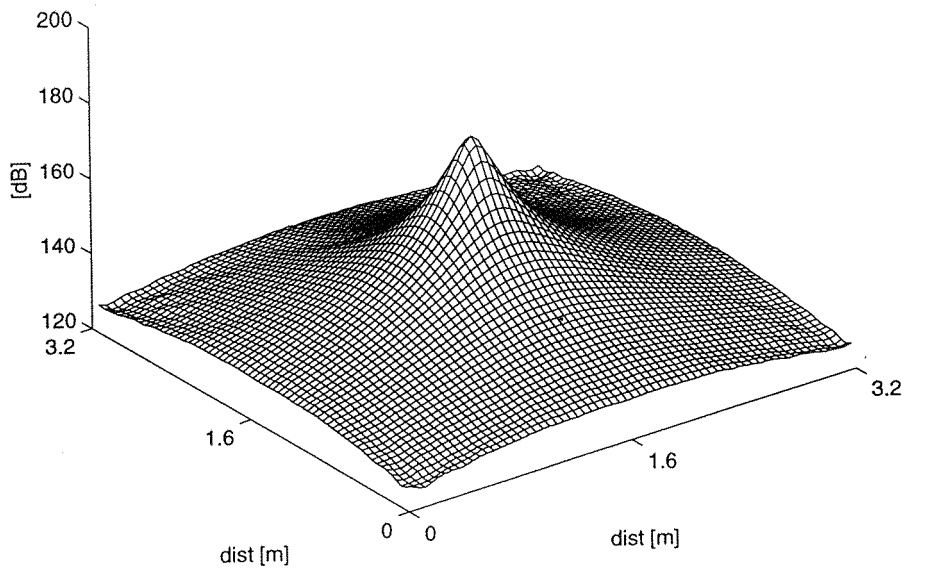

Figure 4.13 - The centre 64×64 points of figure 4.12.
(N=64×64, $\delta x = 0.05$m, $\lambda = 0.1$m, $h = 0.11$m, z=0.01m).

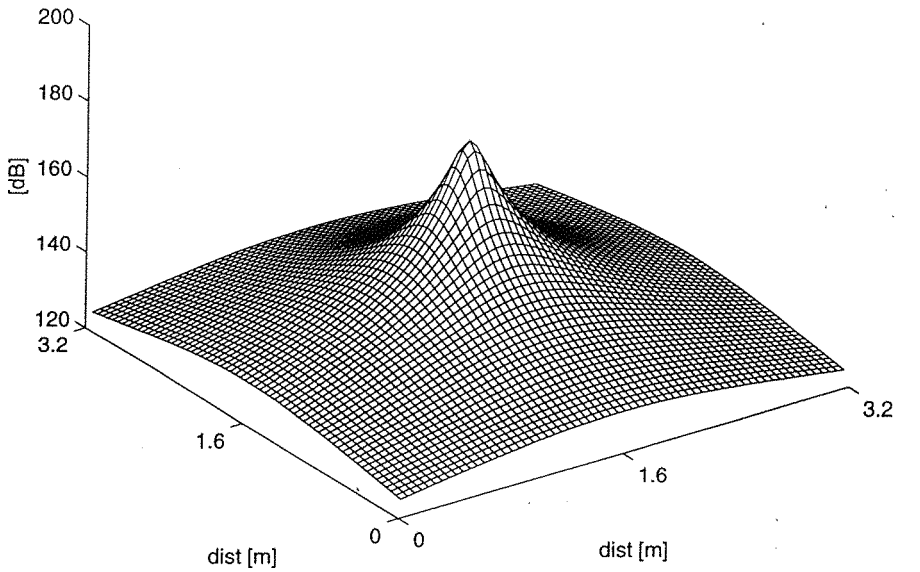

Figure 4.14 - The theoretical correct propagated field from monopole source
(N=128×128, $\delta x = 0.05$m, $\lambda = 0.1$m, $h = 0.11$m, z=0.01m).

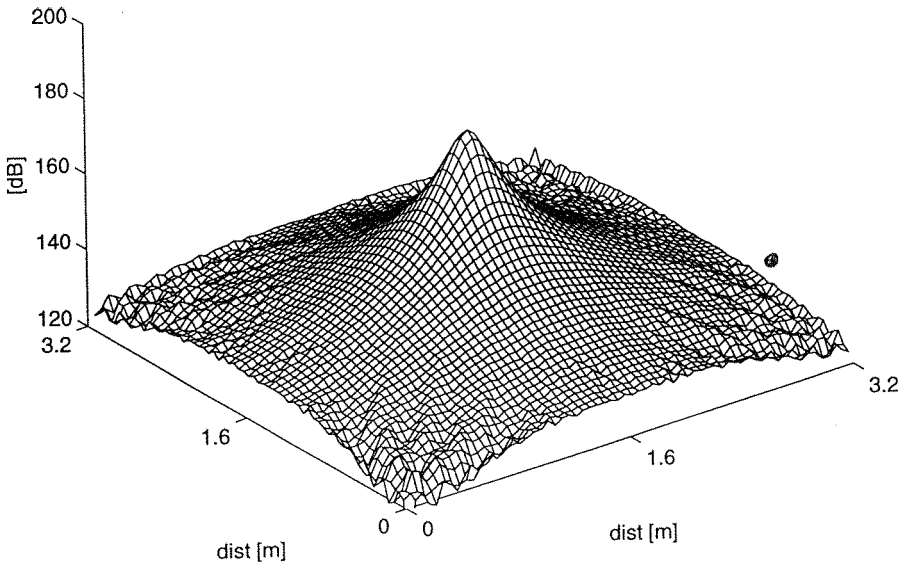

Figure 4.15 - The centre 64×64 points of the propagated array in figure 4.11 without adding the guard band of zeros.
(N=64×64, $\delta x = 0.05$m, $\lambda = 0.1$m, $h = 0.11$m, z=0.01m).

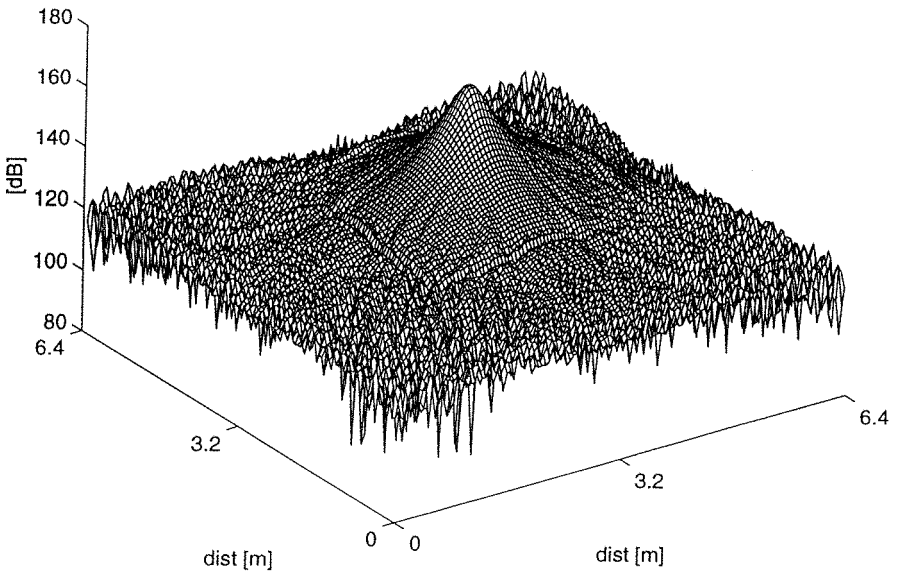

Figure 4.16 - The pressure data in figure 4.11 propagated a distance of 0.1m using the 2D FFT.
(N=128×128, $\delta x = 0.05$m,-$\lambda = 0.1$m, $h = 0.2$m, z=0.1m).

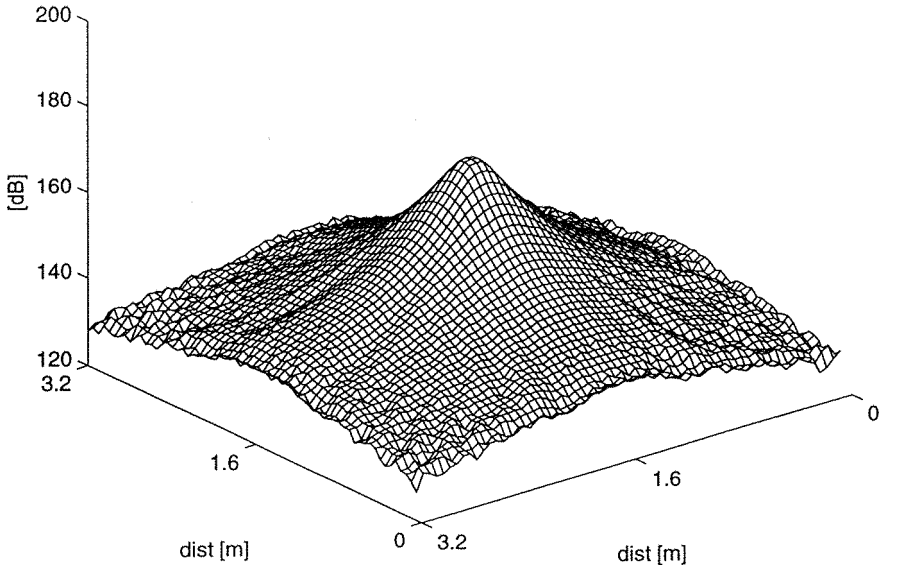

Figure 4.17 - The centre 64×64 points of figure 4.16.
(N=64×64, $\delta x = 0.05$m, $\lambda = 0.1$m, $h = 0.2$m, z=0.1m).

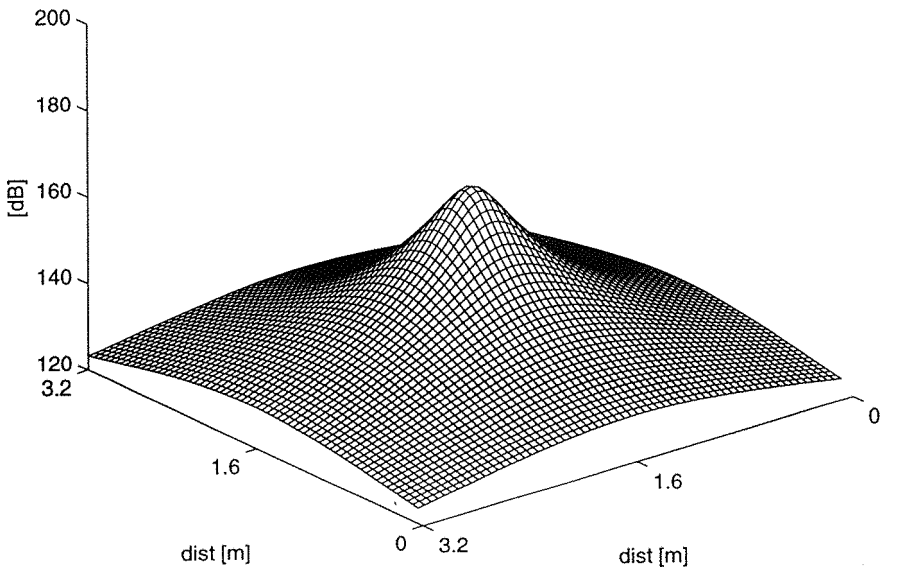

Figure 4.18 - The theoretical correct propagated field from monopole source
(N=64×64, $\delta x = 0.05$m, $\lambda = 0.1$m, $h = 0.2$m, z=0.1m).

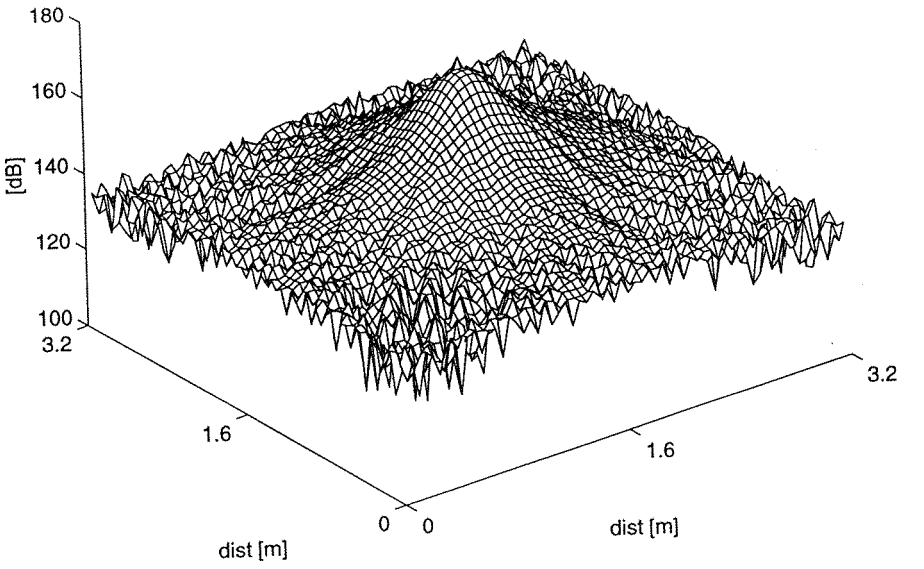

Figure 4.19 - The centre 64×64 points of the propagated array in figure 4.11 without adding the guard band of zeros.
(N=64×64, $\delta x = 0.05$m, $\lambda = 0.1$m, $h = 0.2$m, z=0.1m).

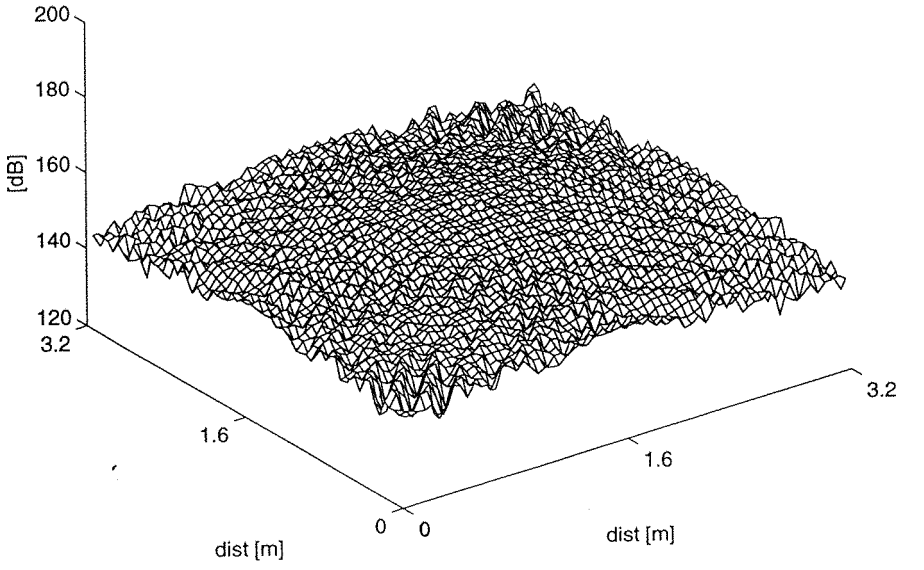

Figure 4.20 - The centre 64×64 points of the pressure data in figure 4.11 propagated a distance of 1m using the 2D FFT.
(N=64×64, $\delta x = 0.05$m, $\lambda = 0.1$m, $h = 1.1$m, z=1.0m).

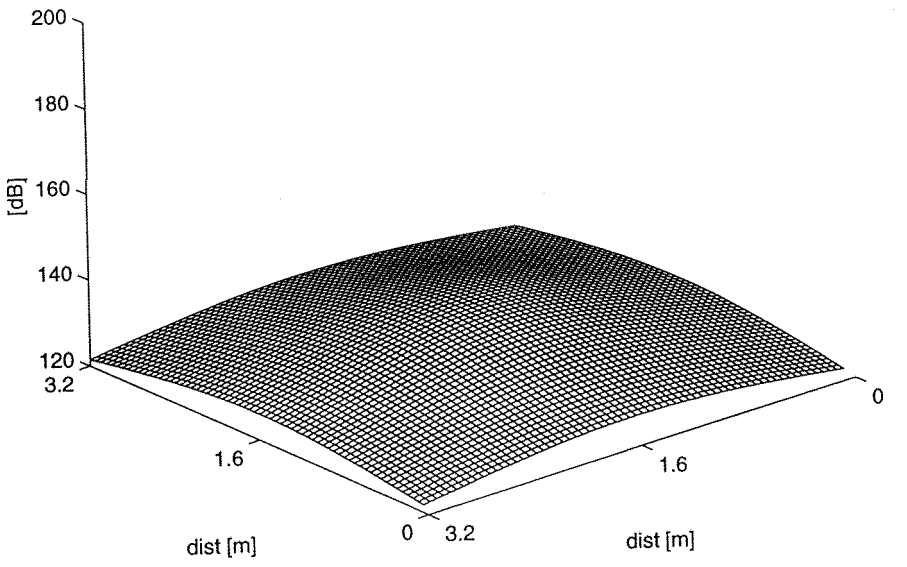

Figure 4.21 - The theoretical correct propagated field from monopole source
(N=64×64, δx=0.05m, λ=0.1m, h=1.1m, z=1.0m).

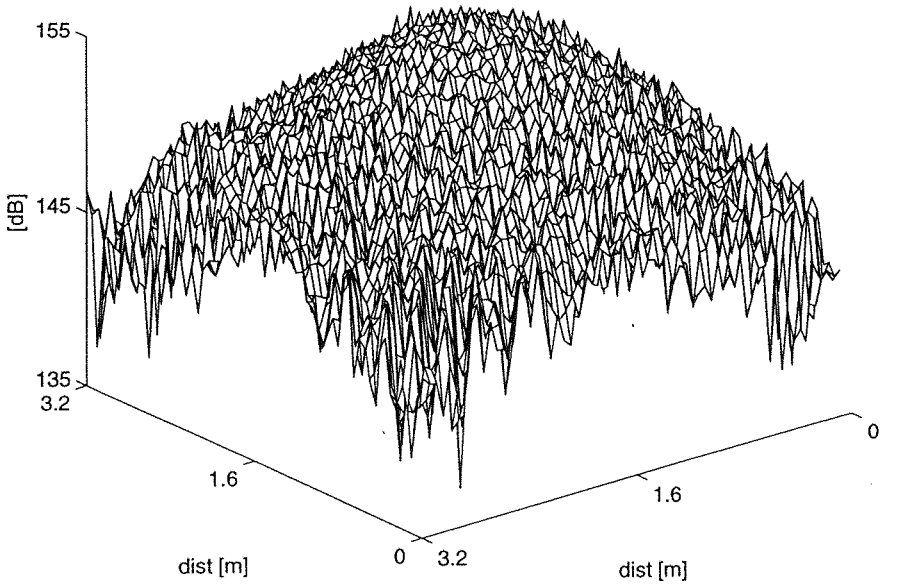

Figure 4.22 - Same as figure 4.20 but vertical axis changed to show errors in the propagated field.
(N=64×64, δx=0.05m, λ=0.1m, h=1.1m, z=1.0m).

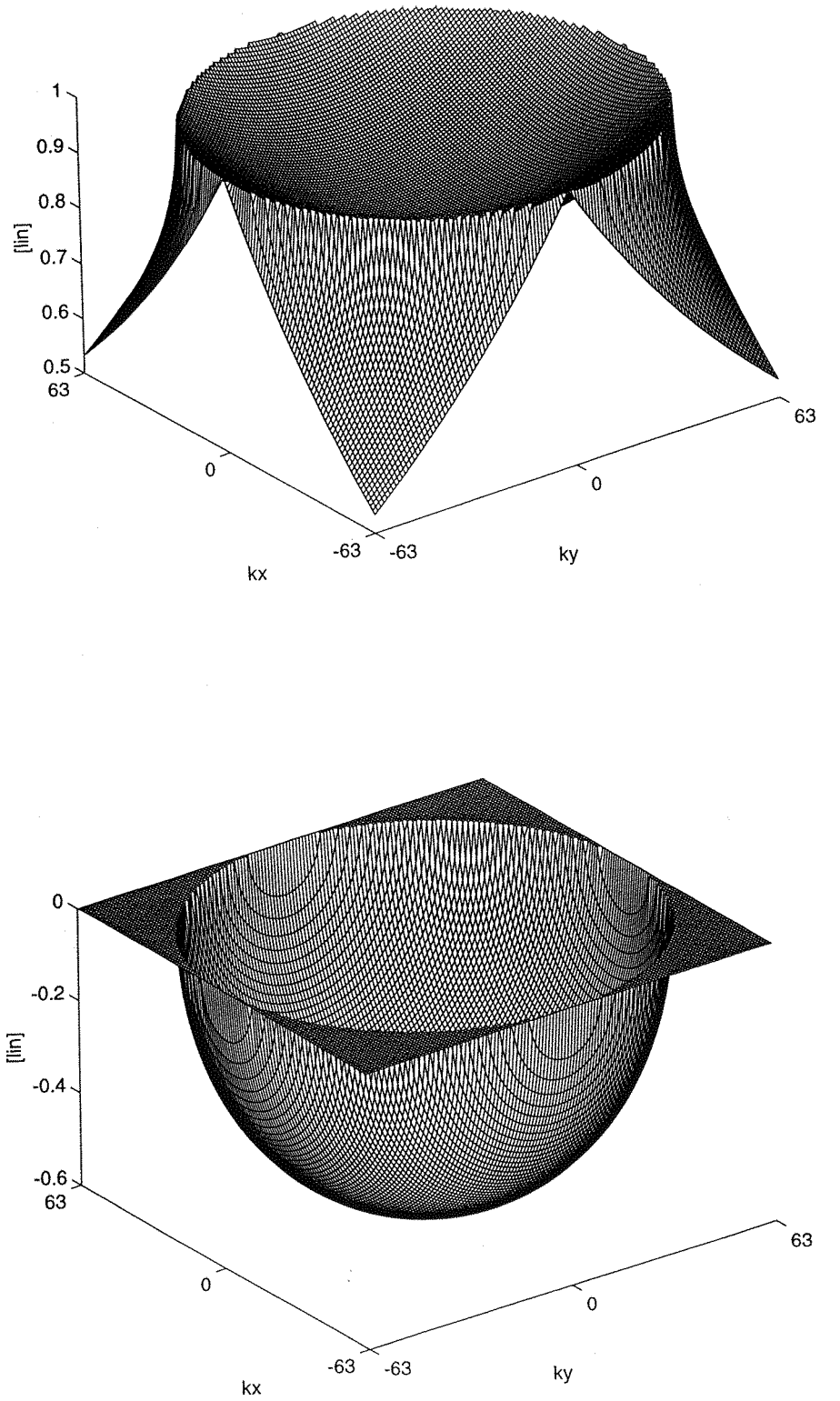

Figure 4.23a - Real and imaginary parts of the wavenumber space propagator function for a propagation distance of 0.01m.

A guard band of 64×64 zeros has been added to the original pressure data.

(N=64×64, $\delta x = 0.05$m, $\lambda = 0.1$m, z=0.01m).

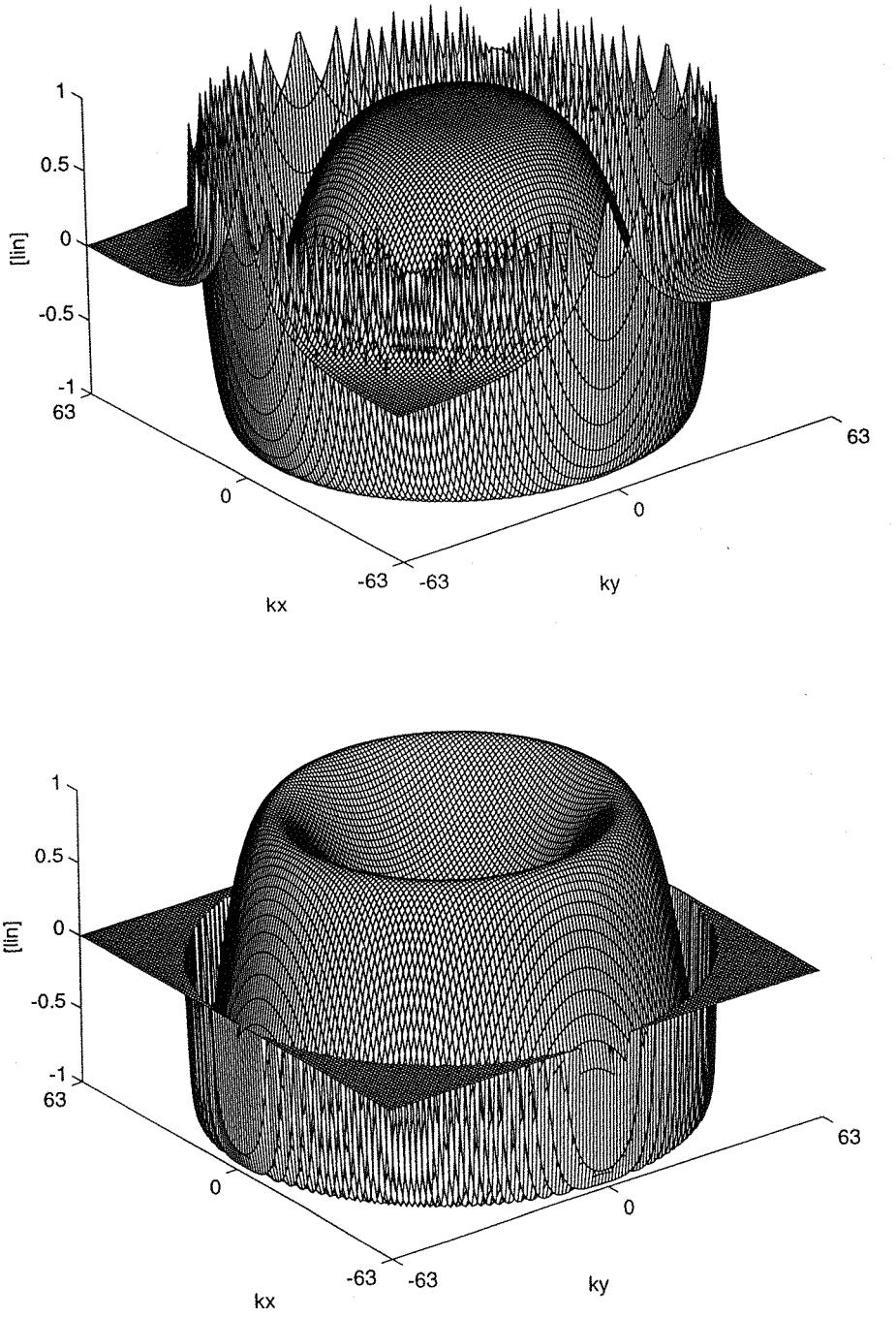

Figure 4.23b - Real and imaginary parts of the wavenumber space propagator function for a propagation distance of 0.1m.

A guard band of 64×64 zeros has been added to the original pressure data.

(N=64×64, $\delta x = 0.05$m, $\lambda = 0.1$m, z=0.1m).

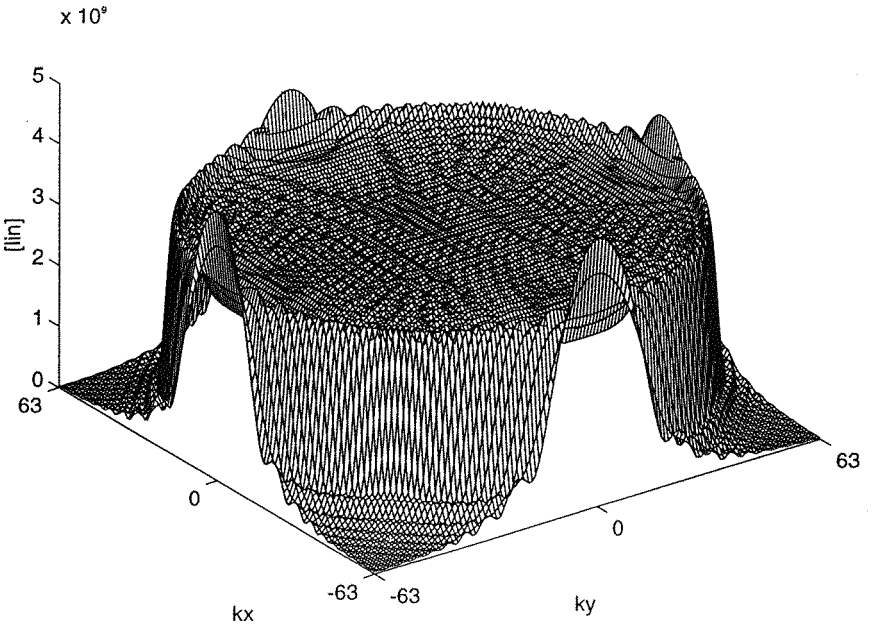

Figure 4.24 - The absolute value of the 2D FFT of the pressure array in figure 4.11. A guard band of 64×64 zeros has been added to the original pressure data. (N=64×64, $\delta x = 0.05$m, $\lambda = 0.1$m, $\delta k_x = \delta k_y = 0.9895$).

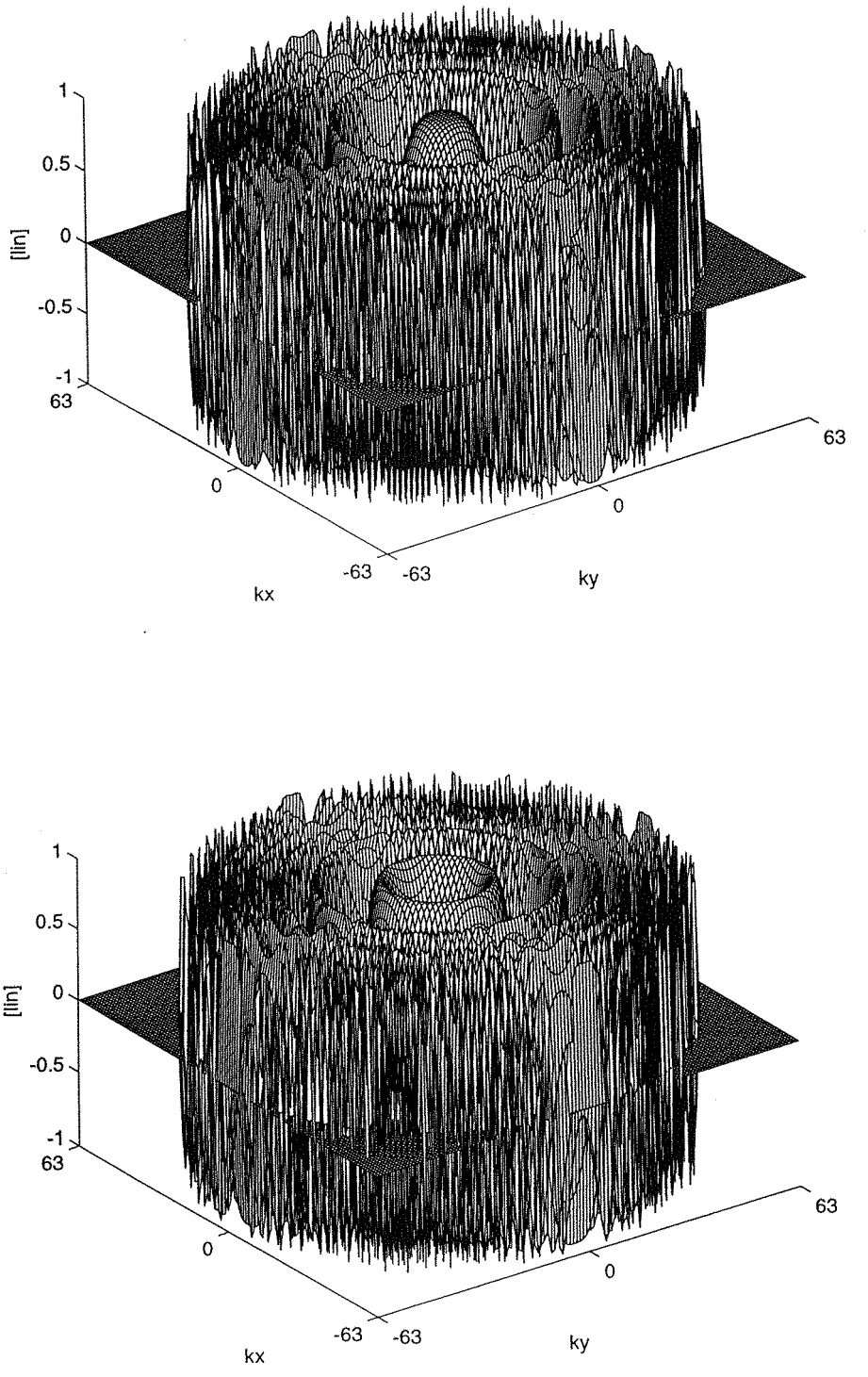

Figure 4.25 - Real and imaginary parts of the wavenumber space propagator function for a propagation distance of 1.0m.

A guard band of 64×64 zeros has been added to the original pressure data.

(N=64×64, $\delta x = 0.05$m, $\lambda = 0.1$m, z=1.0m, $\delta k_x = \delta k_y = 0.9895$).

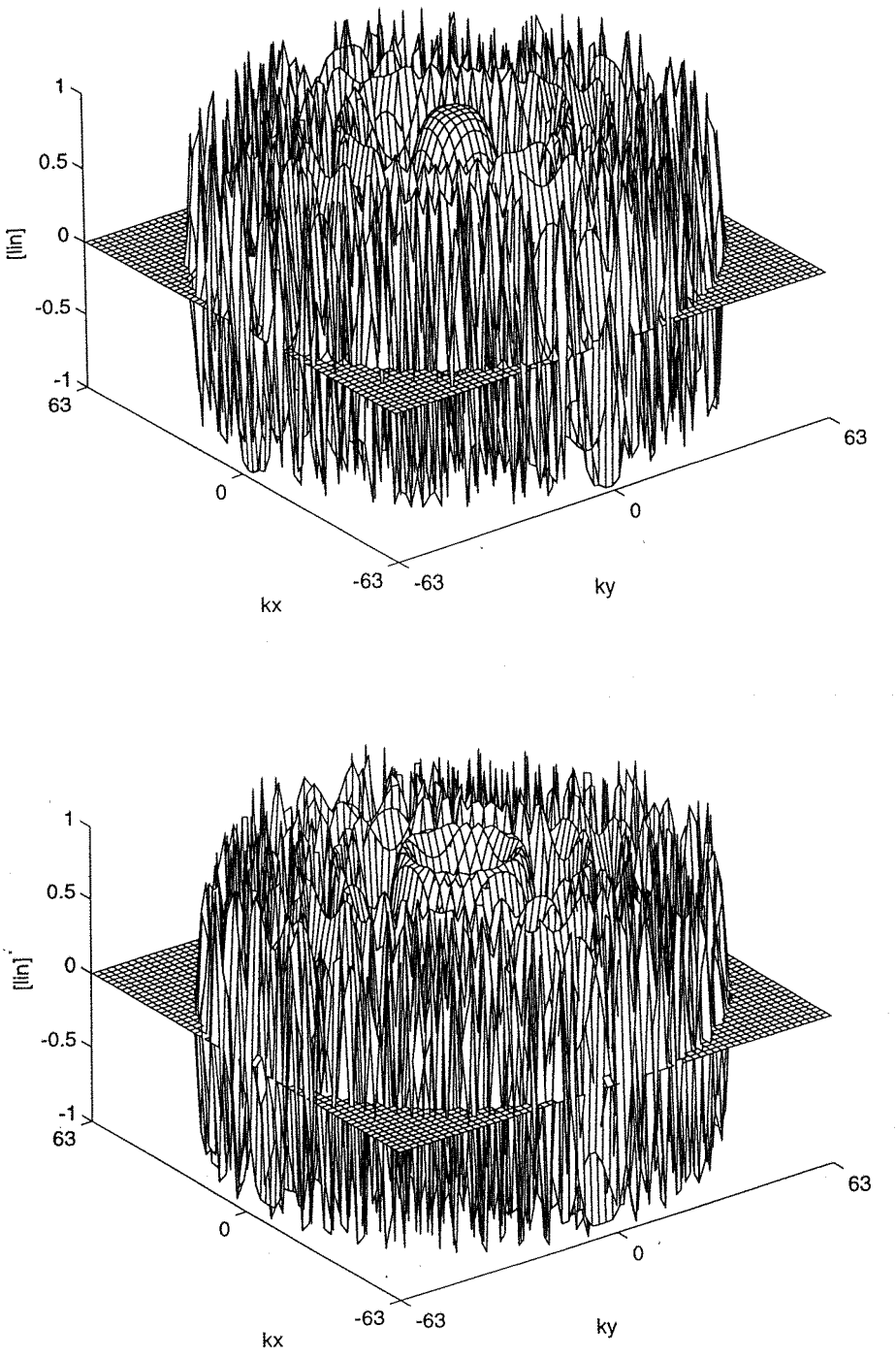

Figure 4.26 - Real and imaginary parts of the wavenumber space propagator function for a propagation distance of 1.0m.

No guard band of zeros has been added to the original pressure data.

(N=64×64, $\delta x = 0.05$m, $\lambda = 0.1$m, z=1.0m, $\delta k_x = \delta k_y = 1.995$).

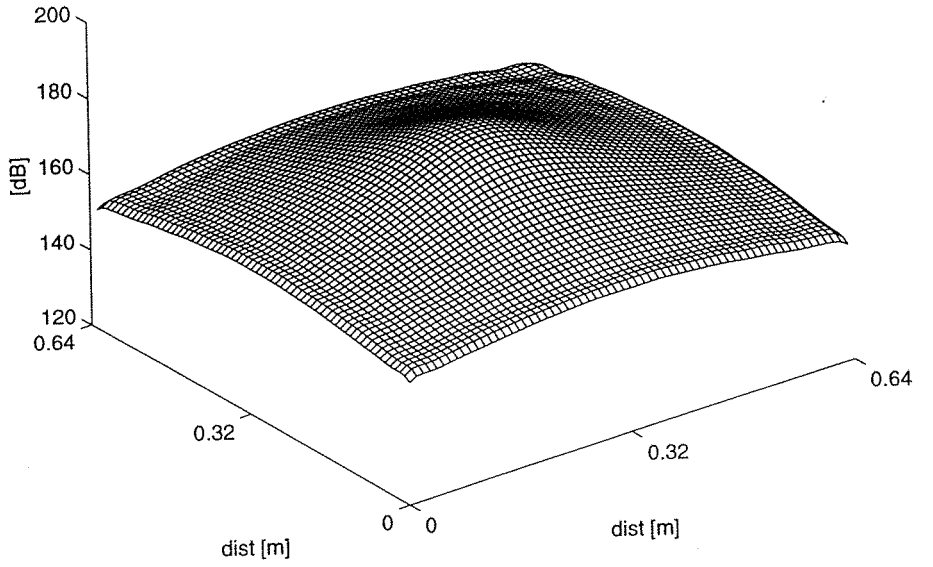

Figure 4.27 - The centre 64×64 points of the field in figure 4.11 propagated a distance of 0.01m using the 2D FFT.
Note that the sampling interval in real space has been reduced to 0.01m.
A guard band of 64×64 zeros has been added to the original pressure data.
(N=64×64, $\delta x = 0.01$m, $\lambda = 0.1$m, z=0.01m).

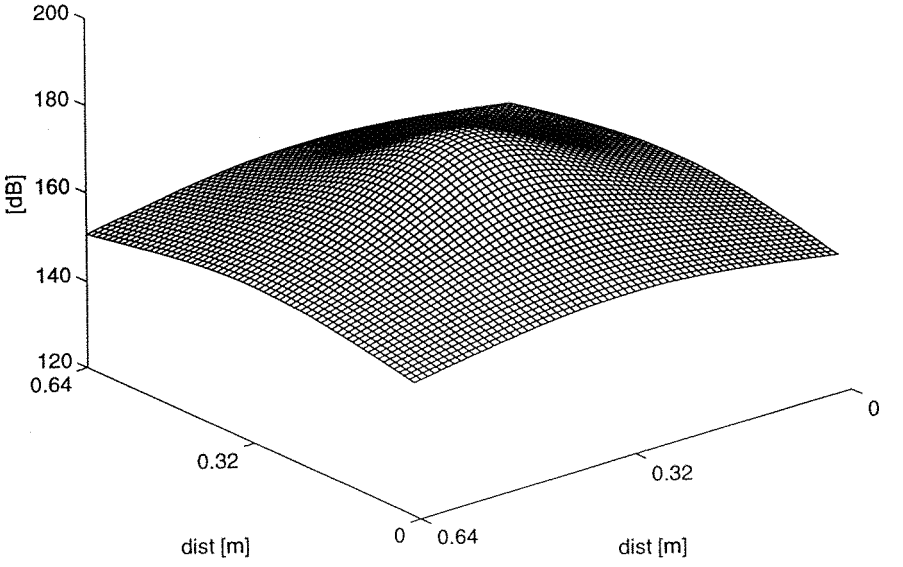

Figure 4.28 - The theoretically correct monopole field propagated a distance of 0.01m.
Note that the sampling interval in real space has been reduced to 0.01m.
(N=64×64, $\delta x = 0.01$m, $\lambda = 0.1$m, z=0.01m).

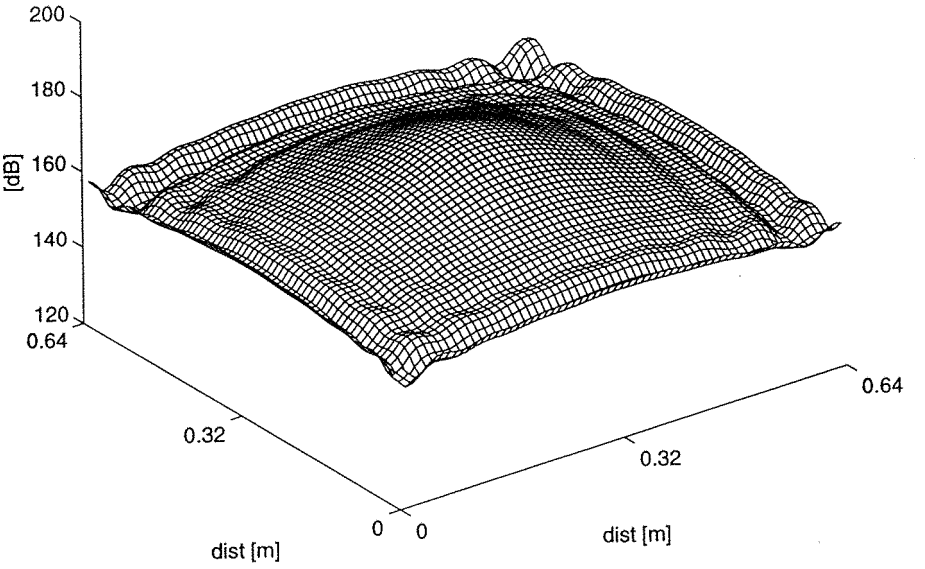

Figure 4.29 - The centre 64×64 points of the field in figure 4.11 propagated a distance of 0.01m using the 2D FFT.
Note that the sampling interval in real space has been reduced to 0.01m.
No guard band of zeros has been added to the original pressure data.
(N=64×64, $\delta x = 0.01$m, $\lambda = 0.1$m, z=0.01m).

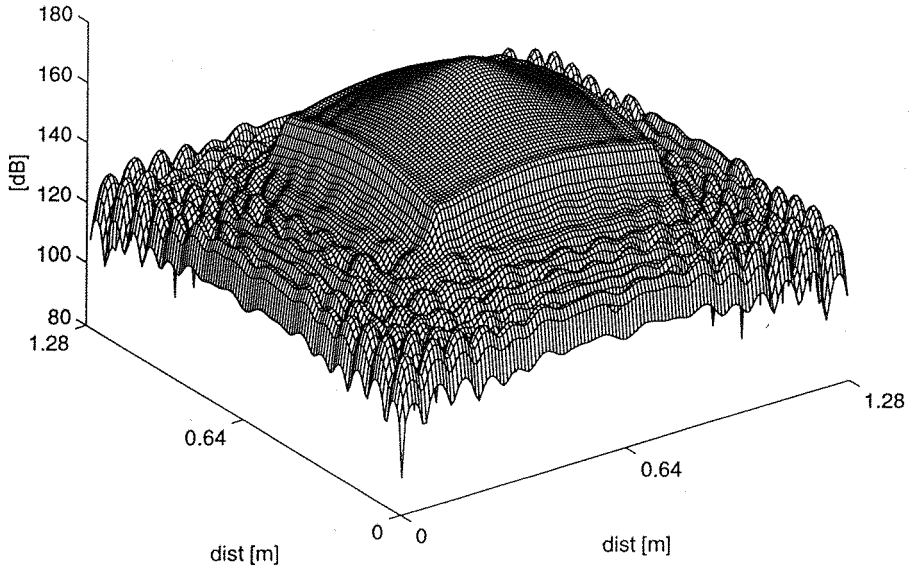

Figure 4.30 - The whole 128×128 points of the field in figure 4.11 propagated a distance of 0.01m using the 2D FFT.
Note that the sampling interval in real space has been reduced to 0.01m.
A guard band of 64×64 zeros has been added to the original pressure data.
(N=128×128, $\delta x = 0.01$m, $\lambda = 0.1$m, z=0.01m).

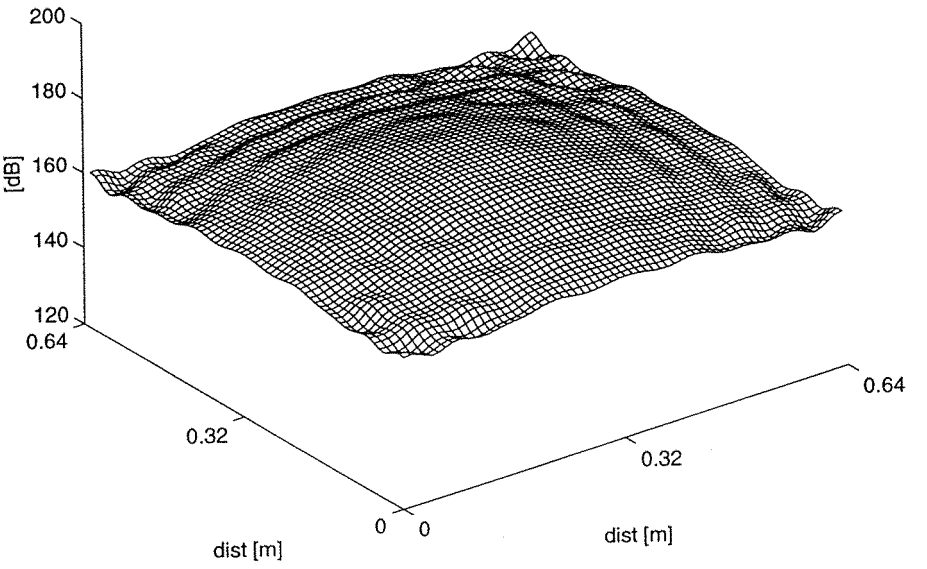

Figure 4.31 - The centre 64×64 points of the field in figure 4.11 propagated a distance of 0.1m using the 2D FFT.
Note that the sampling interval in real space has been reduced to 0.01m.
A guard band of 64×64 zeros has been added to the original pressure data.
(N=64×64, $\delta x = 0.01$m, $\lambda = 0.1$m, z=0.1m).

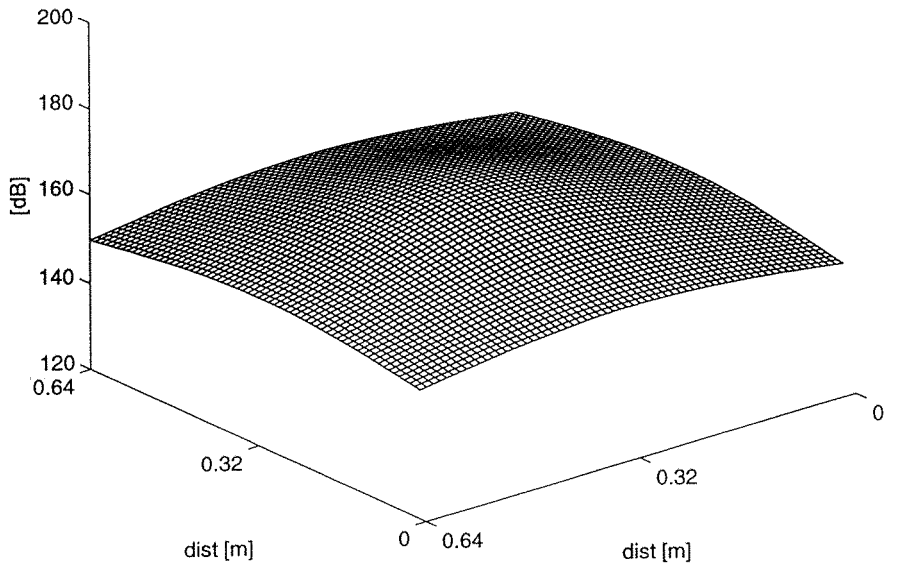

Figure 4.32 - The theoretically correct monopole field propagated a distance of 0.1m.
Note that the sampling interval in real space has been reduced to 0.01m.
(N=64×64, $\delta x = 0.01$m, $\lambda = 0.1$m, z=0.1m).

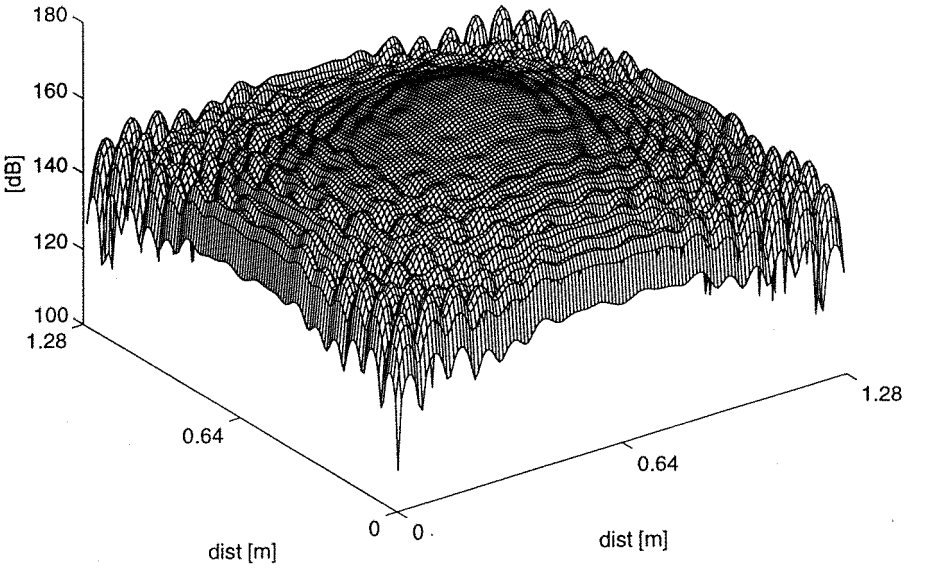

Figure 4.33a - The whole 128×128 points of the field in figure 4.11 propagated a distance of 0.1m using the 2D FFT.
Note that the sampling interval in real space has been reduced to 0.01m.
A guard band of 64×64 zeros has been added to the original pressure data.
(N=64×64, $\delta x = 0.01$m, $\lambda = 0.1$m, z=0.1m).

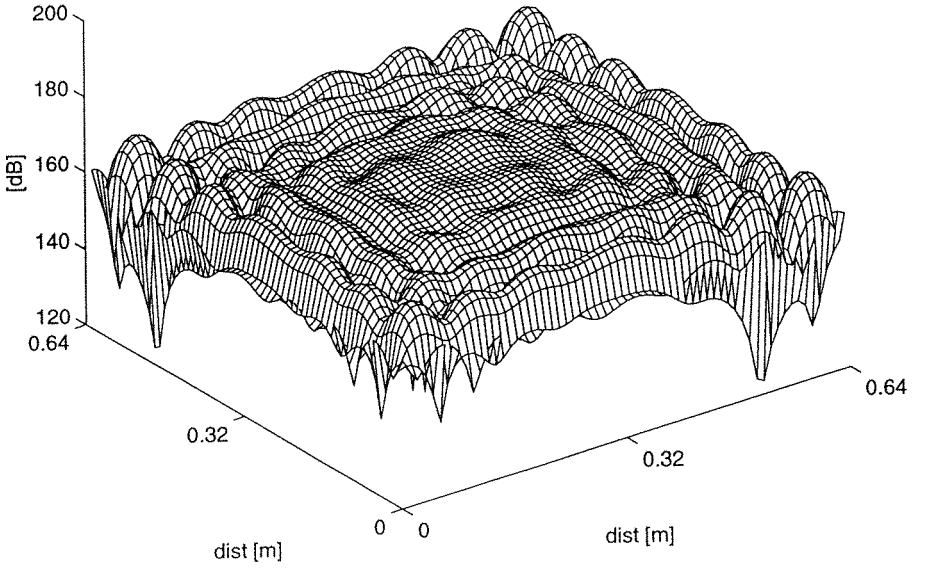

Figure 4.33b - The centre 64×64 points of the field in figure 4.11 propagated a distance of 0.1m using the 2D FFT.
Note that the sampling interval in real space has been reduced to 0.01m.
No guard band of zeros has been added to the original pressure data.
(N=64×64, $\delta x = 0.01$m, $\lambda = 0.1$m, z=0.1m).

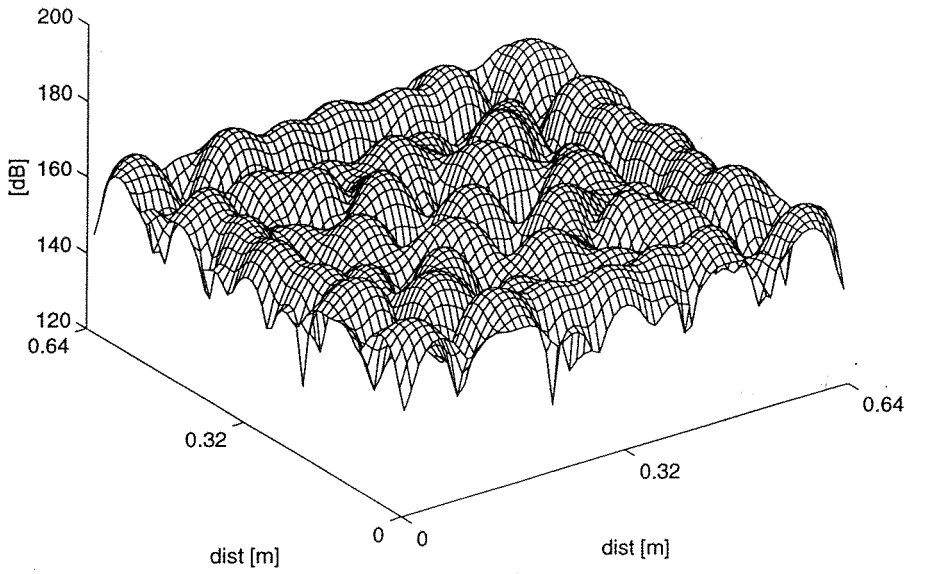

Figure 4.34 - The centre 64×64 points of the field in figure 4.11
propagated a distance of 0.1m using the 2D FFT.
Note that the sampling interval in real space has been reduced to 0.01m.
A guard band of 64×64 zeros has been added to the original pressure data.
(N=128×128, $\delta x = 0.01$m, $\lambda = 0.1$m, z=0.1m).

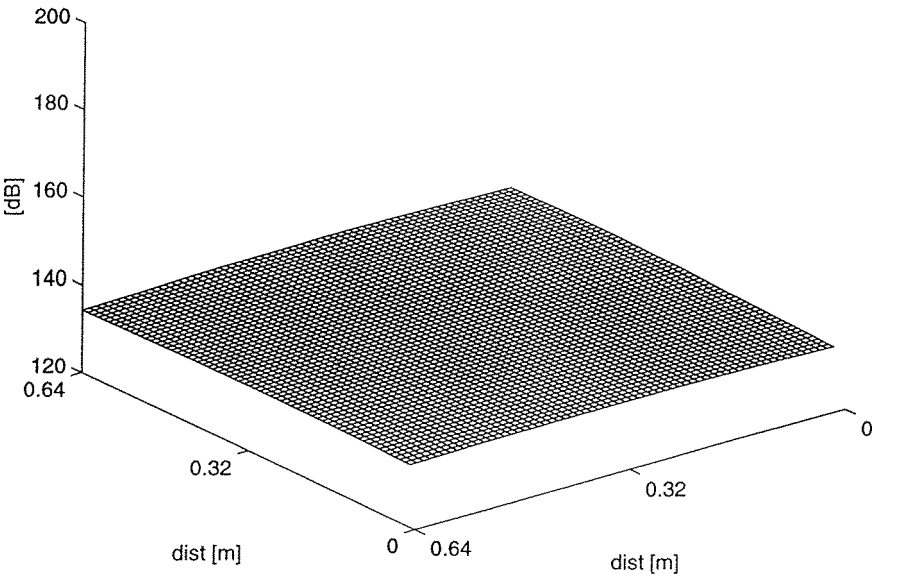

Figure 4.35 - The theoretically correct monopole field propagated a distance of 0.1m.
Note that the sampling interval in real space has been reduced to 0.01m.
(N=128×128, $\delta x = 0.01$m, $\lambda = 0.1$m, z=0.1m).

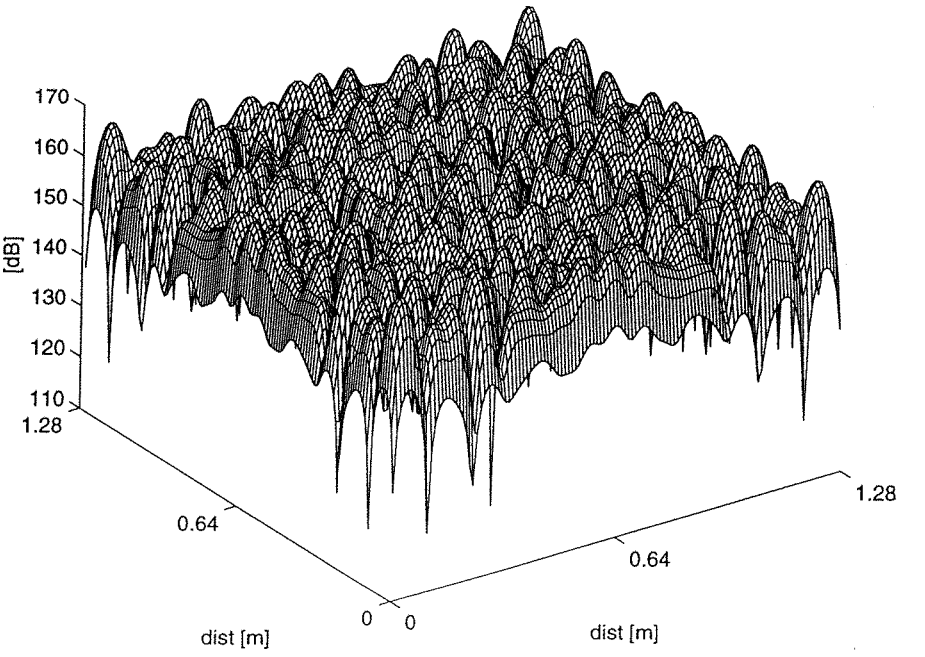

Figure 4.36 - The whole 128×128 points of the field in figure 4.11 propagated a distance of 1m using the 2D FFT.
Note that the sampling interval in real space has been reduced to 0.01m.
A guard band of 64×64 zeros has been added to the original pressure data.
(N=128×128, $\delta x = 0.01$m, $\lambda = 0.1$m, z=1m).

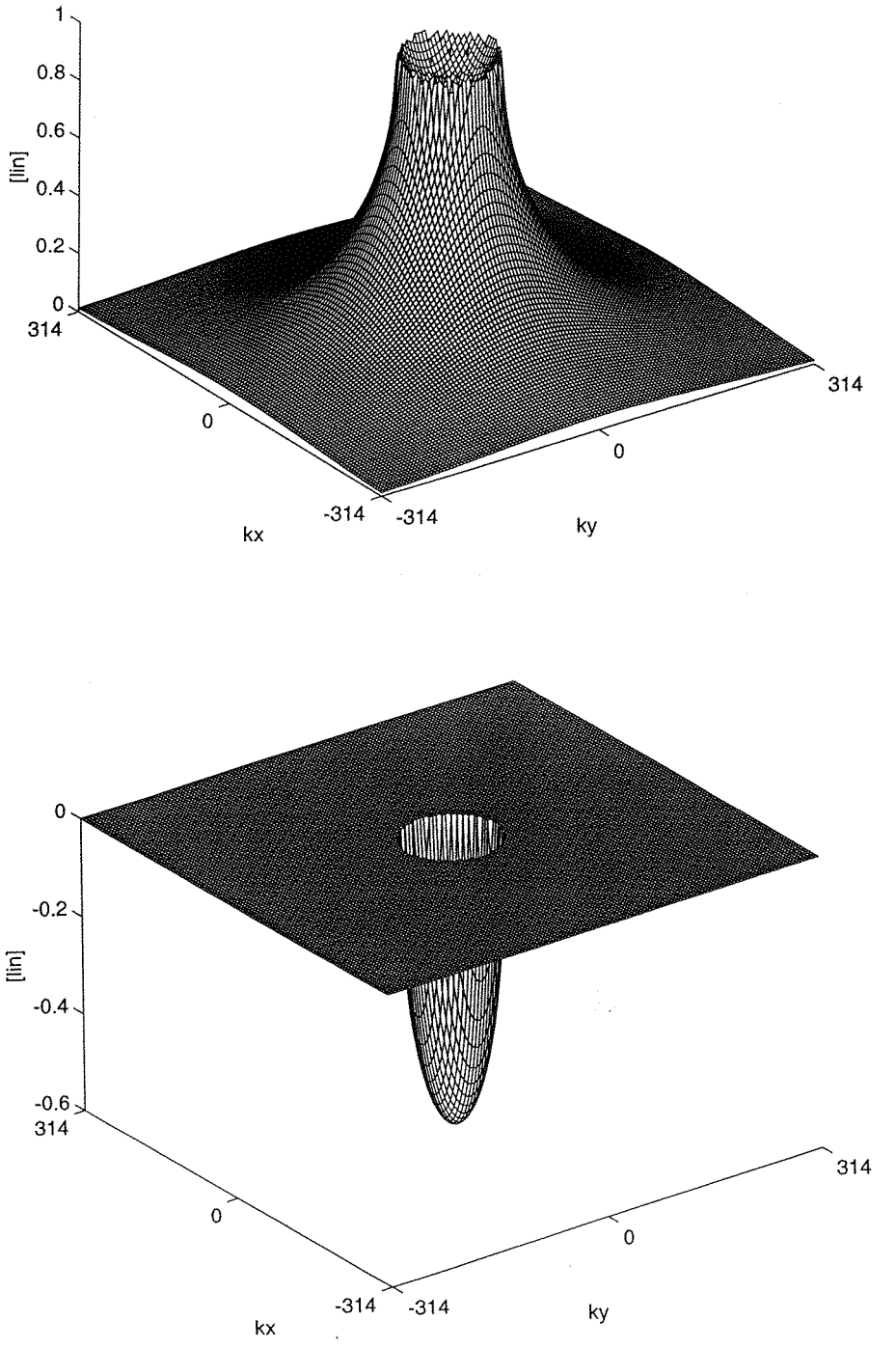

Figure 4.37 - Real and imaginary parts of the wavenumber space propagator function for a propagation distance of 0.01m.

A guard band of 64×64 zeros has been added to the original pressure data.

(N=128×128, $\delta x = 0.05$m, $\lambda = 0.1$m, z=0.01m, $\delta k_x = \delta k_y = 4.947$).

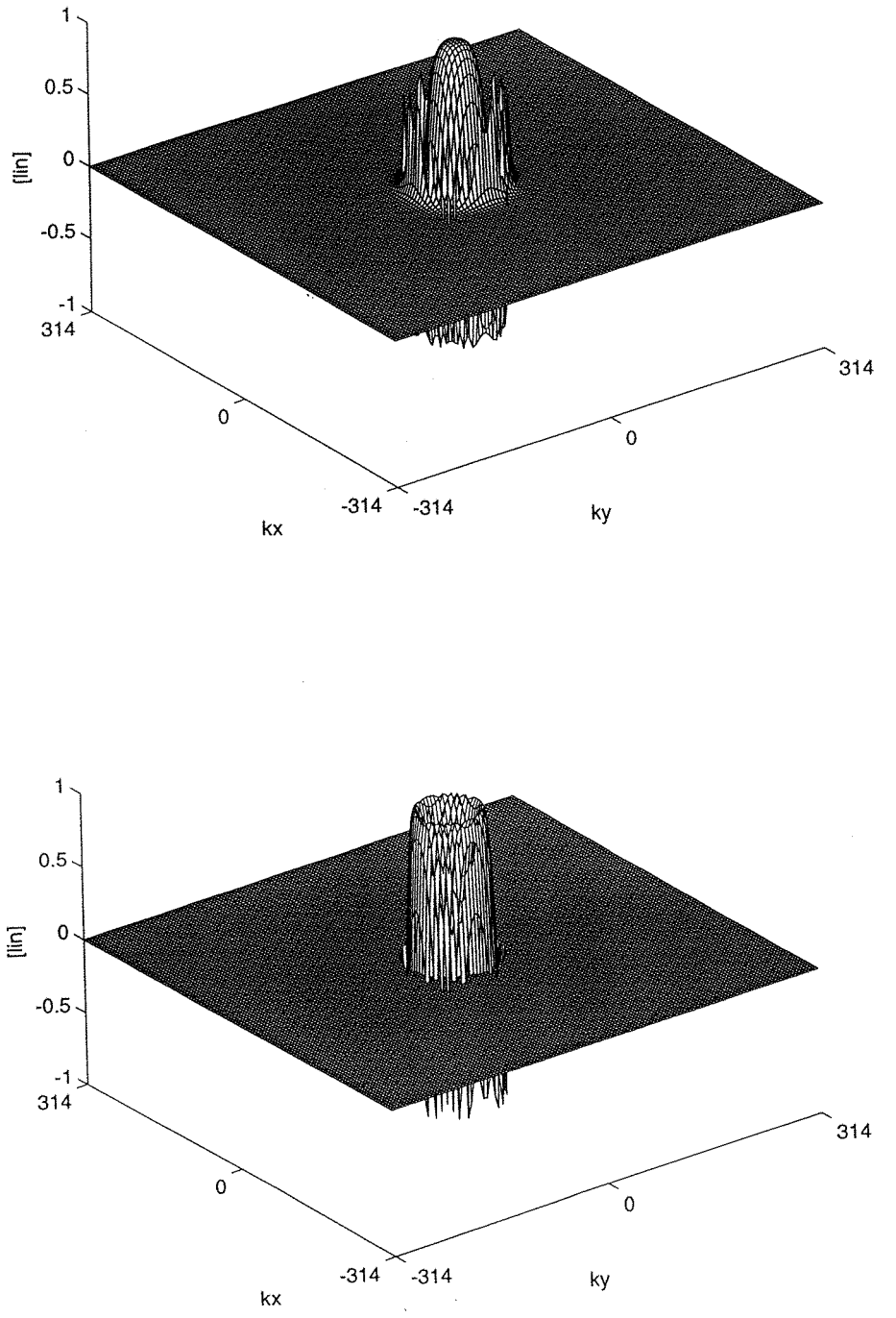

Figure 4.38 - Real and imaginary parts of the wavenumber space propagator function for a propagation distance of 0.1m.

A guard band of 64×64 zeros has been added to the original pressure data.

(N=128×128, $\delta x = 0.05$m, $\lambda = 0.1$m, z=0.1m, $\delta k_x = \delta k_y = 4.947$).

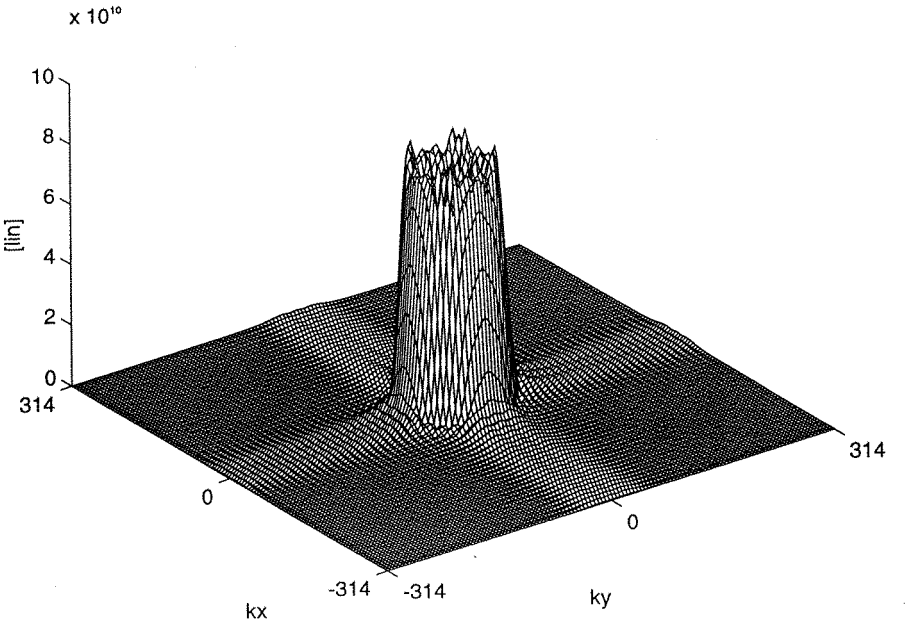

Figure 4.39 - The absolute value of the 2D FFT of the pressure array in figure 4.11. A guard band of 64×64 zeros has been added to the original pressure data. Note that the sampling interval in real space has been reduced to 0.01m. (N=128×128, $\delta x = 0.01$m, $\lambda = 0.1$m, $\delta k_x = \delta k_y = 4.947$).

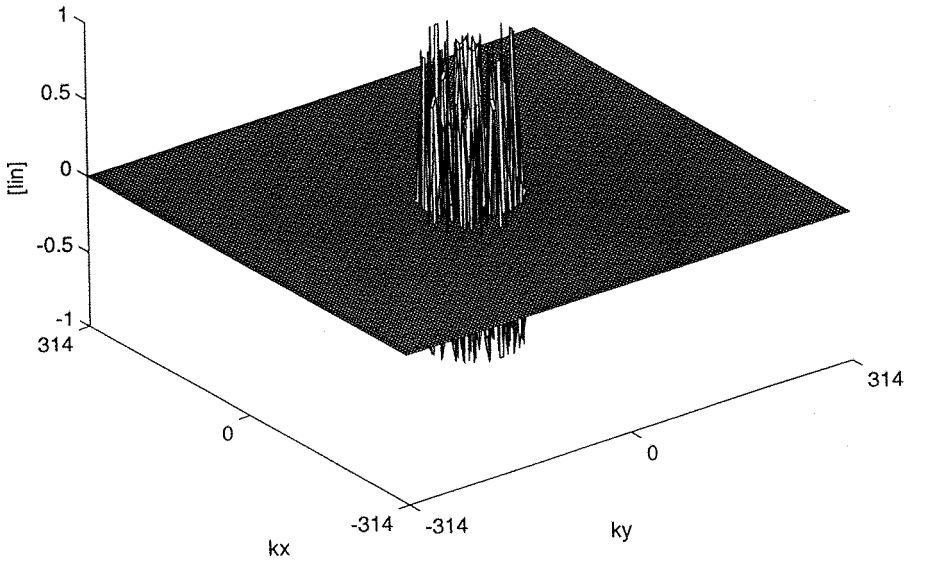

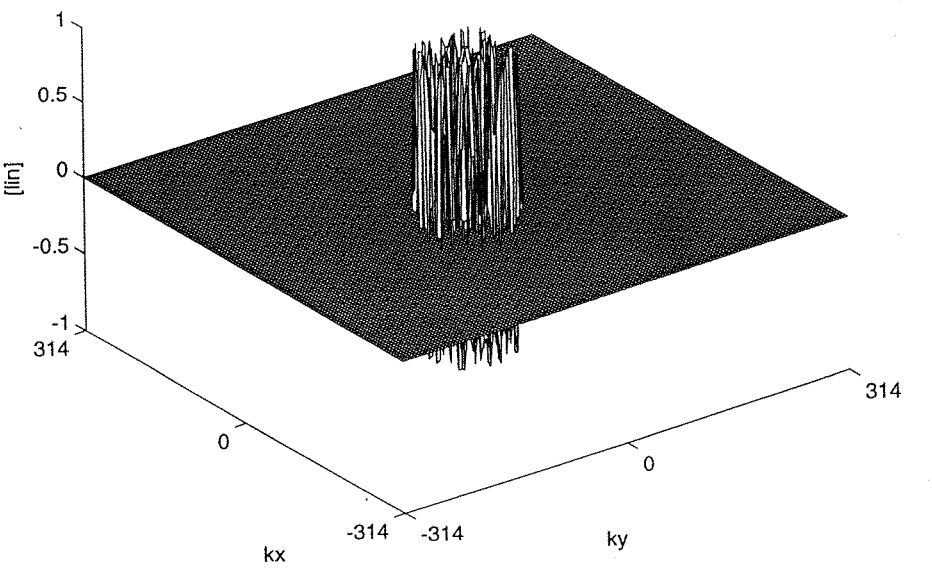

Figure 4.40 - Real and imaginary parts of the wavenumber space propagator function for a propagation distance of 1.0m.

A guard band of 64×64 zeros has been added to the original pressure data.

(N=128×128, $\delta x = 0.05$m, $\lambda = 0.1$m, z=1.0m, $\delta k_x = \delta k_y = 4.947$).

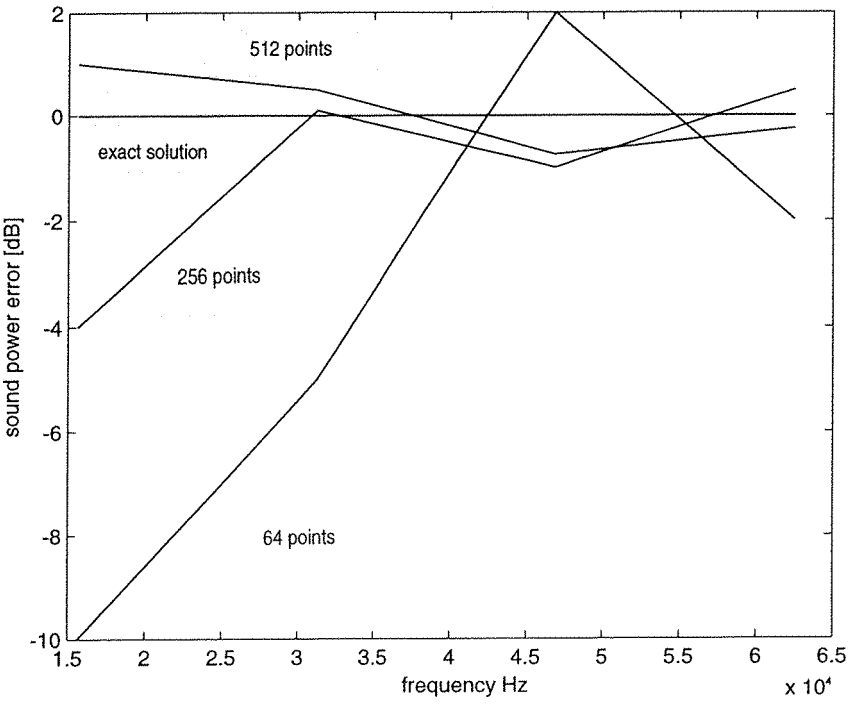

figure 4.41 - Error in the calculated sound power using the 2D FFT for a monopole source in the centre of the duct.

Chapter 5

Conclusions and Recommendations for Future Work

This project has set out to examine the radiation from simple sources within a finite length duct. In particular the radiation from a pressure release lined duct has been examined closely. This is of particular interest in this thesis, since this boundary condition cannot be produced in air. At the commencement of this project, the radiation from the duct was to be examined using an experimentally based technique. It was the intention to measure the field just outside the duct exit, and to use this to predict the far-field. Unfortunately, the method to propagate the measured pressure away from the duct was found to extremely difficult to implement successfully. The technique is described in Chapter 4, and it is hoped that this presentation is useful in alerting other would-be users of some of the practical problems that can arise when trying to employ this technique.

To overcome these problems a different approach to finding the radiation from the duct was made. An analytical model of the radiation from a finite length, circular duct was been derived. This analytical model is described in Chapter 2. Experimental measurements have shown good agreement with theoretical predictions using this model. Comparisons between experiment and theory are presented for a finite length hard walled duct, containing a monopole source. Furthermore, since the duct is immersed in water, an examination of the effect of introducing a pressure release lining at the duct wall has been undertaken. It has been shown that this is a good method for the reducing the radiation of acoustic energy from the duct. For a pressure release lined duct with the source close to the duct wall, then the amplitude of the mode shape function is very small. This is because the boundary condition at the duct wall requires vanishing pressure at the wall. Hence the value of the mode shape function will also be zero at the duct wall. Because the values of the modal amplitude coefficients are proportional to the value of the mode shape function evaluated at the location of the source, then there will be poor coupling between the source and the duct field for this case. The resultant output from a finite length duct has been evaluated by an analytical model described in Chapter 2, and by an experiment detailed in Chapter 3. For a monopole radiating into a hard walled duct, it has been shown that there is good agreement between the theory and experiment. Consequently, the radiation from this duct has been compared with that from a duct having a pressure release lining at the wall. It has been shown that large reductions in the sound power radiated

from the duct are possible when using the pressure release lining in place of the hard wall.

The values of *ka* used in this thesis have been restricted to a maximum of about 13. This was because the original experiment was based upon this maximum value. It is recommended that this work be repeated for much higher values of *ka*. This would mean that there are many more modes that may propagate freely within the duct, and hence the computation of the radiated field would take longer. However, this is offset by a need to know the relative amplitudes of the radiation from a hard wall and pressure release lined duct with a much higher modal density. It is believed that a greater power reduction would be possible using the pressure release lined duct, if there were more modes cut-on within the duct. This of course assumes that the source is placed close to the duct wall.

The analytical model derived in Chapter 2, assumes the duct to be terminated in a rigid baffle. Since there was a need to verify the accuracy of the model with measurements made near to the duct. No far-field data was available, and hence expressions that could be made to calculate in the far-field from an unbaffled duct could not be used. If only the far-field were to be calculated then it would be possible to replace the modal reflection coefficients used to calculate the internal field, with those for an unbaffled duct. This would then give the modal amplitudes for such a duct, and expressions for the far-field, whilst very complex, are available for this case. It is therefore recommended that this the mathematical model be extended to include the radiation from an unbaffled duct.

It is also recommended that the model be used to examine the case of a duct lined with an arbitrary wall impedance. The model developed in Chapter 2 enables the boundary condition at the duct wall to take any value, both real and imaginary. It would then be possible to examine the radiation from a duct whose wall impedance was not quite pressure release for example. This has practical significance, since the it is likely that any pressure release lining developed for practical use would not be an ideal pressure release surface. Therefore it would be useful to examine the necessary tolerance such a lining, to yield satisfactory reductions in the radiated energy from the duct.

Also it would be useful to examine the radiation from other source distributions within the duct, for example dipole-type sources. A simple modification to the model could be made to include such sources, and these could be compared to the results presented in this thesis. A simple modification of the theory presented in Chapter 2 would enable the study of the radiation from an axially oriented dipole source. For the monopole source examined here, the pressure difference on either side of the source plane is zero, and the magnitude of the axial particle velocity difference is equated to the source strength. For an axial dipole, the axial particle velocity difference is zero either side of the source plane, and it is the pressure difference that is used to calculate the modal amplitudes within the duct. This is fine for the restricted case of an axial dipole, However, it would be much better to formulate a solution for the radiation from an arbitrarily oriented dipole. Whilst this is not so straightforward, it is recommended that the model derived in Chapter 2 be extended to include such sources.

Appendix A

Orthogonality of Eigenfunctions in a Circular Duct

In Chapter 2, the principle of the orthogonality of mode shapes was used to calculate the amplitude of each mode in the duct. Appendix A explains this principle and provides a concise derivation.

Modal sound fields in a uniform duct.

In any source-free region, the complex amplitude of the acoustic pressure satisfies the homogeneous Helmholtz equation

$$\nabla^2 p(\mathbf{r}) + k^2 p(\mathbf{r}) = 0, \tag{A.1}$$

where $\mathbf{r}$ is a vector of field co-ordinates, r, θ, z, and ∇^2 is the Laplacian operator.

Modal solutions of this equation are of the form

$$p(\mathbf{r}) = \psi(\mathbf{s}) e^{\pm jk_z z} \tag{A.2}$$

where $\mathbf{s}$ is the two dimensional transverse position vector, and z is the axial co-ordinate. Values of $\psi(\mathbf{s})$ are required which satisfy the two dimensional Helmholtz equation

$$\nabla_\perp{}^2 \psi(\mathbf{s}) + k_\perp{}^2 \psi(\mathbf{s}) = 0 \tag{A.3}$$

where $k_\perp$ is the transverse wavenumber, which is related to the axial wavenumber, k_z by

$$k^2 = k_\perp{}^2 + k_z{}^2 \tag{A.4}$$

A sound field in a uniform duct or waveguide can be of the form of equation (A.2) provided the transverse pressure distribution $\psi(\mathbf{s})$ satisfies the duct- wall boundary condition, as well as equation (A.3). Solutions of $\psi(\mathbf{s})$ with these properties are possible for certain values of $k_\perp$ known as eigenvalues. Successive eigenvalues (e.g. in increasing order of Re $k_\perp$) are labelled with an index:

$$k_{\perp} = k_1, k_1, \ldots k_u, \ldots \tag{A.5}$$

and the corresponding ψ solutions (eigenfunctions) are labelled ψ_u.

Orthogonality of eigenfunctions

From equation (A.3), eigenfunctions ψ_u, ψ_v satisfy the equations

$$\nabla^2\psi_u(\mathbf{s}) + k_u{}^2\psi_u(\mathbf{s}) = 0\,. \tag{A.6}$$

$$\nabla^2\psi_v(\mathbf{s}) + k_v{}^2\psi_v(\mathbf{s}) = 0\,. \tag{A.7}$$

By combining equations (A.6) and (A.7), and, by dropping the explicit (s) dependence for brevity, this gives

$$\psi_v k_u{}^2\psi_u - \psi_u k_v{}^2\psi_v = \psi_u\nabla^2\psi_v - \psi_v\nabla^2\psi_u. \tag{A.8}$$

Rearranging equation (A.8) gives

$$\psi_u\psi_v(k_u{}^2 - k_v{}^2) = \psi_u\nabla^2\psi_v - \psi_v\nabla^2\psi_u \tag{A.9}$$

Integrating equation (A.9) over the duct cross section S, gives

$$(k_u{}^2 - k_v{}^2)\int_S \psi_u\psi_v\,dS = \int_S \psi_u\nabla^2\psi_v - \psi_v\nabla^2\psi_u\,dS. \tag{A.10}$$

The right hand side of equation (A.10) may be alternatively expressed using a special case of the divergence theorem known as Green's second identity. Thus

$$(k_u{}^2 - k_v{}^2)\int_S \psi_u\psi_v\,dS = \int_C (\psi_u\nabla\psi_v - \psi_v\nabla\psi_u)\cdot\mathbf{n}\,dC, \tag{A.11}$$

where the vector **n** denotes the unit outward normal to the boundary C, which is the duct wall. By applying the following boundary conditions to equation (A.11),

the right hand side of this equation vanishes. This is always true for the following cases

$\nabla\psi_u \bullet \mathbf{n} = \nabla\psi_v \bullet \mathbf{n} = 0$, on C, which is the hard wall boundary condition, (A.12)

$\psi_u = \psi_v = 0$, on C, which is the pressure release boundary condition. (A.13)

A condition of validity is given by

$$(\nabla\psi_u \bullet \mathbf{n})/\psi_u = (\nabla\psi_v \bullet \mathbf{n})/\psi_v \tag{A.14}$$

For either boundary condition given by equations (A.12) and (A.13), the right hand side of equation (A.11) vanishes, and this gives

$$(k_u{}^2 - k_v{}^2)\int_S \psi_u\psi_v \, dS = 0. \tag{A.15}$$

Remembering that the eigenvalues were chosen to be distinct, then

$$(k_u{}^2 - k_v{}^2) \neq 0 \tag{A.16}$$

Therefore, from equation (A.15)

$$\int_S \psi_u\psi_v \, dS = 0 \text{ for } u \neq v. \tag{A.17}$$

This is known as the orthogonal property of eigenfunctions.

For the case of a duct of circular cross section, then equations (A.6) and (A.7) become

$$\nabla^2\psi_{mn}(r,\theta) + k_{mn}{}^2\psi_{mn}(r,\theta) = 0, \tag{A.18}$$

$$\nabla^2\psi_{pq}(r,\theta) + k_{pq}{}^2\psi_{pq}(r,\theta) = 0, \tag{A.19}$$

where

$$\psi_{mn}(r,\theta)=\frac{J_m(k_r^{mn}r)}{N_{mn}}e^{-jm\theta}, \tag{A.20}$$

and all the terms in equation (A.20) have been defined in Chapter 2.

For a monopole source in an infinite length duct at r_s, θ_s, $z_s=0$, the modal amplitudes are related to the source by

$$\frac{Q}{r_s}\delta(r-r_s)\delta(\theta-\theta_s)=\frac{2}{k\rho c}\sum_{m=-\infty}^{\infty}e^{-jm\theta}\sum_{n=0}^{\infty}k_z^{mn}A_{mn}\psi_{mn}(r), \tag{A.21}$$

where Q is the strength of the monopole source. As previously, an alternative eigenfunction may be defined such that

$$\psi_{pq}(r,\theta)=\psi_{pq}(r)\psi_{pq}(\theta)=\frac{J_p(k_r^{pq}r)}{N_{pq}}e^{+jp\theta}. \tag{A.22}$$

Note the sign of the exponential term in equation (A.22). It will be shown that this is the *orthogonal* mode shape to that given in equation (A.21) when $m=p$. Multiplying equation (A.21) by equation (A.22), and integrating both sides of the resulting equation over the duct cross section S gives

$$\int_S \frac{Q}{r_s}\delta(r-r_s)\delta(\theta-\theta_s)\psi_{pq}(r)e^{+jm\theta}\,dS = \int_S \frac{2}{k\rho c}\sum_{m=-\infty}^{\infty}e^{-jm\theta}e^{+jm\theta}\sum_{n=0}^{\infty}k_z^{mn}A_{mn}\psi_{mn}(r)\psi_{pq}(r)dS \tag{A.23}$$

Using the sifting property of the delta function (Bracewell, 1986), and noting that $dS=r\,dr\,d\theta$, then equation (A.23) becomes

$$Q\psi_{pq}(r_s)e^{jp\theta_s}=\frac{2k_z^{mn}A_{mn}}{k\rho c}\int_0^{2\pi}e^{-jm\theta}\,e^{+jp\theta}\,d\theta\int_0^{a}\psi_{mn}(r)\,\psi_{pq}(r)\,r\,dr. \tag{A.24}$$

From the principle of orthogonality of the mode shapes, defined by equation (A.13), this equation is zero unless $m = p$ and $n = q$. Therefore equation (A.24) becomes

$$Q\psi_{mn}(r_s)e^{jm\theta_s} = \frac{2k_z^{mn}A_{mn}}{k\rho c}\int_0^{2\pi} d\theta \int_0^a \psi_{mn}^2(r)\, r\, dr, \tag{A.25}$$

which gives

$$Q\psi_{mn}(r_s)e^{jm\theta_s} = \frac{4\pi k_z^{mn}A_{mn}}{k\rho c}\int_0^a \psi_{mn}^2(r) r\, dr. \tag{A.26}$$

The mode shapes are normalised, such that

$$\int_0^a \psi_{mn}^2(r) r\, dr = 1. \tag{A.27}$$

Consider now just the integral in equation (A.27). Upon expansion this becomes

$$\int_0^a \psi_{mn}^2(r) r\, dr = 1 = \frac{1}{N_{mn}^2}\int_0^a J_m^2(k_r^{mn}r) r\, dr. \tag{A.28}$$

The integral on the right hand side of equation (A.28) has a solution given by[1]

$$N_{mn}^2 = \frac{r^2}{2}\left[\left\{1 - \frac{m^2}{k_r^{mn2}r^2}\right\} J_m^2(k_r^{mn}r) + J_m'^2(k_r^{mn}r)\right]\Bigg|_0^a, \tag{A.29}$$

which gives

$$N_{mn} = \frac{a}{\sqrt{2}}\left\{\left(1 - \frac{m^2}{\lambda_{mn}^2 k^2 a^2}\right) J_m^2(\lambda_{mn}ka) + J_m'^2(\lambda_{mn}ka)\right\}^{\frac{1}{2}}. \tag{A.30}$$

Therefore using equations (A.22) and (A.25) it is possible to find the value of the modal amplitude coefficients A_{mn}, which are thus given by

$$A_{mn} = \frac{Q\, k\rho c}{4\pi\, k_z^{mn}} \frac{J_m(k_r^{mn}r_s)}{N_{mn}} e^{jm\theta_s}. \tag{A.31}$$

---

[1] see Watson (1962), page 135, equation 11.

Appendix B

Derivation of the Function $D_{mn}(\tau)$

In Chapter 2, the function $D_{mn}(\tau)$ is used to calculate the modal impedances. In this Appendix a more detailed derivation of the integral used to express this function is provided.

The integral representation of the function $D_{mn}(\tau)$ defined in Chapter 2 is given by

$$D_{mn}(\tau) = k\int_0^a r_0 J_m(\tau k r_0)\psi_{mn}(k r_0)dr_0, \tag{B.1}$$

where all the above symbols were defined in section Chapter 2, Section 2.6. From the definition of the mode shape function

$$\psi_{mn}(k r_0) = \frac{J_m(\lambda_{mn} k r_0)}{N_{mn}}, \tag{B.2}$$

equation (B.1) may be expressed in terms of two Bessel Functions, to give

$$D_{mn}(\tau) = \frac{k}{N_{mn}}\int_0^a r_0 J_m(\tau k r_0) J_m(\lambda_{mn} k r_0)dr_0. \tag{B.3}$$

The integral above may be evaluated directly, (Watson, 1962). The result is

$$D_{mn}(\tau) = \left(\frac{a}{N_{mn}}\right)\frac{\left\{\tau J_{m+1}(\tau k a) J_m(\lambda_{mn} k a) - \lambda_{mn} J_{m+1}(\lambda_{mn} k a) J_m(\tau k a)\right\}}{(\tau^2 - {\lambda_{mn}}^2)}. \tag{B.4}$$

Using the Bessel function identity

$$J_{m+1}(x) = \frac{m}{x}J_{m+1}(x) - J'_m(x), \tag{B.5}$$

equation (B.4) becomes

$$D_{mn}(\tau) = \frac{a}{N_{mn}(\tau^2 - {\lambda_{mn}}^2)} \times$$
$$\left\{ \tau \left(\frac{m}{\tau ka} J_m(\tau ka) - J'_m(\tau ka) \right) J_m(\lambda_{mn} ka) \right. \tag{B.6}$$
$$\left. -\lambda_{mn} \left(\frac{m}{\lambda_{mn} ka} J_m(\lambda_{mn} ka) - J'_m(\lambda_{mn} ka) \right) J_m(\tau ka) \right\}$$

This can be written as

$$D_{mn}(\tau) = \frac{a}{N_{mn}(\tau^2 - {\lambda_{mn}}^2)} \times$$
$$\left\{ \frac{m}{a} J_m(\tau ka) J_m(\lambda_{mn} ka) - \tau k J'_m(\tau ka) J_m(\lambda_{mn} ka) \right. \tag{B.7}$$
$$\left. -\frac{m}{a} J_m(\lambda_{mn} ka) J_m(\tau ka) - \lambda_{mn} J'_m(\lambda_{mn} ka) J_m(\tau ka) \right\}$$

Cancelling common terms gives

$$D_{mn}(\tau) = \frac{a}{N_{mn}(\tau^2 - {\lambda_{mn}}^2)} \left\{ -\tau J'_m(\tau ka) J_m(\lambda_{mn} ka) + \lambda_{mn} J'_m(\lambda_{mn} ka) J_m(\tau ka) \right\} \tag{B.8}$$

Further rearrangement gives

$$D_{mn}(\tau) = \frac{a}{N_{mn}} \frac{\left\{ \tau J'_m(\tau ka) J_m(\lambda_{mn} ka) - \lambda_{mn} J'_m(\lambda_{mn} ka) J_m(\tau ka) \right\}}{({\lambda_{mn}}^2 - \tau^2)}. \tag{B.9}$$

In terms of the duct mode shape function, this becomes

$$D_{mn}(\tau) = \frac{a \left\{ \tau k J'_m(\tau ka) \psi_{mn}(ka) - \lambda_{mn} \psi'_{mn}(ka) J_m(\tau ka) \right\}}{({\lambda_{mn}}^2 - \tau^2)}. \tag{B.10}$$

Appendix C

Derivation of the Impedance Function Z_{mnl} and the Reflection Coefficient R_{mnl}

In Chapter 2, Section 2.6, expressions for the modal impedance and reflection coefficient at the end of the duct were given. This Appendix gives the derivation of these two important parameters.

1. The Modal Radiation Impedance

In order to solve for the modal impedances, it is necessary to equate the expressions for the pressure from within the duct, to the pressure outside the duct, at the duct exit. These 2 expressions are given by

$$p(\mathbf{r}_0) = \sum_{m=-\infty}^{\infty} e^{jm\theta_0} \sum_{j=0}^{\infty} P_{mj} \psi_{mj}(kr_0), \tag{C.1}$$

$$p(\mathbf{r}) = jk \sum_{m=-\infty}^{\infty} e^{jm\theta} \sum_{l=0}^{\infty} V_{ml} \int_0^{\infty} \tau\left(\tau^2 - 1\right)^{-\frac{1}{2}} J_m(\tau kr) D_{ml}(\tau) d\tau. \tag{C.2}$$

Equation (C.1) was derived from the internal field ($z \leq 0$), whereas equation (C.2) was found by examination of the exterior field of the duct $z \geq 0$), and is essentially the Rayleigh Integral. At the duct exit ($z=0$), then it is possible to equate these two equations.

Note that indices for the azimuthal order, m, are the same, whereas those for the radial order are different, and are denoted by j and l respectively. This is because there exits a simple relationship between the azimuthal components in equations (C.1) and (C.2). However, to equate the radial components in each of these equations is non-trivial. Since the azimuthal components may be simply equated it is possible to ignore the summation over m. This gives upon equating equations (C.1) and (C.2)

$$\sum_{j=0}^{\infty} P_{mn} \psi_{mj}(kr_0) = jk \sum_{l=0}^{\infty} V_{mn} \int_0^{\infty} \tau\left(\tau^2 - 1\right)^{-\frac{1}{2}} J_m(\tau kr) D_{ml}(\tau) d\tau. \tag{C.3}$$

Multiplying both sides of equation (C.4) by $\psi_{mn}(kr_0)$ and integrating over the duct cross section gives

$$\int_0^a \sum_{n=0}^{\infty} P_{mj}\psi_{mj}(kr_0)\psi_{mn}(kr_0)\,r\,dr = jk\sum_{l=0}^{\infty} V_{ml}\int_0^{\infty}\int_0^a \tau\left(\tau^2-1\right)^{-\frac{1}{2}} J_m(\tau kr_0)D_{ml}(\tau)\psi_{mn}(kr_0)\,r\,dr\,d\tau \tag{C.4}$$

where the suffix 0 indicates that this is at the end of the duct at $z=0$. For clarity this explicit notation will be dropped in the equations that follow.

From the principle of orthogonality of the mode shape functions

$$\int_0^a r\,\psi_{mj}(kr)\psi_{mn}(kr)\,dr = 0 \quad \text{for} \quad j \neq n, \tag{C.5}$$

$$\int_0^a r\,\psi_{mj}(kr)\psi_{mn}(kr)\,dr = 1 \quad \text{for} \quad j = n. \tag{C.6}$$

Therefore equation (C.5) becomes

$$P_{mn} = jk\sum_{l=0}^{\infty} V_{ml}\int_0^a\int_0^{\infty} \tau\left(\tau^2-1\right)^{-\frac{1}{2}} J_m(\tau kr)D_{ml}(\tau)\psi_{mn}(kr)\,r\,dr\,d\tau. \tag{C.7}$$

Note the appearance of the different index n, on the mode shape function in the right hand side of equation (C.7). From the definition of the function, $D_{mn}(\tau)$

$$D_{mn}(\tau) = k\int_0^a rJ_m(\tau kr)\psi_{mn}(kr)dr. \tag{C.8}$$

Then equation (C.6) becomes

$$P_{mn} = j\sum_{l=0}^{\infty} V_{ml}\int_0^{\infty} \tau\left(\tau^2-1\right)^{-\frac{1}{2}} D_{ml}(\tau)\,D_{mn}(\tau)d\tau. \tag{C.9}$$

Equation (C.9) may be used to express the modal impedance given by

$$P_{mn} = \sum_{l=0}^{\infty} Z_{mnl}V_{ml}, \tag{C.9}$$

where

$$Z_{mnl} = j\int_0^{\infty} \tau\left(\tau^2-1\right)^{-\frac{1}{2}} D_{mn}(\tau)D_{ml}(\tau)d\tau. \tag{C.10}$$

The above integral may be split into the two ranges, (0,1) and (1,∞) to give

$$Z_{mnl} = j\int_0^1 \tau\left(\tau^2-1\right)^{-\frac{1}{2}} D_{mn}(\tau)D_{ml}(\tau)d\tau + j\int_1^\infty \tau\left(\tau^2-1\right)^{-\frac{1}{2}} D_{mn}(\tau)D_{ml}(\tau)d\tau. \quad \text{(C.11)}$$

Using the substitutions

$$\tau = \sin\phi \qquad \text{for} \quad (0 \le \tau \le 1), \quad \text{(C.12)}$$

$$\tau = \cosh\xi \qquad \text{for} \quad (1 \le \tau \le \infty). \quad \text{(C.13)}$$

Noting that for equation (C.12) then $d\tau = \cos\phi\, d\phi$, and for equation (C.13) $d\tau = \cos\xi\, d\xi$, then equation (C.11) becomes

$$\begin{aligned} Z_{mnl} = {} & j\int_0^{\frac{\pi}{2}} \frac{\sin\phi}{\sqrt{\left(\sin^2\phi - 1\right)}} D_{mn}(\sin\phi)\, D_{ml}(\sin\phi)\cos\phi\, d\phi \\ & + j\int_0^\infty \frac{\cosh\xi}{\sqrt{\tau^2\cosh^2\xi - 1}} D_{mn}(\cosh\xi)\, D_{ml}(\cosh\xi)\sinh\xi\, d\xi \end{aligned} \quad \text{(C.14)}$$

Using the following well known identities

$$\cos\phi = j\sqrt{\sin^2\phi - 1}, \quad \text{(C.15)}$$

$$\sinh\xi = \sqrt{\cosh^2\xi - 1}. \quad \text{(C.16)}$$

Then equation (C.14) becomes

$$Z_{mnl} = \int_0^{\frac{\pi}{2}} \sin\phi D_{mn}(\sin\phi)D_{ml}(\sin\phi)\, d\phi + j\int_0^\infty \cosh\xi D_{mn}(\cosh\xi)D_{ml}(\cosh\xi)\, d\xi. \quad \text{(C.17)}$$

This is the required result, and the above equation is used to calculate the modal impedances used in this thesis.

2. The Modal Reflection Coefficient.

Starting with equation (2.8.3) from Chapter 2, Section 8,

$$\sum_{l=0}^{\infty}\left(Z_{mnl}\Omega_{ml}+\delta_{nl}\right)B_{ml}=\sum_{l=0}^{\infty}\left(Z_{mnl}\Omega_{ml}-\delta_{nl}\right)A_{ml}. \tag{C.18}$$

For fixed azimuthal order, m, the above equation becomes

$$\sum_{l=0}^{\infty}\left(Z_{nl}\Omega_{l}+\delta_{nl}\right)B_{l}=\sum_{l=0}^{\infty}\left(Z_{nl}\Omega_{l}-\delta_{nl}\right)A_{l}, \tag{C.18}$$

In matrix form this equation may be written as

$$\mathbf{Z_{nl}\Omega_l\, b_n}+\mathbf{b_n}=\mathbf{Z_{nl}\Omega_l\, a_l}+\mathbf{a_l}. \tag{C.19}$$

Since the delta function ensures that $n=l$, and noting that

$$\mathbf{b_n}=\mathbf{R_{nl}\, a_l}, \tag{C.20}$$

then equation (C.19) becomes

$$\mathbf{Z_{nl}\Omega_l\, R_{nl}a_l}+\mathbf{R_{nl}a_l}=\mathbf{Z_{nl}\Omega_l\, a_l}-\mathbf{a_l}, \tag{C.21}$$

this gives

$$\left[\mathbf{Z_{nl}\Omega_l\, R_{nl}}+\mathbf{R_{nl}}-\mathbf{Z_{nl}\Omega_l}+\mathbf{I}\right]\mathbf{a_l}=0. \tag{C.22}$$

Hence

$$\mathbf{Z_{nl}\Omega_l\, R_{nl}}+\mathbf{R_{nl}}-\mathbf{Z_{nl}\Omega_l}+\mathbf{I}=0. \tag{C.23}$$

$$\left[\mathbf{Z_{nl}\Omega_l\, R_{nl}}+\mathbf{I}\right]\mathbf{R_{nl}}=\left[\mathbf{Z_{nl}\Omega_l}+\mathbf{I}\right]. \tag{C.24}$$

This results in the following expression for the reflection coefficient in terms of modal impedance, for fixed azimuthal order

$$\mathbf{R}_{nl} = \left[\mathbf{Z}_{nl}\Omega_q\, \mathbf{R}_{nl} + \mathbf{I}\right]^{-1} \left[\mathbf{Z}_{nl}\Omega_q + \mathbf{I}\right]. \tag{C.25}$$

Appendix D

Application of L'Hôpital's Rule to the Function $D_{mn}(\tau)$ as $\tau \to \lambda_{mn}$

In Chapter 2, the function $D_{mn}(\tau)$ is used to calculate the modal radiation impedances. These impedances are used to calculate the modal reflection coefficients at the end of the duct. The function $D_{mn}(\tau)$ is given by

$$D_{mn}(\tau) = a\left[\frac{\tau\psi_{mn}(ka)J'_m(\tau ka) - \lambda_{mn}\psi'_{mn}(ka)J_m(\tau ka)}{\lambda_{mn}{}^2 - \tau^2}\right]. \tag{D.1}$$

As $\tau \to \lambda_{mn}$ then the denominator in (D.1) tends toward zero, and it would be reasonable to expect that $D_{mn}(\tau)$ would tend to infinity. This makes the evaluation of this function impossible. More importantly, it would prevent the evaluation of the modal impedances within the duct. These are given by

$$Z_{mnl} = -j\int_0^\infty \tau\left(\tau^2 - 1\right)^{-\frac{1}{2}} D_{mn}(\tau)D_{ml}(\tau)d\tau. \tag{D.2}$$

It is necessary to integrate the function $D_{mn}(\tau)$ over a range which will include possible poles at $\tau = \lambda_{mn}$ and $\tau = \lambda_{ml}$. However, it will be shown in this Appendix that by application of L'Hôpital's rule it can be demonstrated that the function $D_{mn}(\tau)$ is continuous at $\tau = \lambda_{mn}$ and $\tau = \lambda_{ml}$. L'Hôpital's rule may be defined in the following manner (see for example Abramowitz and Stegun, 1970 p.13). Let $f(x)$ and $g(x)$ be differentiable on an interval $a \le x < b$ for which $g'(x) \neq 0$, then if

$$\lim_{x\to b-} f(x) = 0 \text{ and } \lim_{x\to b-} g(x) = 0 \tag{D.3}$$

or if

$$\lim_{x\to b-} f(x) = \infty \text{ and } \lim_{x\to b-} g(x) = \infty \text{ and if } \lim_{x\to b-} \frac{f'(x)}{g'(x)} = l \tag{D.4}$$

then

$$\lim_{x\to a} \frac{f(x)}{g(x)} = l. \tag{D.5}$$

Applying this to equation (D.1), and letting $f(\tau)$ denote the numerator, and $g(\tau)$ denote the denominator, gives

$$f(\tau) = a\tau\psi_{mn}(ka)J'_m(\tau ka) - ka\lambda_{mn}\psi'_{mn}(ka)J_m(\tau ka), \tag{D.6}$$

$$g(\tau) = \lambda_{mn}{}^2 - \tau^2. \tag{D.7}$$

Considering the numerator first

$$f'(\tau) = ka^2\,\tau\psi_{mn}(ka)J''_m(\tau ka) + aJ_m(\tau ka)\psi_{mn}(ka) - ka^2\,\lambda_{mn}\psi'_{mn}(ka)J'_m(\tau ka). \tag{D.8}$$

Differentiating the denominator, gives

$$g(\tau) = -2\tau. \tag{D.9}$$

At $\tau = \lambda_{mn}$, the ratio $\dfrac{f'(\tau)}{g'(\tau)}$ is given by

$$\tfrac{1}{2}ka^2 J'_m(\lambda_{mn}ka)\psi'_{mn}(ka) - \tfrac{1}{2}ka^2 J''_m(\lambda_{mn}ka)\psi_{mn}(ka) - \tfrac{1}{2}\lambda_{mn}a\,J'_m(\lambda_{mn}ka)\psi_{mn}(ka) \tag{D.10}$$

For a hard walled duct, then equation (D.10) gives

$$\lim_{\tau\to\lambda_{mn}} D_{mn}(\tau) = -\tfrac{1}{2}ka^2\psi_{mn}(ka)J''_m(\lambda_{mn}ka), \tag{D.11}$$

which is equivalent to

$$\lim_{\tau\to\lambda_{mn}} D_{mn}(\tau) = \tfrac{1}{4}ka^2\psi_{mn}(ka)\left[J'_{m+1}(\lambda_{mn}ka) - J'_{m-1}(\lambda_{mn}ka)\right]. \tag{D.12}$$

For a pressure release boundary at the duct wall, then equation (D.10) becomes

$$\lim_{\tau\to\lambda_{mn}} D_{mn}(\tau) = \tfrac{1}{2}ka^2 J'_m(\lambda_{mn}ka)\psi'_{mn}(ka), \tag{D.13}$$

which is equivalent to

$$\lim_{\tau \to \lambda_{mn}} D_{mn}(\tau) = \frac{ka^2 J_m'^2(\lambda_{mn} ka)}{2N_{mn}}. \tag{D.14}$$

It can be seen that equations (D.12) and (D.14), are well behaved for all values of m and λ_{mn}.

References

Abramowitz, M. and Stegun, I. A. (1970) Handbook of Mathematical Functions. Dover Publications, New York.

Baker, D. D. (1962) *Journal of the Acoustical Society of America, **34**(11). pp 1737-1744.* Determination of Far-Field Characteristics of Large Underwater Sound Transducers from Near-Field Measurements.

Beckemeyer, R. J. and Sawdy, D.T. 1975. *AIAA Paper 75-516, Hampton, VA.* Computational Methods for Acoustic Radiation from Circular Ducts.

Caille, G. W. (1988). *The acoustic field scattered from some approximate pressure release materials coating a finite cylinder.* PhD thesis. Georgia Institute of Technology, USA.

Clemmow, P. G. (1966) The Plane Wave Spectrum Representation of Electromagnetic Fields. Pergamon Press. Oxford.

Copley, L. G. (1967) *Journal of the Acoustical Society of America, **41**. pp 807-816.* Integral Equation Method for Radiation from Vibrating Bodies.

Copley, L. G. (1968) *Journal of the Acoustical Society of America, **44**. pp 22-32.* Fundamental Results Concerning Integral Representations in Acoustic Radiation.

Doak, P. E. 1973a *Journal of Sound and Vibration, **31**(2), pp.1-72.* Excitation, Transmission and Radiation of Sound from Sources in Hard-Walled Ducts of Finite Length. (1) The Effects of Duct Cross-Section Geometry and Source Space-Time Pattern.

Doak, P. E. 1973b *Journal of Sound and Vibration, **31**(2), pp.137-174* Excitation, Transmission and Radiation of Sound from Sources in Hard-Walled Ducts of Finite Length. (2) The Effects of Duct Length.

Dudgeon, D. E., and Mersereau, R. M. (1984) Multidimensional Digital Signal Processing. Prentice-Hall, Inc., Englewood Cliffs, New Jersey.

Ferris, H. G. (1964) *Journal of the Acoustical Society of America, **36**. pp 1597-1598.* Far-Field radiation pattern of a noise source from near field measurements.

Ferris, H. G. (1966) *Journal of the Acoustical Society of America, 41(2). pp 394-400.* Computation of Far-field Radiation Patterns by Use of a General Integral Solution to the Time-Dependent Scalar Wave Equation.

Goodman, J. W. (1968) Introduction to Fourier Optics. The McGraw-Hill Book Company. New York.

Hald, J. and Roth, O. (1983) *Journal of the Acoustical Society of America, sup 74(1) pp 562-566.* Spatial Transformation of Sound Fields

Hewlett, D. A. K., 1989 *ISVR Contract Report 89/09.* The suitability of closed cell neoprene foam as a pressure release boundary condition.

Hewlett, D A K. *'The Generation of a Dipole Source Underwater from the Superposition of Monopoles.'* Paper presented at the European Conference on Underwater Acoustics, Luxembourg, September 1992.

Hewlett, D. A. K., Morfey, C. L. and Nelson, P. A. (1994) *'The Acoustic Radiation from a Finite Length Circular Duct Immersed in Water'.* Paper presented at Flow Noise: A Technology Audit. Lyon. July 1994.

Homicz, G F., and Lordi. J A. 1975 *Journal of Sound and Vibration, **41** pp283-290.* A note on the radiative directivity patterns of duct acoustic modes.

Horton, C. W. and Innis G. S. (1961) *Journal of the Acoustical Society of America, 33(7). pp 877-880.* The Computation of Far-Field Radiation Patterns from Measurements Made near the Source

Johnson, G W., Ogimoto, K., 1980a *Journal of the Acoustical Society of America, 68 pp1858-1870.* Sound radiation from a finite length unflanged circular duct with uniform axial flow, I: theoretical analysis.

Johnson, G W., Ogimoto, K., 1980b *Journal of the Acoustical Society of America, 68 pp1871-1883.* Sound radiation from a finite length unflanged circular duct with uniform axial flow, II: computed radiation characteristics.

Koopmann, G. H. and Beener, H. (1982) *Journal of the Acoustical Society of America, 71(1). pp 78-89.* Method for computing the sound power of machines based upon the Helmholtz integral.

Lahti, T. (1989) *Analysis methods for acoustical systems based upon FFT and intensity techniques.* PhD thesis, Helsinki University of Technology, Finland.

Lansing, D L. 1969 *Symposium held at Ames Research Centre, Moffett Field, California, October 1969.* Exact solution for radiation of sound from a semi-infinite circular duct with application to fan and compressor noise. Analytic methods in aircraft aerodynamics.

Lansing, D. L. and Zorumski, W. E. 1973 *Journal of Sound and Vibration, 27(1) pp. 85-100.* Effects of Wall Admittance Changes on Duct Transmission and Radiation.

Lansing, D L., Drischler, J A. and Pusey, C G. 1970 *Presented at the 79th meeting of the Acoustical Society of America, Atlantic City, New Jersey, April 21-24.* Radiation of sound from an unflanged circular duct with flow.

Levine, H., and Schwinger, J. 1948 *Physical Review, v73 pp383-406* On the radiation of sound from an unflanged circular pipe.

Linfoot, E. H. (1964) Fourier methods in optical image evaluation. Focal Press. London.

Lordi, J A., 1971 *AIAA Paper no 71-617. AIAA 4th Fluid and Plasma Dynamics Conference, Palo Alto, California, June 21-23.* Noise generation by a rotating blade row in an infinite annulus.

Lordi, J A., Homicz, G F., and Rehm, R G. 1974 *AIAA Paper no 74-555, AIAA 7th Fluid and Plasma Dynamics Conference, Palo Alto, California, June 17-19.* Effects of finite duct length and blade chord on noise generation by a rotating blade row.

Lordi, J A., Homicz, G F., and Rehm, R G. 1973 *Calspan Coporation report AI-2836-A-2.* Theoretical studies on fan noise generation by a transonic compressor blade row.

Matzumoto, A. E. P. (1991). *A Study of Microphone Arrays for the Location of vibrational Sound Sources.* PhD Thesis, University of Southampton, England.

Maynard J D, Williams E G and Lee Y (1985). *Journal of the Acoustical Society of America, 78, 1395-1413.* Nearfield Acoustic Holography: I. Theory of generalised holography and the development of NAH.

Morfey, C. L. 1964 *Journal of Sound and Vibration. 1, pp. 60-87.* Rotating Pressure Patterns in Ducts: Their Generation and Transmission.

Morfey C. L. 1969 *Journal of Sound and Vibration, 9(3). pp. 367-372.* A Note on the Radiation Efficiency of Acoustic Duct Modes.

Morfey C. L. 1982 in *Noise and Vibration.* John Wiley and Sons Ltd. White, R.G. and Walker J.G. editors.

Morse, P. M. 1948 *New York : McGraw-Hill Book Company Inc. 2nd. edition.* Vibration and Sound.

Nobel, B. 1958 *Pergamon Press, New York.* Methods based on the Weiner-Hopf technique.

Pachner, J. (1956a) *Journal of the Acoustical Society of America, 28(1). pp 86-90.* On the Dependence of Directivity Patterns on the Distance from the Emitter

Pachner, J. (1956b) *Journal of the Acoustical Society of America, 28(1). pp 90-92.* Investigation of Scalar Wave Fields by means of Instantaneous Directivity Patterns.

Parrent, G. B. (1959) *Journal of the Optical Society, 49, pp 787-793.*

Rice, E. J. 1969 *Aerodynamic Noise. H.S. Ribner, ed., Univ. of Toronto Press.* Attenuation of Sound in Soft-Walled Circular Ducts.

Rice, E. J . 1975 *NASA Technical Note, TN D-7913.* Spinning Mode Sound Propagation in Ducts with Acoustic Treatment.

Rice, E. J. 1969 *AIAA Journal, 16(9). pp. 906-911.* Multi-Modal Far-Filed Acoustic Radiation Pattern using Mode Cut-Off Ratio.

Rice, E. J. 1976 *NASA Technical Memorandum, TM X-73411.* Acoustic Liner Optimum Impedance for Spinning Modes with Cut-off Ratio as the Design Criterion.

Rice, E. J. 1976 *Advances in Engineering Science, NASA CP-2001, vol. 3, pp. 883-894.* Inlet Noise Suppresser Design Method Based Upon the Distribution of Acoustic Power with Mode Cut-off Ratio.

Saule, A. V. 1977 *NASA Technical Note, TM-73839.* Far-Field Multi-Modal Acoustic Radiation Directivity.

Schenck, H. A. (1967) *Journal of the Acoustical Society of America* ***44****, 41-58.* Improved Integral Formulation for Acoustic Radiation Problems.

Skudrzyk, E. (1971) *The Foundations of Acoustics.* Springer-Verlag, New York.

Stepanishen, P. R. and Benjamin K. C. (1982) *Journal of the Acoustical Society of America* ***71****, 803-812.* Forward and Backward Propagation of Acoustic Fields using FFT methods. [See also erratum in *Journal of the Acoustical Society of America 72, 1324-1325*].

Tanna, H. K. and Morfey, C. L. 1971 *Journal of Sound and Vibration,* ***15****. pp. 325-351.* Sound Radiation from a Point Force in Circular Motion.

Trott, W. J. (1964) *Journal of the Acoustical Society of America,* ***36****. pp 1557-1568.* Underwater-Sound-Transducer Calibration from Nearfield Data.

Tyler J. M. and Sofrin T. G. 1962 *SAE Transactions,* ***70****, pp. 309-332.* Axial Flow Compressor Noise Studies.

Veronesi W A and Maynard J D (1987) *Journal of the Acoustical Society of America,* ***81****, 1307-1321.* Nearfield Acoustic Holography II.: Holographic reconstruction algorithms and computer implementation.

Wang, K S., and Tszeng, T C. 1984 *Journal of Sound and Vibration,* ***39****, pp57-79.* Propagation and radiation of sound in a finite length duct.

Watson, G. N. 1962 *Cambridge University Press.* A treatise on the theory of Bessel Functions.

Weinstein, L A. 1969 *Golem Press, Boulder, Colorado.* Theory of Diffraction and the factorisation Method (Generalised Weiner-Hopf Technique).

Williams, E. G. (1983) *Journal of the Acoustical Society of America, 74(1), 343-347.* Numerical Evaluation of the radiation from unbaffled, finite plates using the FFT.

Williams, E. G., Dardy, H. D. and Fink, R.G. (1985a) *Journal of the Acoustical Society of America, 78(2), 789-798.* Nearfield acoustical holography using an underwater, automated scanner.

Williams, E. G., Dardy, H. D. and Fink, R.G. (1985b) *Journal of the Acoustical Society of America, 78(6), 2061-2068.* A technique for measurement of structure-borne intensity in plates.

Williams, E. G. and Maynard, J. D. (1982) *Journal of the Acoustical Society of America, 72(6), 2020-2030.* Numerical Evaluation of the Rayleigh integral for planar radiators using the FFT.

Wright, S. E. 1972 *Journal of Sound and Vibration, 25(1). pp. 163-178.* Waveguides and Rotating Sources.

Wright, S. E. 1976 *ISVR Technical Report, No. 68.* Finite Source Distributions in Motion.

Zorumski, W. E. 1974 *NASA Technical Report, TR A-419.* Acoustic Theory of Axisymmetric Multi-Sectioned Ducts.

Zorumski, W. E. 1973 *Journal of the Acoustical Society of America, 54(6). pp. 1667-1673.* Generalised Radiation Impedances and Reflection Coefficients of Circular and Annular Ducts.